Hugo Miguel Martins Ferreira da Silva

Mestre

Elastic scattering of protons and oxygen ions from light nuclei

Dissertação para obtenção do Grau de Doutor em

Engenharia Física

Orientador: João Duarte Neves Cruz, Professor Auxiliar, FCT/UNL

Júri:

Presidente: Doutora Maria Adelaide de Almeida Pedro de Jesus

Arguentes: Doutor Hans-Werner Becker

Doutor Rui Manuel Coelho da Silva

Vogais: Doutora Maria Micaela Leal da Fonseca

Doutor Eduardo Jorge da Costa Alves

FACULDADE DE CIÊNCIAS E TECNOLOGIA
UNIVERSIDADE NOVA DE LISBOA

Dezembro de 2018

Elastic scattering of protons and oxygen ions from light nuclei

Acknowledgements

First of all, I would like to dedicate this thesis to my father. This work represents the battle of several years and I never forgot that he always wanted me to finish it. Despite all the people who I worked with in this last years, to whom I thank for their help, my special thanks go to:

To my wife, Cátia Santos Silva, for her support not only as a life mate but also as a colleague in the long runs of data taking.

Dr. João Cruz, who proposed me this Ph.D. thesis and to join the nuclear physics group.

Professor Adelaide Pedro de Jesus and Ángel Sánchez-Benítez, for their expertise in nuclear physics.

Dr. Hélio Luís, Dra. Micaela Fonseca and Dr. Daniel Galaviz for their support in experimental measurements.

To all the people of Laboratório de Aceleradores e Tecnologias da Radiação (LATR), and especially to Jorge Rocha, Filomena Baptista and Rute Pinheiro for the technical support in the implantations, evaporations and Van de Graaff accelerator operation.

Pamela Teubig, for her help with the evaporations at FCUL.

Luiza Oliveira, who was always available to help.

To my family, especially to my mother, who gave me emotional support during this work, but also to my friends.

Finally, to Faculdade de Ciências e Tecnologia (FCT), to Centro Tecnológico e Nuclear (CTN) and to Fundação para a Ciência e Tecnologia (FCT) for administrative and financial support.

Resumo

Este trabalho apresenta o estudo experimental da dispersão elástica de protões e oxigénio, nomeadamente das reações $^{6}Li(p,p)^{6}Li$, $^{7}Li(p,p)^{7}Li$, $^{12}C(p,p)^{12}C$, $^{19}F(p,p)^{19}F$, $^{31}P(p,p)^{31}P$, $^{16}O(^{16}O,^{16}O)^{16}O$ e $^{12}C(^{16}O,^{16}O)^{12}C$ para o intervalo de energias de 1.6 MeV até 3.9 MeV para a dispersão $^{12}C(p,p)^{12}C$, 1 MeV até 2.7 MeV para a dispersão $^{6}Li(p,p)^{6}Li$, $^{7}Li(p,p)^{7}Li$ e $^{19}F(p,p)^{19}F$, 2.6 MeV até 4 MeV para a dispersão $^{31}P(p,p)^{31}P$, 8 MeV para a dispersão $^{16}O(^{16}O,^{16}O)^{16}O$ e 2.8 MeV, 5.1 MeV e 8.1 MeV para a dispersão $^{12}C(^{16}O,^{16}O)^{12}C$.

A dispersão elástica está sempre presente nas reações nucleares e o seu estudo fornece informação que pode ser usada para cálculos teóricos. A necessidade de valores mais precisos para as correspondentes secções eficazes dá uma motivação para a sua medição, juntamente com resultados para diferentes energias e ângulos, especialmente para a frente do plano onde ocorre a reação.

Toda a componente experimental foi desenvolvida no LATR (Laboratório de Aceleradores e Tecnologias de Radiação) do CTN-IST (Campus Tecnológico e Nuclear – Instituto Superior Técnico) Sacavém, Portugal. Envolveu o uso da maior parte dos dispositivos experimentais do laboratório. Melhorias na configuração experimental foram feitas, quando necessárias. A preparação e caracterização de alvos foi alvo de um estudo intensivo, já que representa um desafio em experiências de física nuclear quando uma alta precisão dos resultados é necessária. Algumas das reações nucleares foram medidas com mais do que um alvo, adicionando confiança aos resultados obtidos. Foi efetuada uma comparação com cálculos teóricos, especialmente com os potenciais ópticos existentes na literatura, mostrando que estes necessitam de um ajuste, principalmente para elementos leves. Os resultados deste trabalho mostraram que a medição precisa de secções eficazes elásticas, especialmente a baixos ângulos, onde existem poucos dados disponíveis, pode fornecer informações fidedignas tanto para a obtenção de parâmetros do modelo óptico quanto para a caracterização de estados excitados nucleares.

Palavras-chave: Dispersão elástica, secção eficaz, reações nucleares, protões, oxigénio.

Abstract

This work presents the experimental study of elastic scattering of protons and oxygen ions, namely of the reactions $^{6}Li(p,p)^{6}Li$, $^{7}Li(p,p)^{7}Li$, $^{12}C(p,p)^{12}C$, $^{19}F(p,p)^{19}F$, $^{31}P(p,p)^{31}P$, $^{16}O(^{16}O,^{16}O)^{16}O$ and $^{12}C(^{16}O,^{16}O)^{12}C$ in the energy range from 1.6 MeV to 3.9 MeV for $^{12}C(p,p)^{12}C$ scattering, 1 MeV to 2.7 MeV for $^{6}Li(p,p)^{6}Li$, $^{7}Li(p,p)^{7}Li$ and $^{19}F(p,p)^{19}F$ scattering, 2.6 MeV to 4 MeV for $^{31}P(p,p)^{31}P$ scattering, 8 MeV for $^{16}O(^{16}O,^{16}O)^{16}O$ scattering and 2.8 MeV, 5.1 MeV and 8.1 MeV for $^{12}C(^{16}O,^{16}O)^{12}C$ scattering.

Elastic scattering is always present in nuclear reactions and its study gives us information that can be used for theoretical calculations. The need for more precise values for the corresponding cross sections gives a motivation for its measurement, along with the measurement at different energies and angles, especially forward ones.

The experimental work has been performed at LATR (Laboratório de Aceleradores e Tecnologias de Radiação) of CTN-IST (Campus Tecnológico e Nuclear – Instituto Superior Técnico) Sacavém, Portugal. It involved the use of the main experimental facilities of the laboratory. Improvements to the experimental setup needed for the measurements were made. Target preparation and characterization was also subject of intensive study, since it represents a struggle in nuclear experiments especially when high accuracy in measurements is required. Some of the cross sections were measured with more than one target, adding trust to the results obtained. Comparison with theoretical calculations was done, especially with the optical potential parameters available in the literature, showing that these calculations need some fine tuning, mainly for light elements. Our results showed that the accurate measurement of elastic scattering cross sections, especially at forward angles, where there is little data available, can provide reliable information both for obtaining accurate optical model parameters as well as for the characterization of excited states of nuclides.

Keywords: Elastic scattering, cross section, nuclear reactions, protons, oxygen.

Contents

List of Figures

List of Tables

List of symbols

a Diffuseness parameter

$\vec{B}$ Magnetic field

BS Backscattered fraction ions

b Impact parameter

c Speed of light

d Minimum distance of approach

$d\sigma/d\Omega$ Differential cross section

D_I Retained fluence

D_N Nominal fluence

$E_{c.m.}$ Center-of-mass reference frame energy

E_{lab} Laboratory reference frame energy

E_{eff} Effective energy

E_0 Incident energy

E_0 Effective (Gamow) energy

E_{exc} Energy of the excited state

E_R Resonance energy

e Electric charge

f Fraction of incident particles

$f(\theta)$ Scattering amplitude

FC Faraday Cup

G Gamow factor

h Planck constant

$\hbar$ Reduced Planck constant

j Current density

k Wave number

k_B Bolztmann constant

K Kinematic factor

$\vec{l}$ Orbital angular momentum

m Magnetic quantum number

m Mass

n_a Substrate atomic density

$n(E)$ Particles distribution

N Areal density (number of particles per square centimeter)

N_a Number of incident particles

N_R Number of interactions

$\vec{p}$ Linear momentum vector

P Particle density

P_l Legendre polynomial

q Charge state

Q Reaction Q-value

R_C Coulomb radius

R_p Projected range

r Radius

$\vec{r}$ Position vector

$r(\theta, \phi)$ Angular distribution

S Sputtering yield

S_l S-matrix

$S(E)$ Astrophysical S-factor

t Time

T Kinetic energy

T_9 Absolute temperature in billions of K

u Uncertainty

$\vec{v}$ Velocity vector

$V(r)$ Effective potential

V_C Coulomb potential

V_i Real component of volume central

W_i Imaginary component of volume central

w Width

x Depth

Y Reaction yield per incident particle

Z Atomic number

Γ Resonance width

δ Kronecker delta

δ_l Phase shift

Δ_{lab} Target thickness

Δ_b Beam energy distribution

ΔE_0 Width of Gamow energy distribution

ΔR_p Straggling

ϵ_0 Permittivity of free space

ϵ Stopping power cross section

ϵ_{eff} Effective stopping power cross section

η Sommerfeld parameter

$\theta_{c.m.}$ Scattering angle in center-of-mass frame

θ_{lab} Scattering angle in laboratory frame

μ Reduced mass

π Parity

ρ Density

σ Reaction cross section

σ_l Coulomb phase shift

ϕ Azimuthal angle

ψ Wave function

ψ_T Total wave function

Ω_{lab} Solid angle in laboratory frame

$\Omega_\gamma \varepsilon_\gamma$ Gamma ray detector absolute efficiency

List of acronyms

AMS	Accelerator Mass Spectrometry
CTN	Campus Tecnológico e Nuclear
EBS	Elastic Backscattering Spectrometry
FWHM	Full Width at Half Maximum
IBA	Ion Beam Analysis
IBANDL	Ion Beam Analysis Nuclear Data Library
IST	Instituto Superior Técnico
LATR	Laboratório de Aceleradores e Tecnologias de Radiação
NRA	Nuclear Reaction Analysis
NRV	Nuclear Reactions Video Project
PIGE	Particle Induced Gamma-ray Emission
PIPS	Passivated Implanted Planar Silicon
PIXE	Particle Induced X-ray Emission
RBS	Rutherford Backscattering Spectrometry
SRIM	Stopping and Range of Ions in Matter
XRD	X-ray Diffraction

Introduction

In nuclear physics, experiments must be combined with theoretical evaluations to study the interaction´s potential between the projectile and target due to nuclear forces. Among all the information which can be taken from those interactions, elastic scattering has an essential role, not only because it is always present in nuclear reactions, but also because it gives important information both for experimentalists and for theoreticians.

Elastic scattering occurs when there is no excitation of internal degrees of freedom of the particles in a collision process or when the sum of the kinetic energies of the colliding particles remains constant [1,2,3]. The Rutherford scattering is an example of elastic scattering that is only valid when the scattering is induced by a pure coulomb field. When the distance between the particles interacting in the collision is too small, we should take into account the nuclear forces. By the study of elastic scattering processes it is possible to get information about the interaction´s potential between the projectile and target due to nuclear forces. The goal is to obtain the effective potential from the angular distributions of scattered particles measured experimentally. That is the reason why the elastic scattering processes are so important in nuclear and particle physics. From the analytical point of view, the measurement of elastic scattering cross sections is applied to the characterization of materials using Ion Beam Analysis (IBA), which rely on the available data and its accuracy cannot exceed that of the available cross sections [4,5].

Over the years, experimental data on elastic scattering measured by the scientific community was gathered to produce theoretical evaluations in the range of energy and angles used for materials analysis. Now, these theoretical evaluations can be seen, for example, in IBANDL (Ion Beam Analysis Nuclear Data Library) [6]. Despite these efforts, many gaps have been found in experimental data, especially for light elements at forward angles. There is no theoretical evaluation available for ^{6}Li, ^{7}Li, ^{9}Be, ^{10}B, ^{11}B and for other elements the theoretical evaluation is not available in the range of energy needed or does not match the experimental values, such as for ^{19}F and ^{31}P. Concerning heavier ions, such as ^{16}O, the elastic scattering cross section can be used to calculate fusion cross section (in nuclear fusion processes involving ^{16}O), which is important to understand the process of nucleosynthesis in stellar interiors.

In this work, the elastic scattering of protons and oxygen ions has been studied. For this, a special care was taken with experimental setup development. Additionally, an exhaustive target production and characterization has been carried out, since it is one of the most important tasks in nuclear physics experiments. For protons, $^{6}Li(p,p)^{6}Li$, $^{7}Li(p,p)^{7}Li$, $^{12}C(p,p)^{12}C$, $^{19}F(p,p)^{19}F$ and $^{31}P(p,p)^{31}P$ differential cross sections were measured and the results were compared with previous data and theoretical evaluations available, when possible. $^{12}C(p,p)^{12}C$ was the benchmark reaction for this study, providing us reliability in our experimental results for the other elements. These results will be available for the scientific community both for material analysis and theoretical calculations. Concerning the elastic scattering with oxygen ions, the purpose was to start the work with heavy ions in our laboratory, preparing the setup for future measurements. Reaction of oxygen ions with ^{1}H, ^{12}C and ^{16}O were studied and data was compared with expected values.

This thesis is divided in six chapters. In chapter 1, the discussion about nuclear reactions is presented followed by the definition of reaction cross section that is essential for understanding the scattering experiments and nuclear reactions. After this, the Rutherford scattering was described before introducing the elastic scattering discussion. The optical model is presented along with simulation codes available for the calculation of optical model parameters. In chapter 2, the most relevant data on these reactions is presented showing the need for new measurements. In chapter 3, the description of the experimental setup is made along with experimental procedures that were done during this work. Chapter 4 includes all information regarding target preparation and characterization. Throughout this chapter, the experimental setup used for target preparation and analytical techniques used for its characterization are described. In chapter 5, the elastic cross section measurements are described and the results obtained are presented. Comparison with previous results is done and a discussion of the results is addressed. The conclusions that can be drawn from this work are presented in Chapter 6.

References

[1] K. Krane, Introductory Nuclear Physics, John Wiley & Sons, 1988.

[2] C. Iliadis, Nuclear Physics of Stars, Wiley-VCH, 2007.

[3] C. Fiolhais, R. Marques, Física Nuclear, Fundação Calouste Gulbenkian, 1993.

[4] A.F. Gurbich, Nucl. Intr. and Meth. B 268 (2010) 1703.

[5] J.A. Leavitt, L.C. McIntyre Jr., M.R. Weller, in: J.R. Tesmer, M. Nastasi (Eds.), Handbook of Modern Ion Beam Analysis, MRS, Pittsburgh, PA, 1995.

[6] IBANDL database, IAEA, 2017 at http://www-nds.iaea.org/ibandl/.

1

Chapter 1 - Nuclear Reactions Cross Sections

1.1 Introduction

When particles coming from an accelerator, reactor or a radioactive source hit a target there is the possibility that a nuclear reaction takes place [1]. In this chapter, we will describe the types of reactions and conservation laws, the energetics of nuclear reactions before entering in the discussion of nuclear reactions cross section and present the equations necessary to calculate it.

1.2 Types of reactions and conservation laws

Typically, a nuclear reaction is designated by $a + X \rightarrow b + Y$, where a is the accelerated projectile, X is the target, b and Y are the reaction products. Sometimes, the same reaction can be presented in a compact way X(a,b)Y, which will be seen in this thesis. By definition, the Q-value is given by:

$$Q = \left(m_{initial} - m_{final}\right)c^2$$
$$= (m_X + m_a - m_Y - m_b)c^2 \qquad 1.1$$

where m_i is the mass of each particle and c is the speed of light in vaccum.

There are many ways to classify the nuclear reactions. If the incident and outgoing particles are the same, it is an elastic scattering process if the products are in the ground states or inelastic scattering process if one of the products is in the excited state. In this work, we will focus in the elastic scattering process and how to measure the nuclear reaction rates.

- Elastic scattering $(\boldsymbol{p}, \boldsymbol{p})$:

$p + {}^{A}_{Z}X \rightarrow {}^{A}_{Z}X + p$;

$Q = 0$;

Kinetic energy is conserved;

- Inelastic scattering $(p, p'\gamma)$:

$p + {}^{A}_{Z}X \rightarrow {}^{A}_{Z}X^{*} + p';$

$Q = -E_{exc};$

where E_{exc} is the energy of the excited state ${}^{A}_{Z}X^{*}$.

Considering the interaction process, we can identify two opposites: direct reactions and compound nucleus reactions. In direct reactions, the reaction proceeds in one step: $a + X \rightarrow b + Y$. In this case, only few nucleons take part in the reaction with the remaining nucleons of the targets being only spectators. In compound nucleus reactions, the incoming particle and the target nuclei briefly share the energy before the outgoing nucleon is ejected. In this case, we have $a + X \rightarrow [C] \rightarrow b + Y$. When the cross section dependence on projectile energy shows resonances, the energy available matches an excited state of the compound nucleus for that reaction.

1.3 Energetics of nuclear reactions

The conservation of the total energy in a typical nuclear reaction gives us:

$$m_X c^2 + T_X + m_a c^2 + T_a = m_Y c^2 + T_Y + m_b c^2 + T_b \qquad 1.2$$

where T_i are kinetic energies (for which we can use the nonrelativistic approximation $\frac{1}{2}mv^2$ at low energies) and m_i are rest masses.

The Q-value is the same as the excess of kinetic energy of the products:

$$Q = T_{final} - T_{inicial}$$
$$= T_Y + T_b - T_X - T_a \qquad 1.3$$

The changes in mass and kinetic energy must be related to the expression of special relativity $\Delta E = \Delta m c^2$, where any variation in kinetic energy of the particles system must be balanced by the same variation in rest energy.

The equations are valid in any frame of reference that we choose to work. If we consider a reaction plane by the direction of the incident beam and one of the outgoing

particles, then conservation of the component of the momentum perpendicular to the plane implies that the second particle must lie in the same plane as well.

Conservation of the linear momentum along and perpendicular to the beam direction gives us (figure 1.1):

$$p_a = p_b \cos\theta + p_Y \cos\xi \qquad 1.4a$$

$$0 = p_b \operatorname{sen}\theta - p_Y \sin\xi \qquad 1.4b$$

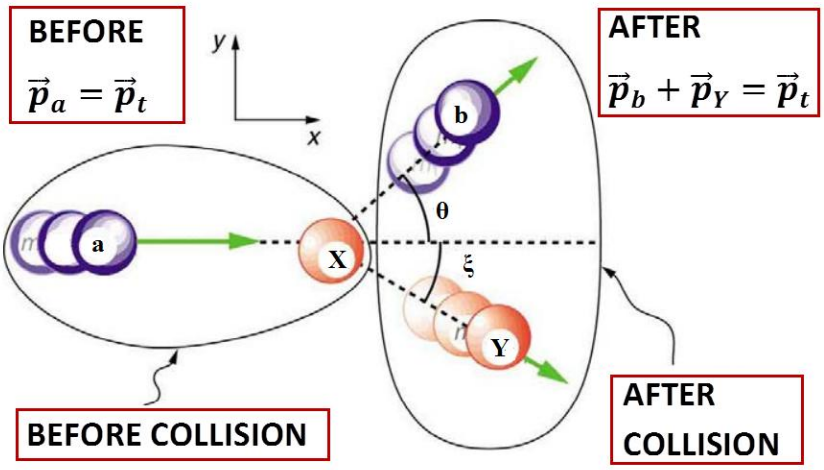

Figure 1.1) Linear momentum conservation in a nuclear reaction.

The three last equations gives us a system of three equations and four unknowns (θ, ξ, T_Y e T_b), if Q and T_a are known quantities and therefore p_a is a parameter that can be controlled. This system has no unique solution.

$$\begin{cases} Q = T_Y + T_b - T_X - T_a \\ p_a = p_b \cos\theta + p_Y \cos\xi \\ 0 = p_b \sin\theta - p_Y \sin\xi \end{cases}$$

As usually we don´t observe the particle Y, it is possible to eliminate ξ and T_Y from the equations and find a relation between T_b and θ. After some algebra (see Appendix A.1 for details), $T_b^{1/2}$ is obtained:

$$T_b^{1/2} = \frac{(m_a m_b T_a)^{1/2} \cos\theta \pm \{m_a m_b T_a cos^2\theta + (m_Y + m_b)[m_Y Q + (m_Y - m_a)T_a]\}^{1/2}}{m_Y + m_b} \qquad 1.5$$

There is an absolute minimum value of T_a below which the reaction is not possible. This happens when $Q < 0$ and it is called threshold energy T_{th} ($\theta = 0°$):

$$T_{th} = (-Q)\frac{m_Y + m_b}{m_Y + m_b - m_a} \quad 1.6$$

If $Q > 0$, there is no condition for which the reaction does not occur.

A double value situation for T_b in equation 1.5 occurs for energies between T_{th} and the upper limit:

$$T_a^{'} = (-Q)\frac{m_Y}{m_Y - m_a} \quad 1.7$$

This situation also occurs only when $Q < 0$ and $\theta < \frac{\pi}{2}$ and is important for reactions involving nuclei with comparable masses.

1.4 Reaction Cross Section

The cross section is a measure of the probability of a given reaction to occur [1,2,3]. A beam of N_a/t (particles per unit time) is entering the nuclear chamber and if the number of target nuclei is N per unit area and considering the reaction cross section to be σ, the number of interactions N_R per unit time is given by:

$$\frac{N_R}{t} = \frac{N_a}{t}\sigma N \Leftrightarrow \sigma = \frac{N_R}{N_a . N} \quad 1.8$$

The units of reactions cross sections are units of area, cm^2 or more frequently barns ($1\ b = 10^{-24} cm^2$).

If a detector is placed in a direction (θ, ϕ) with respect to the beam direction, the detector defines a small solid angle $d\Omega$ at the target and can´t detect all outgoing particles. Thus, only a small fraction dN_R is taken into account and therefore only a small fraction of the cross section is measured.

$$\frac{dN_R}{d\Omega} = N . N_a \frac{d\sigma}{d\Omega} \quad 1.9$$

Moreover, the outgoing particles will not in general be emitted isotropically, but they will have an angular distribution that will depend on θ and possibly on ϕ. If this angular distribution function is represented by a function $r(\theta, \phi)$, we will have that $dN_R = r(\theta, \phi)d\Omega/4\pi$. Then

$$\frac{d\sigma}{d\Omega} = \frac{r(\theta, \phi)}{4\pi N. N_a} \qquad 1.10$$

The quantity $\frac{d\sigma}{d\Omega}$ is called differential cross section and its measure gives us important information about the angular distribution of the reaction products. Knowing that the solid angle is measured in steradian, the unit for the differential cross section is barns/steradian. The reaction cross section can be calculated by integrating $\frac{d\sigma}{d\Omega}$ over all angles. With the substitution $d\Omega = sin\,\theta d\theta d\phi$, we have that:

$$\sigma = \int \frac{d\sigma}{d\Omega} d\Omega = \int_0^{\pi} sin\,\theta\, d\theta \int_0^{2\pi} d\phi\, \frac{d\sigma}{d\Omega} \qquad 1.11$$

If $\frac{d\sigma}{d\Omega}$ is constant, the integral gives us that $\sigma = 4\pi(d\sigma/d\Omega)$.

1.5 Coulomb Scattering

Coulomb scattering is the electrostatic scattering of a beam of charged particles, due to the fact that the nucleus is electrically charged. This scattering can be either elastic or inelastic.

The elastic Coulomb scattering is also called Rutherford scattering in tribute to Ernest Rutherford, who discovered the nucleus from his experiences with alpha particles.

It is considered that far from the nucleus, a particle has negligible potential energy, being endowed of only its kinetic energy. The particle approaches the target nucleus along a straight line that would pass a distance b from the nucleus, which we call impact parameter. As it approaches the nucleus, the particle reaches a minimum distance d that depends on the impact parameter.

At intermediary points in the trajectory, the energy is partly kinetic and partly potential and the conservation law gives us for any impact parameter:

$$\frac{1}{2}mv_0^2 = \frac{1}{2}mv^2 + \frac{1}{4\pi\epsilon_0}\frac{zZe^2}{r} \qquad 1.12$$

where v is the velocity, ze is the charge of the projectile, Ze is the charge of the target and ϵ_0 is the permittivity of free space.

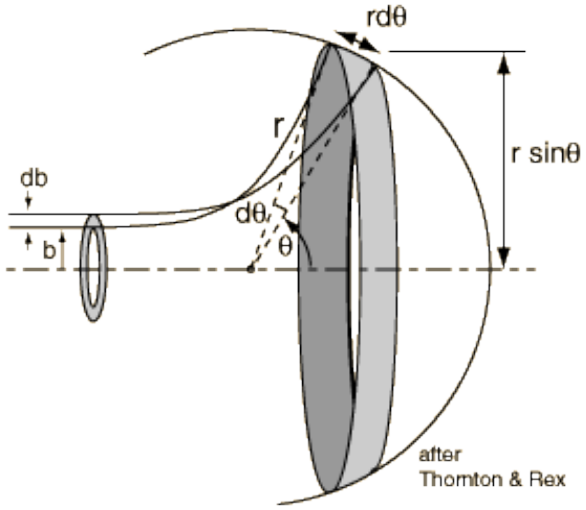

Figure 1.2) Particles entering the ring between *b* and *b*+*db* are scattered inside a ring of angular widht dθ.

This scattering has cylindrical symmetry about the beam axis due to the symmetry of Coulomb force and the differential cross section becomes independent from the azimuthal angle ϕ. Particles with impact parameter between b and $b + db$ are scattered inside the ring with angles between θ and $\theta + d\theta$, as we can see in figure 1.2. If the target nucleus has N nuclei per unit area, assuming that the target is thin enough not to occur a shadow effect of a nucleus by another, the fraction of incident particles which pass through the ring is:

$$df = N(2\pi b db) \qquad 1.13$$

The fraction f for impact parameters less than b is:

$$f = N\pi b^2 \qquad 1.14$$

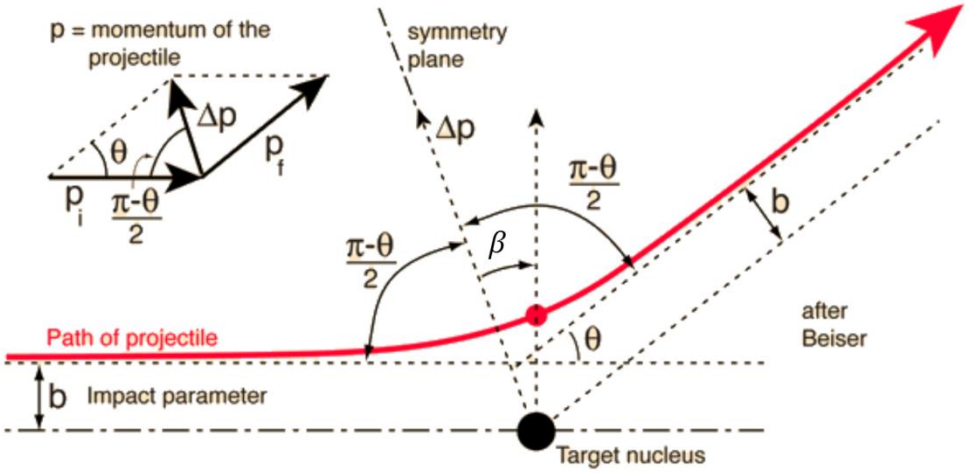

Figure 1.3) The hyperbolic trajectory of a scattered particle. The change on its momentum is $\Delta\vec{p}$.

The linear momentum of scattered particles changes only in direction (figure 1.3). Far from the scattering, the initial and final linear momentum is mv_0 (assuming that the target is so heavy that stays at rest. The change in the momentum is a vector of magnitude (see Appendix A.2):

$$\Delta p = 2p_i sin\frac{\theta}{2} = 2mv_0\, sin\frac{\theta}{2} \qquad 1.15$$

According with Newton´s second law in the form $F = dp/dt$, this is equal to the Coulomb force in that same direction:

$$\Delta p = \int dp = \int F dt = \frac{zZe^2}{4\pi\epsilon_0}\int \frac{dt}{r^2} cos\,\beta \qquad 1.16$$

where β is the angle between the bisector and the instantaneous vector $\vec{r}$ locating the particle. In the initial position, far from the scattering ($t = 0$), the angle β takes the value $-(\pi/2 - \theta/2)$; in the final position ($t = +\infty$), the angle β takes the value $+(\pi/2 - \theta/2)$.

The instantaneous velocity $\vec{v}$ can be written as function of its radial and tangential components:

$$\vec{v} = \frac{dr}{dt}\hat{r} + r\frac{d\beta}{dt}\hat{\beta} \qquad 1.17$$

where $\hat{r}$ e $\hat{\beta}$ are unit vectors in the radial and tangential directions, respectively. Only the tangential direction contributes to the angular momentum relative to the nucleus:

$$l = |m\vec{r} \times \vec{v}| = mr^2\frac{d\beta}{dt} \qquad 1.18$$

Far from the nucleus, the angular momentum takes the value mv_0b, thus the angular momentum conservation gives us that:

$$mv_0b = mr^2\frac{d\beta}{dt} \Leftrightarrow$$

$$\frac{d\beta}{v_0b} = \frac{dt}{r^2} \quad 1.19$$

Replacing it in the linear momentum variation equation:

$$\Delta p = \frac{zZe^2}{4\pi\epsilon_0 v_0 b}\int_{-(\pi/2-\theta/2)}^{+(\pi/2-\theta/2)} \cos\beta\, d\beta$$

$$= \frac{zZe^2}{2\pi\epsilon_0 v_0 b} cos\frac{\theta}{2} \quad 1.20$$

Therefore, the conservation of the linear momentum, angular momentum and energy, imply the following relation between the scattering angle θ and the impact parameter b:

$$b = \frac{d}{2} cot\frac{\theta}{2} \quad 1.21$$

where d is the distance of closest approach.

Reminding that $df = N(2\pi b db)$, we have:

$$|df| = \pi N\frac{d^2}{4} cot\frac{\theta}{2} csc^2\frac{\theta}{2} d\theta \quad 1.22$$

and the rate at which particles reach the ring, per solid angle unit, is given by:

$$r(\theta,\phi) = \frac{N_a|df|}{d\Omega/4\pi} \quad 1.23$$

With $d\Omega = 2\pi \sin\theta\, d\theta$ for an axial geometry ($\sin\theta\, d\theta d\phi$), we have:

$$\frac{d\sigma}{d\Omega} = \left(\frac{zZe^2}{4\pi\epsilon_0}\right)^2 \left(\frac{1}{4T_a}\right)^2 \frac{1}{sin^4\frac{\theta}{2}} \quad 1.24$$

This is the Rutherford differential cross section, valid for the center of mass reference frame or for an infinitely heavy target in the laboratory frame. The dependence of this formula on the kinetic energy T_a and angle θ (figures 1.4 and 1.5) gives us valuable information in nuclear physics experiments.

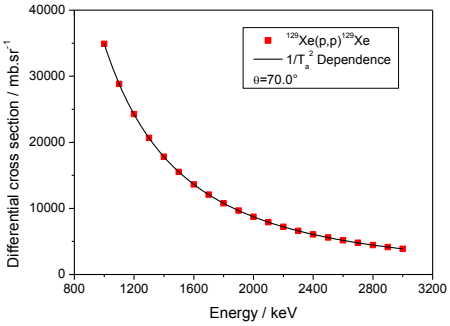

Figure 1.4) Dependence of Rutherford cross section with energy for ^{129}Xe(p,p)^{129}Xe

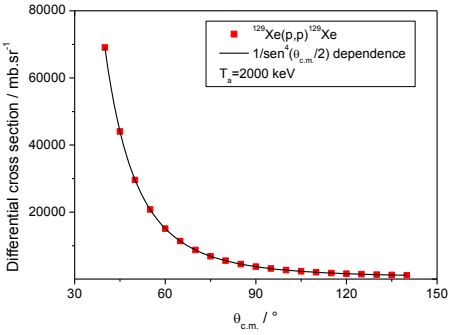

Figure 1.5) Dependence of Rutherford cross section with angle for ^{129}Xe(p,p)^{129}Xe.

To take into account relativistic effects, Rutherford cross section modifies to Mott cross section [4,5], given by:

$$\left(\frac{d\sigma}{d\Omega}\right)_{Mott} = \left(\frac{d\sigma}{d\Omega}\right)_{Ruth} \times \left(1 - \beta^2 . sin^2\left(\frac{\theta_{c.m.}}{2}\right)\right) \qquad 1.25$$

where $\beta = \frac{v}{c}$, being v the velocity and c the speed of light.

The Rutherford cross section presented was deduced taking into account the classical formalism. The same result can be obtained by solving the Schrödinger equation (see below) for a point-Coulomb potential [6].

1.6 Elastic Scattering

Elastic scattering may be described as a collision process where the internal degrees of freedom of the involved partners play no role and the sum of their kinetic energies remain constant. Rutherford scattering is an example of elastic scattering caused by the Coulomb field of the nucleus. When the distance between the nuclei becomes too small, the nuclear potential starts also to contribute to the collision, and shifts from a pure Coulombian process necessarily occur. Therefore, the interactions between nucleons participating in nuclear reactions must be described using quantum mechanics. The scattering problems will be

treated using the center-of-mass coordinates considering the scattering of only one particle with reduced mass by a force located in the center-of-mass.

One of the problems describing nucleon-nucleon interaction is the absence of knowledge of the fundamental strong interaction, so approximations are needed. The use an effective potential is applied instead of the calculation of all nucleon-nucleon interactions [3]. These effective potentials are deduced for specific reaction and energies; so they are not general. They depend on the magnitude of the radius vector, but not on its direction, $V(\vec{r}) = V(r)$, where $\vec{r} = \vec{r}_a - \vec{r}_X$.

The theoretical treatment of elastic scattering involves solutions of the time dependent Schrödinger equation or the scattering of wave packets, which consists in solving scattering problems by decomposing each wave into its constituent angular momentum components and solving using boundary conditions but the more important physics aspects can be derived using the stationary problem of the time-independent Schrödinger equation, which is:

$$\left[-\frac{\hbar^2}{2m}\nabla^2 + V(\vec{r})\right]\psi(\vec{r}) = E\psi(\vec{r}) \qquad 1.26$$

where E is the energy.

The total wave function can be expressed by the sum of two stationary waves, an incoming plane wave and an outgoing spherical wave:

$$\psi(\vec{r}) = C\left[e^{i\vec{k}.\vec{r}} + f(\theta)\frac{e^{ikr}}{r}\right] \qquad 1.27$$

where $e^{i\vec{k}.\vec{r}}$ is the incoming wave traveling in the z-direction (free particle), so $e^{i\vec{k}.\vec{r}} = e^{ikz}$ and $f(\theta)\frac{e^{ikr}}{r}$ represents the spherical wave where $f(\theta)$ is the scattering amplitude and the factor $1/r$ shows the dependence with the inverse square law. C is a overall normalization factor.

The particle density (in units of inverse volume) is given by $P = \psi^*\psi$ and the current density (in units of inverse area per time) of beam particles is given by $j = vP$. For the incoming wave, we have:

$$j_a = v_a\left(Ce^{-ikr}\right)\left(Ce^{ikr}\right) = v_aC^2 \qquad 1.28$$

For the outgoing wave we obtain:

$$j_s = v_s \left[C f^*(\theta) \frac{e^{-ikr}}{r} \right] \left[C f(\theta) \frac{e^{ikr}}{r} \right] = v_s C^2 |f(\theta)|^2 \frac{1}{r^2} \qquad 1.29$$

The differential cross section is given by $\left(\frac{d\sigma}{d\Omega}\right) = \frac{j_s r^2}{j_a} = |f(\theta)|^2$, since for elastic scattering we have that $v_a = v_s$. This result shows that the differential cross section is equal to the square of the scattering amplitude. This result could also be deduced from the quantum expression for the current density:

$$\vec{j} = \frac{\hbar}{2mi} (\psi^* \vec{\nabla} \psi - \psi \vec{\nabla} \psi^*) \qquad 1.30$$

The specific problem is the calculation of the scattering amplitude $f(\theta)$ for a given potential. Once knowing this, the differential cross section is easily calculated as shown before. In the elastic scattering process, for each impact parameter b there is a scattering angle θ.

Usually, we first consider the problem using a force-free particle. The plane wave $e^{i\vec{k}.\vec{r}}$ represents a free particle of momentum $\vec{p} = \hbar\vec{k}$ and energy given by $E = \frac{\hbar^2 k^2}{2m}$. As the potential is $V(r) = 0$, the scattering amplitude is also $f(\theta) = 0$. As said before, the plane wave can also be given by e^{ikz} if we choose the z axis along $\vec{k}$. Since $\vec{L} = \vec{r} \times \vec{p}$, we only need to consider values of $m = 0$ for the magnetic quantum number. The spherical harmonics (see Appendix A.3) for this case are given by:

$$Y_{l0} = \sqrt{\frac{2l+1}{4\pi}} P_l(cos\,\theta) \qquad 1.31$$

where $P_l(\cos\theta)$ is a Legendre polynomial.

With the substitutions $E = \frac{p^2}{(2m)} = \frac{\hbar^2 k^2}{(2m)}$ and $\rho \equiv kr$, the radial equation for a free particle can be written as $\frac{d^2 u_l}{d\rho^2} + \left[1 - \frac{l(l+1)}{\rho^2}\right] u_l = 0$. The solutions are called spherical Bessel functions and it is possible to write for the asymptotic values:

$$u_l{}^{f.p.} = (kr) j_l(kr) = \sin(kr - \tfrac{l\pi}{2}), r \to \infty \qquad 1.32$$

The eigenfunctions for a free particle, $j_l(kr)P_l(\cos\theta)$, form a complete orthonomal set. So, we can expand the plane wave according to

$$e^{ikz} = \sum_{l=0}^{\infty} (2l+1) i^l j_l(kr) P_l(\cos\theta) \tag{1.33}$$

The plane wave with orbital angular momentum kr has been expanded into a set of partial waves, each having an orbital angular momentum $\hbar\sqrt{(l(l+1)}$, an amplitude of $(2l+1)$ and a phase factor i^l. For very large distances appropriate for any experimental detector geometry, we find for a free particle:

$$\psi_T^{f.p.} = \sum_{l=0}^{\infty} (2l+1) i^l \frac{\sin(kr - \frac{l\pi}{2})}{kr} P_l(\cos\theta),\ r \to \infty \tag{1.34}$$

If we take into account the relationship $\sin x = (i/2)\left(e^{-ix} - e^{ix}\right)$ we can write

$$\psi_T^{f.p.} = \frac{1}{2kr} \sum_{l=0}^{\infty} (2l+1) i^{l+1} \left[e^{-i(kr - \frac{l\pi}{2})} - e^{i(kr - \frac{l\pi}{2})} \right] P_l(\cos\theta),\ r \to \infty \tag{1.35}$$

For the special case of s-waves in which $l = 0$, we have ${u_0}^{f.p.} = \sin(kr)$ instead of equation 1.32. For this case, the equations 1.34 and 1.35 are not only valid for $r \to \infty$, but apply to all distances.

For a central potential ($V(r) \neq 0$ and therefore $f(\theta) \neq 0$), the only difference is in the radial equation, that will change. The ${u_l}^{f.p.}$ will change for u_l that differ just for small r where $V(r) \neq 0$. For large distances $V(r) = 0$ and the two functions satisfy the same radial equation.

$$u_l = \sin(kr - \frac{l\pi}{2} + \delta_l),\ r \to \infty \tag{1.36}$$

The only difference between this wave function and the radial wave function for a free particle is the phase shift δ_l that contains the r dependence in the region where $V(r) \neq 0$. For s-waves ($l = 0$) the equation 1.36 applies to all the distances outside the potential.

Now, it´s possible to write the total wave function as a sum of partial waves:

$$e^{ikz} + f(\theta)\frac{e^{ikr}}{r} = \sum_{l=0}^{\infty} b_l \frac{u_l(kr)}{kr} P_l(\cos\theta) \tag{1.37}$$

With the inclusion of the expansion coefficients $b_l = (2l+1) i^l e^{i\delta_l}$ it is possible to rewrite the equation in the form:

$$e^{ikz} + f(\theta)\frac{e^{ikr}}{r} = \sum_{l=0}^{\infty}(2l+1)i^l e^{i\delta_l}\frac{\sin(kr-\frac{l\pi}{2}+\delta_l)}{kr}P_l(\cos\theta), r \to \infty \quad 1.38$$

Using the relation $\sin x = (i/2)\left(e^{-ix} - e^{ix}\right)$ the total wave function can be written as:

$$\psi_T = \frac{1}{2kr}\sum_{l=0}^{\infty}(2l+1)i^{l+1}\left[e^{-i(kr-\frac{l\pi}{2})} - e^{2i\delta_l}e^{i(kr-\frac{l\pi}{2})}\right]P_l(\cos\theta), r \to \infty \quad 1.39$$

The difference between this wave function and the total wave function for a free particle is that the potential modifies at large distances each outgoing spherical wave by a factor $e^{2i\delta_l}$ (S_l matrix) and thereby shifts each outgoing spherical wave by a phase δ_l.

The solutions for the scattering amplitude can be achieved by writing

$$f(\theta)\frac{e^{ikr}}{r} = \psi_T - \psi_T^{f.p.}$$

$$= \frac{1}{2kr}\sum_{l=0}^{\infty}(2l+1)i^{l+1}\left[e^{i\left(kr-\frac{l\pi}{2}\right)}(1 - e^{2i\delta_l})\right]P_l(\cos\theta) \quad 1.40$$

Knowing that $e^{i\frac{l\pi}{2}} = \cos\left(\frac{l\pi}{2}\right) + i\sin\left(\frac{l\pi}{2}\right) = i^l$ and that $e^{i\delta_l}\sin\delta \equiv \left(\frac{i}{2}\right)(1 - e^{2i\delta_l})$ gives:

$$f(\theta) = \frac{i}{2k}\sum_{l=0}^{\infty}(2l+1)(1 - e^{2i\delta_l})P_l(\cos\theta)$$

$$= \frac{1}{k}\sum_{l=0}^{\infty}(2l+1)e^{i\delta_l}\sin\delta_l\, P_l(\cos\theta) \quad 1.41$$

The introduction of a scattering potential shifts the phase of each outgoing partial wave, so the differential cross section can be written as:

$$\left(\frac{d\sigma}{d\Omega}\right) = f^*(\theta)f(\theta) = \frac{1}{4k^2}\left|\sum_{l=0}^{\infty}(2l+1)(1 - e^{2i\delta_l})P_l(\cos\theta)\right|^2 \quad 1.42$$

For each value of l, the function $P_l(\cos\theta)$ translates into a specific angular distribution. Concerning this, we can use the orthogonality relation for Legendre polynomials

$$\int_{d\Omega} P_l(\cos\theta)\, P_{l'}(\cos\theta)\, d\Omega = \frac{4\pi}{2l+1}\delta_{ll'} \quad 1.43$$

Where $\delta_{ll'}$ is a Kronecker symbol, and thus we can obtain the total elastic cross section

$$\sigma_{el} = \int \left(\frac{d\sigma}{d\Omega}\right)_{el} d\Omega = \sum_{l=0}^{\infty} \sigma_{el,l}$$

$$\sigma_{el} = \frac{\pi}{k^2}(2l+1)\left|1 - e^{2i\delta_l}\right|^2 = \frac{4\pi}{k^2}(2l+1)\sin^2\delta_l \qquad 1.44$$

Again, for the cases where $l = 0$ we find

$$\left(\frac{d\sigma}{d\Omega}\right)_{el} = \frac{1}{k^2}\sin^2\delta_0$$

$$\sigma_{el,0} = \frac{4\pi}{k^2}\sin^2\delta_0 \qquad 1.45$$

These results show that the angular distribution becomes isotropic (independent of θ). The cross section is determined by the phase shift δ_l, which approaches 0 when the potential $V(r) \to 0$ for all l.

These results are obtained assuming that at least one of the particles is uncharged. If both particles are charged, the phase δ_l must be replaced by $\delta_l + \sigma_l$, which takes into account short-range nuclear potential and the long-range Coulomb potential. So,

$$1 - e^{2i(\delta_l+\sigma_l)} = \left(1 - e^{2i\sigma_l}\right) + e^{2i\sigma_l}(1 - e^{2i\delta_l}) \qquad 1.46$$

Thus, the scattering amplitude can be described by:

$$f(\theta) = \frac{i}{2k}\sum_{l=0}^{\infty}(2l+1)\left[1 - e^{2i(\delta_l+\sigma_l)}\right]P_l(\cos\theta)$$

$$= \frac{i}{2k}\sum_{l=0}^{\infty}(2l+1)\left(1 - e^{2i\sigma_l}\right)P_l(\cos\theta) + \frac{i}{2k}\sum_{l=0}^{\infty}(2l+1)e^{2i\sigma_l}(1 - e^{2i\delta_l})P_l(\cos\theta) \qquad 1.47$$

The first term of the equation describes the contribution of the Coulomb field for the scattering amplitude (Rutherford scattering). As the second term contains both phase shifts $\delta_l + \sigma_l$, the cross section will be dependent on both nuclear and Coulomb potential. The differential cross section can be given by [7]:

$$\left(\frac{d\sigma}{d\Omega}\right) = |f_c(\theta) + f_n(\theta)|^2 = |f_c(\theta)|^2 + |f_n(\theta)|^2 + 2Re[f_c^*(\theta)f_n(\theta)] \qquad 1.48$$

This series expression for Coulomb scattering does not converge, because the Coulomb potential does not go to zero fast enough for large r, and the phase shifts σ_l never

go to zero for large l. This series only has meaning if a screened Coulomb potential is used, and then the radius let tend to infinity. In this case, the Coulomb scattering amplitude was found to be [6,7]:

$$f_C(\theta) = -\frac{\eta}{2k\sin^2(\theta/2)} e^{[-i\eta \ln(\sin^2(\theta/2))+2i\sigma_0]} \qquad 1.49$$

where η is called the Sommerfeld parameter.

Of course, elastic scattering is not the only process occurring between two particles. Particle capture, inelastic scattering or even fusion can occur. Different channels correspond to a specific set of conditions for the outgoing particle.

If elastic scattering is the only possible process, the number of incoming particles is equal to the number of outgoing particles surrounding the target nucleus. Concerning this, the integral over the current density j_T, corresponding to the total wave function ψ_T is zero

$$\int_\Omega j_T \, d\Omega = 0 \qquad 1.50$$

If there are other nonelastic processes occurring, a fraction of the incoming particles will change their kinetic energies (inelastic scattering) or change identity (particle capture). A defined number of the incoming particles will disappear and there will be a net current of particles into the imaginary sphere. This disappearance from the elastic channel corresponds to the reaction cross section.

$$\sigma_{re} = \frac{r^2}{j_a}\int_\Omega j_T \, d\Omega \qquad 1.51$$

The total wave function ψ_T corresponding to a current density j_T is the total wave function for elastic scattering. It is important to relate the reaction cross section to the phase shifts. The quantum mechanical expression for the current density was presented in equation 1.30.

For the incoming plane wave e^{ikz} we have:

$$j_a = \frac{\hbar}{2mi}\left[e^{-ikz}\left(e^{ikz}ik\right) - e^{-ikz}(-ik)e^{ikz}\right] = \frac{\hbar k}{m} \qquad 1.52$$

The substitution of the total elastic scattering wave function ψ_T gives us:

$$j_T = \frac{\hbar}{4mkr^2}\left\{\left|\sum_{l=0}^{\infty}(2l+1)i^{l+1}e^{il\pi/2}P_l(\cos\theta)\right|^2 - \left|\sum_{l=0}^{\infty}(2l+1)i^{l+1}e^{2i\delta_l}e^{-il\pi/2}P_l(\cos\theta)\right|^2\right\} \quad 1.53$$

Applying the orthogonality relation for Legendre polynomials (equation 1.43) we get:

$$\sigma_{re} = \sum_{l=0}^{\infty}\sigma_{re,l}$$

$$\sigma_{re,l} = \frac{\pi}{k^2}(2l+1)\left(1 - \left|e^{2i\delta_l}\right|^2\right) \quad 1.54$$

where $\left|e^{2i\delta_l}\right|^2 \leq 1$ in order to $\sigma_{re,l} \geq 0$. Usually the phase shift δ_l is a complex number, where $\delta_l = \delta_{l_1} + i\delta_{l_2}$. If δ_l is real we have $\left|e^{2i\delta_l}\right|^2$=1. It means that the only process occurring is the elastic scattering.

We can find a maximum at $e^{2i\delta_l} = -1$, where $\sigma_{el,l}^{max} = \frac{4\pi}{k^2}(2l+1)$, and $\sigma_{re,l} = 0$. The maximum reaction cross section is obtained when $e^{2i\delta_l} = 0$, having $\sigma_{re,l}^{max} = \sigma_{el,l} = \frac{\pi}{k^2}(2l+1)$.

The results show that is possible the elastic reaction to occur without the presence of other reactions, but the inverse is not possible, as we can see in figure 1.6. It is also possible to note that when the reaction cross section exhibits a maximum, both the reaction cross section and the elastic cross section have the same value.

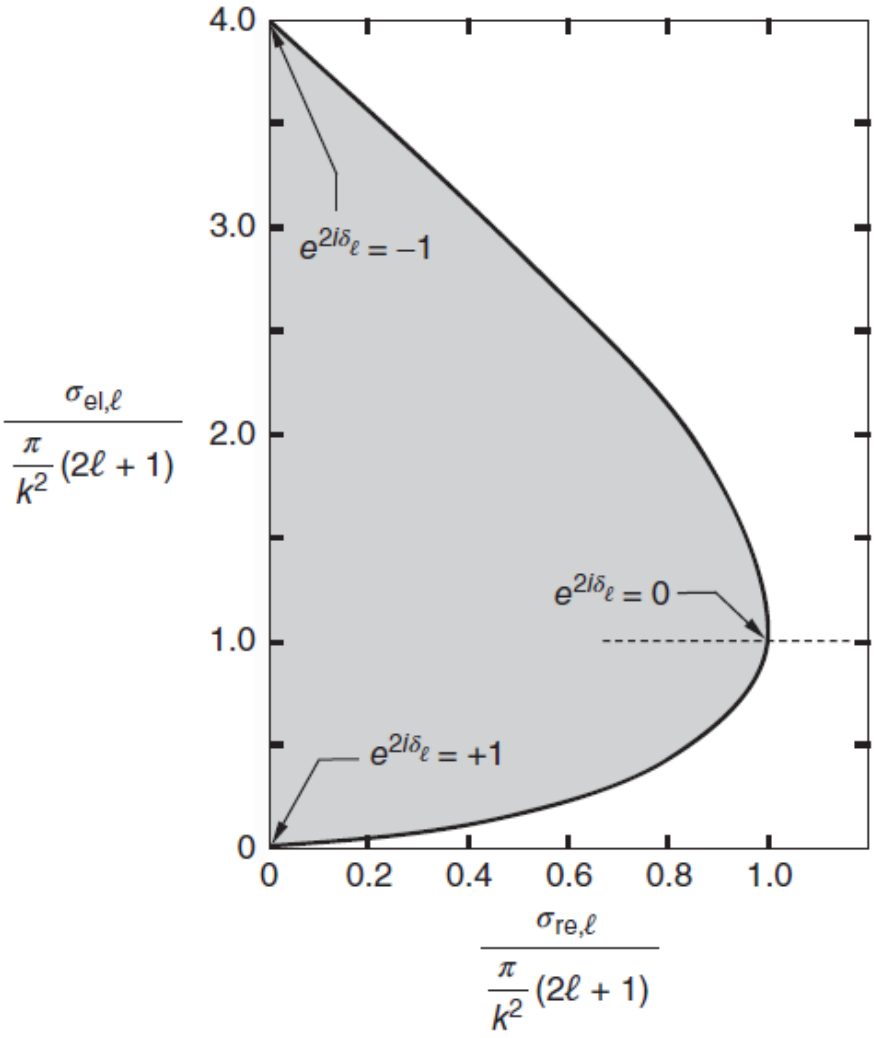

Figure 1.6) Upper and lower limits for elastic cross section in a nuclear reaction.

The theory of scattering has been used for studying the nuclear potential. The differential cross section $d\sigma/d\Omega$ is obtained by experiment and used to find the potential $V(r)$. The experimental phase shifts δ_l are obtained by fitting the cross section formula to experimental angular distribution data. A fit is achieved using a small number of terms in the partial wave expansion. This method is used for several values of incident kinetic energy. After this, a potential $V(r)$ is obtained, reproducing the observed phase shifts, by solving the schrödinger equation numerically for each value of l.

1.7 The Optical Model

The interaction potential between a nucleon and a spherical nucleus is usually described by an attractive nuclear well of depth V_R with radius r_R slightly larger than the nuclear radius, and a diffuse nuclear surface (a_R), being r the distance between the center of mass of the two nuclei [6]. The nuclear scattering is treated in similar form as the scattering of light by a glass sphere and the name of the model derives of this analogy. Most commonly we have the Woods-Saxon shape:

$$V_R(r) = \frac{-V_R}{1 + e^{(r-r_R)/a_R}} \qquad 1.55$$

Usually, the central depth is about 50 MeV and the diffuseness a_R is about 0.6 fm. The radius r_R is proportional to the size of the nucleus and commonly around $r_R = r_r A^{1/3}$ for a nucleus with A nucleons where r_r is approximately 1.2 fm. When the interaction is between two nuclei with mass numbers A_1 and A_2, we have $r_R = r_r\left(A_1^{1/3} + A_2^{1/3}\right)$.

Charged particles experience also a Coulomb potential. If the charge Ze is uniformly distributed over a radius of $R_C = r_C A^{1/3}$ for a nucleus of A nucleons, then for a incident nucleon of charge $Z_p e$, the Coulomb contribution is given by:

$$V_C = \frac{Z.Z_p e^2}{2R_C}\left(3 - \frac{r^2}{R_C^2}\right), if\ r \le R_C$$

$$= \frac{Z.Z_p e^2}{r}, if\ r > R_C \qquad 1.56$$

The nuclear and Coulomb potentials are usually combined with an imaginary term and a spin-orbit part. The imaginary term, which takes into account the absorption effects (including inelastic scattering), is also often described by a Woods-Saxon form:

$$W_I(r) = \frac{-W_I}{1 + e^{(r-r_I)/a_I}} \qquad 1.57$$

For a similar geometry, $r_I \ge r_R$ and $a_I \approx a_R$ and the depth W_I fitted to the experiments. There will be also spin-orbit forces that couple the nucleon spin to its orbital motion.

All the parameters (depth, radii and diffuseness) should come from some model or by fitting the elastic scattering angular distributions. Usually the radii for the imaginary parts are slightly larger than the real radii, reflecting that the absorption occurs from direct reaction just at and outside the nuclear surface.

The phenomenological optical model parameters for a nucleon-nucleus scattering, $U(r)$, is defined as:

$$U(r) = V_C(r) + V_R(r) + V_S(r) + iW_I(r) + iW_D(r) + [V_{SO}(r) + iW_{SO}(r)].(\vec{l}.\vec{s}) \quad 1.58$$

where $V_C(r)$ is the Coulomb potential, $V_{R,S,SO}$ and $W_{I,D,SO}$ are the real and imaginary components of the volume-central (R, I), surface-central (S, D) and spin-orbit (SO) potentials, respectively. $V_R(r)$, $V_C(r)$ and $W_I(r)$ have been defined from equations 1.55 to 1.57. The other terms are given by:

$$V_S(r) = 4a_S V_S \frac{d}{dr} f(r, r_S, a_S)$$

$$W_D(r) = 4a_D W_D \frac{d}{dr} f(r, r_D, a_D)$$

$$V_{SO}(r) = V_{SO} \left(\frac{\hbar}{m_\pi c}\right)^2 \frac{1}{r} \frac{d}{dr} f(r, r_{SO}, a_{SO})$$

$$W_{SO}(r) = W_{SO} \left(\frac{\hbar}{m_\pi c}\right)^2 \frac{1}{r} \frac{d}{dr} f(r, r_{SO}, a_{SO}) \quad 1.59$$

where $f(r, r_i, a_i) = \frac{1}{1+e^{(r-r_i)/a_i}}$ is the Woods-Saxon form factor and m_π is the pion mass.

$W_I(r)$ is responsible for the absorption in the whole volume of the nucleus, but $W_D(r)$, built from the derivate of the function $f(r, r_I, a_I)$, acts specifically in the region close to the nuclear surface. At low energies there are no available unoccupied states inside the nucleus and the interactions are mostly at the surface, so $W_D(r)$ becomes important. At high energies, the incident particle has larger penetration and $W_I(r)$ becomes important.

1.8 Model Calculations for $^{16}O+^{16}O$ Elastic and Fusion Reaction

In a stellar environment, the reacting particles (a+X) are described by a Maxwell-Boltzmann distribution:

$$n(E)dE \propto e^{-E/k_BT}\sqrt{E}dE \tag{1.60}$$

where E is the center of mass energy, T is the temperature and k_B is the Stefan-Bolztmann constant.

The cross section is related to:

$$\sigma(E) \propto \frac{1}{E}e^{-2G} \tag{1.61}$$

where G is the Gamow factor and is given by:

$$G = \frac{e^2}{4\pi\epsilon_0}\frac{\pi Z_a Z_X}{\hbar v} \tag{1.62}$$

$$2G \cong Z_a Z_X \mu^{1/2} E^{-1/2} \tag{1.63}$$

where $\hbar$ is the reduced Planck constant, v is the relative velocity, Z_a and Z_X present the atomic number of the interacting nuclei, ϵ_0 the permitivity of free space and μ is the reduced mass. The energy is given in MeV.

The barrier penetration factor increases with increasing energy, while the number of particles decreases.

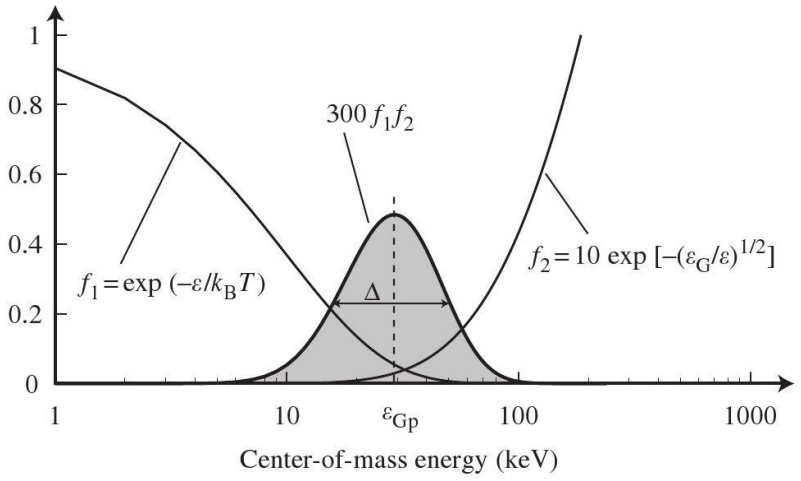

Figure 1.7) Dependence of $n(E)$ and $\sigma(E)v$ on energy. Their product is the shaded region. Effective energy (E_0) in a thermonuclear reaction and its width (Δ)

The reaction rate depends on the product σv and the number of particles available at a specific energy:

$$rate \propto n(E)\sigma(E)v$$

$$\propto \left(\sqrt{E}e^{-E/kT}\right)\left(\frac{1}{E}e^{-2G}\right)\sqrt{E} = e^{-E/kT-2G} \qquad 1.64$$

which is the shaded region in figure 1.7. The effective energy E_0 (Gamow energy) and width of the distribution, ΔE_0, are given by:

$$E_0 = \left(\frac{1}{2}kTZ_aZ_X\mu^{1/2}\right)^{2/3} \qquad 1.65$$

$$\Delta E_0 = 2^{7/6}3^{-1/2}\left(\frac{1}{2}kTZ_aZ_X\mu^{1/2}\right)^{1/3}(kT)^{5/6} \qquad 1.66$$

The nuclear reactions in stars must be studied in energies of E_0, not at energies of kT.

The equation 1.61 can be written:

$$\sigma(E) = \frac{1}{E}e^{-2G}S(E) \qquad 1.67$$

where $S(E)$ is the astrophysical S-factor and contains all the nuclear effects other than the barrier penetration factor.

In massive stars, at an advanced stage of stellar evolution, the gravitational collapse increases the core temperature and density and ignites the carbon and oxygen burning (a process that strongly depends on the mass of the star). The fusion reaction $^{16}O+^{16}O$ is essential for understanding the nuclides burning processes in such advanced stages of stellar evolution, contributing significantly to the production of heavier elements. The temperature ranges from $T = (1-4) \times 10^9\ K$, $\rho = 10^5 - 10^8\ g\ cm^{-3}$ and temporal scales from seconds to years. The effective energy, $E_0 = 3.9T_9^{2/3}$, being T_9 the absolute temperature in billions of K, ranges from 3.9 MeV até 9.8 MeV [8]. The nuclear study of this reaction of astrophysical interest includes the measurement of both elastic and fusion cross section.

The first trial to understand the general trend of heavy-ion fusion reactions was carried out by Stokstad *et al*. [9], which used a strong-absorption optical potential with $V_0 = 50\ MeV$, $W_0 = 10\ MeV$, $r = 1.27fm$ and $a = 0.40fm$ over a 6 MeV range around the interaction barrier, for nine pairs of heavy ions reactions. The parameters are those from Woods-Saxon potential

$$V(r) = \frac{-V_0 - iW_0}{1 + e^{(r-R)/a}} \qquad 1.68$$

Good agreement with energy dependence for all systems was obtained, except for $^{16}O+^{16}O$ reaction. Adding to this, to a different excitation function, the absolute measured cross section was nearly a factor of 2 higher than the calculated value.

After this, Christensen and Switkowski [10] used the Incoming Wave Boundary Condition to fit elastic and fusion cross sections for the reactions $^{12}C+^{12}C$, $^{12}C+^{16}O$ and $^{16}O+^{16}O$. For each reaction, the model parameters were determined by fitting the experimental elastic scattering data and the same set of parameters were used to fit the fusion data. Good agreement was obtained for the $^{12}C+^{12}C$ and $^{12}C+^{16}O$ reactions. For $^{16}O+^{16}O$, the measured fusion cross sections were higher by a factor of 2 than the calculated values. Hence, the discrepancy between the calculated values and experimental data remained unsolved for the $^{16}O+^{16}O$ system.

More recently, Haider *et al*. [11] used a molecular (optical) potential to describe the general features of the low-energy fusion and elastic scattering cross sections for the astrophysical reactions $^{16}O+^{16}O$, $^{16}O+^{12}C$ and $^{12}C+^{12}C$. In this model, the imaginary part of the potential is energy-dependent and the real part is energy-independent and contains an exponential repulsive core. The real part of the potential is composed of an attractive

intermediate-range potential of the Woods-Saxon type, an exponential repulsive core and the Coulomb interaction. It has the form

$$V(r) = V_0\{1 + \exp[(r - R_0)/a]\}^{-1} + V_1 \exp\left(-\frac{r}{R_1}\right) + V_C \qquad 1.69$$

where R_0 and a are, respectively, the radius and diffuseness of the Woods-Saxon potential. R_1 is the core radius that determines the thickness of the repulsive core. The Coulomb potential is taken to be that between two uniformly spherical charge distributions and is given by equation 1.55.

The imaginary part of the potential is energy dependent. It has the form

$$W(r) = V_2(E)exp[-(r/R_2)^2] \qquad 1.70$$

where $V_2(E) = V_2(1 + C_1E + C_2E^2)$ and C_1 and C_2 are constants.

The Shrödinger equation with the potential was solved numerically to obtain the elements of the S_l matrix (corresponding to the lth partial wave). The elastic cross section and reaction cross section were then given by equations 1.42 and 1.54, respectively.

Besides these theoretical calculations, there are now many computer codes able to calculate elastic cross section for almost any reaction. NRV code [12] is used to calculate both elastic and fusion cross sections. It is possible to choose in this code the classical model, semiclassical model or optical model calculation for elastic scattering calculations, while empirical model and channel coupling model are available for fusion cross section calculations. In the channel coupling Fusion code of the NRV a new effective algebraic method is used for numerical solution of a set of coupled Shrödinger equations [13]. This method has no limitation on the number of coupled channels and allows one to calculate fusion cross sections of very heavy nuclei used for synthesis of super-heavy elements.

A combined analysis of the multidimensional potential energy surface relief and behavior of the multi-channel wave function in the vicinity of the Coulomb barrier gives a clear interpretation of near-barrier fusion dynamics.

A calculation for the p+^{12}C elastic scattering for laboratory energy of 1.6 MeV was performed using the optical model calculation of the NRV. The parameters for these calculations are presented in table 1.1.

Coulomb r_0(R), fm 1.537 (3.519)	Real part			Imaginary part		
	V_0, MeV	r_0(R), fm	a, fm	W_0, MeV	r_0 (R), fm	a, fm
Volume	-56.156	1.126 (2.578)	0.676	-0.254	1.126 (2.578)	0.676
Surface	-	-	-	-5.458	1.306 (2.99)	0.525
Spin-Orbit	5.728	0.902 (2.065)	0.59	-0.012	0.902(2.065)	0.59

Table 1.1) Default Optical Model parameters for p+^{12}C elastic cross section.

Results for the Optical model interaction and differential cross section are presented in the figures 1.8 and 1.9.

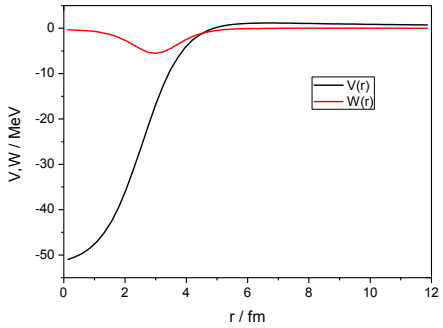

Figure 1.8) Optical Model Interaction.

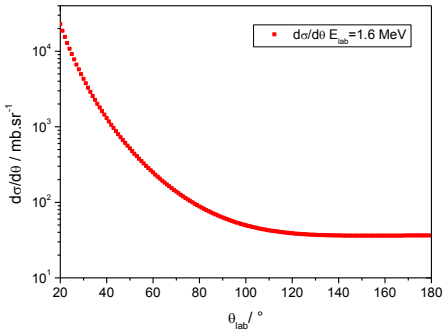

Figure 1.9) Calculated differential cross Section for E_{lab}= 1.6 MeV.

1.9 References

[1] K. Krane, Introductory Nuclear Physics, John Wiley & Sons, 1988.

[2] C. Iliadis, Nuclear Physics of Stars, Wiley-VCH, 2007.

[3] T. Mayer-Kuckuk, Física Nuclear, Fundação Calouste Gulbenkian, 1993.

[4] L. D. Landau, E. M. Lifshitz, Quantum Mechanics, Non-Relativistic Theory, 1958.

[5] N. F. Mott, Proc. Roy. Soc. A 126 (1930) 259-267.

[6] I. Thompson, F. Nunes, Nuclear Reactions for Astrophysics, Cambridge University Press, 2007.

[7] P. G. Burke, R-Matrix Theory of Atomic Collisions, Springer, 2011.

[8] H. Spinka and W. Winkler, Astrophys. J. 174 (1972) 455.

[9]R. G. Stokstad, Z.E. Switkowski, R.A. Dayras and R.M. Wieland, Phys. Rev. Lett. 37 (1976) 888.

[10] P.R. Christensen, Z.E. Switkowski and R.A. Dayras, Nucl. Phys. A 280 (1977) 189-204.

[11] Q. Haider, S.A. Reed, Nucl. Part. Phys. 17 (1991) 1253-1259.

[12] V.I. Zagrebaev *et al*. OM code of NRV, http://nrv.jinr.ru/nrv/.

[13] V.I. Zagrebaev and V.V. Samarin, Yad. Fiz., 67, No.8 (2004) 1488.

2

Chapter 2 - Elastic Scattering Previous Measurements

2.1 Introduction

In this chapter, the state of the art concerning the elastic scattering of protons and oxygen ions will be presented. This includes the description of previous measurements and the presentation of evaluated cross sections when available. First, the previous measurements for the elastic scattering of protons will be presented. Also, a brief discussion for the elastic scattering of oxygen ions will also be done, showing the importance of new elastic cross sections measurements for these two ions.

2.2 Elastic Scattering Previous Measurements

The elastic scattering, as seen before, is always present in a nuclear reaction. The elastic scattering of protons and oxygen ions has been studied in the last decades for different purposes.

The measurement of proton elastic cross sections has become more important over the last years for material analysis, especially at backscattering angles. Not only these cross sections are important but also the uncertainties of these measurements must be minimal. With experimental data available in a large range of energies and angles, a theoretical evaluation may be done [1]. However, to make a full theoretical evaluation of these cross sections, experimental data over a full range of angles is needed, which also contributes to the calculation of optical potentials for the nuclides in study. The absence of experimental data for proton elastic scattering in light nuclides, such as ^{6}Li, ^{7}Li, ^{12}C, ^{19}F and ^{31}P makes its measurement relevant for the scientific community, not only for material analysis but also for theoretical calculations, since the evaluation is still pending [2]. Also, forward angles measurements are also needed for these evaluations.

The elastic scattering of heavy ions, such as ^{16}O, is still under investigation since it may provide important information of the entrance channels of the fusion reaction involving this nuclide, which is very relevant for astrophysical studies. Most of these studies have several years, since they were made along with the first attempts to measure the fusion cross section. For ^{16}O+^{16}O and ^{16}O+^{12}C elastic reactions, new accurate measurements must be done

to compare the results with the previous data and determine the fusion cross section from the elastic cross section measurement.

This chapter presents the former measurements of the elastic cross sections for these nuclides, showing the need for new data. A description of the state of the art for each nuclide will be done, showing the absence of data needed for theoretical evaluations.

2.2.1 $^{12}C(p,p)^{12}C$

Carbon is the fourth most abundant element in nature and is very important in science and technology. It can appear in pure form or through its presence in various forms of polymers, carbide, fibers and glasses. Also, is along with hydrogen an important contaminant surrounding us. Despite this, not much effort was done to study the elastic cross sections at forward angles and the theoretical cross sections available must be replied by experimental data.

The experimental data available for carbon (p,p) elastic cross section have been reviewed by A.F. Gurbich [3]. In this work, the author compiled the experimental data available for this reaction in the energy range up to 4 MeV. The optical model with resonance scattering has been taken into account using S-matrix theory in order to find a proper basis for the calculations. Using a large number of experimental data and combining with the theoretical model it was possible to produce a recommended excitation function in a large interval of backward angles. Both angular distributions and excitation functions were fitted. Some discrepancies with the available data were found showing that new experimental data are needed for the resonance at E_p=1.74 MeV for the excitation function near 110° scattering angle for proton energies lower than 1.7 MeV.

In figure 2.1, a comparison between the results of S. Mazzoni *et al*. [4] and R. Amirikas *et al*. [5] for 110° and between the results of S. Mazzoni *et al*. and H.O. Meyer *et al*. [6] for 115° is presented, alongside with a theoretical evaluation. R. Amirikas *et al*. used a self-supporting C foil (~200 nm) sputtered on ~16 nm of Au as a target to measure the $^{12}C(p,p)^{12}C$ differential cross section from 1000 keV to 3500 keV at three different angles: 110°, 150° and 170° with an angular resolution of ±0.5°. The estimated uncertainty was 3%. The resonance regions were measured with steps of 2 keV in energy. S. Mazzoni *et al*.

measured the proton elastic scattering in carbon in the angular range from 100° to 170° (in steps of 5°) for beam energies from 350 keV to 3000 keV. Thin self-supporting natural carbon foils have been used with two thicknesses: ~13 µg/cm^2 for measurements from 350 keV to 700 keV and ~50 µg/cm^2 for measurements above 700 keV. The normalization, in this case, was done using the scattering spectrum recorded at 15°, which is purely Rutherford at all energies. The estimated uncertainty for this measurement was 4%. H.O. Meyer *et al.* measured the proton elastic scattering in carbon from 300 keV to 2000 keV at three different angles: 84.3°, 114.4° and 144.1°, using self-supporting carbon foils. The angular resolution was 1.5° and the energy resolution was 0.5 keV.

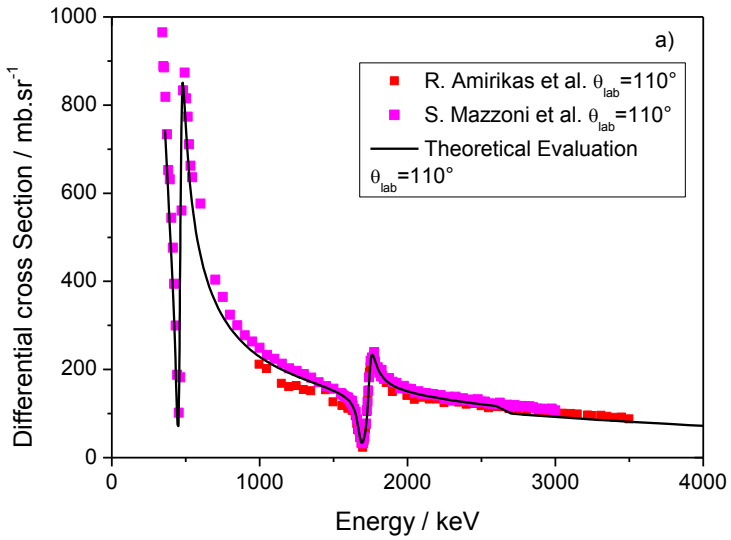

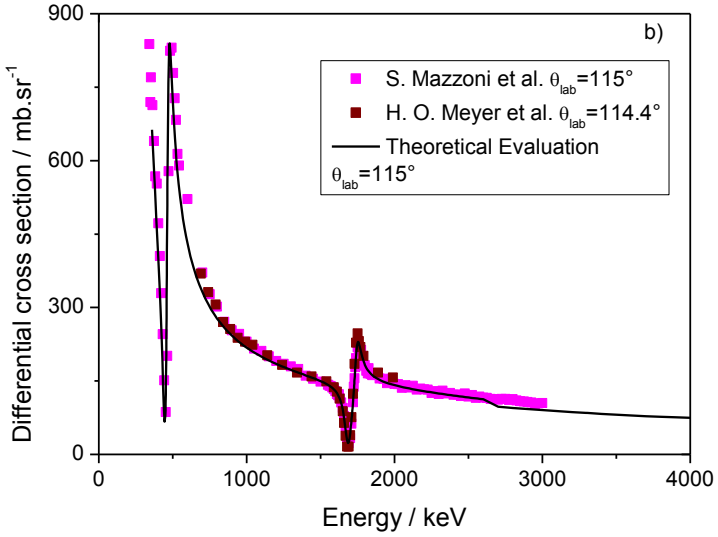

Figure 2.1) Comparison of the evaluated cross section [3] and experimental data for a) θ_{lab}=110° [4,5] and b) θ_{lab}=115° [4,6].

As we can see from the figures, the two data do not match with the available theoretical evaluation. This scenario is even worse if we take the scarce available data for forward angles and compare to the available theoretical evaluation, as we can see in figure 2.2. J.C. Armstrong *et al.* [7] measured the $^{12}C(p,p)^{12}C$ reaction cross section from 1480 to 2020 keV at scattering angles of 23.1°, 32.4°, 41.8°, 51.0°, 65.7°, 75.4°, 85.2° and 121.1°. Self-supporting carbon targets were prepared both by deposition on a glass plate from a carbon arc and by cracking methyl iodide onto a thin nickel foil. The measured thickness of the targets ranged from 20 to 70 μg/cm^2. The energy resolution was 1 keV. The main purpose of this measurement was to investigate the anomaly in the 1.7 MeV region. However, as we can see from figure 2.2, experimental data and theoretical calculation are not in agreement, especially in the resonance region.

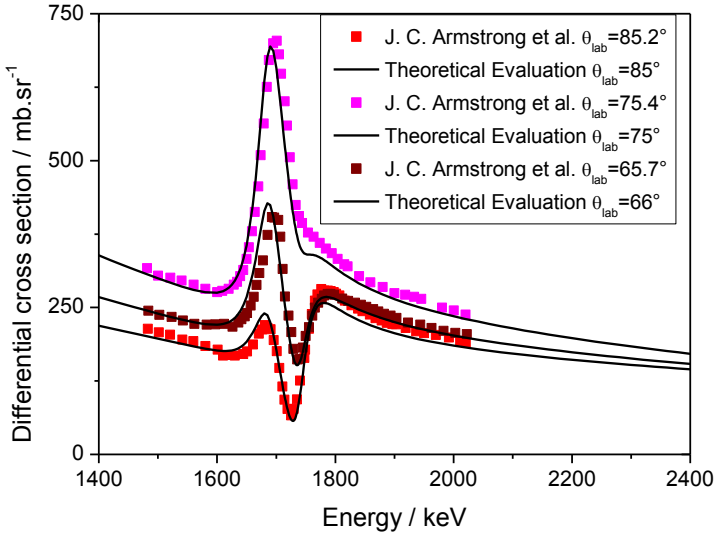

Figure 2.2) $^{12}C(p,p)^{12}C$ elastic cross sections measured by J.C. Armstrong *et al*. at θ_{lab}=65.7°, 75.4° and 85.2° [7] and comparison with theoretical evaluation [3].

The available theoretical evaluation was extended for energies above 2500 keV, using the experimental data obtained by D. Abriloa *et al*. [8]. The target used for this measurement consisted of a thin carbon foil of 52 ± 2 μg/cm^2 and a thin gold layer of 14 ± 1 μg/cm^2. The differential cross section was obtained in the energy range from 2690 keV to 7000 keV, for the detection angles of 140°, 150°, 160° and 170°. A new extended validation was done using the experimental data obtained in this work and is now available for the scientific community at IBANDL (http://www-nds.iaea.org/ibandl/) in the energy range from 360 keV to 7100 keV [9].

Figure 2.3 shows the theoretical evaluation for this element for an angle of 50°. The energy ranges from 360 keV to 7100 keV.

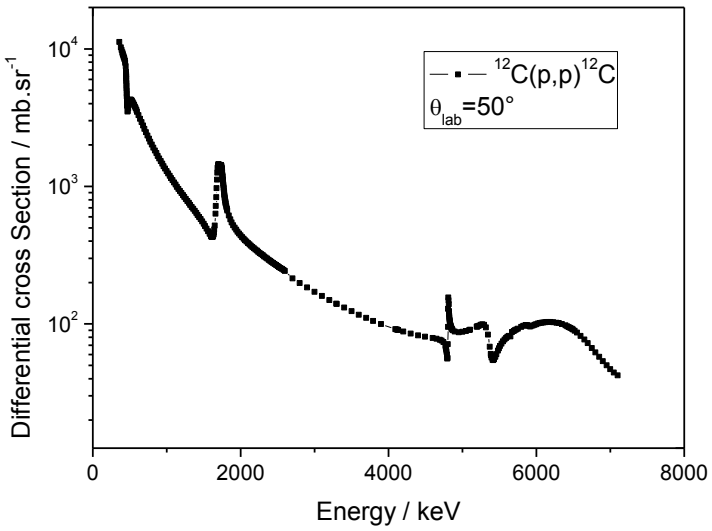

Figure 2.3) $^{12}C(p,p)^{12}C$ theoretical differential cross section at $\theta_{lab}=50°$ [9].

The absence of experimental data in the resonance region and at low scattering angles justifies the measurement of this elastic cross section, especially at forward angles where, to the best of our knowledge, there is data from only one author. Also, these new measurements are important to benchmark our experimental setup and as a starting point to other nuclides.

2.2.2 $^{6}Li(p,p)^{6}Li$ and $^{7}Li(p,p)^{7}Li$

Lithium is a very common element in nature with two isotopes, ^{6}Li (natural abundance of 7.5%) and ^{7}Li (natural abundance of 92.5%). It has a very important technological interest, since it´s quantitative determination is relevant for the characterization of materials such as aluminum and magnesium alloys, ceramics, glasses and rechargeable batteries. The main problem concerning the depth profiling of lithium is that it usually appears in matrices with medium or high Z elements, thus the determination of its concentration by IBA techniques represents a huge challenge. Elastic scattering is the most suitable technique to measure its concentration, due to the high capability for the determination of several light elements concentrations in complex matrices [10].

The differential cross section for ^{6}Li has not been studied in the last years. The main work concerning the elastic scattering of protons from this nuclide has been made by U.

Fasoli *et al*. [11], W.D. Harrison *et al*. [12] and M. Haller *et al*. [13]. U. Fasoli *et al*. measured the ^{6}Li(p,p)^{6}Li reaction in the energy range from 1300 keV to 5600 keV for 5 angles: 100.4°, 116.7°, 140.7°, 143.8° and 166.4°, using a target made by vacuum evaporation of 99.3% enriched ^{6}Li metal onto a 100 nm Nickel foil. The target thickness was equivalent to 30 keV energy loss for 1.3 MeV protons. W.D. Harrison *et al*. measured the differential cross section for the elastic scattering of protons by ^{6}Li in the energy range from 2400 keV to 12 MeV and laboratory angles from 33.8° to 160°. Targets were made by evaporating separated ^{6}Li (isotopic abundance 99%) onto a carbon foil or onto a thin nickel foil. The thickness of ^{6}Li on the various targets ranged from 30 to 300 µg/cm^{2}. M. Haller *et al*. measured complete angular distributions (laboratory angles between 30° and 165° in steps of 5°) in a wide range of energies (1600 to 10000 keV). A sandwich target was used consisting in a C-^{6}Li-C (50 µg/cm^{2} ^{6}Li). A Au target was used for normalization purposes.

Figure 2.4 shows four datasets from two different authors (W.D. Harrison *et al*. and M. Haller *et al*.). As we can see, there is no agreement among datasets. The scenario is even worst at energies lower than 5000 keV.

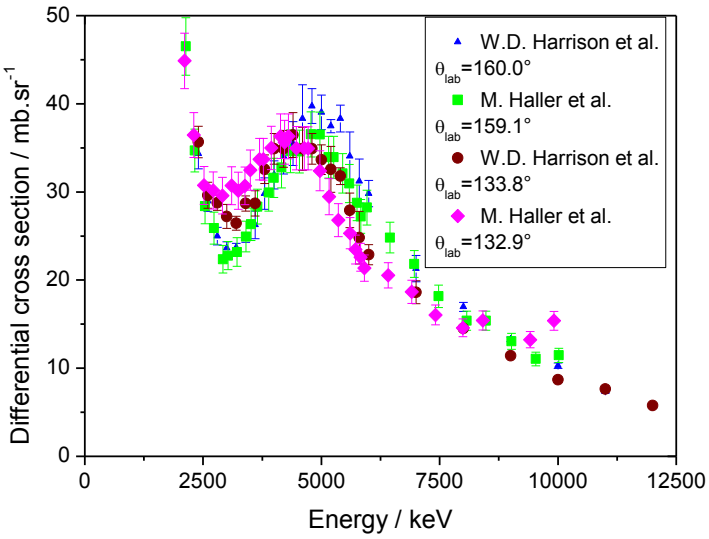

Figure 2.4) ^{6}Li(p,p)^{6}Li experimental differential cross section for four different angles from two different authors [12,13].

In relation to forward angles, for ^{6}Li, there are two measurements near 90°, one made at 90° by W.D. Harrison *et al*. [12] in the energy range from 2400 keV to 12000 keV and

another at 89.5°, in the energy range from 1060 to 9000 keV with 30 experimental points, made by M. Haller *et al*. [13] as figure 2.5 shows.

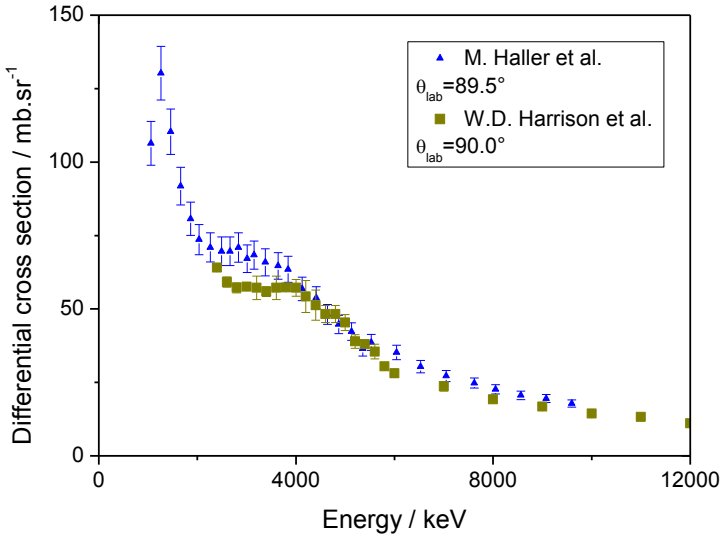

Figure 2.5) ^{6}Li(p,p)^{6}Li experimental differential cross section at θ_{lab}=89.5° and 90° [12,13].

As we can see from the figure, the two experimental data at angles near 90° do not match in the full energy range and there is only one dataset for energies below 2400 keV. There is not a theoretical evaluation for this element. The other experimental data available for angles below 90° are at 80.5° and 81.3°, as seen in figure 2.6, are from J.A. Maccray [14] and H.J. Kim *et al*. [15]. In this case, the two experimental data are in agreement in the energy range from 750 to 2750 keV.

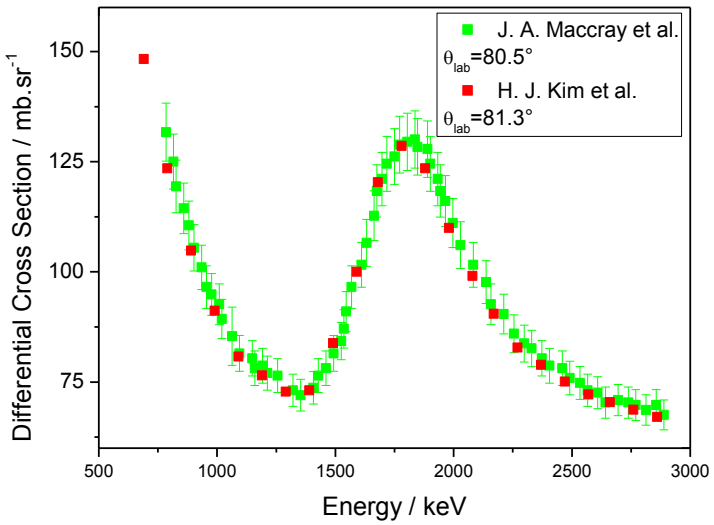

Figure 2.6) ^{6}Li(p,p)^{6}Li experimental differential cross section at θ_{lab}=80.5° and 81.3° [14,15].

In conclusion, for ^{6}Li, the purpose is to have new datasets at different energies and angles (backward and forward angles) in order to make possible a theoretical evaluation for this element, which would be very important for both theoretical and analytical purposes.

Opposite to the ^{6}Li(p,p)^{6}Li reaction, the elastic scattering of protons by ^{7}Li has been studied in the last years by many experimental groups. Most of the datasets are at backscattering angles, with few measurements at forward angles, such as the ones made by W.D. Warters *et al*. [16], in energies from 250 keV to 500 keV at three different angles: 81.1°, 62.7° and 44.4°, which are not relevant for either analytical or theoretical purposes. There are also two datasets at 90°. The last work concerning this element was made by V. Paneta *et al*. [10]. In this work, ^{7}Li(p,p)^{7}Li reaction was measured in the energy range from 1.5 MeV to 7 MeV using a variable step and for detection angles between 140° and 170° in steps of 10°. The target used for the cross section measurement consisted of a LiF layer $(960 \pm 38) \times 10^{15}$ at/cm^2 evaporated onto a thin carbon foil with 52 ± 2 µg/cm^2 thickness. Also, a thin gold layer 4.4 ± 0.3 µg/cm^2 was evaporated over the LiF layer for charge collection normalization. It is also possible to identify other works from A. Caccioli *et al*. [17], U. Fasoli *et al*. [18] and K. Kilian *et al.* [19]. In the work of A. Caccioli, the cross section has been measured for beam energies from 3 to 7 MeV at a scattering angle of 150° with a multilayered C/LiF/Au sample. A thin LiF film (about 50 µg/cm^2) was evaporated on a self-supporting C target (about 30 µg/cm^2) and further coated with a thin Au layer (about

20 µg/cm^2) for beam charge normalization. The gold layer could also prevent lithium fluoride from being oxidized. The overall accuracy is estimated to be better than ±5.0% at all beam energies. U. Fasoli used the cross section measured for ^{6}Li to measure the ^{7}Li(p,p)^{7}Li elastic cross section from 3.0 to 5.5 MeV with a LiF target knowing the isotopic abundance. K. Kilian used a 150 µg/cm^2 ^{7}Li (99.99%) evaporated onto a Nickel foil (45 µg/cm^2). Results for these works at backscattering angles are presented in figure 2.7.

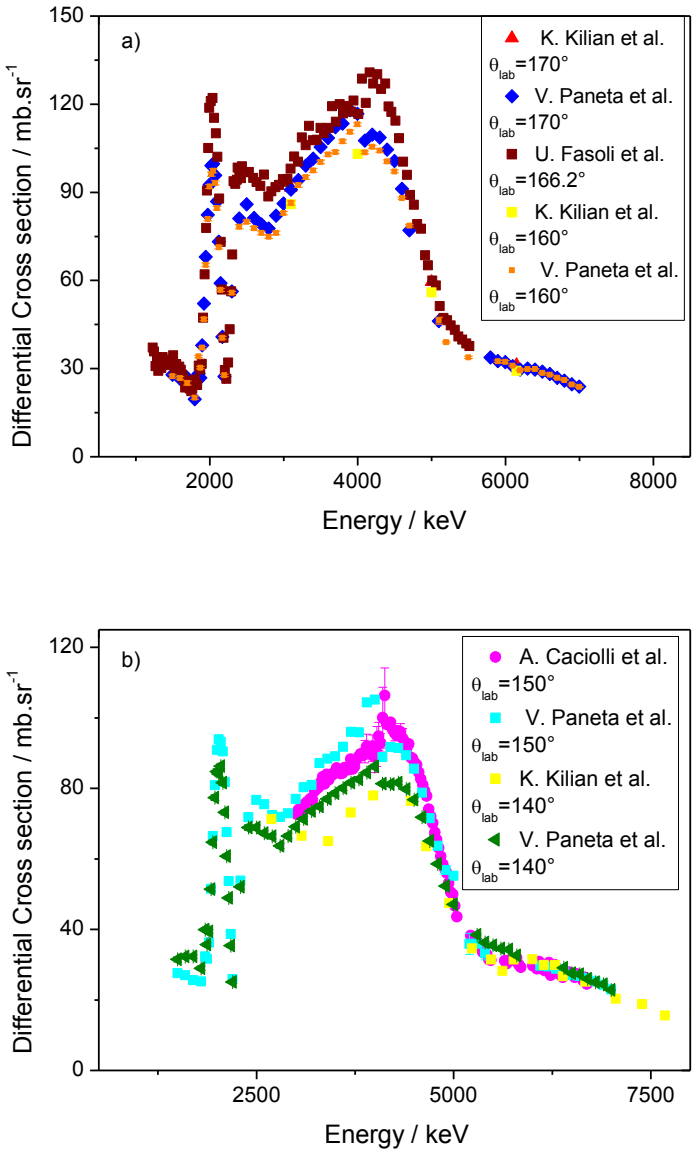

Figure 2.7) ^{7}Li(p,p)^{7}Li experimental differential cross section from different authors for a) θ_{lab}=170°, 166.2°, 160° [10,18,19] and b) θ_{lab}=150° and 140° [10,17,19].

From figure 2.7 it is possible to verify that there is no good agreement among data for $E_p < 5000$ keV. Recent works like those from Caciolli *et al.* and Paneta *et al.* show no agreement in the obtained results. Figure 2.8 shows two datasets near 90°, which are not comparable due to small overlap in energy.

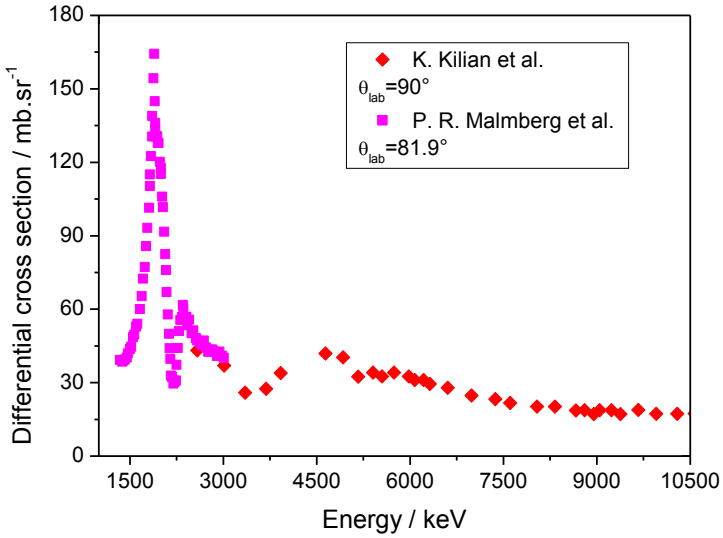

Figure 2.8) ^{7}Li(p,p)^{7}Li experimental differential cross section near 90° [19,20].

P.R. Malmberg *et al.* [20] measured the ^{7}Li(p,p)^{7}Li elastic cross section from 1350 keV to 3000 keV at 6 different angles: 62.7°, 81.9°, 102.0°, 123.1°, 145.3° and 164.9°. The target was a thin lithium layer evaporated from a furnace onto a backing while was placed in the target chamber. The target backing was a thin Zapon film upon which a layer of Aluminum had been evaporated.

In conclusion, for the ^{7}Li(p,p)^{7}Li reactions, the absence and lack of agreement of experimental data justifies the measurement of the respective cross sections at energies relevant for material analysis. Also these new measurements will be used for theoretical evaluation of this reaction and for the calculation of optical potentials for this nuclide.

2.2.3 $^{19}F(p,p)^{19}F$

Fluorine, like lithium, is also a very common element with high interest. It also appears in complex matrices with high Z elements. The characterization of Fluorine is usually done by PIGE, however reliable data for proton elastic scattering from this element over a wide range of energy and angles is required.

Due to the use of a target consisting of a LiF layer in most cases, we can identify the same authors as those referred to for Li measurements. Recent works from V. Paneta *el al*. [10], A. Caciolli *et al*. [17] and A.P. Jesus *et al*. [21] provide proton elastic scattering cross sections at backscattering angles in a range of energies relevant for material analysis. In the work of A.P. Jesus *et al*., $^{19}F(p,p)^{19}F$ elastic cross section was measured from 0.75 MeV to 2.8 MeV using a GdF_3 target evaporated onto carbon foils with thickness of 45, 69 and 78 μg/cm^2. Corrections for target thickness and beam energy dispersion effects were introduced. An important work in this nuclide is presented by S. Ouichaoui *et al*. [22,23] that measured the $^{19}F(p,p)^{19}F$ elastic cross section from 2000 keV to 3420 keV at 5 different angles and from 1520 keV to 2100 keV at 8 different angles. A C_2F_6 gas target was used and normalization was done to a heavy element. Absolute cross sections were obtained with an accuracy of 10%. The theoretical evaluation for Fluorine is available in IBANDL for energies from 550 keV to 1740 keV [9]. More recently, a new theoretical investigation of the $^{19}F(p,p)^{19}F$ elastic cross section was performed up to 2.3 MeV [24], but experimental data is needed to validate the calculations made.

The experimental data for proton elastic scattering, as we can see in figure 2.9 and 2.10 are in poor agreement. The theoretical curves for the scattering angles in the interval 159°–165° are indistinguishable and so the difference between the data sets cannot be attributed to the cross section angular dependence. The theoretical evaluation is presented only for energies above 1300 keV, due to the absence of experimental data for energies below this value.

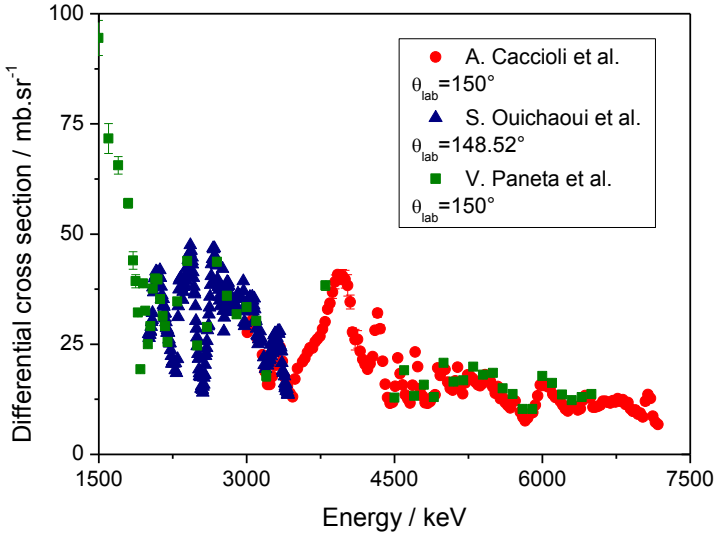

Figure 2.9) $^{19}F(p,p)^{19}F$ experimental differential cross section for θ_{lab}=148.52° and 150° [10,17,23].

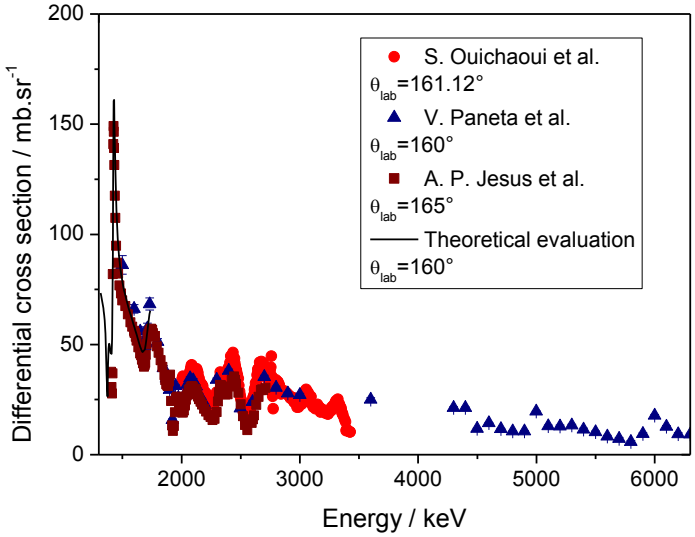

Figure 2.10) $^{19}F(p,p)^{19}F$ experimental differential cross section for θ_{lab}=165°, 161.12°, 160° [10,21,23] and comparison with IBANDL theoretical calculation for θ_{lab}=160° [9].

The experimental data available for angles below 90° by S. Ouichaoui *et al.* is presented in figure 2.11. To the best of our knowledge, for forward angles there are no other measurements and no theoretical evaluation.

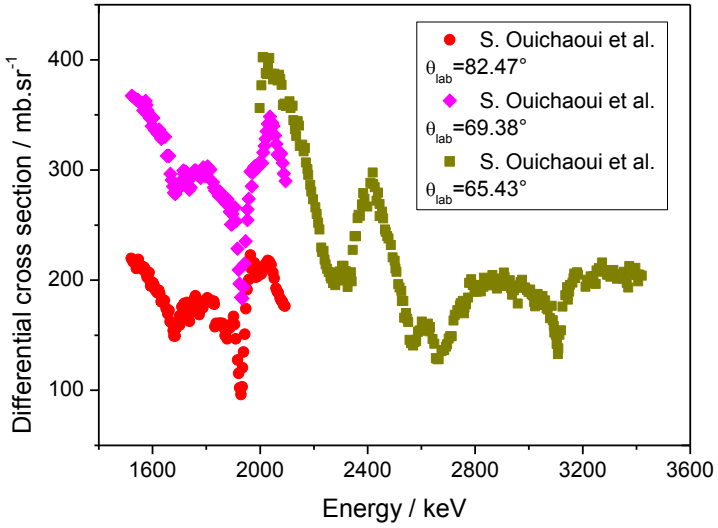

Figure 2.11) $^{19}F(p,p)\ ^{19}F$ experimental differential cross section for θ_{lab}=82.47°, 69.38° and 65.43° [22,23].

Again, considering the published work, we may state that new datasets are required for the $^{19}F(p,p)^{19}F$ reaction in order to benchmark the available theoretical evaluation and extend it to a wide range of energies required for material analysis.

2.2.4 $^{31}P(p,p)^{31}P$

Phosphorous is a major component of bone mineral structure and is an essential element for the normal bone homeostasis. Usually, phosphorous content in samples is quantified by the use of the inelastic reaction $^{31}P(p,p'\gamma)^{31}P$, by detection of the 1266 keV gamma rays. The cross section for the elastic scattering of protons was measured by D.F. Fang *et al*. [25], J. Cohen-Ganouna *et al*. [26] and K.V. Karadzhev *et al*. [27]. The resonance fine structure was investigated by J. Vernotte *et al*. [28]. The measurements showed significant discrepancies. A theoretical evaluation for this reaction is available from 1000 to 2000 keV [9]. In figure 2.12 a comparison between the available theoretical evaluation and the data from K. Cohen-Ganouna *et al*. is presented. The resonance near 1750 keV does not match with the evaluation and with other works.

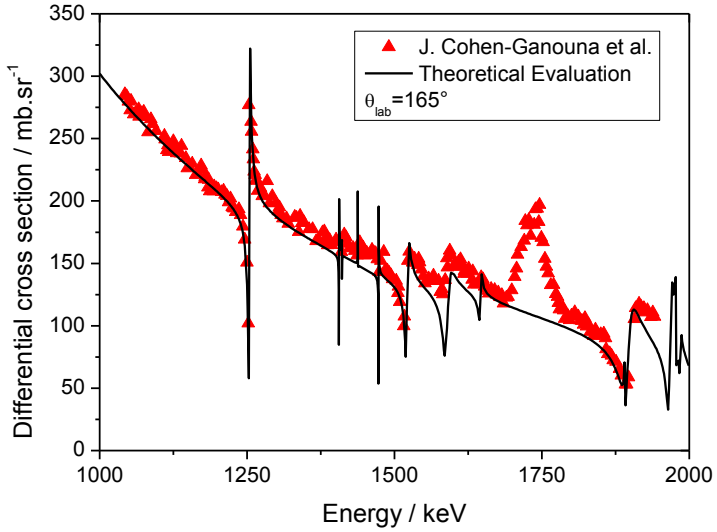

Figure 2.12) $^{31}P(p,p)\ ^{31}P$ experimental differential cross section [26] and theoretical evaluation for θ_{lab}=165° [9].

D.F. Fang *et al*. measured the $^{31}P(p,p)^{31}P$ elastic cross section from 1000 keV to 4000 keV at a θ_{lab}=165°, using a Zn_3P_2 evaporated onto ultrapure Ni coated (~0.5 µg/cm^2) carbon foils (4-5 µg/cm^2) and by K.V. Karadzhev *et al*. from 1000 keV to 3510 keV at a θ_{lab}=150°. The two datasets are showed in figure 2.13 along with the theoretical evaluation available from 1000 to 2000 keV.

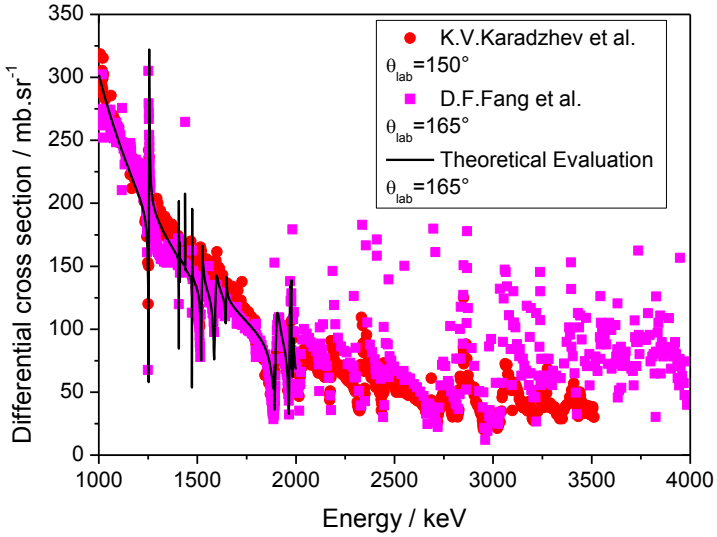

Figure 2.13) $^{31}P(p,p)\ ^{31}P$ experimental differential cross section for θ_{lab}=165°, 150° [25,29] and comparison with IBANDL theoretical calculation for θ_{lab}=150° [9].

As we can see from figure 2.13, the theoretical evaluation was done using the data from D.F. Fang *et al*., with some points out of range. For higher energies, the discrepancy between data and an absent theoretical evaluation justifies a new measurement, where the cross sections for the resonances measured might be too high, according to the previous evaluation. Concerning $^{31}P(p,p)^{31}P$ elastic cross section, it will be measured concurrently with the $^{31}P(p,p'\gamma)^{31}P$ reaction, providing information both on gamma ray emission and particles detection.

2.2.5 $^{16}O(^{16}O,\,^{16}O)\,^{16}O$ and $^{12}C(^{16}O,\,^{16}O)\,^{12}C$

Concerning the elastic scattering of oxygen ions, the motivation of this measurement is to have accurate cross section measurements to input in theoretical calculations in order to determine the fusion cross section, which is very small for this reaction at low energies. As said before, the effective energy, E_0, ranges from 3.9 to 9.8 MeV for the $^{16}O+^{16}O$ fusion reaction. In recent decades, this reaction has been studied both theoretically [29,30,31] and experimentally [32,33,34,35,36]. In a recent work [29,30] molecular effects were investigated since at sub-barrier energies the radial motion of the nuclei is expected to be adiabatically slow compared to the rearrangement of the mean field of nucleons. As shown in Fig. 2.14, consideration of molecular effects change the prediction of S(E) at low energies, particularly when a radial dependent mass parameter (cranking mass) is used instead of the usual constant reduced mass parameter in solving the radial Schrödinger equation. A comparison with the results obtained with the Broglia-Winther (BW) potential [37] and the calculations done by Neff *et al*. within the Fermionic Molecular Dynamics (FMD) approach [38] is done.

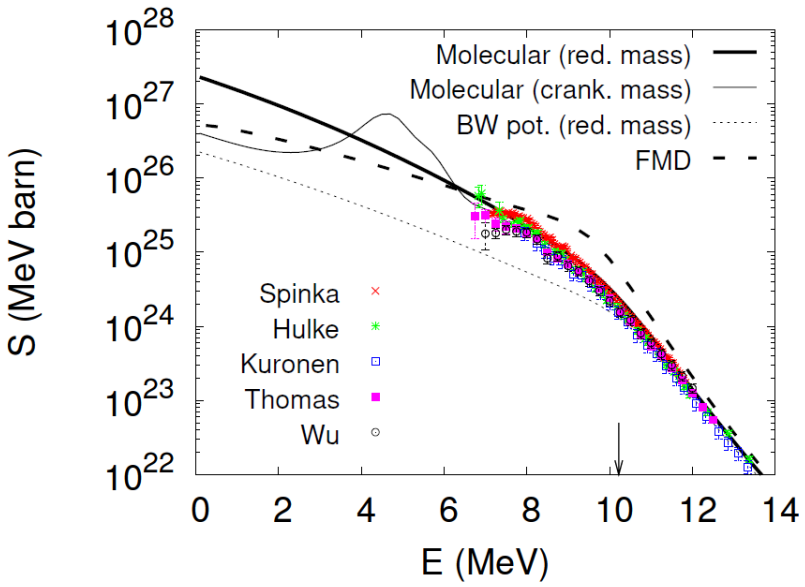

Figure 2.14 $^{16}O+^{16}O$ fusion cross section for different authors [32,33,34,35,36] and theoretical models [29,37,38].

Figure 2.15 shows the available data of fusion cross sections for this reaction and both channel coupling and empirical calculations to fit the fusion cross section.

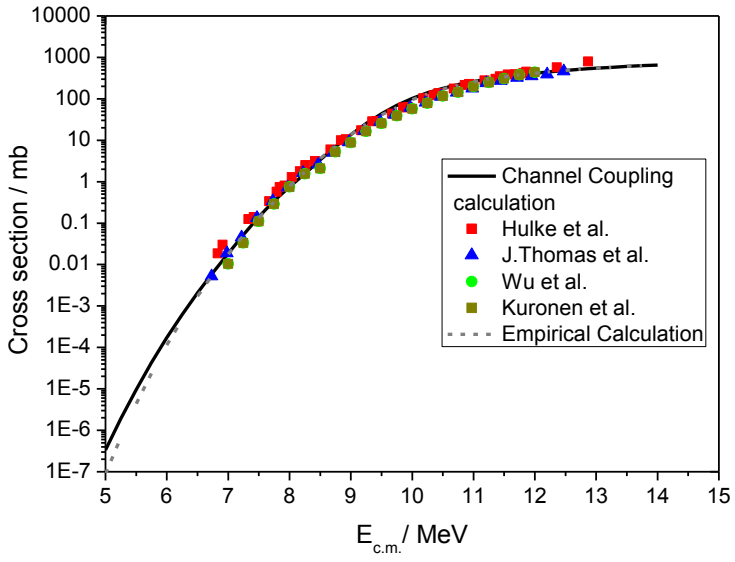

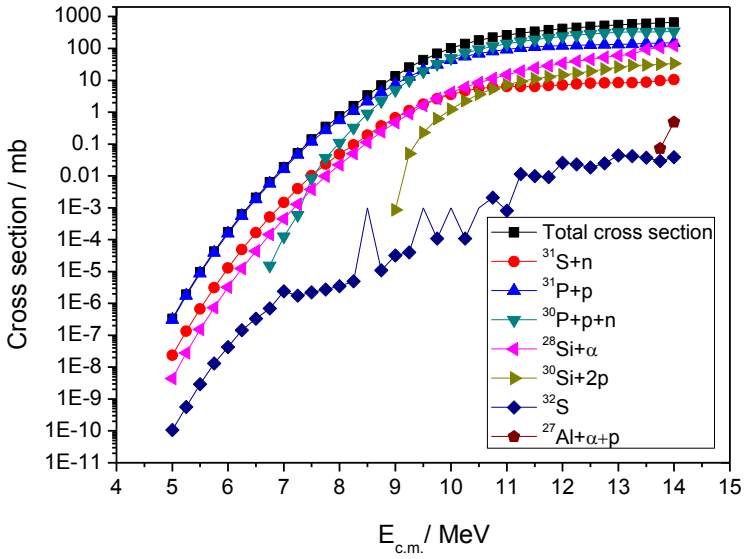

Figure 2.15) $^{16}O+^{16}O$ total (a) and partial (b) fusion cross sections obtained with a channel coupling calculation of NRV [39].

Table 2.1 shows the comparison of partial cross sections for fusion cross section among different authors. Also, the branching ratio for the different exit channels is given by channel coupling calculation of NRV [39].

Channel	Wu et al.	Hulke et al.	Cheng et al.	Kolata et al.	CC calculation
$^{31}P+^{30}Si$	32.6%	38.5%	27%	6.5%	32.9%
^{28}Si	10.6%	17.2%	7.9%	6.4%	8.2%
^{24}Mg	5.2%	11.3%	11.1%	15.3%	-
^{30}P	16.5%	27.6%	12.1%	11.2%	57.2%
^{27}Al	34.2%	5.4%	41.5%	60.6%	-
^{31}S	0.9%	-	-	-	1.7%
total	438	480	200	125	415

Table 2.1) Branching ratios for different exit channels in $^{16}O+^{16}O$ fusion reaction.

Despite these measurements, only H. Spinka *et al*. [32] measured the fusion cross section using particle detection, while the other authors used gamma ray detection. Also, the elastic cross section was measured by H. Spinka *et al*., Bromley *et al*. [40,41], Maher *et al*. [42], S.C. Wu *et al*. [36] and G. Hulke *et al*. [33]. Spinka used a gas target to measure the $^{16}O+^{16}O$ elastic scattering at $\theta_{lab}=45°$ (figure 2.16). The purpose was to determinate the target thickness and beam intensity far below the Coulomb barrier, where the elastic cross section is purely Mott. The elastic cross section was then measured from $E_{c.m.}=7.34$ to 14.37 MeV using the ratio of $^{16}O+^{16}O$ elastic scattering to pure Rutherford scattering ($^{16}O+^{40}Ar$). The results from Spinka have a shift in energy from former results [36,40,41] in approximately 250 keV, suggesting that no corrections for target thickness were made in the past measurements. S.C. Wu used a thin SiO transmission layer on a self supporting carbon target. Due to the carbon content of the target, scattering measurements of $^{16}O+^{12}C$ were also done on a 10 μg/cm^2 self-supporting carbon target. So, for each $^{16}O+^{16}O$ scattering spectrum, a correction was made to subtract the contribution of recoil carbon particles, by normalizing to the scattering ^{16}O yield the scattering of ^{16}O from carbon at the same energy and angle. The angular positions of the detectors were checked by comparing the scattered ^{16}O particles at 43° and 47° at 6.89, 8.91, 10.91, 11.92 and 12.92 MeV in the center-of-mass frame. The results obtained were similar to those obtained by Spinka *et al*., proving that the $^{16}O+^{16}O$ elastic cross section follows the Mott scattering below the Coulomb barrier. Hulke *et al*. used the elastic scattering yield to control the relative number of projectiles, due to the difficulties of a reliable current integration in a gas target. Hulke obtained the same results of those obtained by Wu and Spkinka. Results from Spinka for $^{16}O+^{16}O$ elastic cross section (ratio to Mott) are presented in figure 2.16.

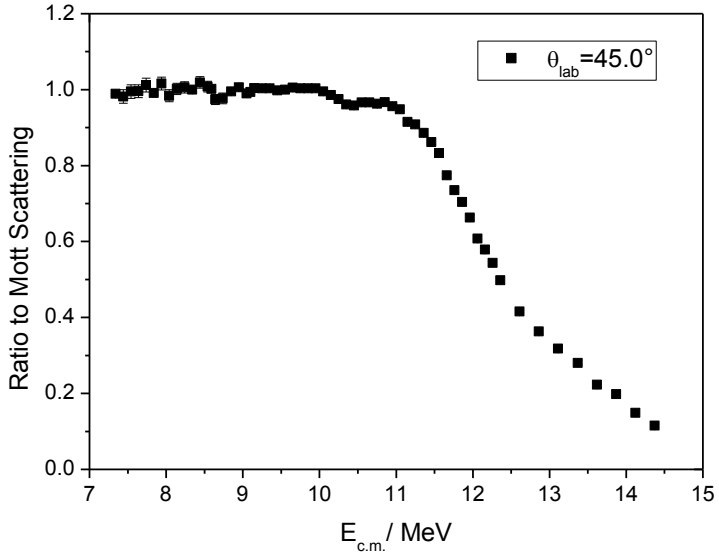

Figure 2.16) Ratio of $^{16}O+^{16}O$ elastic scattering cross section measured by Spinka *et al*. to pure Mott scattering cross section at $\theta_{lab}=45.0°$.

Considering these differences in the fusion reaction data, we intend to measure the elastic cross section for the $^{16}O(^{16}O,^{16}O)^{16}O$ reaction. This elastic reaction has a huge dependence on angle, since the scattering is between two identical particles. Figure 2.17 shows the theoretical curves expected for energies below the Coulomb barrier.

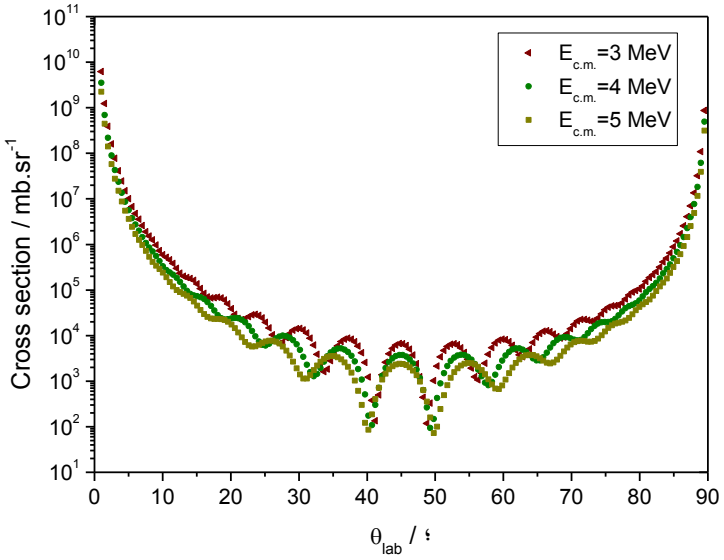

Figure 2.17) Theoretical predictions for $^{16}O+^{16}O$ elastic scattering cross section.

The accurate measurement of this cross section will allow us to find or not some discrepancies at low energies with available data and also have information on the fusion cross section.

The $^{12}C(^{16}O,^{16}O)^{12}C$ elastic reaction can be also measured along with the $^{16}O+^{16}O$ elastic cross section. Spinka *et al*. measured this reaction using a differentially pumped gas target (mixture of high purity CH_4 and argon). Results for the measured angles are presented in figure 2.18.

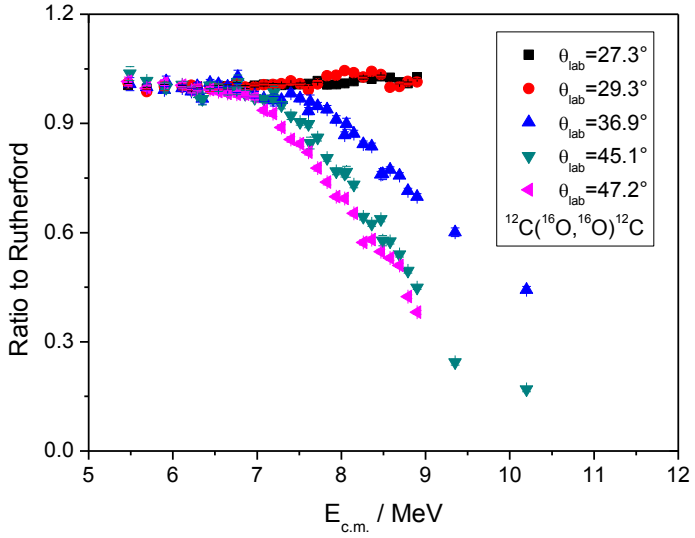

Figure 2.18) Ratio of $^{16}O+^{12}O$ elastic scattering cross section measured by Spinka *et al*. to Rutherford scattering cross section.

It is also expected to follow the Rutherford cross section in the energies that we intend to measure. However, a new measurement can find new discrepancies between theoretical calculations and experimental data. Figure 2.19 shows a comparison between $^{16}O+^{16}O$ elastic cross section and $^{16}O+^{12}C$ elastic cross section for a $E_{c.m.}$=5 MeV.

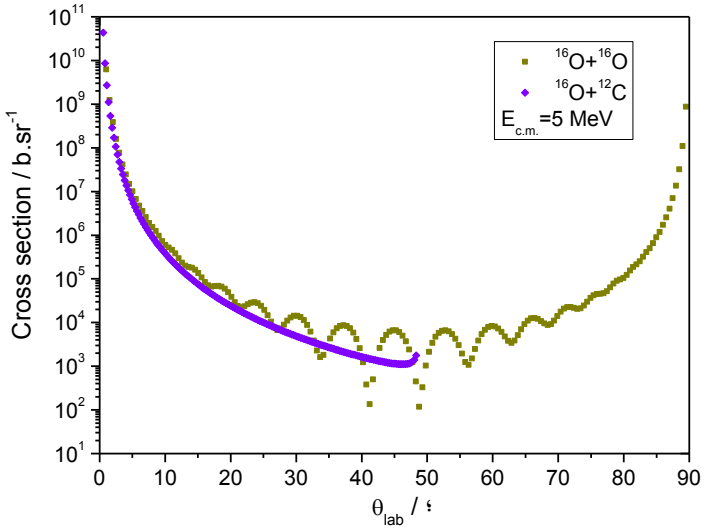

Figure 2.19) $^{16}O+^{16}O$ and $^{16}O+^{12}C$ differential elastic cross section for $E_{c.m.}$=5 MeV.

2.3 References

[1] A.F. Gurbich, Nucl. Instr. And Meth. B 129 (1997) 311.

[2] A.F. Gurbich, Nucl. Instr. And Meth. B 268 (2010) 1703-1710.

[3] A.F. Gurbich, Nucl. Instr. And Meth. B 136-138 (1998) 60-65.

[4] S. Mazzoni, M. Chiari, L. Giuntini, P. A. Mandò and N. Taccetti, Nucl. Instr. And Meth. B 136-138 (1998) 86-90, data retrieved from the IBANDL database, IAEA, 2017, at http://www-nds.iaea.org/ibandl/.

[5] R. Amirikas, D.N. Jamieson and S.P. Dooley, Nucl. Instr. And Meth. B 77 (1993) 110, data retrieved from the IBANDL database, IAEA, 2017, at http://www-nds.iaea.org/ibandl/.

[6] H.O. Meyer, G.R. Plattner and I. Sick, Z. Phys. A 279 (1976) 41, data retrieved from the IBANDL database, IAEA, 2017, at http://www-nds.iaea.org/ibandl/.

[7] J.C. Armstrong, M.J. Baggett, W.R. Harris and V.A. Latorre, Physical Review 144 (1966) 823, data retrieved from the IBANDL database, IAEA, 2017, at http://www-nds.iaea.org/ibandl/.

[8] D. Abriola, A.F. Gurbich, M. Kokkoris, A. Lagoyannis and V. Paneta, Nucl. Instr. And Meth. B 269 (2011) 2011-2016.

[9] IBANDL database, IAEA, 2017 at http://www-nds.iaea.org/ibandl/.

[10] V. Paneta, A. Kafkarkou, M. Kokkoris and A. Lagoyannis, Nucl. Instr. And Meth. B 288 (2012) 53-59, data retrieved from the IBANDL database, IAEA, 2017, at http://www-nds.iaea.org/ibandl/.

[11] U. Fasoli, E.A. Silverstein, D. Toniolo and G. Zago, Jour. Nuovo Cimento 34 (1964) 1832, data retrieved from the IBANDL database, IAEA, 2017, at http://www-nds.iaea.org/ibandl/.

[12] W.D. Harrison and A.B. Whitehead, Jour. Physical Review 132 (1963) 2607, data retrieved from the IBANDL database, IAEA, 2017, at http://www-nds.iaea.org/ibandl/.

[13] M. Haller, M. Betz, W. Kretschmer, A. Rauscher, R. Schmitt and W. Schuster, Nucl. Phys. A 496 (1989) 189-204, data retrieved from the IBANDL database, IAEA, 2017, at http://www-nds.iaea.org/ibandl/.

[14] J.A. Mccray, Jour. Physical Review 130 (1963) 2034, data retrieved from the IBANDL database, IAEA, 2017, at http://www-nds.iaea.org/ibandl/.

[15] H.J. Kim *et al*., Nuclear Data Tables A2 (1966) 353, data retrieved from the IBANDL database, IAEA, 2017, at http://www-nds.iaea.org/ibandl/.

[16] W.D. Warters *et al*., Jour. Physical Review 91 (1953) 917.

[17] A. Caccioli, M. Chiari, A. Climent-Font, M.T. Fernandez-Jimenez, G. García-López, F. Lucarelli, S. Nava and A. Zucchiatti, Nucl. Inst. And Meth. B 249 (2006) 95, data retrieved from the IBANDL database, IAEA, 2017, at http://www-nds.iaea.org/ibandl/.

[18] U. Fasoli, D. Toniolo and G. Zago, Jour. Nuovo Cimento 34 (1964) 542, data retrieved from the IBANDL database, IAEA, 2017, at http://www-nds.iaea.org/ibandl/.

[19] K.Kilian, G. Clausnitzer, W. Dürr, D. Fick, R. Fleischmann and H.M. Hofmann, Jour. Nuclear Physics A 126 (1969) 529, data retrieved from the IBANDL database, IAEA, 2017, at http://www-nds.iaea.org/ibandl/.

[20] P.R. Malmberg, Phys. Review 101 (1956) 114, data retrieved from the IBANDL database, IAEA, 2017, at http://www-nds.iaea.org/ibandl/.

[21] A.P. Jesus, B. Braizinha, J. Cruz and J.P. Ribeiro, Nucl. Instr. Meth. B 174 (2001) 229.

[22] S. Ouichaoui, H. Beaumevieille, N. Bendjaballah, C. Chami, A. Dauchy, B. Chambon, D. Drain and C. Pastor, Il Nuovo Cimento 86 (1985) 170, data retrieved from the IBANDL database, IAEA, 2017, at http://www-nds.iaea.org/ibandl/.

[23] S. Ouichaoui, H. Beaumevieille, N. Bendjaballah and A. Genoux-Lubain, Il Nuovo Cimento 94 (1986) 133, data retrieved from the IBANDL database, IAEA, 2017, at http://www-nds.iaea.org/ibandl/.

[24] V. Paneta, A.F. Gurbich, M. Kokkoris, Nucl. Instr. And Meth. B 371 (2016) 54-58.

[25] D.F. Fang, E.G. Bilpuch, C.R. Westerfeldt and G.E. Mitchell, Physical Review C 37 (1988) 28, data retrieved from the IBANDL database, IAEA, 2017, at http://www-nds.iaea.org/ibandl/.

[26] J. Cohen-Ganouna, M. Lambert and J. Schmouker, Nuclear Physics 40 (1963) 67-81, data retrieved from the IBANDL database, IAEA, 2017, at http://www-nds.iaea.org/ibandl/.

[27] K.V. Karadzhev *et al*., Yadernaya Fizika 7 (1968) 242, data retrieved from the IBANDL database, IAEA, 2017, at http://www-nds.iaea.org/ibandl/.

[28] J. Vernotte, S. Gales, M. Langevin and J.M. Maison, Nuclear Physics A 212 (1973) 493-530, data retrieved from the IBANDL database, IAEA, 2017, at http://www-nds.iaea.org/ibandl/.

[29] A. Diaz-Torres, W. Scheid, Nucl. Phys. A 757 (2005) 373.

[30] A. Diaz-Torres, L.R. Gasques, M. Wiescher, Physics Letters B 652 (2007) 255.

[31] L. Jiang, K.E. Rehm, B.B. Back, R.V.F. Janssens, Phys. Rev. C 75 (2007) 015803.

[32] H. Spinka, W. Winkler, Astrophys. J. 174 (1972) 455.

[33] G. Hulke, C. Rolfs, H.P. Trautvetter, Z. Phys. A 297 (1980) 161.

[34] A. Kuronen, J. Keinonen, P. Tikkanen, Phys. Rev. C 35 (1987) 591.

[35] J. Thomas, Y.T. Chen, S. Hinds, D. Meredith, M. Olson, Phys. Rev. C 33 (1986) 1679.

[36] S.C. Wu, C.A. Barnes, Nucl. Phys. A 422 (1984) 373.

[37] W. Reisdorf, J. Phys. G 20 (1994) 1297.

[38] T. Neff, H. Feldmeier and K. Langanke, arXiv: nucl-th/ 0703030.

[39] V.I. Zagrebaev *et al*. OM code of NRV, http://nrv.jinr.ru/nrv/.

[40] E. Almqvist, D.A. Bromley and J.A. Kuehner, Phys. Rev. Letter 4 (1960) 515.

[41] D.A. Bromley, J.A. Kuehner and E. Almqvist, Phys. Rev. 123 (1961) 878.

[42] J.V. Maher, M.W. Sachs, R.H. Siemssen, A. Weidinger and D.A. Bromley, Phys. Rev. 188 (1969) 1665.

3

Chapter 3 - Experimental setup

3.1 Introduction

In the previous chapters, the importance of measuring elastic cross sections was discussed along with the previous measurements overview. In this chapter, a description of the experimental setup will be done. The elastic cross sections were measured at the 3.0 MV Tandem accelerator located at LATR/CTN-IST (Sacavém, Portugal); the measurements of target thickness and elemental composition were done at the 2.5 MV Van de Graaff accelerator at the same laboratory; ion implantation was done at the Danfysik 1090 high current implanter. Concerning the 3.0 MV Tandem accelerator, a detailed description of this system will be done since its improvement was a central part of this work. The main features of the 2.5 MV Van de Graaff accelerator and Danfysik high current implanter will also be presented.

3.2 Tandem accelerator

The 3 MV Tandem accelerator located at LATR provided proton and oxygen beams (this one in multiple charge states). Due to the complexity of this system, its description will be divided in several components: Duoplasmatron ion source, the beam transport system, the accelerator itself and the nuclear reactions chamber. Figure 3.1 represents a detailed scheme of the 3.0 MV Tandem accelerator including all ion sources and reaction lines. For a better understanding, in figure 3.1, the Duoplasmatron ion source is identified as H^- ion source and the nuclear reactions chamber is at the end of the NRA line.

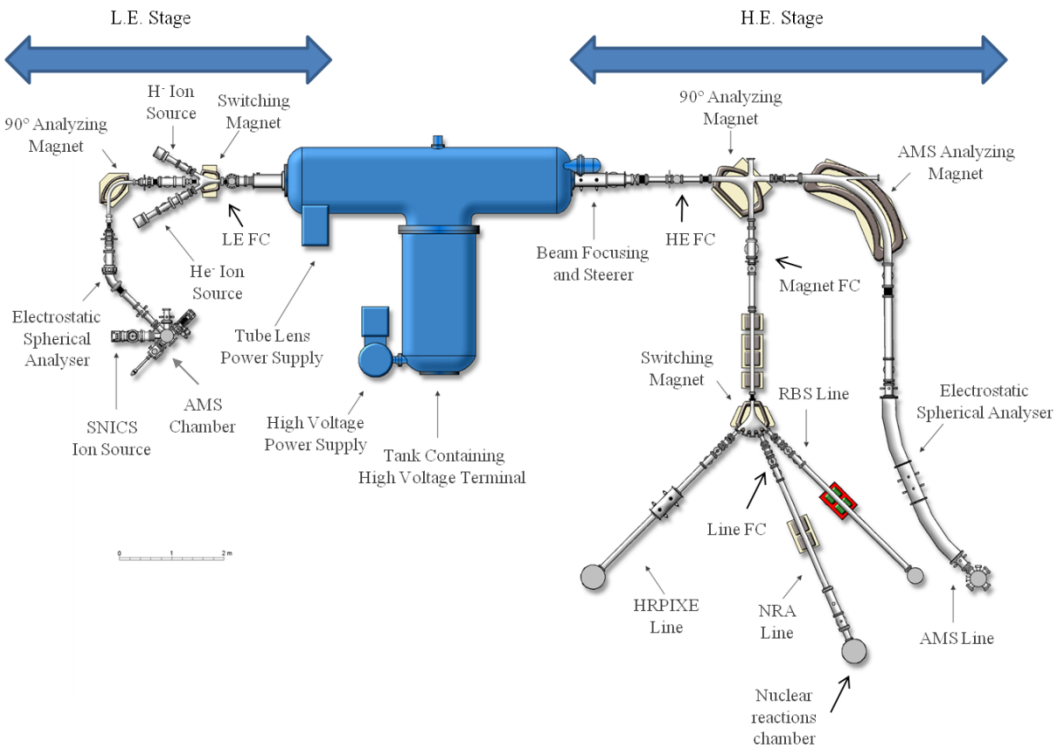

Figure 3.1) Scheme of the 3 MV Tandem accelerator at LATR/CTN-IST.

3.2.1 Duoplasmatron ion source

The Duoplasmatron ion source (figure 3.2) is a modified Von Ardenne ion source, in which a low pressure arc discharge in the gas to be ionized is electrostatically constricted by a funnel shaped intermediate electrode, placed between the electron-emitting cathode, which is called hot filament, and the anode. A strong magnetic field is developed between the cathode and anode, which constrains the discharge to a narrow plasma beam along the axis of the exit aperture. It is possible to change the gas bottle in order to have different elements in the plasma. For the proton beam, a hydrogen bottle was used. For oxygen, a CO_2 bottle was used. The Duoplasmatron ion source can produce, amongst others, H^- and oxygen beams with intensities up to 30 µA. This ion source is managed by several power supplies and meters: Filament (up to 20 A), Magnet Control (≈0.5A), Gas Control (a.u.), Arc Voltage (≈100V), Extraction (1 mA) and High Voltage Power Supply (15 kV).

Figure 3.2) Duoplasmatron Ion source.

3.2.2 Beam transportation system

After exiting the Duoplasmatron ion source, the particles are injected into the accelerator and, after being stripped from their negative electronic charge, are accelerated to high energies and taken to the target chamber. The beam transportation is done by a system combining three switching magnets (one in the low energy stage and two in the high energy stage), electrostatic quadrupoles, triplets, doublets and also multiple faraday cups for current measurement along with collimators systems in a more than 20 m vaccum line [1]. The beam transport system (see figure 3.1) is divided in two stages: low energy stage (L.E.), before the accelerator, and high energy stage (H.E.), after the accelerator, which are divided by the accelerator itself.

3.2.3 L.E. Stage

As said before, the beam exits the ion source with currents up to 30 μA. At this stage, the beam has an energy $E_i = e.V_i$ (approximately 15 keV), where V_i is the extraction voltage of the Duoplasmatron ion source and e is the total charge of the ion. The L.E. switching magnet (see figure 3.1) makes the first m/q selection of the ions that will enter the accelerator.

Typical magnet current at this point is 1.5 A for protons and 10.5 A for oxygen. At this point, the beam current is maximized at the L.E. Faraday cup (see figure 3.1), by optimizing the Duoplasmatron ion source parameters and the current of the L.E. switching magnet. Also, on the L.E. side, there two sets of lenses, the matching lenses and the tube lenses, and also a set of deflector plates (x and y).

The beam after the acceleration stage may be measured and optimized in the H.E. Faraday cup (see figure 3.1).

3.2.4 3 MV Tandem accelerator

The Tandem accelerator is an electrostatic accelerator of 3 MV produced by High Voltage Engineering®. The accelerator tank is filled with SF_6 gas at high pressure (approximately 6 bar), and contains, amongst other components, a high voltage Crockcroft-Walton generator of 3 MV, which creates the terminal voltage of the accelerator, plus a stripping channel, which is a tube filled with argon gas with a pressure of a few mbar. The Crockcroft-Walton generator is a voltage multiplier that converts AC or pulsing DC electrical power from a low voltage level to a higher DC voltage level. It is made up of a voltage multiplier ladder network of capacitors and diodes to generate high voltages. The high voltage terminal creates a positive electric potential in the center of the accelerator, where the stripping occurs, that causes negative ions coming from the source at the L.E. stage to be accelerated towards the center of the accelerator. Once inside the accelerator, the beam is stripped and accelerated to higher energies. This stripping process consists of using a gas or foil to strip the outer electrons of the ions passing through it, thus changing their charge state from negative to positive (figure 3.3 a). This process will break all the molecules in the beam [2], producing a high energy beam consisting only of monatomic ions, thus eliminating practically all molecular interferences.

In the second stage of acceleration, the ions are accelerated by the same positive potential and the energy after the accelerator is given by:

$$E_f = E_i + (q+1).e.V \qquad 3.1$$

where q is the positive charge state that a particular ion achieves in the stripping channel and V is the terminal voltage of the accelerator. For protons, the energy is approximately twice the terminal voltage. For oxygen ions, it will depend on the charge state. After exiting the accelerator, the ions enter the high energy stage. A photograph of the Accelerator tank is presented in figure 3.3 b).

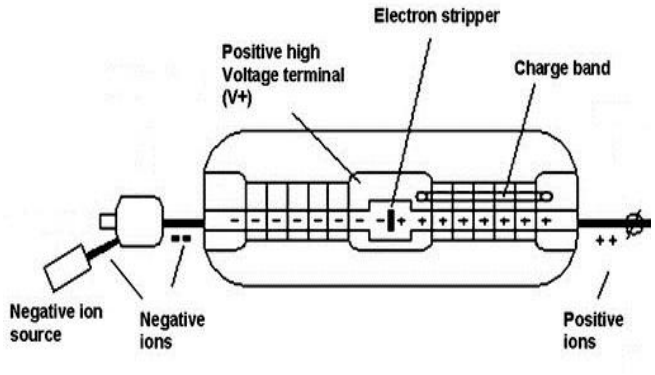

Figure 3.3) a) Illustrative scheme of a stripping process in a Tandem accelerator [3].

Figure 3.3) b) 3 MV Tandem Accelerator at LATR/CTN-IST.

3.2.5 H.E. Stage

On the high energy side, there are a set of x and y deflector plates and a set of X and Y focusing electrostatic quadrupoles. Just before the high energy Faraday cup (see figure 3.1), a set of 4 slits is used to change the beam diameter. Also, the elements used in the low energy stage are used for the current optimization at the high energy stage. After this FC, there is a 90° analysing magnet that makes another m/q selection, being the current measured by another Faraday cup, this one called magnet Faraday cup. Figure 3.4 shows a relation between magnet current and magnetic field for the 90° magnet. Expected values for magnet currents for the different ions and charge states are obtained with this relation (table 3.1).

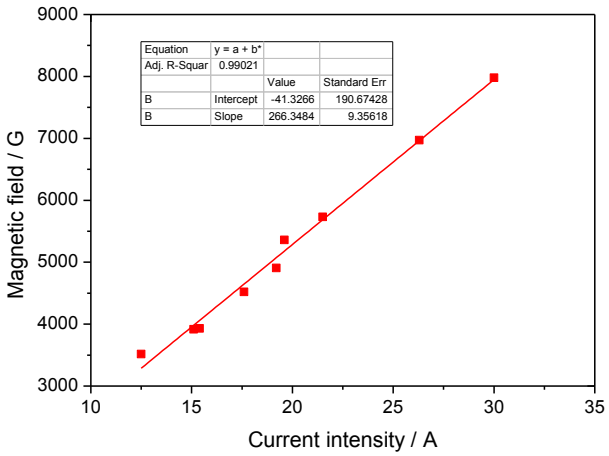

Figure 3.4) Magnetic field as a function of magnet current for the 90° analyzing magnet.

Element	Charge state	Terminal voltage / kV	Energy / keV	I / A
^{1}H	1+	1500	3000	18.5
^{16}O	2+	1500	4500	45.1
^{16}O	3+	1500	6000	34.8
^{16}O	4+	1500	7500	29.2
^{16}O	5+	1500	9000	25.6

Table 3.1) 90° Analysing Magnet current values as a function of charge state and terminal voltage for ^{1}H and ^{16}O.

Usually, the transmission between the high energy FC and magnet FC is 100%. After the magnet FC, a set of magnetic quadrupole triplets are used to focus the beam onto a switching magnet, which deflects the beam 22.5° to the nuclear reactions line (see figure 3.1). After the switching magnet, a collimator consisting of a tantalum plate with three apertures with 2, 3 and 5 mm of diameter is used to choose the size of the beam (figure 3.5), followed by a Faraday cup called Line FC.

Figure 3.5) Collimator consisting of a tantalum plate with 2, 3 and 5 mm diameter holes [4].

Before the beam enters the nuclear reaction chamber, there is a set of electrostatic steerer plates (x and y) and a magnetic quadrupole doublet. The target chamber is a Faraday cup itself, which is electrically insulated from the beam line, the detector and the collimators. In the chamber we have, apart from the detectors:

1. Collimating system (figures 3.6 and 3.7): at the entrance of the target chamber there is a collimating system composed by a PVC structure with a nickel plate protection and an aperture of 10 mm, which is the first collimator. On the opposite side of the collimating system, there is another nickel collimator with a 2 mm diameter covered by a film of Au to avoid unwanted contaminations in the gamma ray measurements. Also, there is an aluminum shielding that suppresses the secondary electrons that enter the chamber, minimizing the uncertainties in the charge collection measurements.

Figure 3.6) Nickel plate that protects the plastic structure at the entrance of the target chamber [4,5].

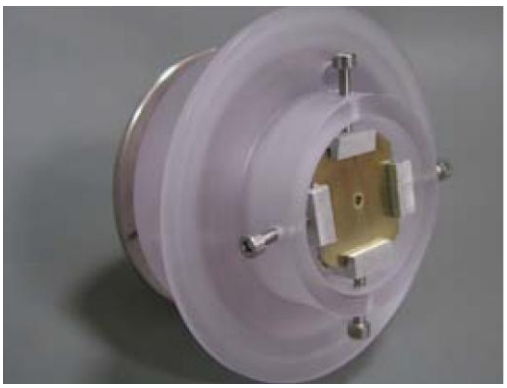

Figure 3.7) Nickel collimator with Au evaporated [4,5].

2. Target holder: constructed to allow the rotation of the targets with respect to the beam axis. It is possible to tilt the target at 45°.

3. Beam stopper (figure 3.8 D): Removable structure placed at the end of the nuclear chamber and aligned with the beam. It is made in stainless steel with a tantalum sheet in its end. An extension tube is used to minimize the backscattering particles that reach the detectors. It stops the beam that passes through thin targets.

4. Insulating Rotating Flanges: connected to the turbo-pump connecting flange.

The chamber is equipped with two particle detectors and one γ-ray detector:

1. 2 Canberra® PIPS (Passivated Implanted Planar Silicon) detector (PD-50-12-100 RM) with 50 mm^2 active area, 100 μm depletion layer and a nominal resolution of 12 keV for the 5486 keV alphas from ^{241}Am decay to ^{273}Np. These detectors are called MOVD and MOVE and they rotate in Cornell geometry. The angle with respect to the beam direction covered by the detectors ranges from 30° to 165°. They are inside a teflon and metal box with a circular aperture of 6 mm, that can be reduced to 2 mm, and mounted in a movable arm in the chamber. In the ^{12}C(p,p)^{12}C measurements, the angular separation between the two detectors was 22.3°. After this, due to a mechanical adjustment, the angular separation was 20.5°. The detectors were aligned using a device constructed for that purpose, which allows the alignment relative to the geometric center of the chamber along with a level. The angular precision is better than 0.2° in these conditions. The distance of the detectors to the target is 88±1 mm. This corresponds to a solid angle of $\Omega = \frac{\pi r^2}{d^2} = \frac{\pi 3^2}{88^2} = (3.65 \pm 0.09) \times 10^{-3} sr$ for the collimator of 6 mm diameter.

2. EG&G Ortec® GEM-45190-P HPGe detector with a crystal diameter of 64.0 mm, a length of 62.6 mm, has a resolution of 1.76 keV and a relative efficiency of 45 % for the 1.33 MeV of ^{60}Co. The detector is 55.5 mm away from the target and at 130° from the beam axis. The gamma detector enters in the chamber through a sleeve and to ensure the electric insulation with the chamber it is covered by a mylar coat with a thickness of 6.3 μm. It is also cooled with liquid nitrogen.

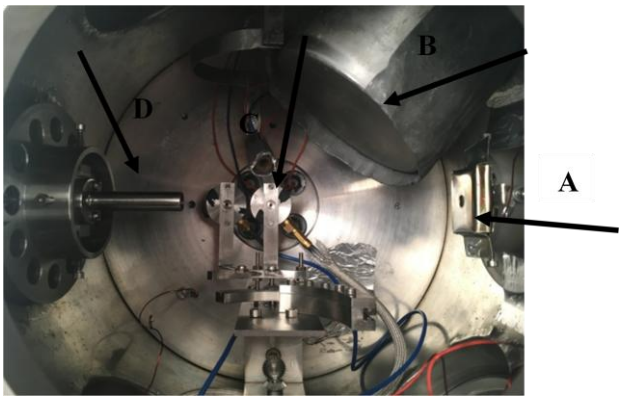

Figure 3.8) Upper view of the target chamber with A) Collimating system, B) Sleeve where the EG&G Ortec® GEM-45190-P HPGe detector enters, C) 2 Canberra PIPS and rotating system and D) Beam stopper.

The vacuum system of the nuclear reaction beam line (figure 3.9) is divided in two stages: in the first the vacuum is ensured by a rotatory pump and a turbomolecular pump from *Pfeiffer*. At this point, there are two meters *Pirani* and *Penning* from *Edwards*. In the second stage, there is a rotatory pump and a turbomolecular pump from *Varian*, and a meter from *Edwards*. The typical pressure in the chamber in good vacuum condition is 8×10^{-7} mbar.

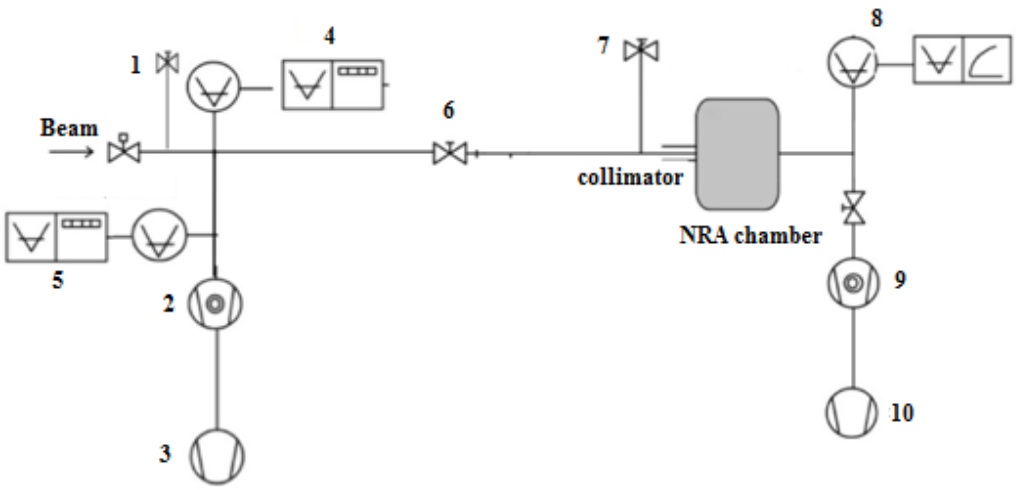

Figure 3.9) (1) Pneumatic valve; (2) Turbomolecular pump; (3) Rotatory pump from Varian; (4) Pirani meter; (5) Penning meter; (6) Válvula manual; (7) Pneumatic valve; (8) Penning meter; (9) Turbomolecular pump from Pfeiffer; (10) Rotatory pump from Pfeiffer.

3.2.6 Experimental procedures in Tandem accelerator

Among others, it is important to point out two procedures that were carried out by the author in order to produce the needed accelerated beams, with a well-known energy: the filament preparation and conditioning and the accelerator calibration in energy.

The filament preparation consists of preparing a new coating for the Duoplasmatron ion source filament and involves the following procedure:

a) Clean the platinum mesh with royal water (figure 3.10) which is prepared in the moment with a solution of HCl and HNO_3 3:1 (20% in water).
b) Wash the filament with water.
c) Dry the filament with a dryer. If necessary, use hot air.
d) Sink the filament in a solution of barium carbonate and butyl acetate 2:1.
e) Warm the filament with a torch until it gets a red toning.
f) Sink again the filament in a solution of barium carbonate and butyl acetate.
g) At the end, dry the filament with cold air.

Figure 3.10) The platinum mesh of the filament after cleaning with royal water [4].

After this, the filament conditioning is achieved by the slow increase of the filament current in vacuum conditions.

Concerning the energy calibration of the accelerator, more than one technique can be used. For instance, it is possible to do the energy calibration of the accelerator measuring the $\vec{B}$ of the 90° magnet or calibrate using resonances from nuclear reactions with well known energies. In this work, the second technique was used. The calibration was done using both

thin and thick targets in a wide range of energies, so the calibration could be valid for a wide range of energies. The resonances chosen for this purpose were the following:

1) $^{19}F(p,\alpha\gamma)^{16}O$, $E_r = 672$ keV, $\Gamma = 6$ keV, $E_\gamma = 6125$ keV.
2) $^{19}F(p,\alpha\gamma)^{16}O$, $E_r = 872$ keV, $\Gamma = 4$ keV, $E_\gamma = 6125$ keV.
3) $^{19}F(p,\alpha\gamma)^{16}O$, $E_r = 1371$ keV, $\Gamma = 6$ keV, $E_\gamma = 6125$ keV.
4) $^{23}Na(p,p'\gamma)^{23}Na$, $E_r = 1645$ keV, $\Gamma = 8$ keV, $E_\gamma = 440$ keV.
5) $^{23}Na(p,p'\gamma)^{23}Na$, $E_r = 1930.7$ keV, $\Gamma = 6.9$ keV, $E_\gamma = 440$ keV.
6) $^{16}O(p,p)^{16}O$, $E_r = 3470$ keV, $\Gamma = 1.5$ keV.

The experimental gamma-ray yields obtained in one of the calibration procedures are shown in fig. 3.11.

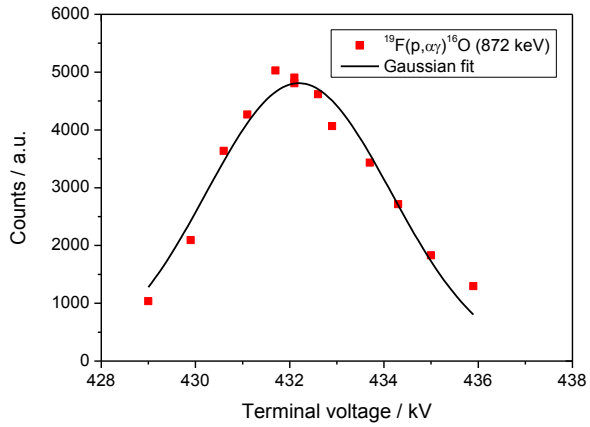

Figure 3.11) Ressonance of $^{19}\mathrm{F}(\mathrm{p},\alpha\gamma)^{16}\mathrm{O}$ reaction at E_r= 872 keV.

The energy of the measured resonance at 50% of its maximum, according to Iliadis [6], is given by:

$$E_{50\%} = E_r + \frac{\Delta E}{2} \pm \frac{1}{2}\sqrt{\Gamma^2 + \Delta E^2} \qquad 3.2$$

where E_r is the resonance energy, ΔE is the target thickness in energy and $\sqrt{\Gamma^2 + \Delta E^2}$ is the experimental width of the resonance.

The energy calibration of the Tandem accelerator was obtained from the experimental resonances measured. A good agreement was observed between the slope (1.99329) of the linear fit (figure 3.12) for this calibration and the theoretical energy given by the a Tandem accelerator $E_f = E_i + (q+1).e.V$, which for protons is twice the terminal voltage value. Also the origin intercept is in agreement with the extraction voltage (15 kV).

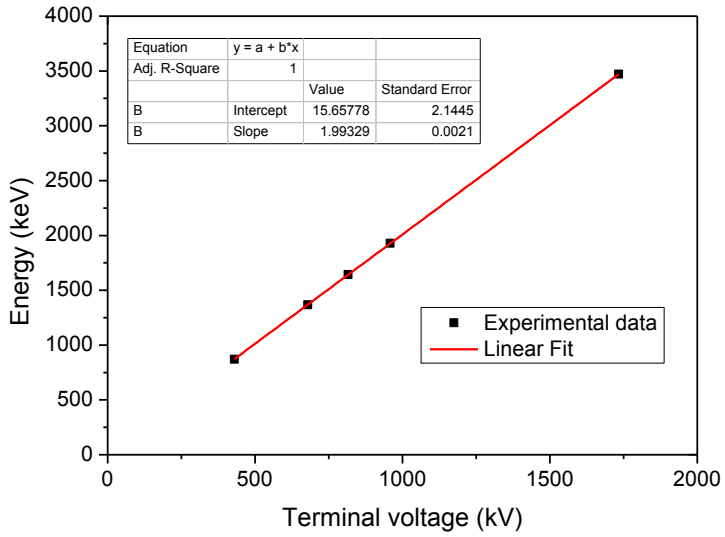

Figure 3.12) Energy calibration of the 3 MV Tandem presented as a linear fit.

Comparison between the $E_{50\%}$ values obtained from equation 3.2 and from fitting was done. The values are presented in table 3.2.

Terminal voltage / kV - $E_{50\%}$	$E_{50\%}$ / keV (from equation 3.2)	$E_{50\%}$ / keV (from fitting)
430.2	871.5	873.2
678.8	1367.9	1368.7
815.9	1643.1	1642.0
958.5	1928.8	1926.2
1733.6	3470.0	3471.2

Table 3.2) Comparison between theoretical and experimental values for the resonances measured at $E_{50\%}$.

This energy calibration was assumed as a valid calibration during the measurements. The energy uncertainty in these conditions is 3 keV at all energies.

3.3 Van de Graaff accelerator

The stoichiometry and thickness of the targets were determined by means of RBS, EBS and NRA. Most of these measurements were carried out at the 2.5 MV Van de Graaff accelerator at LATR/CTN-IST. Since this accelerator was only used for target characterization, a brief description of the Van de Graaff accelerator will be done. A scheme of the 2.5 MV Van de Graaf accelerator is presented in figure 3.13.

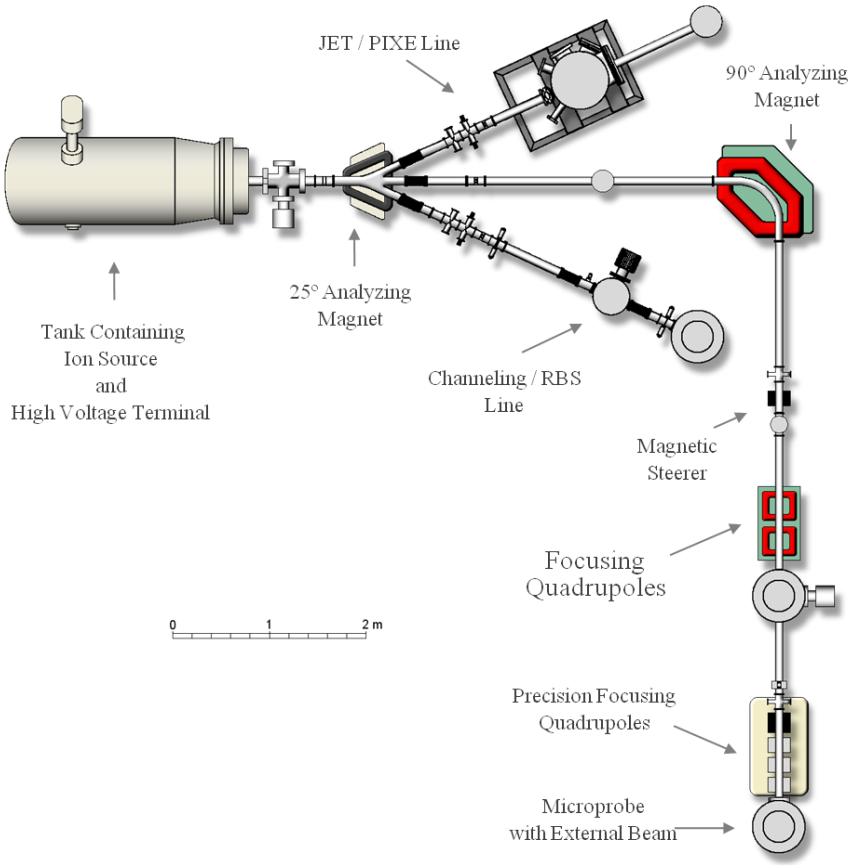

Figure 3.13) Scheme of the 2.5 MV Van de Graaff accelerator at LATR.

The Van de Graaff accelerator is an AN-2500 Type-A Model, manufactured by High Voltage Engineering Europe® and is a horizontal electrostatic accelerator, with the capacity to reach terminal voltages in the order of 2.5 MV.

The accelerator is inside a metallic cylinder (tank) and is pressurized with a mixture containing SF_6 (50%) and N_2 (50%) to avoid discharges between the terminal and the tank.

This accelerator provided H^+ and He^+ beams with energies up to 2000 keV and currents between 1 and 20 nA. A 2 MeV $^4He^+$ beam (1 mm^2 spot size) was used.

The beam is produced by a RF ion source and is focused by an einzel lens located after the source. After the accelerator tank (figure 3.13), there are two x and y electrostatic deflectors.

Figure 3.14) Tank of the Van de Graaff Accelerator at LATR.

The beam enters the RBS/Channeling beam line after passing through a 25° analyzing magnet and through a pair of slits. The energy calibration of the accelerator is done using the calibration of this magnet. In this line, there are two chambers. However, in this work, just the first chamber was used, called small chamber. In the chamber, three detectors are placed, being the scattered particles detected with silicon detectors placed at θ_{lab}=-140° (RBS2), θ_{lab}=-165° (RBS1) and θ_{lab}=+165° (ERD) with respect to the beam axis (figure 3.15). The lower scattering angle was chosen to avoid scattering particles from the chamber in the spectrum.

The charge collection is made in the target, so for thin targets no measure of current is possible. For our measurements, the presence of a heavy element in the spectrum allows charge normalization, overcoming this drawback.

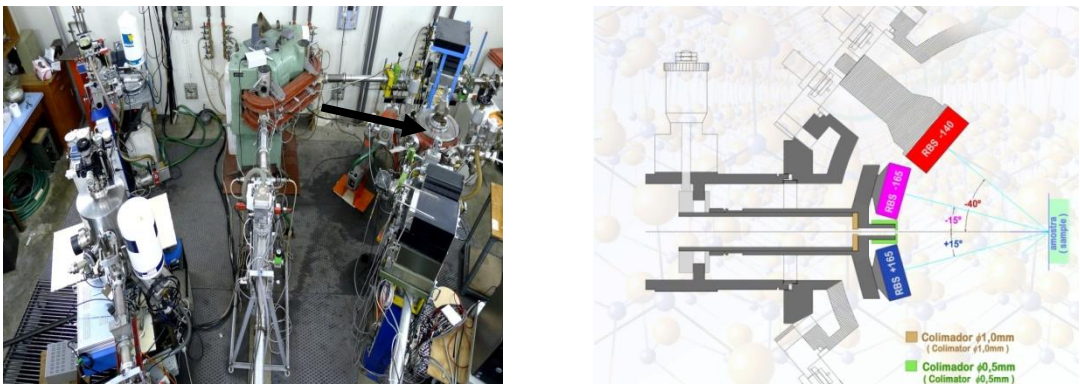

Figure 3.15) RBS setup (line and detectors position inside the RBS chamber).

3.4 Danfysik high current implanter

The implantations of ^{7}Li, ^{16}O, ^{59}Co and ^{129}Xe were done at the Danfysik 1090 high current implanter at LATR/CTN-IST. The source of ions is the model 921A high current ion source (Chordis). The maximum acceleration voltage is 210 kV (50 kV at the extraction and 160 kV at the throttle tube) with currents up to 10 mA, target temperature between -150 and 600 °C, implanted area up to 40x40 cm^2 and magnetic beam focusing and sweeping. A scheme of the Ion Implanter is presented in figure 3.16.

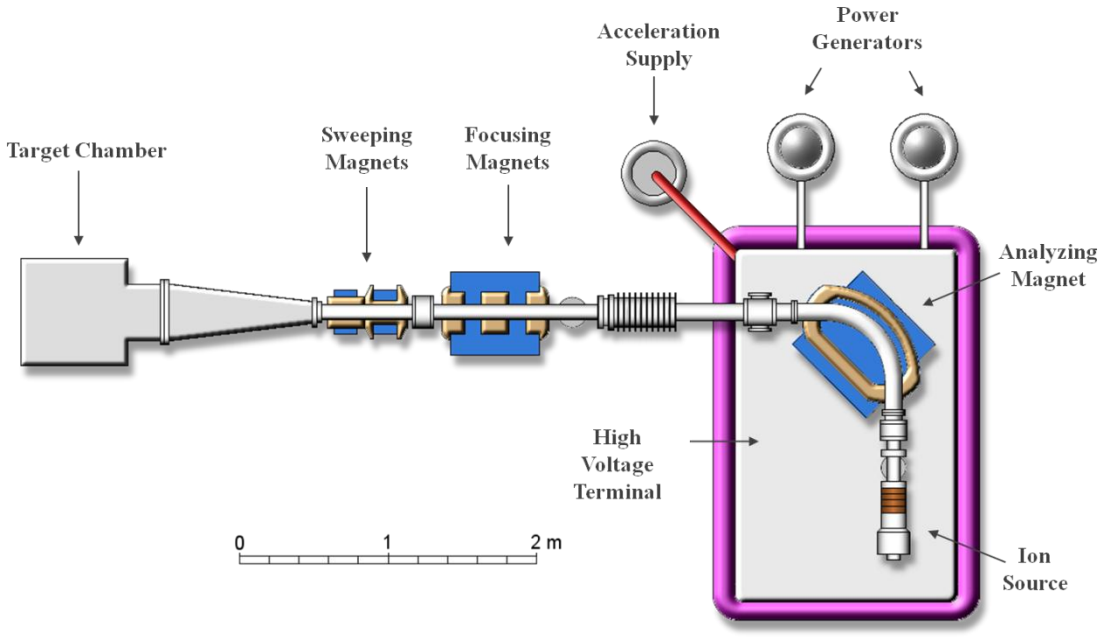

Figure 3.16) Scheme of the Danfysik ion implanter at LATR/CTN.

The analyzing magnet consists of a 90° double magnet with a mass resolution $m/\Delta m$ from 150 to 250. The ion beam is focused by the focusing magnets, which are a triplet of magnetic quadrupoles. To avoid high instantaneous charges in the target, the beam may be unfocused to larger dimensions, which was the case in this work.

The samples are placed in the implantation chamber and mounted on a large metal target support with two rotating axes.

For the implantation with low energies (which is the case for ^{7}Li), a deceleration system was installed on the sample holder in order to decelerate the ion beam before hitting the sample (figure 3.17).

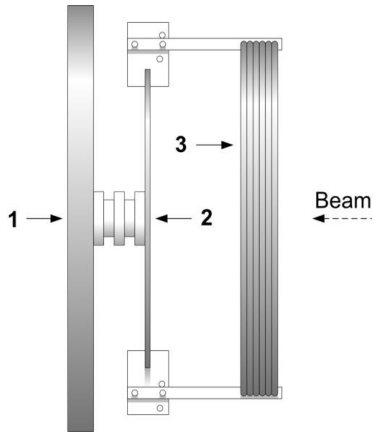

Figure 3.17) Deceleration system: 1) Implanter target; 2) Deceleration target and 3) Lens.

The deceleration system consists of an insulated target plate mounted over the implanter target and a single electrode lens to compensate beam dispersion due to target biasing. The lens is composed by a group of 6 stacked aluminum rings and is positioned 10 cm downstream of the target.

3.5 References

[1] H. Luís, PhD thesis, Lisboa, 2013.

[2] Yuki Tosaki *et al*., *Water 3* (2011) 64-78.

[3] V. Camacho-Móran et al., Petroleum Science and Technology 25 (2007) 1391-1400.

[4] M. Fonseca, PhD thesis, Lisboa, 2009.

[5] C. Santos, PhD thesis, Lisboa, 2016.

[6] C. Iliadis, Nuclear Physics of Stars, Wiley-VCH, 2007.

4

Chapter 4 - Target preparation and characterization

4.1 Introduction

In the previous chapter, the experimental setup was described, including the accelerator and implanter devices. In this chapter, target preparation and characterization will be addressed. Along with this, analytical techniques used for its characterization will be presented. RBS (Rutherford Backscattering Spectrometry), NRA (Nuclear Reaction Analysis) and PIGE (Particle Induced Gamma Ray Emission) will be briefly described before the presentation of the results obtained with these techniques. PIXE (Particle Induced X-ray Emission) and XRD (X-ray Diffraction) were used as complementary techniques for target analysis, so its description will not be addressed. This chapter is divided in two sections: the first one deals with the production and characterization of thin targets for elastic scattering cross section measurements; in the second section, a comparative study of targets for astrophysical purposes will be described, concerning the $^{16}O+^{16}O$ fusion reaction, despite the results for this fusion reaction cross section not being included in this thesis.

4.2 Production of thin targets for elastic scattering cross section measurements

The use of thin transmission targets is relevant to measure the elastic scattering of protons and oxygen ions. The areal density of the targets must be high to maximize the reaction products yields, but not so high as to allow a correct calculation of the effective beam energy. Besides this, the targets must withstand high beam current densities without noticeable deterioration, and contaminants must be minimal. In this work, the production of thin targets is performed with a novel approach [1].

In this work, the implantation and evaporation techniques were combined for thin targets production. The implantation technique allows single isotope implantation in a substrate. The evaporation technique allows the production of thin self-supporting layers for certain elements (C, Ag, Al) and also the evaporation of stable compounds (such as LiF, LiCl, LiI) on a thin substrate.

The targets produced with these techniques must fulfill the following requirements:

- Self-supporting thin targets with good mechanical resistance;
- Areal density: compromise between a high value (maximize the reactions yield) and a low value (best effective beam energy calculation);
- Target stability: capability to withstand beam interactions without noticeable deterioration;
- Contaminants kept as low as possible in order to avoid interference effects;
- The presence of a heavy element for charge normalization purposes;

The fluence/target thickness was calculated to achieve the same reaction yield for both elements in order to obtain good counting statistics (less or around 1% uncertainty) for both elements, at a reasonable (less than 5%) acquisition dead time.

The targets stability was tested during experiments: the ratio between the yields of the elements of interest was verified for the same experimental conditions and RBS analysis of the targets was performed before and after the experiments in order to check their composition. All the targets remained stable in yield at all energies.

In this work, several targets were prepared after multiple trials:

1) ^{16}O and ^{59}Co implanted in self-supporting C.
2) ^{129}Xe implanted in self-supporting C.
3) ^{7}Li implanted in self-supporting Al and C (in the last case, also ^{129}Xe was implanted).
4) LiF evaporated on self-supporting C which was implanted before with ^{129}Xe.
5) $LiWO_4$ evaporated on self-supporting C.
6) LiI and LiCl evaporated on self-supporting C.
7) $Ca_3(PO_4)_2$ evaporated on self-supporting Ag.

In the following sections, the target preparation and characterization will be described for each target.

4.2.1 ^{16}O and ^{59}Co implanted in self-supporting C

Target preparation by implantation takes advantage of the Danphysik ion implanter at LATR.

High fluence ion implantation at low energies has a widespread use to change mechanic and chemical surface properties modification. In this work, ion implantation is used with a different purpose: target fabrication, providing the implantation of single isotopes in multiple backings.

The selection of the energy, fluence to be implanted (nominal fluence) and the backing material was done considering the following issues:

- Backing material: concerning the production of thin targets, the self-supporting materials produced by evaporation must withstand the ion implantation without deterioration. Aluminum and silver thin films (~40 μg/cm^2) tended to broke up during implantation stage. Only carbon provided thin films resistant enough to withstand the implantation.
- Fluence and implantation energy: using Monte Carlo simulations, namely SRIM2003 [2], calculations were done of range, straggling, sputtering yields and backscattered ions for each pair-implanted ion plus backing. These values are then used to obtain the theoretical implanted profile, $n(x)$, which in at/cm^3 can be given by the equation [3]:

$$n(x) = \frac{n_a(1-BS)}{2S}\left[erf\left(\frac{x - R_p + D_N(\frac{S}{n_a})}{\sqrt{2}\Delta R_p}\right) - erf\left(\frac{x-R_p}{\sqrt{2}\Delta R_p}\right)\right] \quad 4.1$$

where x is the depth, n_a is the substrate atomic density, BS is the backscattered fraction ions, S is the sputtering yield, R_p is the projected range, ΔR_p is the straggling and D_N is the nominal fluence. We can calculate the retained fluence (D_I) in at/cm^2 using the equation:

$$D_I = \int_0^\infty n(x)dx \quad 4.2$$

Equation 4.1 is based on the assumptions that the sputtering yield is constant, and equal for both substrate and implanted ions, there is no knock-on effect and the volume

change due to radiation damage can be neglected. It also does not take into account any saturation or diffusion towards the surface effect, so it may start failing to predict correctly high fluence implantation profiles. It is, nevertheless, a good starting point to the prediction of implantation profiles. Figure 4.1 shows the implanted profile evolution with increasing fluence as predicted by eq. 4.1, for ^{16}O implantation in Ta at 70 keV.

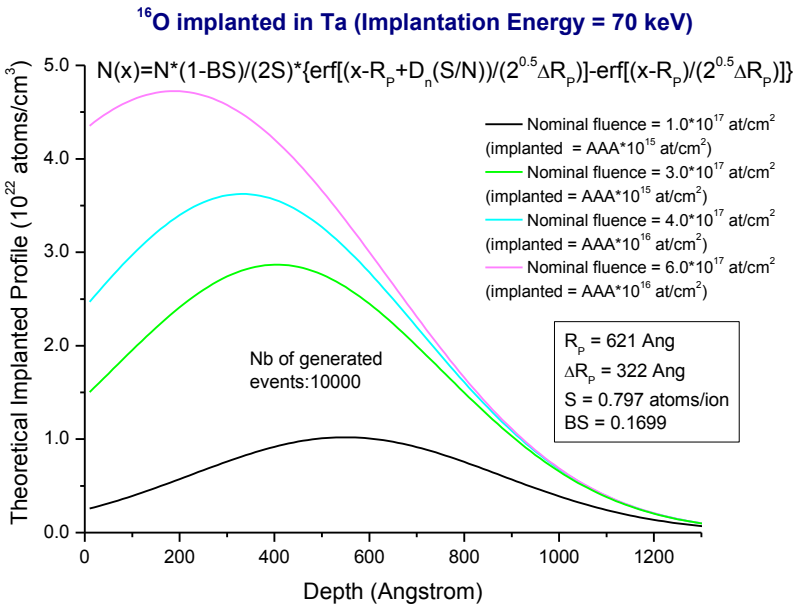

Figure 4.1) Implantation profile of ^{16}O in Ta for different nominal fluences at 70 keV.

The production of thin targets is done with a novel approach, in which a thin layer of C (few nm thick) is produced over a glass sheet (figure 4.2 a) by evaporation of graphite in vacuum conditions at a pressure of ~10^{-6} mbar (figure 4.2 b). The carbon layer on the top of the glass is implanted with the wanted element. After that, the separation between the implanted carbon film and the glass sheet is achieved by submerging the glass sheet in water carefully. As the glass slowly sinks the carbon film will stay floating on the water surface. The carbon film is finally fixed on a target frame and placed in a suitable target holder under controlled atmosphere (figure 4.2 c).

Figure 4.2) a) Glass sheet with carbon evaporated.

Figure 4.2) b) Evaporator at LATR/CTN.

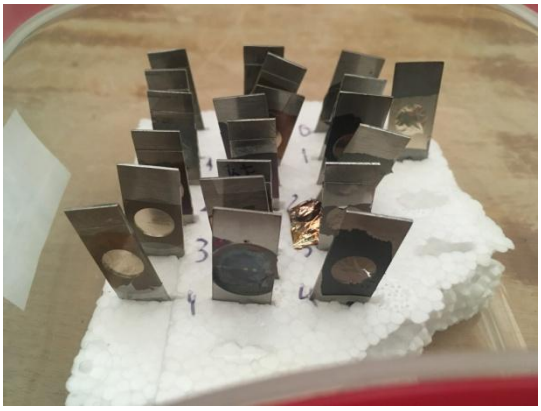

Figure 4.2) c) Target holder with multiple targets produced.

Figure 4.2) d) Experimental apparatus for carbon evaporation.

We have implanted ^{16}O and ^{59}Co. The inclusion of a heavy element allows the normalization to the Rutherford cross section, minimizing the systematic uncertainties.

Concerning the implantation of ^{16}O, two targets were prepared by this process. For the first target, the implantation was done at the beam energy of 20 keV ($3x10^{17}$ at.cm^{-2}) for ^{16}O implantation and 100 keV ($2x10^{16}$ at.cm^{-2}) for ^{59}Co implantation. Concerning the second one, the implantation was done at the beam energy of 60 keV ($3x10^{17}$ at.cm^{-2}) and 30 keV ($1.6x10^{17}$ at.cm^{-2}) for ^{16}O implantation and 100 keV ($2x10^{16}$ at.cm^{-2}) and 80 keV ($1.4x10^{16}$ at.cm^{-2}) for ^{59}Co implantation. Implantations using one energy give a maximum deposition in the middle of the carbon film. Implantations using two energies give a more homogeneous depth distribution.

The stoichiometry and thickness of the targets were determined by means of RBS (Rutherford Backscattering Spectrometry). These measurements were carried out at the 2.5 Van de Graaff accelerator. A 2 MeV $^4He^+$ beam (1 mm^2 spot size) was used, being the scattered particles detected with a silicon detector placed at θ_{lab}=140° with respect to the beam axis.

The RBS technique is an analytical technique, which makes use of the accelerators. It is based on the Rutherford scattering and gives information of the stoichiometry, thickness and depth distribution of the elements in the sample. In this work, we were interested to obtain the film thickness for each element with this technique.

Usually alpha particles are used for RBS and we measured the amount of energy loss of those particles due to the collision with the target atomic nuclei. This loss depends on the mass of each element present in the target. There are three fundamental physical quantities in the RBS technique: the kinematic factor, the Rutherford cross section and the stopping power. In the spectrum, each element present in the target corresponds to a peak, in which the width relates with the amount of energy loss in the material and the position mainly relates to the mass of the element. The kinematic factor is given by the ratio between the energy of the projectile after the collision, E_r, and the energy of the projectile before the collision, E_0:

$$K = \frac{E_r}{E_0} \tag{4.3}$$

The kinematic factor depends on the masses of the incident ion and the target elements and on the scattering angle and is given by the following expression:

$$K = \left[\frac{(M_2^2 - M_1^2 \sin^2 \theta_{lab})^{\frac{1}{2}} + M_1 \cos \theta_{lab}}{M_1 + M_2}\right]^2 \tag{4.4}$$

where θ_{lab} is the scattering angle in the laboratory frame, M_1 and M_2 are the masses of the incident ion and the target element, respectively. The parameters θ_{lab}, M_1 and E_0 are usually known, thus is possible to identify M_2. Equation 4.4 is valid presuming that the interaction is elastic, the projectile energy E_0 is much larger than the binding energy of the atom in the target and nuclear reactions and resonances are absent.

As there is greater separation between the energies of particles backscattered from light elements than from heavier elements due to the fact that an important amount of

momentum is transferred from the incident particle to a light target ion, RBS has a better mass resolution for light elements than for heavier elements. However, the elements lighter than the incident particle cannot be detected as these elements will scatter the incident particles at forward angles.

For the energies used in this work, the scattering is Rutherford (pure Coulomb scattering), then the differential cross section is given by [4]:

$$\sigma_R(E,\theta_{lab}) = \left(\frac{Z_1 Z_2 e^2}{4E}\right)^2 \times \frac{4\left[(M_2^2 - M_1^2 \sin^2\theta_{lab})^{\frac{1}{2}} + M_2 \cos\theta_{lab}\right]^2}{M_2 \sin^4\theta_{lab}\,(M_2^2 - M_1^2 \sin^2\theta_{lab})^{\frac{1}{2}}} \quad 4.5$$

where Z_1 and Z_2 are the atomic numbers of the incident and target ions, respectively, and e is the charge of electron. This equation is given in cgs units.

It is possible to note that the Rutherford cross section increases with the square of the atomic number of the target ions and decreases with the inverse of squared energy $\left(\frac{1}{E^2}\right)$. For thin targets, the areal density, N_i, in atoms per unit area for each element is given by:

$$N_i = \frac{A_i}{N_p \Omega_{\text{lab}} \sigma_R(E,\theta_{lab})} \quad 4.6$$

where N_p is the number of incident projectiles, A_i is the integral of the peak counts of the *i*th element in the film and Ω_{lab} is the detector solid angle. An intrinsic efficiency of 100% is assumed for the detection.

The energy of particles backscattered from a target can be calculated using figure 4.3 as an example, taking M_1 and E_0 as the mass and energy of incident particles, which are backscattered with energy E_1 and detected at an angle θ_{lab}, with energy E_2 transferred to the target element of mass M_2. Usually θ_1 and θ_2 are angles between the sample normal and the direction of the incident beam and of the scattered particle. The energy E_1 is given by:

$$E_1 = KE_0 \quad 4.7$$

The energy $E_1^{'}$ will be given by:

$$E_1^{'} = K(E_0 - \Delta E_{in}) - \Delta E_{out}$$

$$= KE_0 - \left[\frac{K}{\cos\theta_1}\left(\frac{dE}{dx}\right)_{in} + \frac{K}{\cos\theta_2}\left(\frac{dE}{dx}\right)_{out}\right].\Delta x \qquad 4.8$$

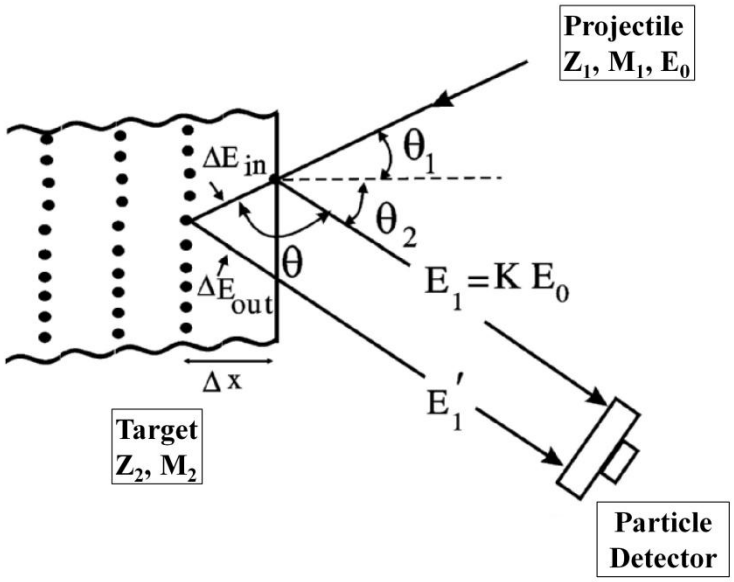

Figure 4.3) Energy loss of the projectile ion in the target material.

SIMNRA [5] and WiNDF [6] are simulation codes for RBS calculations which make easier the calculations with a faster approach and the possibility to consider impurities whose peaks are present in the spectra.

A lower scattering angle was chosen to avoid scattering particles from the chamber in the spectrum. Experimental data were simulated with SIMNRA. The PIXE technique was also used to confirm the presence of contaminants in the film. PIXE measurements were carried out using a 3 MeV proton beam produced by the 3 MV Tandem accelerator. The collected charge was 10 μC. PIXE measurements were analyzed using GUPIXWIN [7].

The RBS spectra and depth profile for the first target is presented in figure 4.4, showing the presence of O and Co. The spectrum also shows the presence of iron and zinc as contaminants, which are confirmed by PIXE. From SIMNRA simulations we obtained a thickness of $(1.30\pm0.05)\cdot10^{18}$ at/cm^2 for the carbon layer and a retained fluence of $(1.2\pm0.1)\cdot10^{17}$ at/cm^2 for oxygen and $(2.3\pm0.5)\cdot10^{16}$ at/cm^2 for cobalt. For the contaminants, a total of $(8\pm4)\cdot10^{16}$ at/cm^2 and $(10\pm4)\cdot10^{16}$ at/cm^2 were obtained for iron and zinc, respectively.

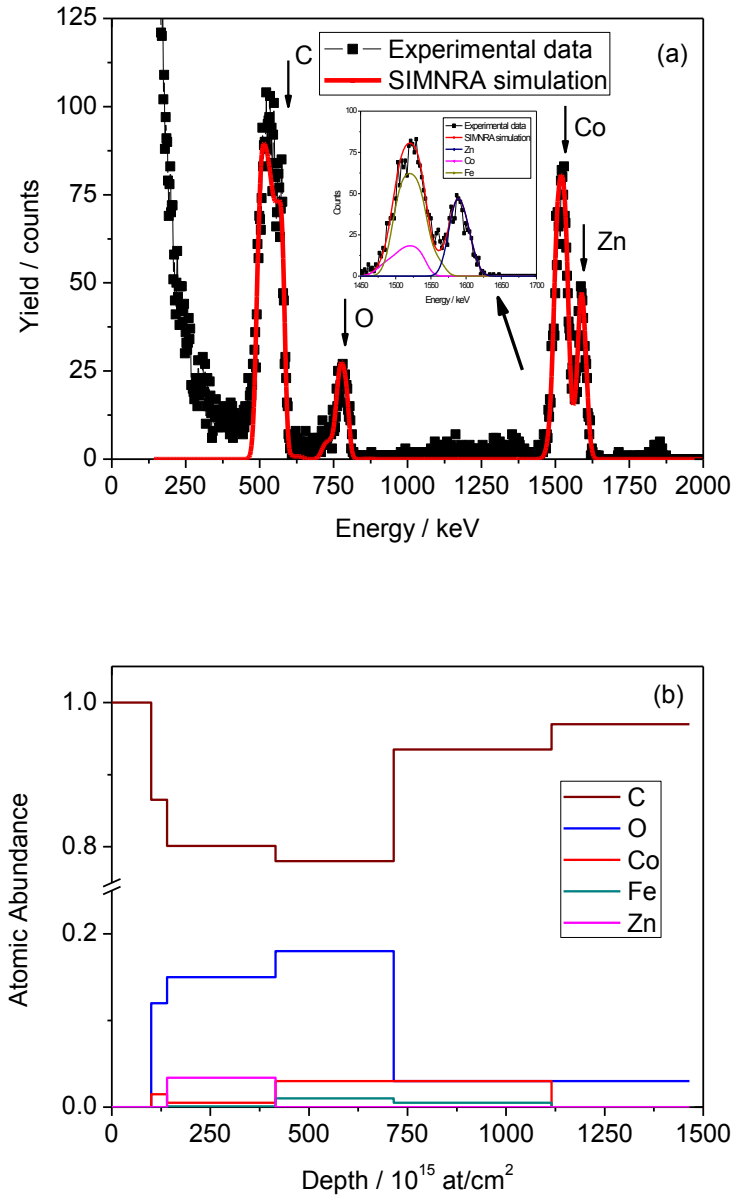

Figure 4.4) (a) Experimental RBS spectra and simulation fitting performed with SIMNRA (b) Depth profile obtained from the RBS analysis.

The depth profile corresponding to these two spectra is shown in figure 4.4 (b) and confirms that the implantation for the oxygen and cobalt follows the one predicted by SRIM simulations, with the deposition almost in the middle of the carbon film.

For cross checking the presence of contaminants in the sample, PIXE measurements were done. A comparison between the two techniques is shown in table 4.1.

	Co (10^{15} at/cm^2)	Fe (10^{15} at/cm^2)	Zn (10^{15} at/cm^2)
RBS	23 ± 5	8 ± 4	10 ± 4
PIXE	29 ± 3	19 ± 2	15 ± 2

Table 4.1) Concentrations of Co, Fe and Zn given by RBS and PIXE.

The results within uncertainties are in agreement, except for Fe. As Co inside the film is mixed in the RBS spectrum with Fe, it is expectable that the iron content given by RBS is less reliable than the one given by PIXE. The presence of Fe and Zn resulted from the polishing procedure of the graphite cylinder before evaporation. The implementation of a new polishing process using a silicon carbide grit was successful in removing these two elements. The second target was produced with this new approach. This target was produced with a higher fluence of oxygen and cobalt. The RBS spectrum for this target is shown in figure 4.5.

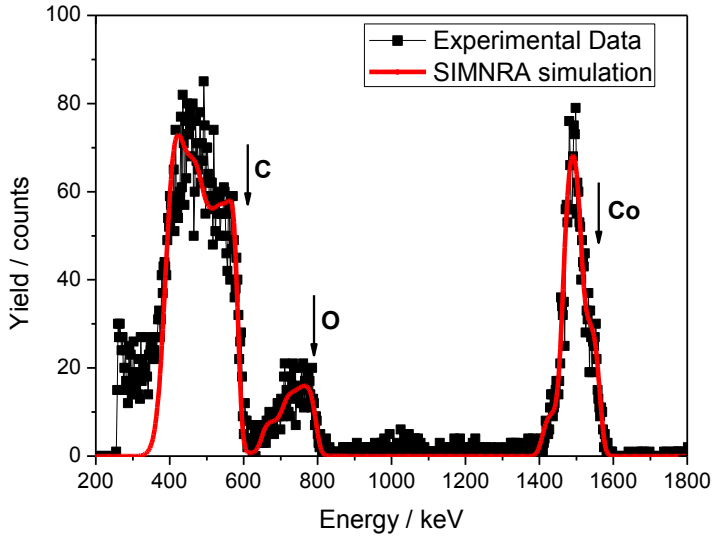

Figure 4.5) Experimental RBS spectra and simulation fitting for $^{16}O+^{59}Co$ Implantation.

The nominal and the retained fluence for the implanted elements are resumed in table 4.2 for the two targets.

	Nominal Fluence ^{16}O (10^{15} at/cm^2)	Retained Fluence ^{16}O (Measured) (10^{15} at/cm^2)	Nominal Fluence ^{59}Co (10^{15} at/cm^2)	Retained Fluence ^{59}Co (Measured) (10^{15} at/cm^2)
Target 1.1	300	123 ± 10	20	23 ± 5
Target 1.2	460	208 ± 9	34	54 ± 2

Table 4.2) Retained fluence (measured) vs Nominal fluence in the implanted targets.

It is possible to verify that for oxygen, the ratio between the retained and nominal fluences are similar for the two targets, 0.41 and 0.45, respectively. Considering the large uncertainty of nominal fluencies which can be as high as 30% for low fluences, there is a fair agreement between retained and nominal fluencies.

4.2.2 ^{129}Xe implanted in self-supporting C

Concerning the measurement of the $^{12}C(p,p)^{12}C$ elastic cross section at forward angles, a thin target was produced by implanting ^{129}Xe in the carbon film.

The implantation was done at the beam energy of 150 keV ($3.4x10^{16}$ at.cm^{-2}) for ^{129}Xe. The RBS spectrum obtained for this target is presented in figure 4.6. As a side note, there is no oxygen contamination in the target, in spite of, after the implantation when carbon foils are floating on water, they absorb plenty of water. As this is easily removed in vacuum and especially during the ion bombardment, no oxygen is left on the foils.

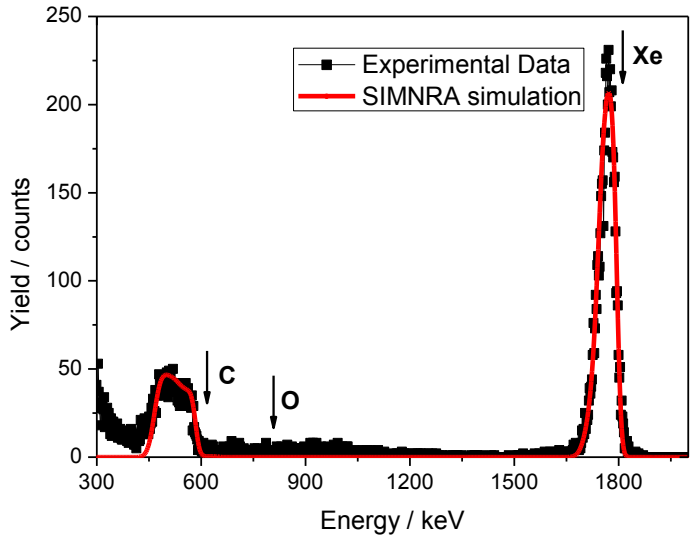

Figure 4.6) Experimental RBS spectra and simulation fitting performed with SIMNRA.

From SIMNRA simulation it was obtained a $(1.78\pm0.05)\cdot10^{18}$ at/cm^2 for the carbon layer and a retained fluence of $(45\pm2)\cdot10^{15}$ at/cm^2 for ^{129}Xe.

4.2.3 ^{7}Li implanted in self-supporting Al and C

Targets produced by implantation of ^{7}Li in two backings (Al and C) were performed.

Considering Al as a backing, self-supporting Al was produced by vacuum evaporation at the evaporator of LATR/CTN. After this, an implantation was done at the beam energy of 10 keV ($4x10^{17}$ at.cm^{-2}) for ^{7}Li. The purpose was to implant ^{7}Li in the middle of the Al film.

The target characterization was done in two steps: since ^{7}Li is not visible in the RBS spectrum obtained for alpha particles with the geometry available in the RBS chamber, a first RBS analysis was done to quantify an Aluminum sample without implanted ^{7}Li. After this, the Al target implanted with ^{7}Li was analyzed by RBS and the ^{7}Li(p,α)^{4}He nuclear reaction, which for the energies and angles used in the laboratory is well known. For the RBS measurement, a 2 MeV ^{4}He^{+} beam was used, being the scattered particles detected with a silicon detector placed at θ=140° with respect to the beam axis.

The RBS profiling of heavy elements in a heavy matrix is limited due to the dependence on the element atomic number of the scattering cross sections. However, these elements with a low atomic number can be analyzed by nuclear reactions, NRA, which takes benefit of using accelerated particles like RBS. NRA is also governed by the rules of nuclear reactions rules and kinematics. When an ion beam bombards the target (mainly, with energy above the Coulomb barrier), a nuclear reaction can take place, resulting in an excited nucleus. The Coulomb barrier is of the order of 1 MeV for interactions between protons and the lightest nuclei. The primary ion is absorbed by the target nucleus and a different particle is emitted. This technique is useful, although these reactions are isotopic specific and not broad based like RBS and most nuclear reactions have sharp resonances in the cross section at certain energies. According to equation 1.3, the Q-value corresponding to the fundamental state of the residual nucleus can also be given by:

$$Q = T_Y + T_b - T_a \tag{4.9}$$

Being the total energy, $E_T = T_a + Q = T_Y + T_b$, it is possible to establish relations applying the same laws of energy and momentum conservation as described in chapter 1.

The ratio between the energy of light product and the total energy is given by [8]:

$$\frac{T_b}{E_T} = B\left[\cos\theta \pm \left(\frac{D}{B} - \sin^2\theta\right)^{1/2}\right]^2 \tag{4.10}$$

The ratio between the energy of heavy product and the total energy is given by:

$$\frac{T_Y}{E_T} = A\left[\cos\theta \pm \left(\frac{C}{A} - \sin^2\theta\right)^{1/2}\right]^2 \tag{4.11}$$

where

$$A = \frac{M_a M_Y}{(M_a + M_X)(M_b + M_Y)}\frac{T_a}{E_T}$$

$$B = \frac{M_a M_b}{(M_a + M_X)(M_b + M_Y)}\frac{T_a}{E_T}$$

$$C = \frac{M_X M_b}{(M_a + M_X)(M_b + M_Y)}\left(1 + \frac{M_a Q}{M_X E_T}\right)$$

$$D = \frac{M_X M_Y}{(M_a + M_X)(M_b + M_Y)}\left(1 + \frac{M_a Q}{M_X E_T}\right) \qquad 4.12$$

Considering the $^{7}Li(p,\alpha)^{4}He$ nuclear reaction, a 1.6 MeV H^{+} beam was used, with the outgoing particles being detected by the same detectors collecting the RBS spectrum. The spectra for these two measurements are presented in figures 4.7.

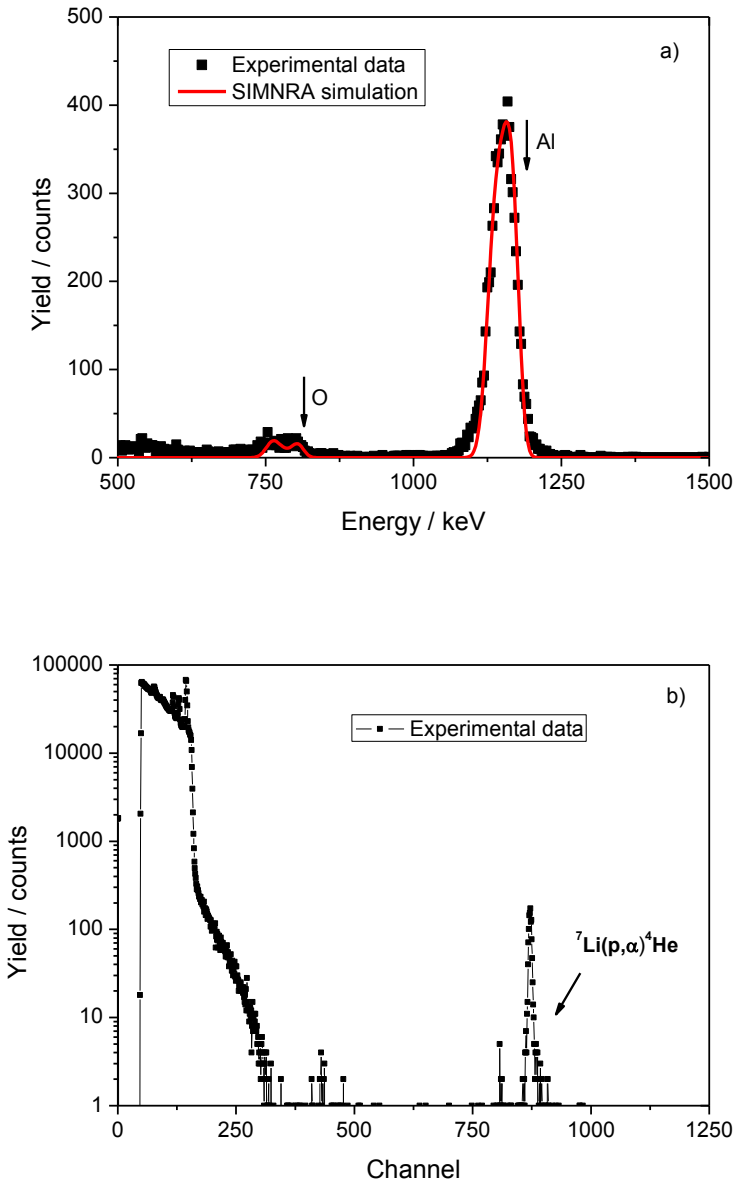

Figure 4.7) a) 2 MeV $^{4}He^{+}$ backscattering spectrum measured at θ_{lab}=140° with a simulation performed with SIMNRA and b) 1.6 MeV H^{+} backscattering spectrum measured at θ_{lab}=140°.

From the RBS analysis along with SIMNRA simulations we obtained a thickness of (4.8±0.3)·10^{17} at/cm^2 for the aluminum layer. The quantification of ^{7}Li present in the sample was calculated considering the following equations:

$$Y_{Al}(E,\theta_{lab}) = N_p.N_{Al}.\sigma_{Al}(E,\theta_{lab}).\Omega_{lab} \quad 4.13a$$

$$Y_{Li}(E,\theta_{lab}) = N_p.N_{Li}.\sigma_{Li}(E,\theta_{lab}).\Omega_{lab} \quad 4.13b$$

where Y_{Al} and Y_{Li} are the detected yields corresponding to alpha-particles scattered from Al and coming from the ^{7}Li(p,α)^{4}He reaction, respectively; N_{Al} and N_{Li} are the Al and Li areal densities; N_p is the number of incident protons; Ω_{lab} is the detector solid angle, $\sigma_{Al}(E,\theta_{lab})$ is the Al(p,p)Al cross section and $\sigma_{Li}(E,\theta_{lab})$ is the ^{7}Li(p,α)^{4}He cross section. Since the quantities N_p and Ω_{lab} are the same for both measurements, we can merge 4.13a and 4.13b equations to obtain N_{Li}:

$$N_{Li} = \frac{Y_{Li}(E,\theta_{lab}).\sigma_{Al}(E,\theta_{lab}).N_{Al}}{\sigma_{Li}(E,\theta_{lab}).Y_{Al}(E,\theta_{lab})} \quad 4.14$$

Calculations give an areal density for ^{7}Li, N_{Li} of (8.8±0.4)·10^{16} at/cm^2, which corresponds to a very low retained fluence considering the nominal fluence, 4x10^{17} at.cm^{-2}.

For carbon as backing, self-supporting C was produced by vacuum evaporation of graphite as described before.

After this, implantation of ^{129}Xe and ^{7}Li was performed. The implantation was done at the beam energy of 150 keV (4x10^{16} at.cm^{-2}) for ^{129}Xe and 10 keV (4x10^{17} at.cm^{-2}) for ^{7}Li. Again, the purpose was to implant ^{7}Li in the middle of the C film. The retained fluences for ^{129}Xe and ^{7}Li were calculated by means of RBS and through the ^{7}Li(p,α)^{4}He reaction.

Calculations give an areal density for ^{7}Li, N_{Li} of (1.00±0.05)·10^{17} at/cm^2 and an areal density for ^{129}Xe, N_{xe} of (4.5±0.2)·10^{16} at/cm^2. Table 5.3 resumes the retained and nominal fluences for both targets.

	Nominal Fluence ^{7}Li (10^{15} at/cm^2)	**Retained Fluence (Measured) (10^{15} at/cm^2)**	**Nominal Fluence ^{129}Xe (10^{15} at/cm^2)**	**Retained Fluence (Measured) (10^{15} at/cm^2)**
^{7}Li implanted in Al	400	88 ± 4	-	-
^{7}Li implanted in C	400	100 ± 5	40	45 ± 2

Table 4.3) Retained fluence (measured) vs Nominal fluence in ^{7}Li implanted targets in Al and C.

From the results, we can see that the retained fluence is almost the same for both backings. However, for cross section measurements, the use of a target with ^{7}Li implanted in C is more suitable, due to the fact that the energy loss of protons in carbon is less than the energy loss in aluminum for the same thickness. For normalization purposes, the use of ^{129}Xe as a heavy element is better than Al, considering the fact that the ^{129}Xe(p,p)^{129}Xe reaction is Rutherford for the energies used in this work and the ^{27}Al(p,p)^{27}Al reaction is not Rutherford in the whole range of energy. Due to a higher target roughness after the implantation stage, preliminary spectra of protons elastic scattered from this target were taken. Figure 4.8 shows a spectrum for proton energy of 1605 keV for ^{7}Li implanted in carbon. The implantation of ^{7}Li increased the roughness of the target, providing a drawback in the use of this target for elastic cross section measurements.

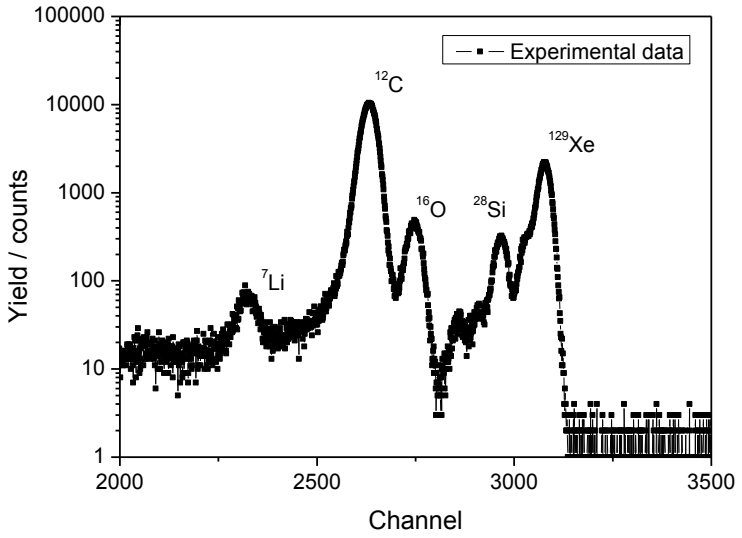

Figure 4.8) 1605 MeV H^+ forward scattering spectrum measured at θ_{lab}=90°.

4.2.4 LiF evaporated on self-supporting C implanted with ^{129}Xe

Besides the production of ^{7}Li implanted targets, in order to obtain a higher ^{7}Li areal density, the production of evaporated targets using a compound including lithium was done.

The first compound considered for this purpose was LiF, which evaporation was done before by several experimental groups and it was used for cross section measurements of ^{7}Li and ^{19}F in the past [9,10]. Considering this and the fact that a heavy element was needed for normalization purposes, LiF was evaporated on ^{12}C thin targets implanted with ^{129}Xe. For the target production, 50 mg of LiF was weighted (in order to have ~50 µg/cm^2 of evaporated LiF) and evaporated on the target already existing. The purpose was to find a compromise between enough Li areal density and a small energy loss of protons in the target. The drawbacks of evaporating LiF are the presence of unwanted nuclear reaction with F, ^{19}F(p,p$_1$)^{19}F and ^{19}F(p,p$_2$)^{19}F and also the presence of the other isotope of Li in the target, ^{6}Li, right near to the ^{7}Li peak. In order to overcome the second drawback, the solid angle of the particle detector in cross section measurements was reduced by a factor of 9 by decreasing the diameter of the particle detectors collimators by a factor of 3.

Figure 4.9 shows the RBS spectrum for this target. RBS analysis showed that the LiF layer was well defined over the ^{12}C layer. The SIMNRA simulation was done just adding the LiF layer to the simulations already existing for ^{12}C targets implanted with ^{129}Xe.

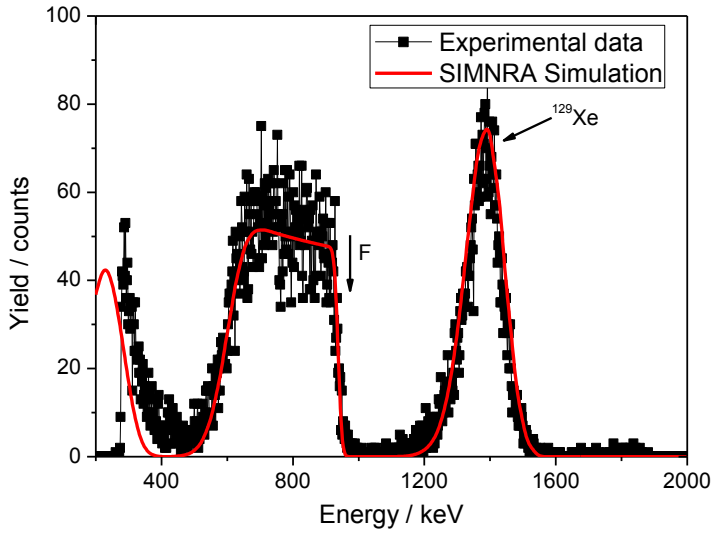

Figure 4.9) 2 MeV $^{4}He^{+}$ backscattering spectrum measured at θ_{lab}=140° with a simulation performed with SIMNRA for LiF into ^{12}C implanted with ^{129}Xe.

Taking into account a 1:1 stoichiometry between Li and F, from SIMNRA simulation it was obtained a $(6.0\pm0.1)\cdot10^{18}$ at/cm^2 for LiF layer and a retained fluence of $(45\pm2)\cdot10^{15}$ at/cm^2 for ^{129}Xe.

4.2.5 $LiWO_4$ evaporated on self-supporting C

In order to overcome the described drawbacks of using LiF as a target, evaporated targets containing $LiWO_4$ were produced. For the evaporation of this coumpond, different masses of $LiWO_4$ were weighted, from 50 to 200 mg. However, a small amount of $LiWO_4$ remained in the target. Figure 4.10 shows the RBS spectra for this target, for the evaporation of 100 mg of $LiWO_4$.

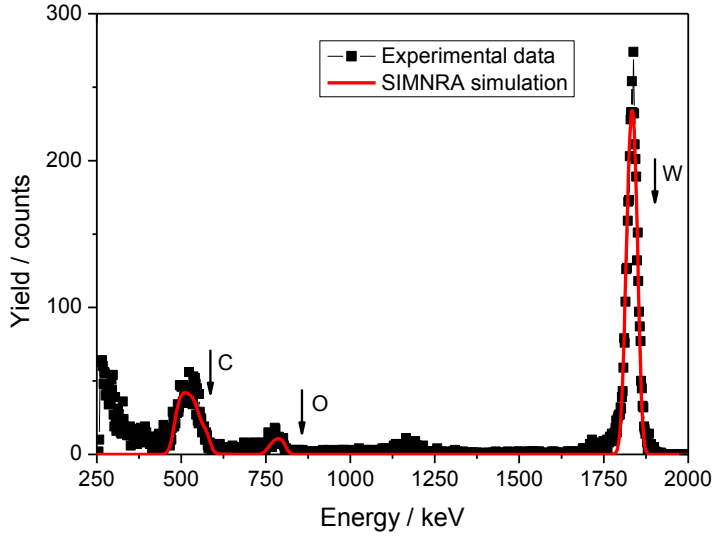

Figure 4.10) 2 MeV $^{4}He^{+}$ backscattering spectrum measured at θ_{lab}=140° with a simulation performed with SIMNRA for $LiWO_4$ evaporated into ^{12}C.

SIMNRA simulation showed the presence of $(140\pm8)\cdot10^{15}$ at/cm^2 of $LiWO_4$, which was not enough for cross section measurements. $LiWO_4$ proved not to be a stable compound during the evaporation stage, with most of the compound merging with the Molybdenum boat. However, this target was used to remeasure the $^{12}C(p,p)^{12}C$ elastic cross section, since this target had a thickness different than the ones used previously. Lithium compounds with oxygen proved not be suitable for evaporation purposes.

Two more targets were prepared, LiI and LiCl evaporated on C.

4.2.6 LiI and LiCl evaporated on self-supporting C

LiI and LiCl were prepared by evaporating these compounds in C. For this, 20 mg of LiI and 2 mg of LiCl were weighted for the evaporation. These masses were calculated aiming at the same energy loss of protons in these compounds as the energy loss in LiF.

For target characterization, PIGE technique was used to confirm the 1:1 stoichiometry between Li and the heavy element.

Like NRA, PIGE (Particle Induced Gamma Ray Emission) is a nuclear technique governed by the rules of nuclear reactions and kinematics. It is very useful for material analysis of light elements. In the case of ^{7}Li, the quantification is made using the ^{7}Li(p,p´γ)^{7}Li reaction with the emission of a gamma with an energy of 478 keV.

For thin targets, the methodology for material analysis is similar to the one used for NRA. Out of resonances, or for resonances in which the width in energy is higher than the width in energy of the target, the yield of gamma radiation of ^{7}Li, $Y_{\gamma}^{Li}(E,\theta_{lab})$, induced by the proton beam is given by:

$$Y_{\gamma}^{Li}(E,\theta_{lab}) = N_p . N_{Li} . \sigma_{Li}(E,\theta_{lab}) . \Omega_{\gamma}\varepsilon_{\gamma} \qquad 4.15$$

where N_p is the number of incident protons, N_{Li} is the areal density of ^{7}Li in the target, Ω_{γ} is the gamma ray detector solid angle, ε_{γ} is the detector efficiency and $\sigma_{Li}(E,\theta_{lab})$ is the ^{7}Li(p,p´γ)^{7}Li cross section.

The absolute efficiency of the gamma ray detector was determined using the radioactive sources ^{133}Ba, ^{56}Co and ^{152}Eu calibrated in activity with an uncertainty of 5%. Figure 4.11 shows the detector efficiency curve for gamma energies up to 3.5 MeV determined with resource to the mentioned sources.

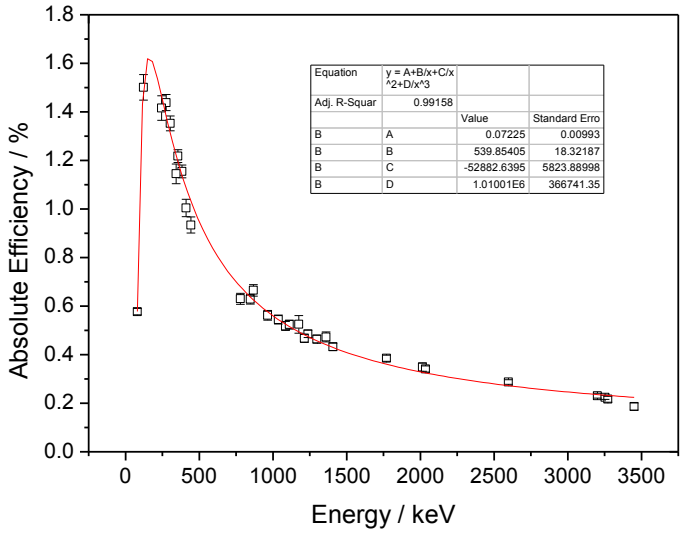

Figure 4.11) Absolute efficiency as function of energy for Ge(Hp) gamma ray detector.

The detector efficiency is given by a polynomial of degree 3:

$$\Omega_\gamma \varepsilon_\gamma = -2078.4x^3 - 2078x^2 + 5.006x + 0.001 \qquad 4.16$$

where x is the inverse of energy $(1/E)$, with the energy given in keV.

Since we have also a heavy element in the target that follows the Rutherford cross section for the used energies, we can also write:

$$Y_I(E, \theta_{lab}) = N_p . N_I . \sigma_I(E, \theta_{lab}) . \Omega_{lab} \qquad 4.17$$

Again, rewriting the expressions we can have the stoichiometry ratio r:

$$r = \frac{N_{Li}}{N_I} = \frac{Y_{Li}(E, \theta_{lab}) . \sigma_I(E, \theta_{lab}) . \Omega_{lab}}{\sigma_{Li}(E, \theta_{lab}) . Y_I(E, \theta_{lab}) . \Omega_\gamma \varepsilon_\gamma} \qquad 4.18$$

The measurements for the calculation of the ratio between Li and I were taken at E_{lab}=3000 KeV. This energy was chosen due to the fact that at this energy the ^{7}Li(p,p′γ)^{7}Li cross section is a slowing varying function with energy.

The gamma spectrum is presented in figure 4.12. From this spectrum along with the particle spectrum a ratio $r = (0.98 \pm 0.02)$ was obtained. The ratio between Li and Cl was also calculated by PIGE and was $r = (0.99 \pm 0.03)$.

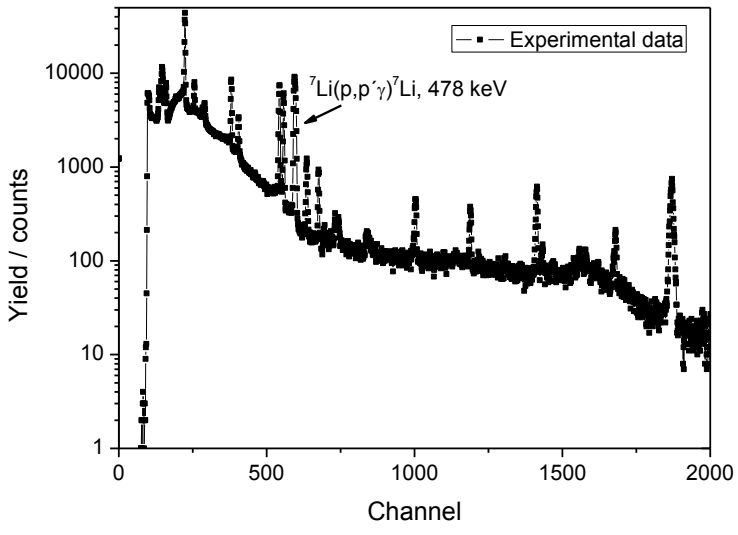

Figure 4.12) Gamma ray spectrum at energy E_{lab}=3000 keV.

4.2.7 $Ca_3(PO_4)_2$ evaporated on self-supporting Ag

Concerning the measurement of the $^{31}P(p,p)^{31}P$ reaction a calcium phosphate target evaporated into a silver backing was prepared. The target was prepared by evaporation of 20 mg of calcium phosphate on a thin silver target. The thin silver targets were previously prepared by evaporation of 50 mg of silver powder in glass slides. After evaporation, the glass slides are immersed in tap water and the silver film is released from the glass surface, being than picked up with sample holders in such a way that this film will cover the hole in the middle of the sample holder. Target characterization was achieved by Rutherford Backscattering Spectrometry with a 2000 keV $^4He^+$ beam produced by the Van de Graaff accelerator. The RBS spectrum obtained is shown in figure 4.13. The fit of the spectrum, also in figure 4.13, was achieved by SIMNRA software, considering that the target is composed of two layers, the first one with a thickness of $(28 \pm 2) \times 10^{16}$ atoms/cm^2 with 20% of phosphorous and 80% of oxygen and the other one, a layer of Ag of thickness $(41 \pm 1) \times 10^{16}$ atoms/cm^2. The target stability was verified by measuring the stoichiometric ratio with $^4He^+$ beam before and after the proton measurements and by repeating proton measurements at some values of proton energy.

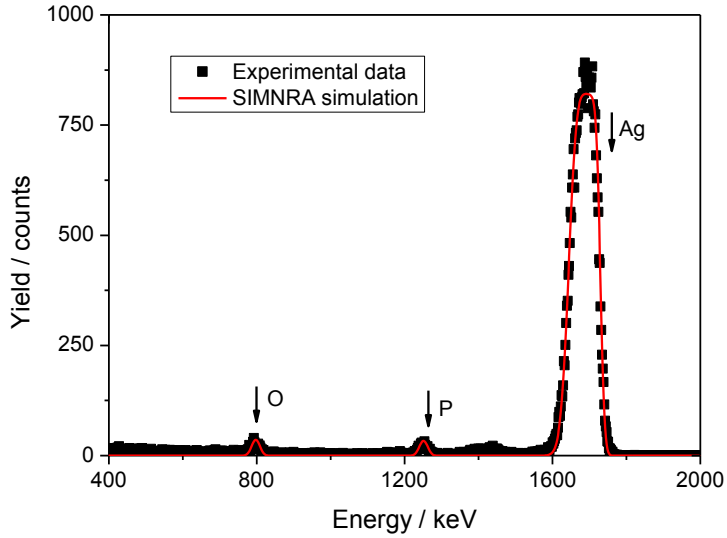

Figure 4.13) 2 MeV $^4He^+$ backscattering spectrum measured at θ_{lab}=140° with a simulation performed with SIMNRA for $Ca_3(PO_4)_2$ evaporated on self-supporting Ag.

From the spectrum, we can see that there is no calcium in the target. We suppose that this is to the separation between calcium ions and phosphate ions during the evaporation stage. This is not a problem since calcium is not object of study during this experiment.

4.3 Comparative Analysis of anodized, implanted and sputtered tantalum oxide targets for the study of the $^{16}O+^{16}O$ fusion reaction

The measurement of the total cross section of the $^{16}O+^{16}O$ fusion reaction in the region of astrophysical interest is a real challenge due the very small cross sections involved and the large number of possible exit channels [11-15]. Thus, the targets used for the experiments must fulfill some specifications: i) their thickness must be known with high accuracy; ii) they must sustain high beam currents (from hundreds of nA until tens of μA) for a long period of time; iii) they must have a constant stoichiometry so that the energy-loss may be calculated; iv) the presence of contaminants must be minimal in order to not interfere with the measurements. Considering the extremely small cross sections involved, the ^{16}O areal density of the target must be high to maximize the reaction products yields, but not too high to preclude a correct calculation of the effective beam energy. Tantalum pentoxide (Ta_2O_5) has been proposed as a suitable candidate because of its high density in oxygen and its stability [16]. This material can be prepared by different methods, including anodizing [17,18], implantation [19,20] and magnetron sputtering [21].

In this work [22], we report the production of tantalum oxide targets using three different techniques: anodizing, oxygen implantation and deposition by magnetron sputtering. The basic properties (stoichiometry, thickness, crystalline character) of Ta_2O_5 targets were analyzed by means of Rutherford backscattering spectrometry (RBS) and X-ray diffraction (XRD).

The stability of the targets was evaluated by performing long runs of ^{16}O implantation at medium energies.

4.3.1 Target Preparation

Three different types of targets were used in this experiment, including: anodized, implanted and sputtered Ta_2O_5 targets. One anodized target was prepared by anodic oxidation [17,18]. This target was first polished using a chemical attack, dipping it in a solution of H_2SO_4, HNO_3 and HF (5:2:2). After that, the tantalum backing was anodized using a well-established process, in which the film growth occurred in the 40-220 V voltage range, using a constant current density of 2 mA/cm^2. The film growth rate was approximately 3.2 nm/V. Two implanted targets were prepared, after the same chemical attack process, using a $^{16}O^+$ beam at two different energies to create a homogeneous profile. The implantation was carried out at a high current ion beam implanter (Danfysik 1090). The power density was kept below 1 W/cm^2 and the temperature was monitored with a thermocouple and never overcame 330 ºC. The implantation was done at 180 keV ($5x10^{17}$ at.cm^{-2}) and 70 keV ($3x10^{17}$ at.cm^{-2}) for the first implantation and 180 keV ($5x10^{17}$ at.cm^{-2}) and 70 keV ($5x10^{17}$ at.cm^{-2}) for the second one. The fluence was higher in the second implantation to achieve a more uniform oxide profile at the surface. One of the implanted targets obtained with higher fluence was annealed in vacuum conditions at 500 °C during 30 minutes. Four thin samples with a nominal thickness between 200 nm and 600 nm were also prepared by magnetron sputtering of Ta in an oxygen rich atmosphere. For the deposition, a mixture of Ar and O_2 gases was used, keeping different ratios of Ar/O_2: 70/30, 80/20, 90/10 and 95/5 with a working pressure of 10^{-2} mbar. High purity Ta targets, placed at 100 mm from the substrate, were used. The applied power was 500 W and the oxide was deposited onto a Si(100) substrate at room temperature.

4.3.2 Target Characterization

The stoichiometry and thickness of the targets were determined by means of RBS. Like before, a 2 MeV $^4He^+$ beam (1 mm^2 spot size) was used, being the scattered particles detected with a PIN silicon detector placed at θ=165° instead of θ=140° with respect to the beam axis. The beam current was monitored in real time and kept below 4 nA to avoid pile up. Experimental data were simulated with SIMNRA [5] and WiNDF [6] codes in order to make a cross-check of the results (for clarity purposes, in most of the cases only one

simulation is shown). X-ray diffraction (XRD) measurements, to investigate the cristallinity of the samples, were carried out with a Bruker-AXS D8 discover diffractometer using a grazing angle configuration (θ=2°).

Figure 4.14 pertains to the RBS spectrum of the anodized target. The spectrum shows a well defined step, confirming the existence of a tantalum oxide layer at the surface of the tantalum backing. Best fits from SIMNRA and WiNDF consistently confirm a thickness $(7.45\pm0.10)\times10^{17}$ at/cm^2 and $(7.35\pm0.10)\times10^{17}$ at/cm^2, respectively. The stoichiometry (Ta/O ratio) deduced from the fits was 0.42±0.02 and 0.43±0.02, respectively, consistent with the expected value of 0.40. The estimated thickness was 95 nm, assuming the bulk density of amorphous Ta_2O_5, 8.2 g/cm^3.

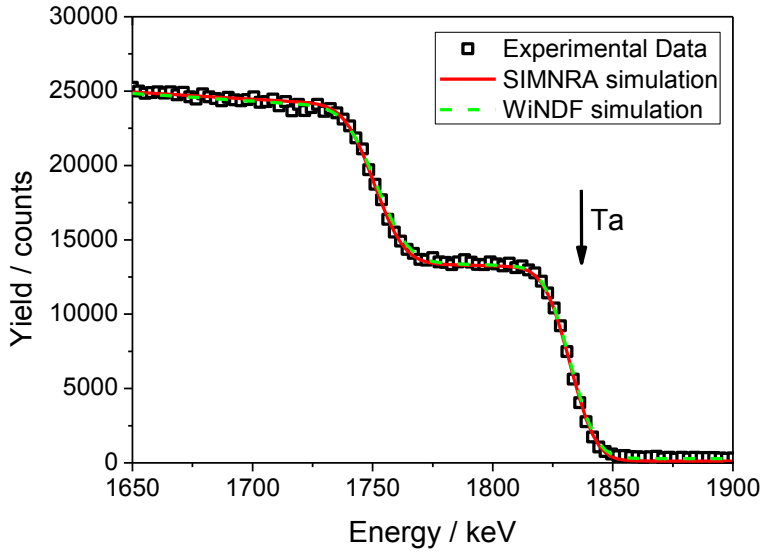

Figure 4.14) Experimental RBS spectrum and simulation fitting performed with SIMNRA and WiNDF.

Homogeneity tests were made by measuring three different points of the target. The good reproducibility of both stoichiometry and thickness was confirmed: Ta/O ratio was found to be 0.43±0.02, 0.41±0.02, 0.42±0.02, respectively, with a similar thickness of $(755\pm10)\times10^{15}$ at/cm^2 in all the cases. From the structural point of view, the XRD diffractograms showed no changes in the Ta structure after the anodizing process, indicating that the Ta_2O_5 film is amorphous.

For the implanted target, simulations using SRIM [2] were used to predict the implantation profiles. Table 4.4 shows the difference between the implanter nominal fluence and retained fluence (predicted by SRIM and determined from RBS spectra).

	Nominal Fluence (10^{15} at/cm^2)	**Retained Fluence (SRIM) (10^{15} at/cm^2)**	**Retained Fluence (Measured) (10^{15} at/cm^2)**
Implanted 1	800	650	460
Implanted 2	1000	740	590
Implanted 2 + annealed	1000	740	530

Table 4.4) Retained fluence (measured and predicted) vs Nominal fluence in the implanted targets.

The results show that, although the ratio between the predicted retained fluence and the nominal fluence is higher for the first implantation, the ratio between the measured retained fluence and the predicted one has the same value, 0.58 and 0.59, for both implantations. The retained fluence obtained in this work was higher by a factor of 1.6 than the one obtained by S. Seuthe *et al*. [20] for similar implantation conditions. The maximum O/Ta ratio that is possible to achieve through implantation is 1.40 (achieved in implantation 2), below the O/Ta ratio in Ta_2O_5 (2.5). Therefore, it was not possible to calculate a thickness in nm. After the annealing, the retained fluence decreases probably due to the release of oxygen to the atmosphere during this operation. The comparison of experimental data for the implanted targets before and after the annealing, proves that some oxygen is released to the atmosphere, with the atomic concentration of oxygen in the target being less after the annealing.

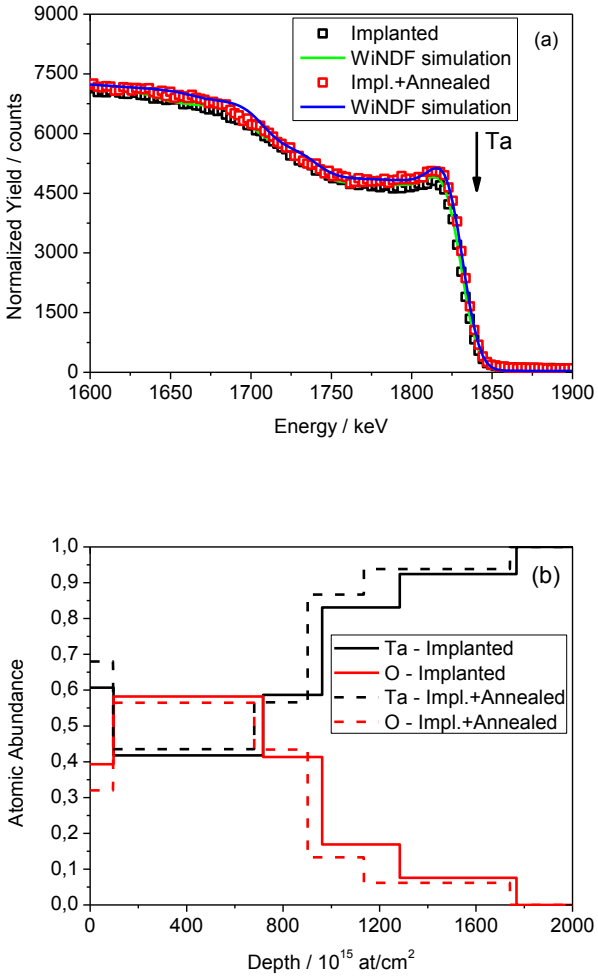

Figure 4.15) (a) Implanted and Implanted + annealed RBS spectra and (b) Depth profile obtained from the RBS analysis.

The depth profiles before and after the annealing show almost the same content in oxygen with the exception of the first layer as can be seen in figure 4.15. The RBS results are confirmed by the XRD spectra, in which we can see an increase in the lattice parameter that is reduced after the annealing. XRD diffractograms (Figure 4.16) evidence a clear shift in the (200) and (211) satellite peaks, ascribed to the oxidized layer, when comparing the implanted and the annealed sample. This shift confirms that there is a reduce of the lattice parameter upon annealing, also suggesting the loss of O.

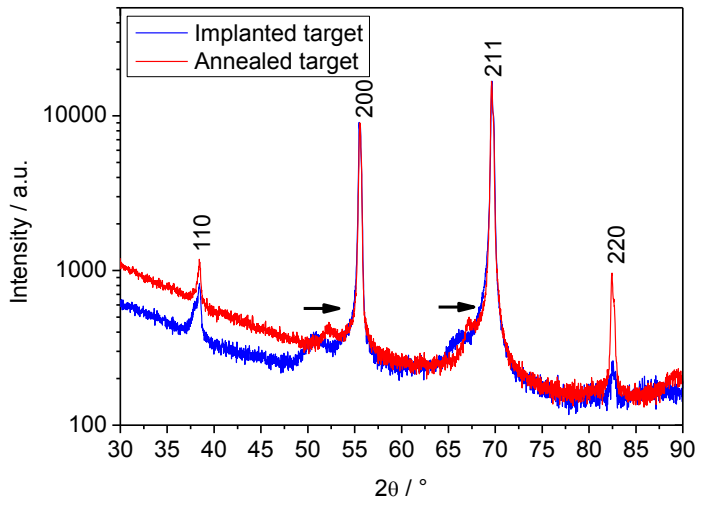

Figure 4.16) XRD spectra for the Implanted 2 and Impl. 2 + annealed targets. The arrows mark the shift induced by the thermal annealing.

In relation to the sputtered targets, two spectra are presented in Figure 4.17. Thanks to the use of a light substrate as Si, in RBS spectra both Ta and O can be clearly distinguished (this latter overlapping the Si background).

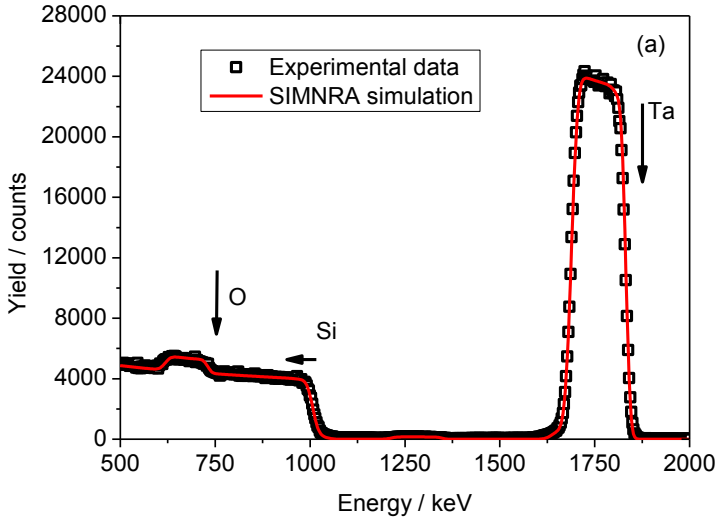

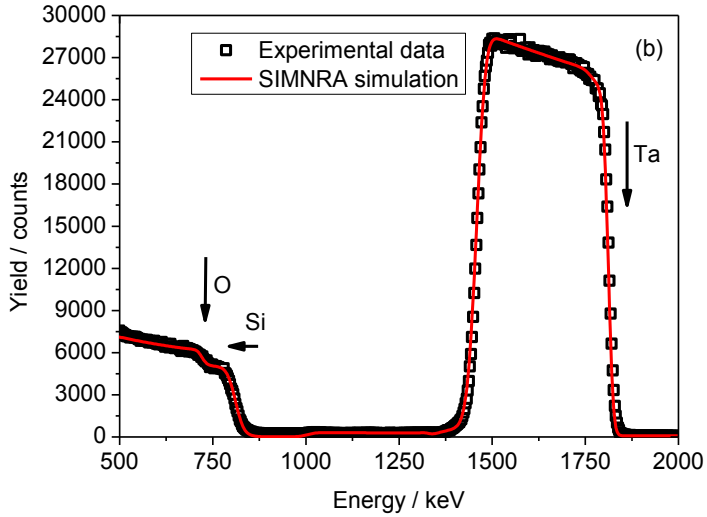

Figure 4.17) RBS spectra for sputtered targets with a ratio between Argon and Oxygen of (a) 70/30 and (b) 95/5.

Table 4.5 summarizes the results obtained for the four samples. For an adequate fitting, a roughness of $1.5x10^{17}$ at/cm^2 was included. In all cases, the films contained a small quantity of Ar (used as a precursor in the mixture).

	Sample 1 (70/30)	**Sample 2 (80/20)**	**Sample 3 (90/10)**	**Sample 4 (95/5)**
Ta_2O_5 (10^{15} at/cm^2)	1370±10	1435±10	1705±10	3355±10
% Ta	25.7	27.0	25.0	26.6
% O	71.8	70.5	71.0	69.9
% Ar	2.5	2.5	4.0	3.5
Ta/O	0.358±0.02	0.383±0.02	0.380±0.02	0.381±0.02
Thickness (nm)	172	180	214	421

Table 4.5) Thickness, atomic abundance and Ta/O ratio in the oxide layer for the sputtered targets.

Results show that the gas mixture affects the growth rate as greater thickness is obtained for larger Ar/O_2 ratios. Stoichiometry is not significantly altered by the Ar/O_2 ratio in samples 2, 3 and 4, although it does show a significant change in sample 1 (70/30 ratio). This fact suggests that the target reaches a stable oxidation state when the Ar content is high (80% and higher), while it keeps an O-rich character below it (70% Ar). It should be noted that, in comparison with the preparation of anodizing and implanted targets, sputtering targets exhibit a slightly substoichiometric composition. Previously measured values [21] are in agreement with our results.

4.3.3 Stability tests

For stability tests, the targets were bombarded by a $^{16}O^{+}$ beam using the same conditions as described before for the implanted targets. The fluence applied to the targets was $7x10^{17}$ at.cm^{-2} with a charge of 0.1 C/cm^2.

After the analysis with RBS, target bombardments were done in order to assess the stability of the targets upon $^{16}O^{+}$ irradiation. The main goal here was to test the sputtering effects in the first layers of the targets since, at the nominal energies required for the $^{16}O+^{16}O$ fusion reaction no implantation is expected (the range at 4 MeV is ~ 2190 nm, much higher than the thickness of our targets).

Results of the stability tests are presented in figure 4.18, where we can deduce that the surface layers in stoichiometry and structure are not affected. This is confirmed by the XRD spectrum where no changes in the lattice parameter are seen. This is an important result as these first layers are the ones contributing to most of the $^{16}O+^{16}O$ fusion reaction yield.

Nevertheless, we may see that the amount of oxygen retained in depth is higher in the anodized and implanted targets due to the implantation effect. For the sputtered target, despite the deposition of oxygen in Ta_2O_5, due to the range of $^{16}O^{+}$ at this energy, fig. 4.18c) shows that the stoichiometry in the surface layers remains unchanged and the thickness the same as before. It is possible to verify that the Ar was sputtered off the surface due to the bombardment, which is not unexpected, concerning that this gas does not make any chemical compound with the other elements. However, as we said before, these changes are not relevant for our $^{16}O+^{16}O$ measurement.

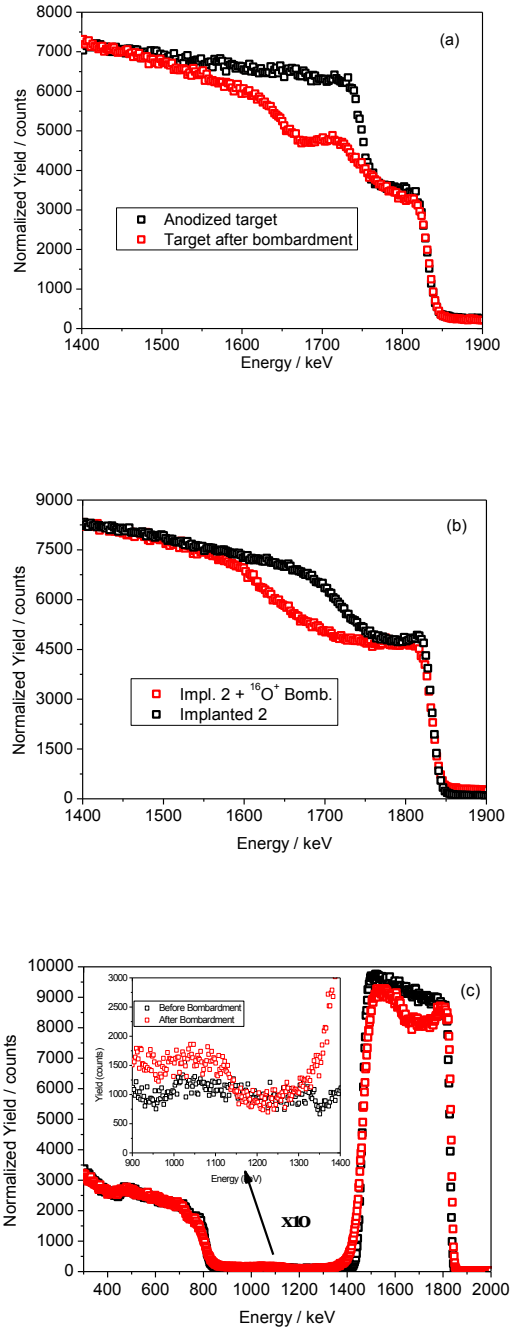

Figure 4.18) RBS spectra before and after the ion bombardment for the (a) Anodized, (b) Implanted and (c) Sputtered targets.

The XRD spectrum showed no changes in the lattice parameter, proving that the Ta_2O_5 layer grown is stable.

The results show that the anodized and sputtered targets are more suitable for measuring the $^{16}O+^{16}O$ fusion reaction, due to their higher oxygen density and to the formation of a stable oxide compound, tantalum pentoxide (Ta_2O_5).

4.4 References

[1] H. Silva, J. Cruz, A.M. Sánchez-Benítez, C. Santos, H. Luís, M. Fonseca and A.P. Jesus, Nucl. Inst. Meth. B 406 (2017) 135-138.

[2] J.F. Ziegler, J.P. Biersack and M.D. Ziegler, SRIM The Stopping and Range of Ions in Matter (2008).

[3] H. Ryssel, J. Ruge, Ion implantation, Vol. I, John Wiley & Sons (1986).

[4] J.A. Leavitt, L.C. McIntyre Jr., M.R. Weller, in: J.R. Tesmer, M. Nastasi (Eds.), Handbook of Modern Ion Beam Analysis, MRS, Pittsburgh, PA, 1995.

[5] M. Mayer, AIP Conf. Proc. 475, 541 (1999).

[6] N.P. Barradas, C. Jeynes, R.P. Webb, Appl. Phys. Lett. 71 (1997) 291.

[7] J.A. Maxwell, W.J. Teesdale, J.L. Campbell, Nucl. Inst. Meth. B 95 (1995) 407.

[8] H.R. Verna, Atomic and Nuclear Analytical Methods, Springer (2007).

[9] V. Paneta, A. Kafkarkou, M. Kokkoris and A. Lagoyannis, Nucl. Instr. And Meth. B 288 (2012) 53-59.

[10] A. Caccioli, M. Chiari, A. Climent-Font, M.T. Fernandez-Jimenez, G. García-López, F. Lucarelli, S. Nava and A. Zucchiatti, Nucl. Inst. And Meth. B 249 (2006) 95.

[11] H. Spinka, W. Winkler, Astrophys. J. 174 (1972) 455.

[12] G. Hulke, C. Rolfs, H.P. Trautvetter, Z. Phys. A 297 (1980) 161.

[13] A. Kuronen, J. Keinonen, P. Tikkanen, Phys. Rev. C 35 (1987) 591.

[14] J. Thomas, Y.T. Chen, S. Hinds, D. Meredith, M. Olson, Phys. Rev. C 33 (1986) 1679.

[15] S.C. Wu, C.A. Barnes, Nucl. Phys. A 422 (1984) 373.

[16] M.P. Seah *et al*., Nucl. Inst. Meth. B 30, 128 (1988).

[17] A. Caccioli *et al*., Eur. Phys. J. 48 (2012) 144.

[18] G. Amsel *et al*., Nuclear Instruments and Methods, 149:705-712, 1978.

[19] J. Cruz, M. Fonseca, H. Luís, R. Mateus, H. Marques, A.P. Jesus, J.P. Ribeiro, O.M.N.D. Teodoro and C. Rolfs, Nucl. Inst. Meth. B 267 (2009) 478-481.

[20] S. Kim, C. Hwangbo, Journal of the Korean Physical Society, Vol. 43, No. 4, 616 (2003).

[21] H. Silva, J. Cruz, A. Redondo-Cubero, C. Santos, M. Fonseca, H. Luís and A.P. Jesus, Nucl. Inst. Meth. B 331 (2014) 78-81.

[22] S. Seuthe *et al.*, Nucl. Inst. Meth. A 260 33 (1987).

5

Chapter 5 - Results and discussion

5.1 Introduction

In the previous chapters, the theoretical backgrounds, previous measurements, experimental setup, target preparation and characterization were described in detail. This chapter is divided in three major sections. In the first one, the procedure used to extract the elastic cross sections and corresponding uncertainties is described. The second one presents the results for the elastic scattering of protons. When possible, it is also presented a comparison with previous measurements and theoretical validations. Finally, the results obtained for the elastic scattering of oxygen ions is presented.

5.2 Elastic cross section measurement methodology

The measurement of elastic cross sections using a thin target setup, containing a heavy element for normalization purposes, is a standard procedure that is well described in the literature. In this section, we will review it along with the description of effective stopping cross section, effective energy calculation, center of mass to laboratory solid angle transformation and error analysis.

5.2.1 Cross section measurement methodology

In order to describe the cross section measurement methodology, we have chosen the ^{12}C as a light element and ^{129}Xe as a heavy element on the target. In this case, the purpose was the measurement of the differential elastic cross section of protons from ^{12}C. The differential cross section of protons scattered from ^{129}Xe is purely Coulombian in the range of energies studied.

The elastic scattered protons from ^{12}C and ^{129}Xe were collected by the particle detectors at the same time. The yield of ^{12}C, $Y_C(E_{eff}, \theta_{lab})$, is given by:

$$Y_C(E_{eff}, \theta_{lab}) = N_p . N_C . \sigma_{el}^{C}\left(E_{eff}, \theta_{lab}\right) . \Omega_{lab} \qquad 5.1$$

where N_p is the number of incident protons, N_C is the areal density of ^{12}C in the target, $\sigma_{el}^{C}(E_{eff}, \theta_{lab})$ is the elastic cross section for a given effective energy and angle and Ω_{lab} is the particle detector solid angle.

The yield of ^{129}Xe is given by:

$$Y_{Xe}(E_{eff}, \theta_{lab}) = N_p . N_{Xe} . \sigma_{Ruth}^{Xe}(E_{eff}, \theta_{lab}) . \Omega_{lab} \quad 5.2$$

where N_p is the number of incident protons, N_{Xe} is the areal density of ^{129}Xe in the target, $\sigma_{Ruth}^{Xe}(E_{eff}, \theta_{lab})$ is the Rutherford cross section for a given effective energy and angle and Ω_{lab} is the particle detector solid angle.

When combining the two above mentioned equations, the result is the hereunder equation which is independent of charge and detector solid angle:

$$\sigma_{el}^{C}(E_{eff}, \theta_{lab}) = \frac{Y_C(E_{eff}, \theta_{lab}) . \sigma_{Ruth}^{Xe}(E_{eff}, \theta_{lab}) . N_{Xe}}{N_C . Y_{Xe}(E_{eff}, \theta_{lab})} \quad 5.3$$

Nevertheless, this relationship shows that, to calculate the elastic cross section, we need to know the effective energy and, consequently, the effective stopping cross section.

5.2.2 Effective energy and Effective stopping cross section

Let us consider that the cross section σ is approximately constant over the target thickness, which is the case for broad resonances or for a non-resonant mechanism. Also, the energy lost in the target is small, so the stopping power is constant as well.

In this case, off resonances or on-resonances having large widths when compared to the target energy thickness, the target thickness is taken into account using an effective energy given by:

$$E_{eff} = E_{lab} - \Delta_{lab}/2 \quad 5.4$$

where E_{lab} is the incident energy of the beam and Δ_{lab} is the energy loss in the target.

By the other hand, if the stopping power remains constant and the cross section varies over the target thickness, then the effective energy is given by [1]:

$$E_{eff} = E_{lab} - \Delta_{lab} + \Delta_{lab}\left[-\frac{\sigma_2}{\sigma_1 - \sigma_2} + \sqrt{\frac{\sigma_1^2 + \sigma_2^2}{2(\sigma_1 - \sigma_2)^2}}\right] \quad 5.5$$

where σ_1 and σ_2 are the cross sections values at E_{lab} and $E_{lab} - \Delta_{lab}$, respectively. To calculate the energy loss in the target, Δ_{lab}, we need to know the effective stopping power cross section, $\epsilon_{eff}(E)$.

For a target having an areal density N_a in at/cm^2 of active nuclei and an areal density N_i of inactive nuclei in at/cm^2, the effective stopping cross section, $\epsilon_{eff}(E)$, is given by a relation which depends on both the number of active nuclei and inactive nuclei [1]:

$$\epsilon_{eff}(E) = \epsilon_a(E) + \frac{1}{N_a}\sum_i N_i \epsilon_i(E) \qquad 5.6$$

The units of effective stopping cross section are usually given in $eV/(at/cm^2)$. The stopping power cross section was calculated using the software SRIM. The ϵ values were calculated for different energies and a polynomial function was used to parameterize the obtained data. Figure 5.1 and 5.2 present the stopping power cross sections as function of energy for protons and oxygen in ^{12}C, together with a fit to a polynomial function of fourth degree.

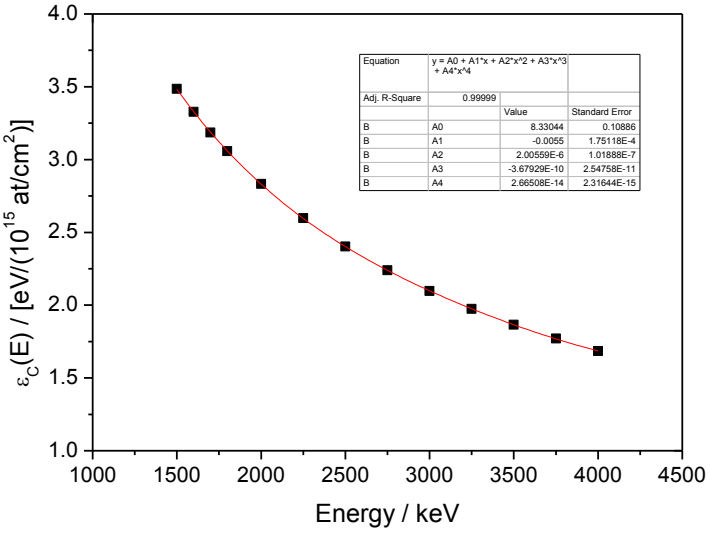

Figure 5.1) Stopping cross section of ^{12}C for protons, ϵ_C, as function of energy, for the energy range from 1500 to 4000 keV.

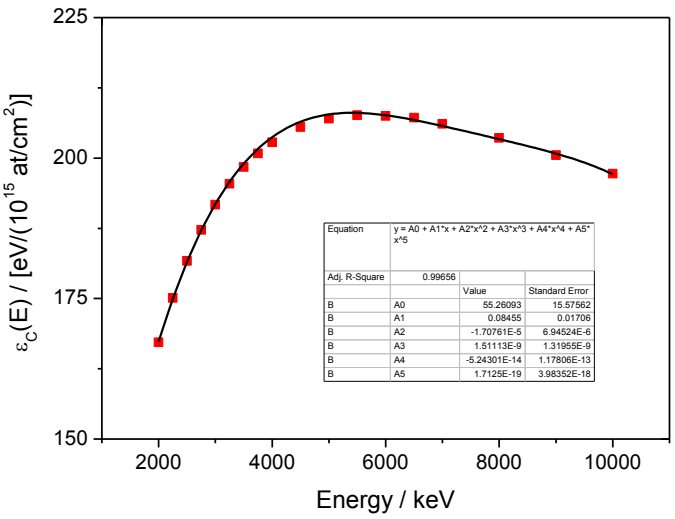

Figure 5.2) Stopping cross section of ^{12}C for oxygen, ϵ_C, as function of energy, for the energy range from 2000 to 10000 keV.

5.2.3 Center of mass to laboratory solid angle transformation

In experimental nuclear physics, all observations take place in a reference frame called laboratory frame or laboratory coordinate system. However, in theoretical calculations, the motion of the center of mass does not bring consequences to the properties of a nuclear reaction. The importance lies in the motion relative to the center of mass.

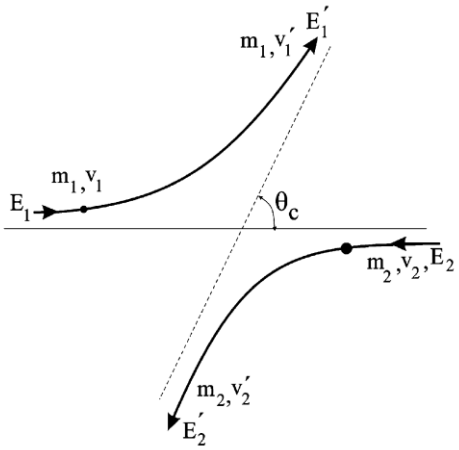

Figure 5.3) Scattering of two particles as viewed in the center of mass frame. θ_c is the scattering angle in the center of mass frame ($\theta_{c.m.}$).

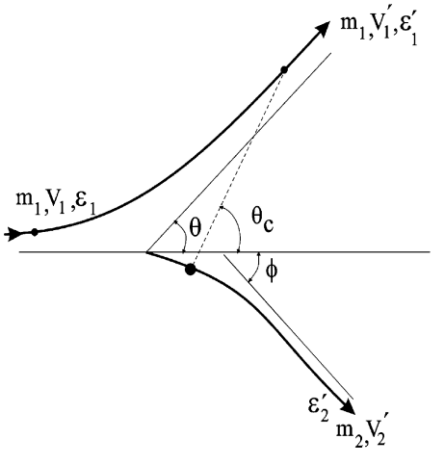

Figure 5.4) Scattering of two particles as viewed in the laboratory frame. θ is the scattering angle in the laboratory frame (θ_{lab}).

In the center of mass system, both projectile and target atoms are in movement in opposite directions. Instead, in the laboratory frame, target atoms are at rest. In the center of mass frame, energy conservation implies that $E = E_1 + E_2 = E_1^{'} + E_2^{'}$, where E_i and $E_i^{'}$ are the energy of projectile and target before and after the collision. In the laboratory frame, we have $\varepsilon = \varepsilon_1 = \varepsilon_1^{'} + \varepsilon_2^{'}$, where ε_1 is the projectile kinetic energy before the collision and $\varepsilon_i^{'}$ are the kinetic energies of the projectile and target after the collision.

Based on these equations, we find the relation between the energy in the center of mass and laboratory system:

$$E = \left(\frac{m_2}{m_1 + m_2}\right)\varepsilon \qquad 5.7$$

Taking into consideration figures 5.3 and 5.4, we can also find the following relation:

$$\tan\theta_{lab} = \frac{\sin\theta_{c.m.}}{\cos\theta_{c.m.} + (m_1/m_2)} \qquad 5.8$$

And

$$\tan\phi = \frac{\sin\theta_{c.m.}}{1 - \cos\theta_{c.m.}} \qquad 5.9$$

which implies that

$$\phi = \left(\frac{\pi}{2} - \frac{\theta_{c.m.}}{2}\right) \qquad 5.10$$

When differentiating the equation 5.8 with respect to $\theta_{c.m.}$, we have that

$$\frac{\mathrm{d}\tan\theta_{lab}}{\mathrm{d}\theta_{c.m.}} = \frac{1 + (m_1/m_2)\cos\theta_{c.m.}}{(\cos\theta_{c.m.} + (m_1/m_2))^2} \qquad 5.11$$

This equation will allow the scattering angle transformation between both coordinate systems.

5.2.4 Error analysis

The uncertainties for elastic cross section, $u(\sigma_{el})$, follow the standard error propagation law. If a quantity X depends on other quantities through multiplications and divisions, the relative uncertainty of X is given by the square root of the sum of squares of the relative uncertainties. Considering again the elastic cross section of protons from ^{12}C with ^{129}Xe as a heavy element we have:

$$\frac{u(\sigma_{el}^{C})}{\sigma_{el}^{C}} = \sqrt{\left(\frac{u(Y_C)}{Y_C}\right)^2 + \left(\frac{u(Y_{Xe})}{Y_{Xe}}\right)^2 + \left(\frac{u(N_C)}{N_C}\right)^2 + \left(\frac{u(N_{Xe})}{N_{Xe}}\right)^2} \qquad 5.12$$

Each term of the equation above is calculated having into account the following:

a) $u(Y_C)$ and $u(Y_{Xe})$

The uncertainties of the yields corresponding to ^{12}C and ^{129}Xe, $u(Y_C)$ and $u(Y_{Xe})$, can be calculated in two different ways:

1) If the yield is the given by $z = x - y$, where z is the net area, x is the integral and y is the background, thus $u(z) = \sqrt{u(x)^2 + u(y)^2}$.
2) If the yield is calculated by fitting the spectrum (which is the case when the peaks of each element are not separated in the spectrum), the uncertainty arises from the fitting uncertainty.

b) $u(N_C)$ and $u(N_{Xe})$

The uncertainties $u(N_C)$ and $u(N_{Xe})$ are obtained from RBS analysis. In this case, the uncertainty arises from the SIMNRA simulation and is considered to be the minor deviation from values given by the best spectrum simulation of data and values given by a simulation which does not fit the spectrum. For PIGE and NRA analysis, the uncertainty is derived from the equivalent to equation 5.12 applied to the relevant expressions of these two techniques.

Considering that the uncertainties arising from the RBS measurements are lower than 5% for each nuclide and the uncertainties of the yields are kept under 2%, we expect relative uncertainties in the elastic cross section measurements to be approximately 5 to 6%.

5.3 Elastic scattering of protons

In this section, the results for ^{12}C(p,p)^{12}C, ^{6}Li(p,p)^{6}Li, ^{7}Li(p,p)^{7}Li, ^{19}F(p,p)^{19}F and ^{31}P(p,p)^{31}P are presented. The experimental details and targets used are described in each subsection. In each subsection, a discussion of the results is presented along with a comparison with previous results/theoretical data, when available.

5.3.1 $^{12}C(p,p)^{12}C$

All measurements of $^{12}C(p,p)^{12}C$ differential cross section were carried out at the 3.0 MV Tandem accelerator. The details of the experimental setup are described in section 3.1. The target preparation and characterization is described in sections 4.1.2 and 4.1.5. In this subsection, the results for 8 different scattering angles (from 45.0° to 90.0°) are presented in the energy range from 1.6 MeV to 3.9 MeV. The corrections of the beam energy, due to the target thickness, were also performed. The beam current was kept under 100 nA for the dead time to be below 2%. The measured solid angle values for the two experimental conditions, which will be described right after in this section, were 3.65×10^{-3} sr and 4.06×10^{-4} sr.

The well known dependences of the Rutherford cross section with $1/E^2$ and θ_{lab} of the Rutherford cross section were kept under control for the heavy element, as shown in figures 5.5 and 5.6.

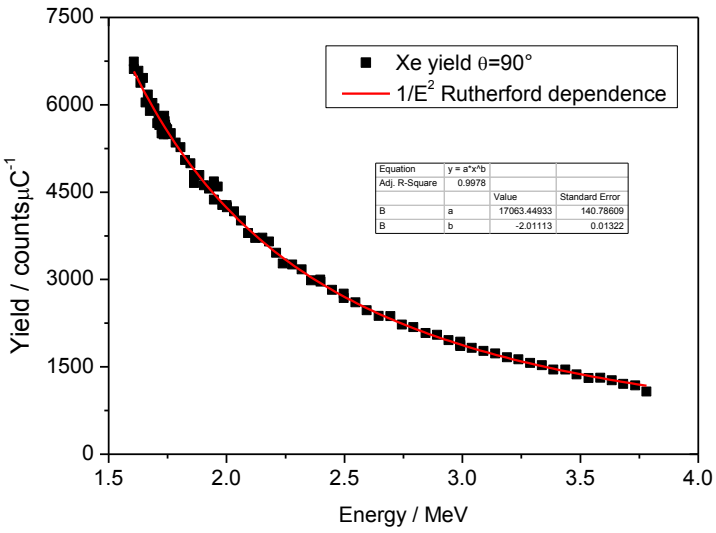

Figure 5.5) Yield of Xe as a function of energy for θ_{lab}=90°. The red curve represents the fitting with an allometric function.

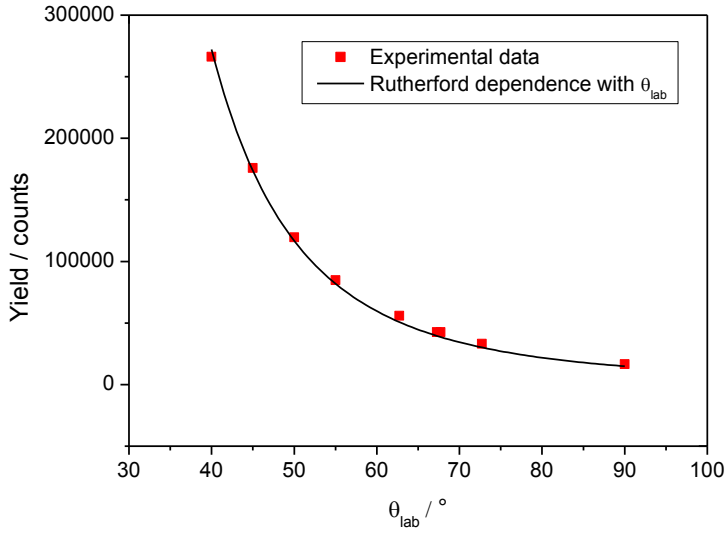

Figure 5.6) Yield of Xe as a function of angle for E_{lab}=1621 keV. The black curve represents the angular dependence of Rutherford´s formula.

As may be seen in figures 5.5 and 5.6, very good agreement is obtained for the heavy element (in this case ^{129}Xe), as a function of energy and angle. These results are a good benchmark for elastic cross section measurement, since they show a consistency in the experimental setup and in the collected charge, although this is not necessary for the calculations.

The figures presented below (figures 5.7 and 5.8) show spectra for two different targets (described before) at the same incident energy, E_{lab}=1610 keV. The spectra show a very good separation between C and the heavy element. Additionally, it is possible to notice, in target 2, the presence of oxygen due to the evaporation of Li_2WO_4, despite the small quantity evaporated.

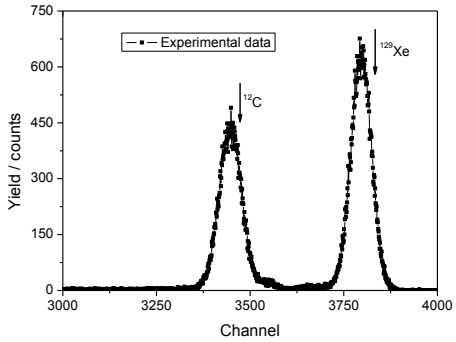

Figure 5.7) The 1610 keV H^+ forward spectrum for target 1 at θ_{lab}=90°.

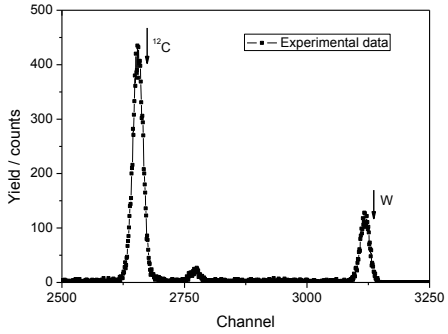

Figure 5.8) The 1610 keV H^+ forward spectrum for target 2 at θ_{lab}=90°.

The differential cross section for θ_{lab}=90° for the two targets is presented in figure 5.9 along with the theoretical evaluation for this scattering angle. Some changes were introduced to the second measurement conditions: the charge collection was made in the beam stopper for the first measurement and in the second the chamber was used as a Faraday Cup; the detector solid angle was reduced from 3.65×10^{-3} sr to 4.06×10^{-4} sr by introducing a collimator with a aperture three times lower; the target thickness was reduced by a factor of two. In spite of these modifications, we had the same shape in the resonance region.

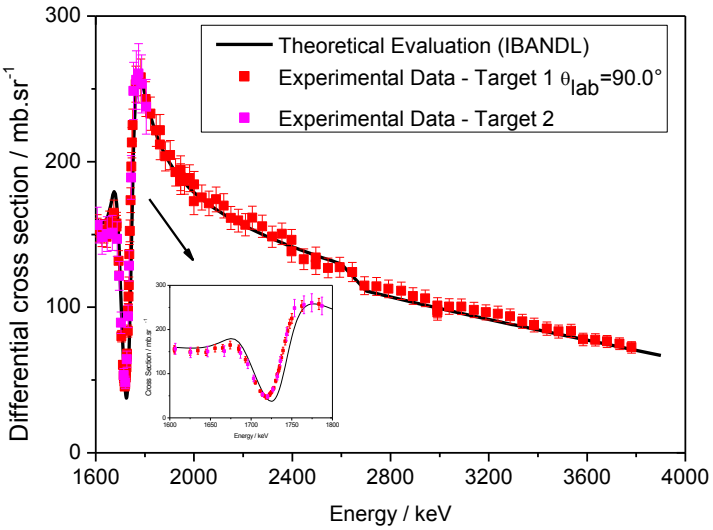

Figure 5.9) $^{12}C(p,p)^{12}C$ differential cross section for θ_{lab}=90°.

A magnification of the resonance zone is shown in figure 5.10. It is possible to notice an energy shift between experimental data and theoretical evaluation. This result can be due to the energy calibration of the accelerator, although the accelerator was calibrated before the

experimental measurements. The effective energy was calculated considering equation 5.4. The results obtained suggest that the theoretical calculations for this region must be seen in more detail.

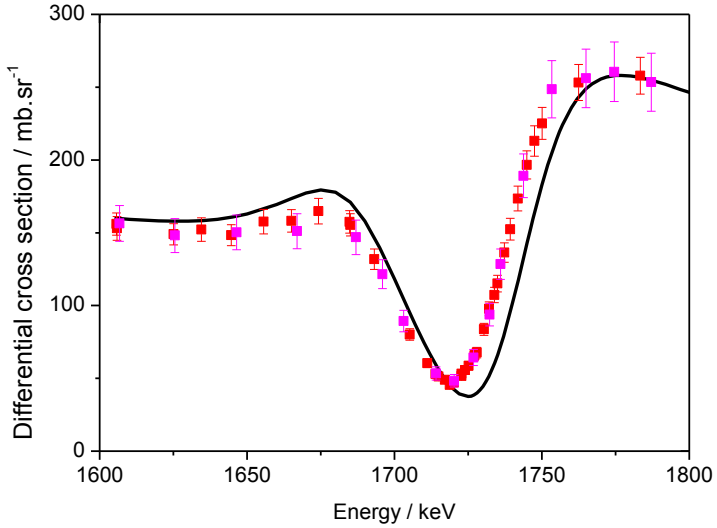

Figure 5.10) Resonance region in $^{12}C(p,p)^{12}C$ differential cross section for θ_{lab}=90.0°.

In order to confirm that the target thickness does not affect the resonance, the resonance region was fitted taking into account the target thickness. The measured yield results from the integration of the nuclear reaction cross section over the target thickness. Assuming a small solid angle of particle detection we have [1]:

$$N_{^{12}C}(E_{lab},\theta_{lab}) = N_p \frac{N_{^{12}C}}{x}\Omega_{lab}\int_0^x \frac{d\sigma_{el}^{^{12}C}(E,\theta_{lab})}{d\Omega_{lab}}dx$$

$$= \frac{N_p}{x}\frac{N_{^{12}C}}{\epsilon(E_{lab})}\Omega_{lab}\int_{E_{lab}-\Delta_{lab}}^{E_{lab}} \frac{d\sigma_{el}^{^{12}C}(E,\theta_{lab})}{d\Omega_{lab}}dE$$

$$= \frac{N_p N_{^{12}C}}{\Delta_{lab}}\Omega_{lab}\int_{E_{lab}-\Delta_{lab}}^{E_{lab}} \frac{d\sigma_{el}^{^{12}C}(E,\theta_{lab})}{d\Omega_{lab}}dE \qquad 5.13$$

where x is the target thickness and $\epsilon(E_{lab})$ is the stopping power cross section at incident energy.

According to Spyrou *et al*. [2], the beam energy distribution, $\Delta_b = 1\ keV$, and the energy straggling of protons inside the target [2] may be described by a single gaussian function, $g(E_{lab}, E, x')$, where E and x' are the energy and depth, respectively.

$$g(E_{lab}, E, x') = Bexp\left[-\frac{(E_{lab} - E - \epsilon(E_{lab})x')^2}{0.36\Gamma_t}\right] \quad 5.14$$

In this equation, B is the normalization factor and Γ_t is the total FWHM (Full Width at Half Maximum) of the energy spreading, which is given by:

$$\Gamma_t = \left(\Delta_b^2 + 0.86z^2\frac{\bar{Z}}{\bar{A}}x'\right)^{1/2} \quad 5.15$$

where x' is given in units of μg/cm^2, $\bar{Z}$ and $\bar{A}$ are the average atomic number and weight, respectively, and z is the atomic number of the projectile.

Taking into account these effects, equation 5.13 can be written as:

$$N_{^{12}C}(E_{lab}, \theta_{lab}) = N_p\frac{N_{^{12}C}}{x}\Omega_{lab}\int_0^x\int_0^\infty \frac{d\sigma_{el}^{^{12}C}(E, \theta_{lab})}{d\Omega_{lab}}g(E_{lab}, E, x')dEdx' \quad 5.16$$

The double integral was calculated numerically for the two targets using a FORTRAN program developed by J. Cruz [3], and using the following parameterization for the cross section:

$$\frac{d\sigma_{el}^{^{12}C}(E, \theta_{lab})}{d\Omega_{lab}} = \sigma_0 f(E) \quad 5.17$$

where

$$f(E) = 1 + \frac{a\Gamma^2 + 2b\Gamma(E - E_r)}{\Gamma^2 + 4(E - E_r)^2} \quad 5.18$$

where Γ is the resonance width, E_r is the resonance energy, a and b are adjustable parameters. For each target, two different fittings were performed: one using equations 5.16 and 5.18 to fit the data; another one, using equation 5.4 to calculate the effective energy and equation 5.18 to fit the data. The results of these fittings of the experimental values of the resonance region are presented in figures 5.11 and 5.12.

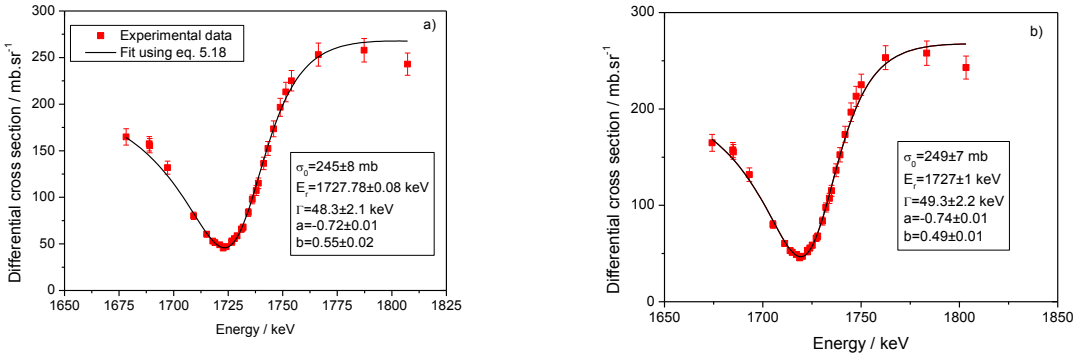

Figure 5.11) a) Resonance fitting for target 1 using equations 5.16 and 5.18 and b) Resonance fitting for target 1 using equations 5.4 and 5.18.

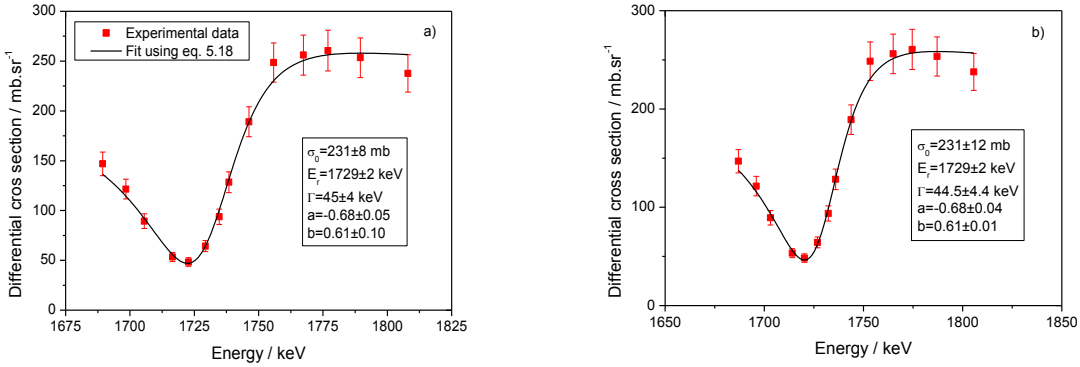

Figure 5.12) a) Resonance fitting for target 2 using equations 5.16 and 5.18 and b) Resonance fitting for target 2 using equations 5.4 and 5.18.

Fittings using both methods are in agreement, showing that equation 5.4 is valid to calculate the effective energy in this resonance. The resonance energy obtained for target 1 was 1727.8±0.1 keV and 1727±1 keV using the two fittings, while for target 2 the resonance energy obtained was the same using both methods, 1729±2 keV. The width of the resonance, Γ, was also similar using both methods. Due to the lower number of experimental points for target 2, the uncertainties arising from the fittings to this target were larger than the ones obtained for target 1.

From the fits, it is possible to verify that for both targets the resonance energy is lower than other experimental values [5,6,7,8], where the resonance was found at 1734 keV, but similar to the position obtained in a recently published work [9], where the energy of the resonance obtained was 1726 keV.

The differential cross section for θ_{lab}=77.7°, θ_{lab}=72.7°, θ_{lab}=67.7°, θ_{lab}=67.3°, θ_{lab}=62.7°, θ_{lab}=55.0° and θ_{lab}=45.0° are presented in figures 5.13 to figure 5.18.

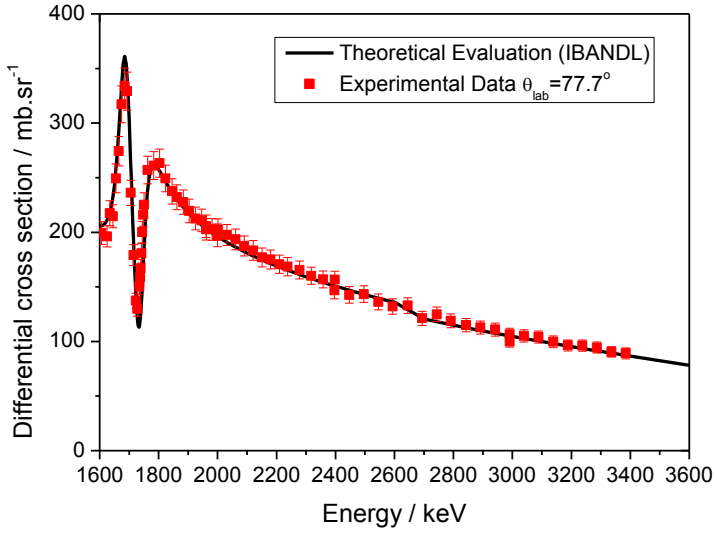

Figure 5.13) $^{12}C(p,p)^{12}C$ differential cross section for θ_{lab}=77.7°.

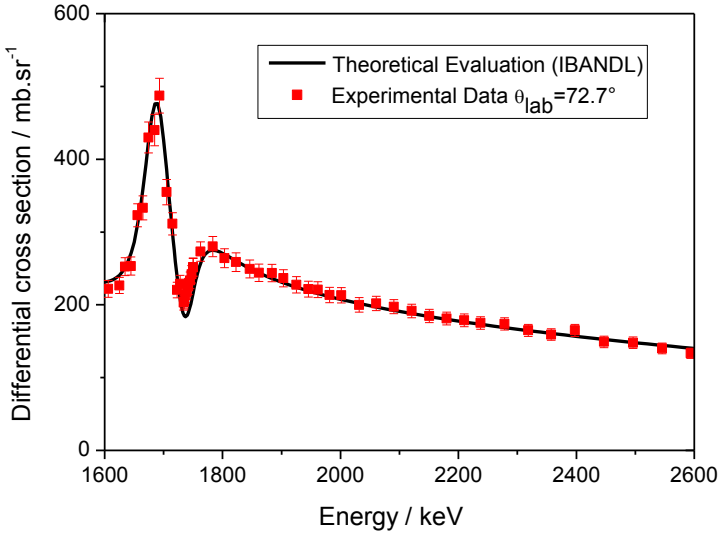

Figure 5.14) $^{12}C(p,p)^{12}C$ differential cross section for θ_{lab}=72.7°.

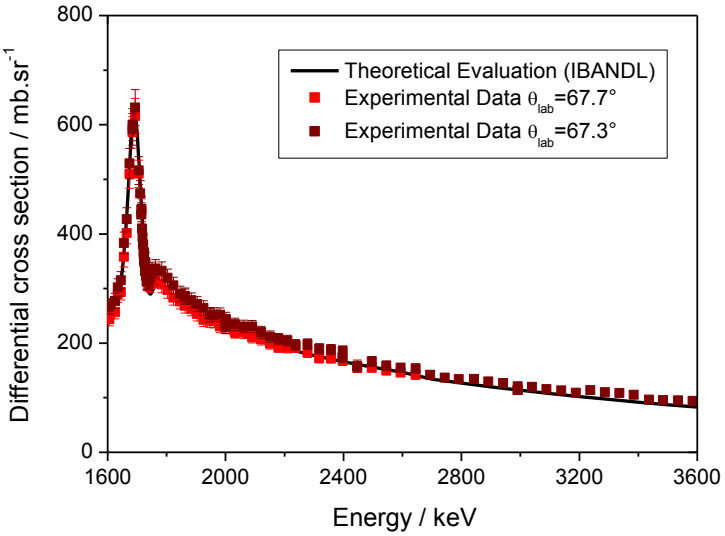

Figure 5.15) $^{12}C(p,p)^{12}C$ differential cross section for $\theta_{lab}=67.7°$ and $\theta_{lab}=67.3°$.

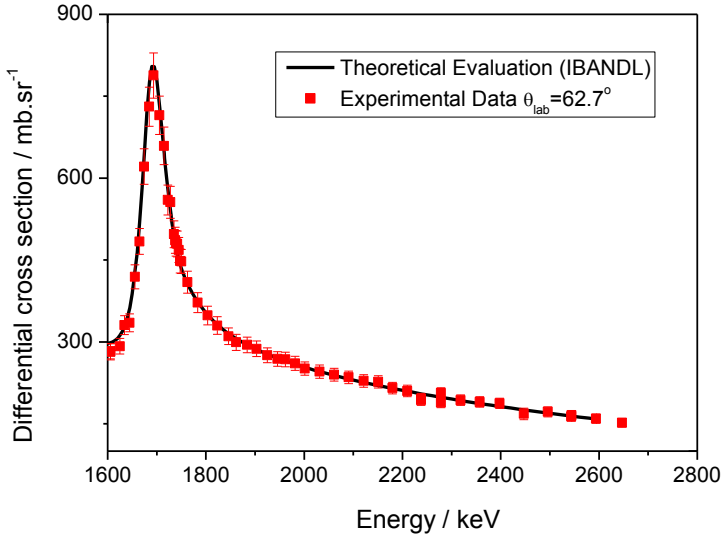

Figure 5.16) $^{12}C(p,p)^{12}C$ differential cross section for $\theta_{lab}=62.7°$.

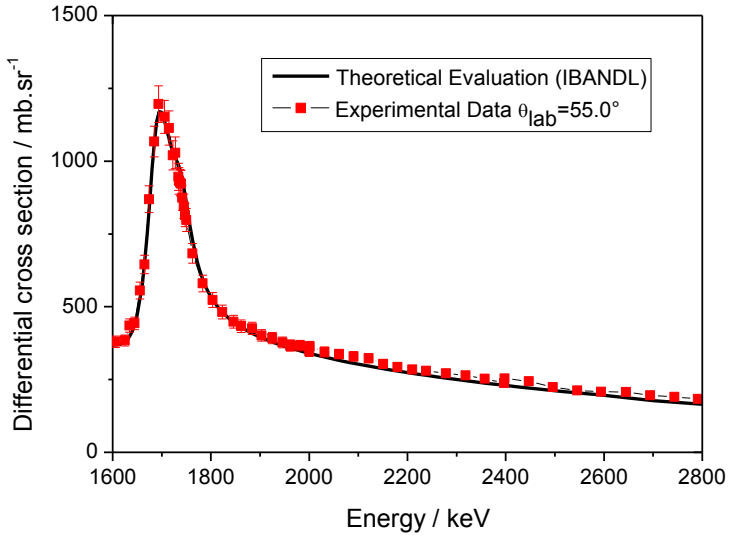

Figure 5.17) $^{12}C(p,p)^{12}C$ differential cross section for θ_{lab}=55.0°.

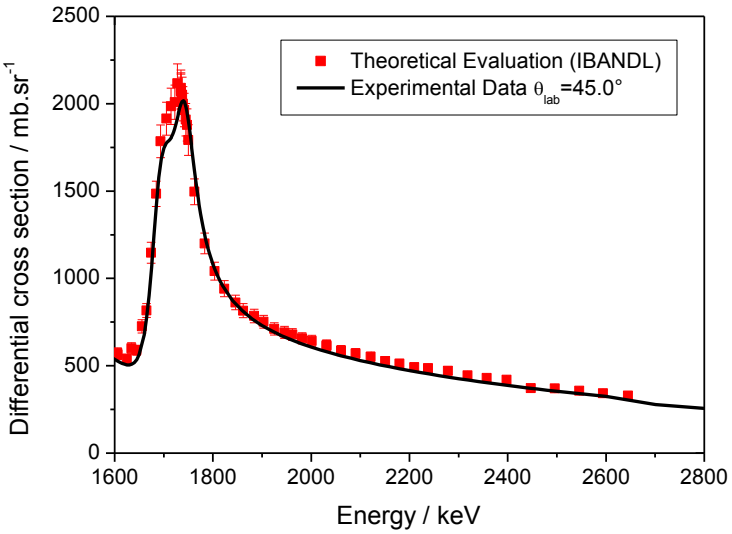

Figure 5.18) $^{12}C(p,p)^{12}C$ differential cross section for θ_{lab}=45.0 °.

In this energy range, the excitation function is dominated by the 1686 keV and 1734 keV resonances. The first corresponds to the $^{13}N\ \frac{3}{2}^{-}$ state at 3502 ± 2 keV ($\Gamma_{c.m.} = 62 \pm 4$ keV) and the second one to the $^{13}N\ \frac{5}{2}^{+}$ state at 3547 ± 2 keV ($\Gamma_{c.m.} = 47 \pm 7$ keV) [4], as it is possible to see in figure 5.19. The results obtained show a very good agreement between experimental data and the theoretical evaluation available in IBANDL, except for the resonance zone at angles near 90°, where there is a negative interference. From the analysis of the results, it is possible to conclude that the target thickness does not affect the measured

cross section, as expected. Following this and since the data presented agree in the position of the 1686 keV resonance, our results suggest that either the position of the 1734 keV resonance is not correct or its natural width must be adjusted.

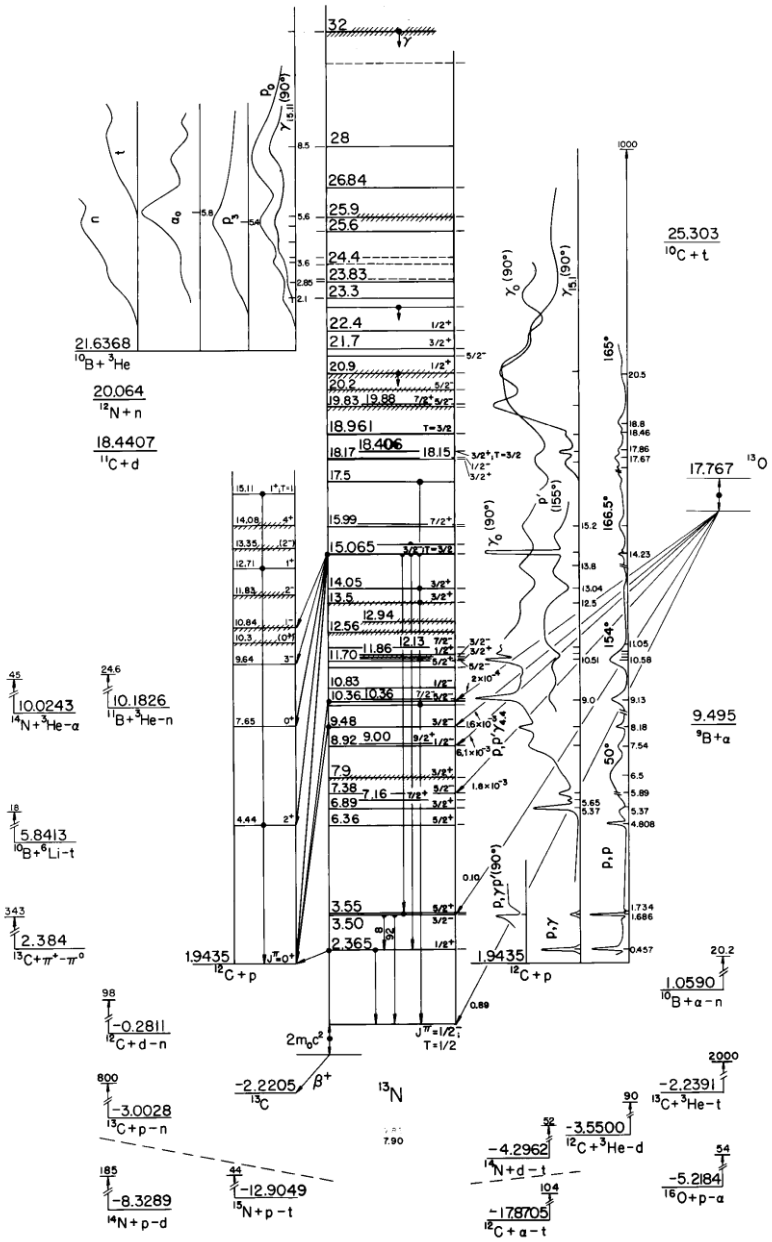

Figure 5.19) ^{13}N nuclear level scheme.

For forward scattering angles, few datasets exist. A comparison between our results and the results of J.C. Armstrong [10] is presented in figure 5.20.

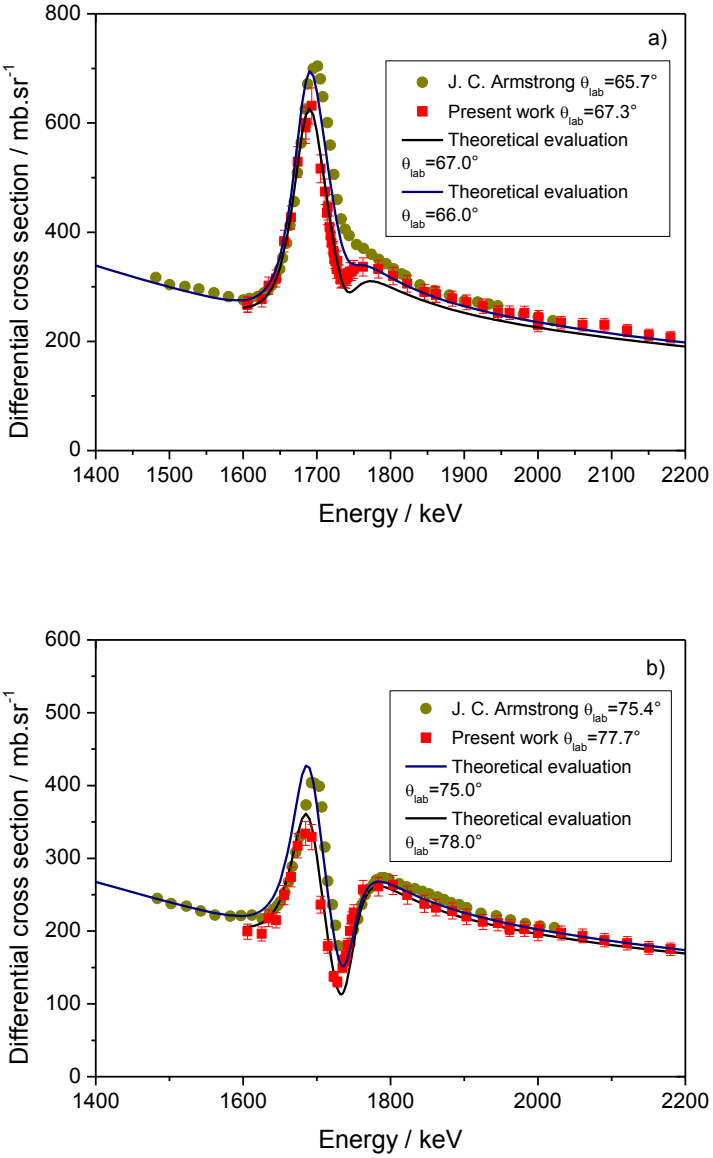

Figure 5.20) a) Comparison between $^{12}C(p,p)^{12}C$ differential cross section for θ_{lab}=67.3° (present work) and θ_{lab}=65.7° (J. C. Armstrong [10]) and b) Comparison between $^{12}C(p,p)^{12}C$ differential cross section for θ_{lab}=77.7° (present work) and θ_{lab}=75.4° (J. C. Armstrong [10]).

The comparison shows an energy shift for similar angles. The results obtained by J.C. Armstrong show a disagreement with theoretical validation in both sides of the resonance zone, suggesting that no corrections in energy for target thickness were made. No information regarding this was found in the published data [10]. The results presented are in good agreement and a better adjustment to theoretical curves is accomplished.

Off resonances, angular distributions can be fitted using optical model calculations. For protons, equation 1.47 modifies to [11]:

$$\left(\frac{d\sigma}{d\Omega}\right) = |A(\theta)|^2 + |B(\theta)|^2 \quad 5.15$$

where the scattering amplitudes $A(\theta)$ and $B(\theta)$ are defined by the following relations:

$$|A(\theta)| = f_c(\theta) + \frac{1}{2ik}\sum_{l=1}^{\infty}[(l+1)S_l^+ + lS_l^- - (2l+1)]e^{2i\sigma_l}P_l(\cos\theta) \quad 5.16$$

$$|B(\theta)| = \frac{1}{2ik}\sum_{l=0}^{\infty}(S_l^+ - S_l^-)e^{2i\sigma_l}P_l^1(\cos\theta) \quad 5.17$$

where $P_l^1(\cos\theta)$ are associated Legendre Polynomials, S_l^+ and S_l^- are scattering matrix elements for different spin orientation.

Using the optical model parameters given by A. Gurbich [12], a simulation using the NRV code [13] was done for three different energies: 1606 keV, 2496 keV and 2991 keV. A NRV fitting was later performed allowing the variation of V_R (depth of real central volume) in the parameters given by A. Gurbich. Optical model parameters introduced in the NRV code are presented in table 5.1, where the values of V_R after the fitting are in parenthesis. The simulation results are presented in figure 5.21.

Energy (keV)	V_R (MeV)	r_R (fm)	a_R (fm)	V_{SO} (MeV)	r_{SO} (fm)	a_{SO} (fm)	r_C (fm)	χ^2
1606	61.7	1.23	0.59	7.2	1.01	0.75	1.23	13.548
	(60.27)							(12.330)
2496	61.7	1.23	0.59	7.2	1.01	0.75	1.23	6.742
	(64.18)							(5.065)
2991	61.7	1.23	0.59	7.2	1.01	0.75	1.23	1.645
	(64.35)							(0.583)

Table 5.1) Optical model parameters used in the NRV code simulations.

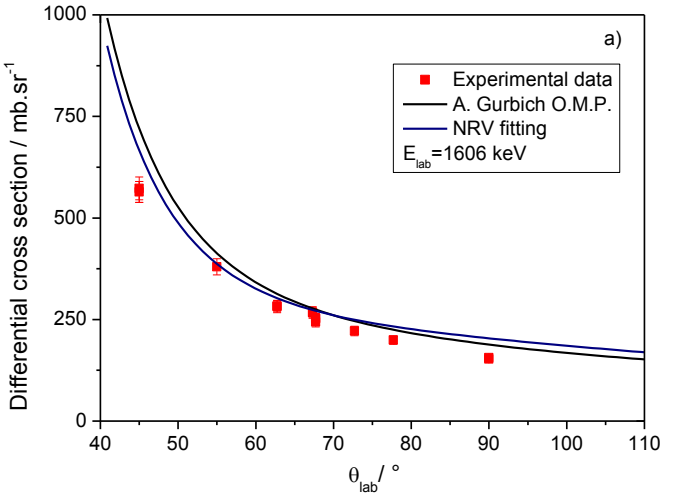

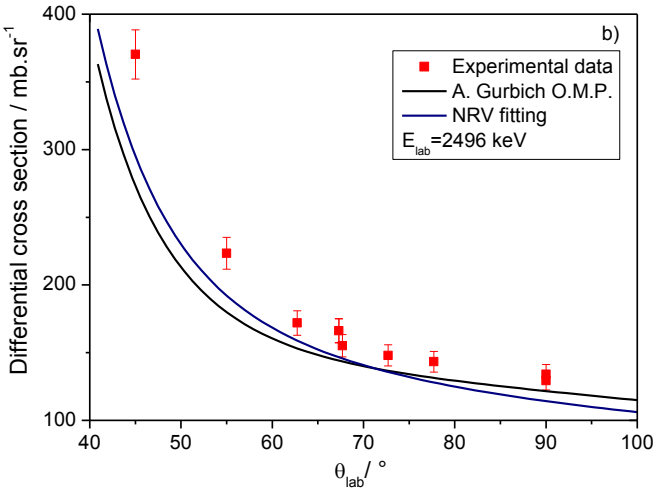

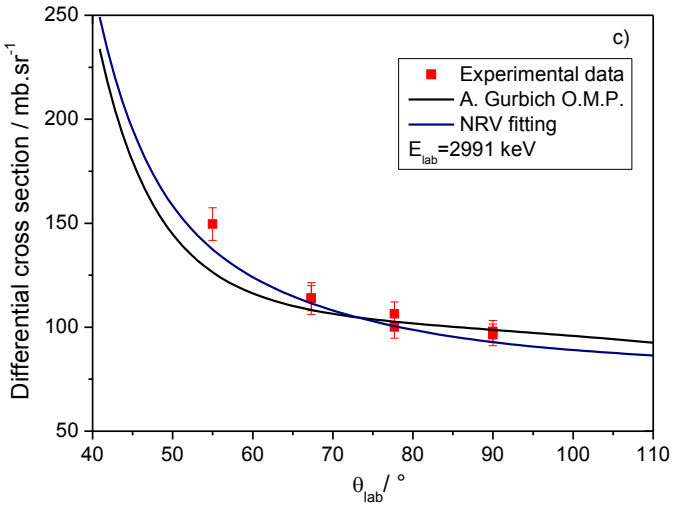

Figure 5.21) NRV simulation using A. Gurbich optical model parameters and NRV fitting for a) 1606 keV b) 2496 keV and c) 2991 keV.

As we can see from figure 5.21, good agreement is verified for 1606 keV and 2991 keV. It is also possible to notice that, if we don´t take into account experimental data for the lowest scattering angle (45°), the χ^2 is reduced from 12.330 to 1.508 for the first energy (1606 keV) and from 5.065 to 3.054 for 2496 keV. A possible reason for this is the fact that the calculation was made mainly with backscattering data. The global optical model parameterizations given by A. Koning *et al*. [14] were also tested, but a larger deviation from experimental data was verified.

From the NRV code, the values obtained for the scattering matrix elements $|S_l^+|$ and $|S_l^-|$ were approximately 1. These were expected results since no absorptive potential was introduced in the optical parameters, so only elastic scattering happens.

Phase shifts δ_l^+ and δ_l^- were also calculated by data fitting with the same code. Figure 5.22 shows the real and imaginary components of δ_l as function of the orbital angular momentum l. Since only elastic scattering occurs, the imaginary component of δ_l, Im(δ_l)≈0, following the theoretical predictions given in equation 1.54. As energy increases, the contribution of higher values of l is necessary to fit the data. From the figure, it is possible to conclude that incoming protons with $l \leq 3$ should be considered in the calculations.

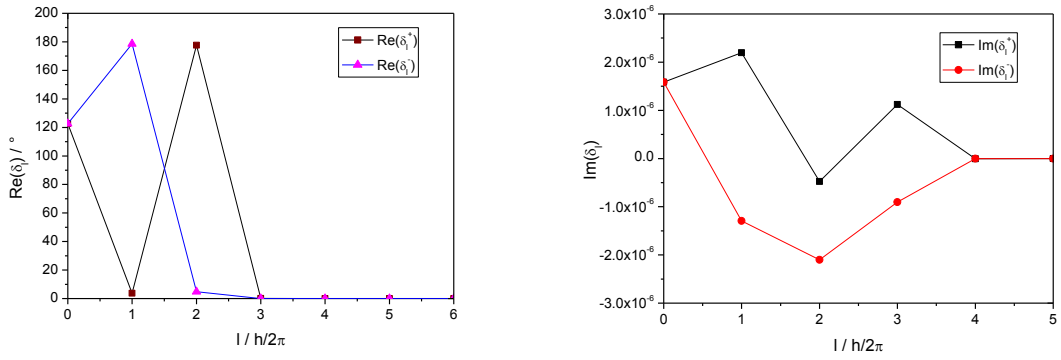

Figure 5.22) a) Re(δ_l) as function of orbital angular momentum l and b) Im(δ_l) as function of orbital angular momentum l.

Results of NRV simulations of experimental data proved that the optical model parameters are critically affected by the lower scattering angle data, which supports our measurements.

From the experimental point of view, the results for the $^{12}C(p,p)^{12}C$ differential cross section also provided a good benchmarking of the experimental setup for the other cross section measurements, providing the reliability of the experimental results obtained.

5.3.2 $^{6}Li(p,p)^{6}Li$ and $^{7}Li(p,p)^{7}Li$

The measurements of the $^{6}Li(p,p)^{6}Li$ and $^{7}Li(p,p)^{7}Li$ differential cross sections were carried out at the 3.0 MV Tandem accelerator. These two differential cross sections were measured together for three targets and concurrently with the $^{19}F(p,p)^{19}F$ elastic cross section for one target. Measuring the $^{6}Li(p,p)^{6}Li$ differential cross section was a challenging task due to the small areal density of ^{6}Li in the targets along with the small solid angle used, $4.06 \times 10^{-4}\ sr$. To improve the separation between ^{6}Li and ^{7}Li peaks, the two PIPS detectors were replaced by new detectors with nominal resolution of 12 keV. For situations where ^{6}Li and ^{7}Li peaks were not enough separated for area calculation, the two peaks were fitted together using a Gaussian fit. For that, the ^{6}Li peak width, $w_{6_{Li}}$, has been fixed by the ^{7}Li width, $w_{7_{Li}}$, by the following equation:

$$w_{6_{Li}} = \frac{k_{6_{Li}} + \dfrac{1}{\cos\theta_{lab}}}{k_{7_{Li}} + \dfrac{1}{\cos\theta_{lab}}} w_{7_{Li}} \qquad 5.20$$

where $k_{6_{Li}}$ and $k_{7_{Li}}$ are the kinematical factors for ^{6}Li and ^{7}Li, respectively.

Another restriction to the differential cross section measurement for the LiF target is the presence of unwanted nuclear reactions from ^{19}F, $^{19}F(p,p_1)^{19}F$ and $^{19}F(p,p_2)^{19}F$, corresponding to the decay to ground state from $J=1/2^-$ (E=109.9 keV) and $J=1/2^+$ (E=197.1 keV), respectively, although at these energies the $^{19}F(p,p_2)^{19}F$ has a very small value when compared with the other two cross sections. The outgoing energy was calculated for all the elements present in the target. The figures 5.23 and 5.24 below show spectra for LiF and LiCl targets at similar energies, E_{eff}=1596 keV and E_{eff}=1592 keV.

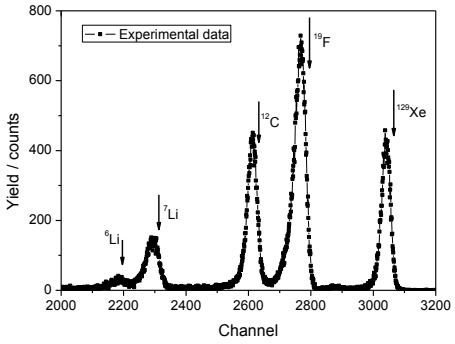

Figure 5.23) The 1596 keV H^+ forward spectrum for LiF target at θ_{lab}=90°.

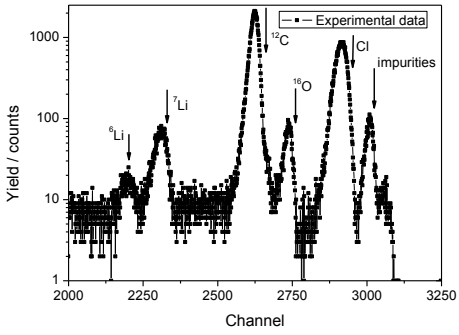

Figure 5.24) The 1592 keV H^+ forward spectrum for LiCl target at θ_{lab}=90°.

For the ^{6}Li(p,p)^{6}Li reaction, the small yield makes its measurement difficult, along with the proximity of the ^{7}Li peak in the spectrum. The ^{6}Li(p,p)^{6}Li cross sections were measured for two angles (69.5° and 90.0°) for two targets (LiF and LiCl). The results of the differential cross sections for these two angles for both targets are presented in figures 5.25 and 5.26.

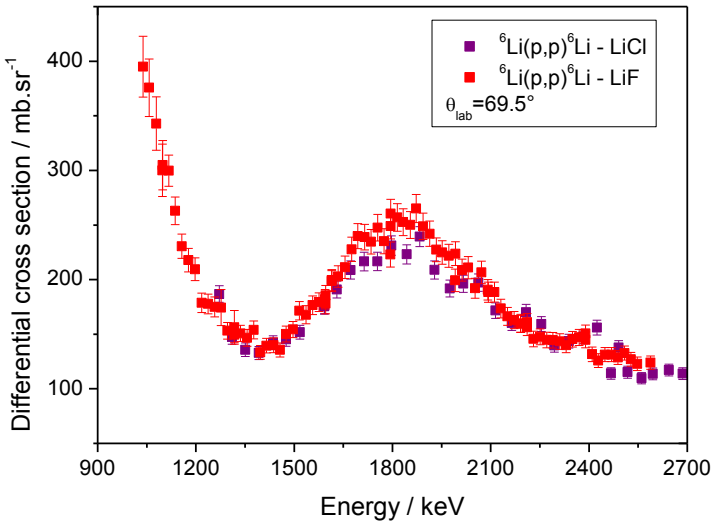

Figure 5.25) ^{6}Li(p,p)^{6}Li differential cross section for θ_{lab}=69.5°.

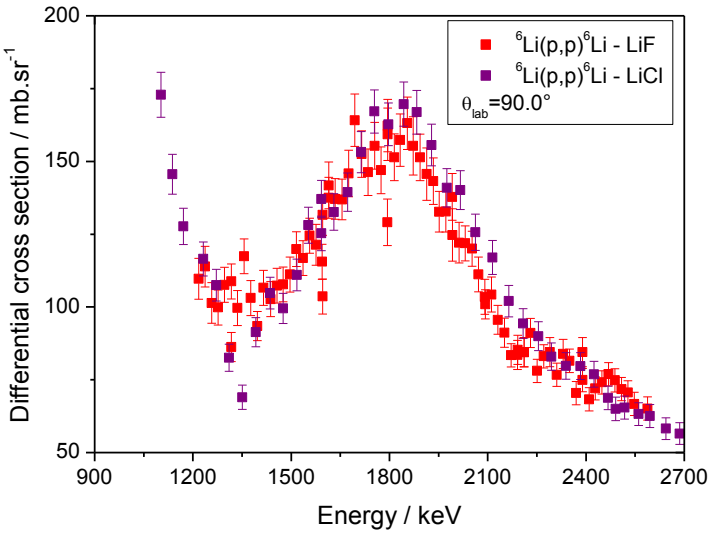

Figure 5.26) ^{6}Li(p,p)^{6}Li differential cross section for θ_{lab}=90.0°.

The results for the two targets used in this work are in good agreement in the range of energies measured. In this range of energies, the broad resonance corresponds to the ^{7}Be $\frac{5^-}{2}$ state at 7210 ± 60 keV ($\Gamma_{c.m.} = 400 \pm 50$ keV) [15], as can be seen in figure 5.27.

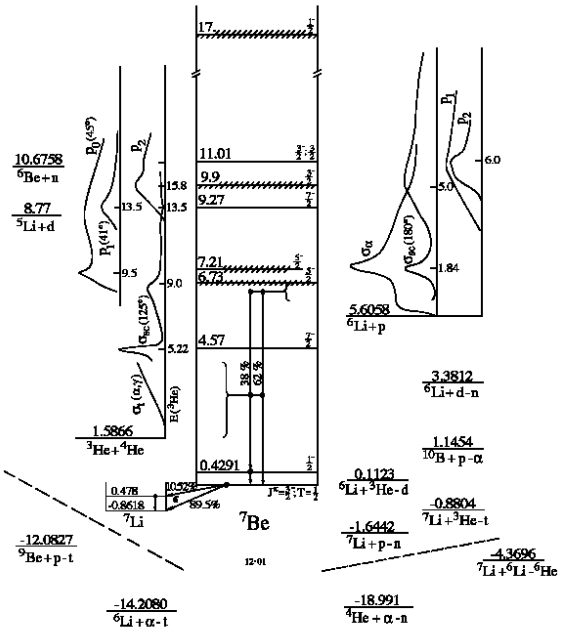

Figure 5.27) ^{7}Be nuclear level scheme.

Such a broad resonance can be reasonably described by a Gaussian function. Considering this, a Gaussian fit was performed using LiF results at θ_{lab}=69.5°. The results are presented in figure 5.28.

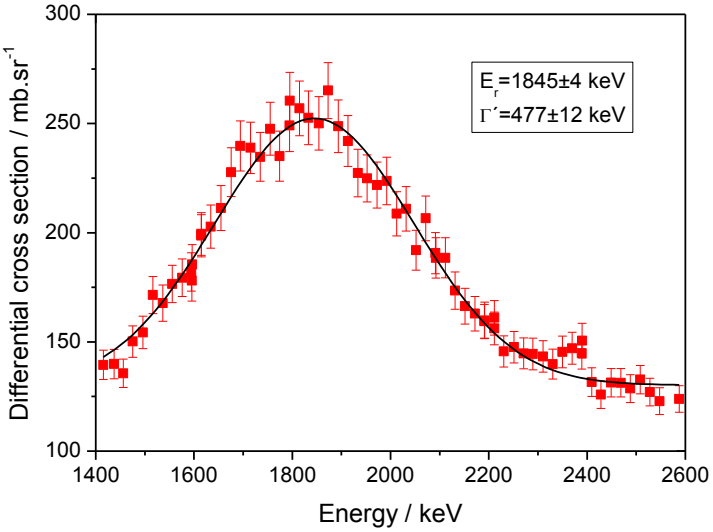

Figure 5.28) Resonance region of the ^{7}Li(p,p)^{7}Li differential cross section at θ_{lab}=69.5° fitted with a gaussian function.

Considering equation 3.2, the experimental width of the resonance, Γ′, is given by:

$$\Gamma' = \sqrt{\Delta E^2 + \Gamma^2} \qquad 5.21$$

where ΔE is the target thickness in energy and Γ is the resonance natural width.

From the fitting information, it was possible to get the resonance energy, $E_r = (1845 \pm 4)$ keV and the experimental width $\Gamma' = (477 \pm 12)$ keV. Considering that $\Gamma' \gg \Delta E$, we have $\Gamma' \approx \Gamma$. These results for Γ are in agreement with the theoretical values given for the resonance energy but the natural width is higher than the theoretical value [15].

When we compare with results from previous authors [16,17], as per the information in figure 5.29, despite the same shape in the resonance region, there is a significant discrepancy in the cross section value, not explainable by the different θ_{lab} used. The cross sections for θ_{lab}=81.3° and θ_{lab}=80.5° are smaller than the cross sections obtained in the present work for θ_{lab}=90.0°. Considering our angular resolution and the normalization for a heavy element, there are no reasons to believe that the absolute values of the cross section are wrong, especially having present that the measurement have been made for two targets. Furthermore, the results from J.A. Mccray [16] were obtained from a thick target integration, which can result in a higher uncertainty in charge measurement.

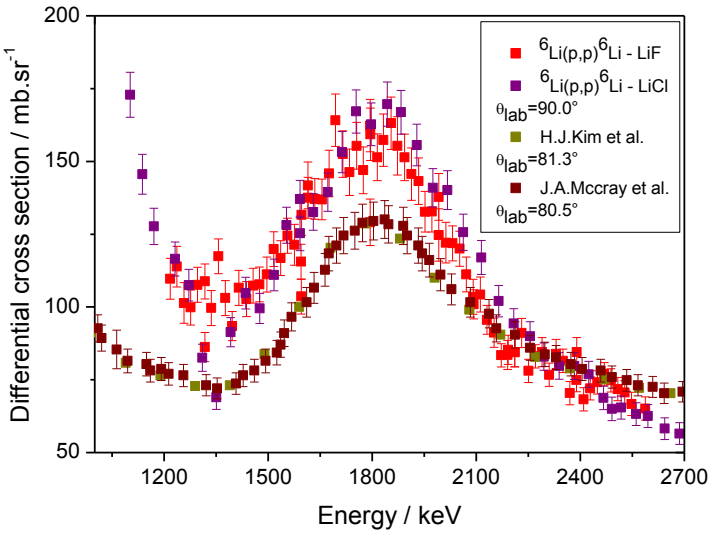

Figure 5.29) ^{6}Li(p,p)^{6}Li differential cross section for present work for θ_{lab}=90.0° and comparison with previous works [16,17] for θ_{lab}=81.3° and θ_{lab}=80.5°.

Comparing our results with the ones from W.D. Harrison *et al*. [18] and M. Haller *et al*. [19], it is possible to notice that the broad resonance at 1840 keV is not reproduced by the experimental data. The comparison of the present data with previous works for similar θ_{lab} is presented in figure 5.30.

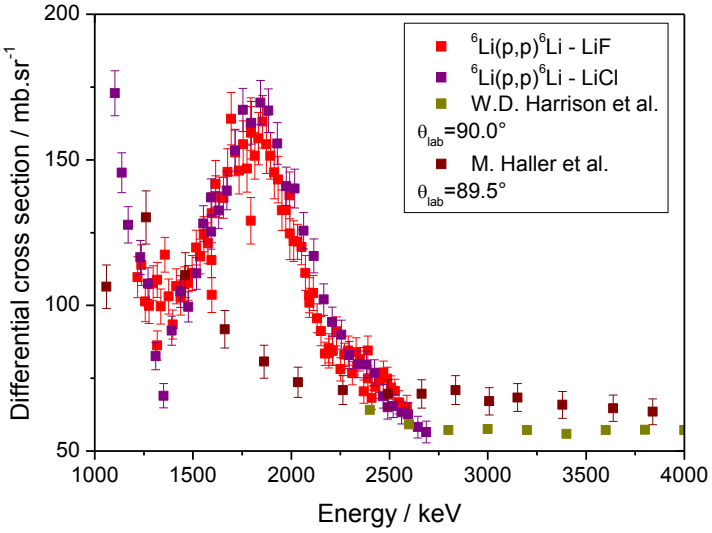

Figure 5.30) ^{6}Li(p,p)^{6}Li differential cross section for present work for θ_{lab}=90.0° and comparison with previous works [18,19].

Analyzing figure 5.30, it is possible to see that the discrepancy between datasets is higher, especially in the region from 1500 to 2000 keV. However, other works [16,17] indicate the presence of a broad resonance in agreement with data from present work.

Concerning the $^{7}Li(p,p)^{7}Li$ elastic cross section, results are presented for 69.5° for two targets (LiF and LiCl) and for 90.0° for three targets (LiF, LiCl and LiI). Also, angular distributions are presented for two targets (LiF and LiCl) for several energies.

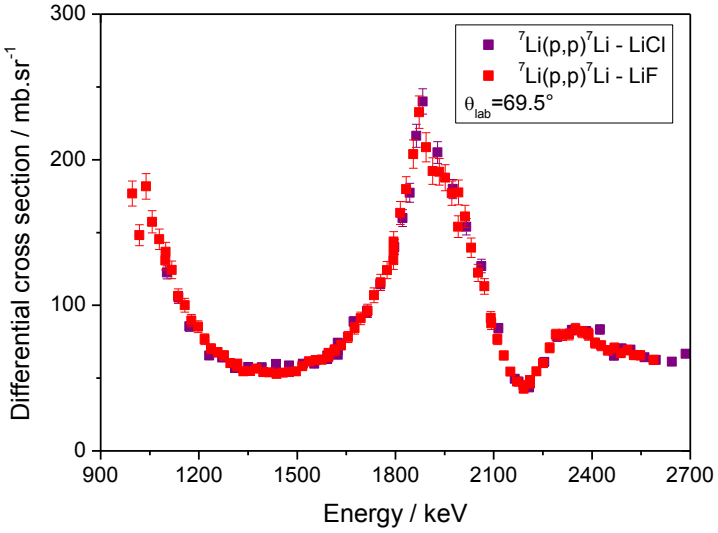

Figure 5.31) $^{7}Li(p,p)^{7}Li$ differential cross section for present work for θ_{lab}=69.5°.

As we can see from figure 5.31, the experimental data for the two targets at θ_{lab}=69.5° are in perfect agreement. In figure 5.32, the experimental data for the three targets at θ_{lab}=90.0° is presented. In figure 5.33, a comparison between the results obtained and results from a previous work for angles near 90.0° is presented. From the figures, there is an excellent agreement between data, especially in the resonance region. Also, there is an energy match between data, which is very important to theoretical calculations and also because there is a correction in energy for target thickness.

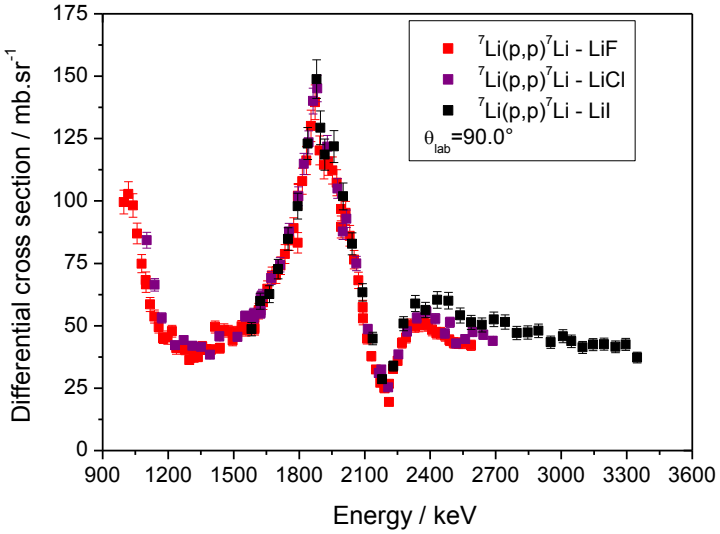

Figure 5.32) ^{7}Li(p,p)^{7}Li differential cross section for present work for θ_{lab}=90.0°.

For θ_{lab}=90.0°, the only region where there is a little discrepancy between datasets is in energies from 2150 keV to 3000 keV, especially for the LiI target. As we can see in figure 5.33, the data from P.R. Malmberg [20], measured at θ_{lab}=81.9°, lies between the present work datasets, which is expected due to the measurement at a small angle. Also, the maximum value for this measurement is high in the resonance region.

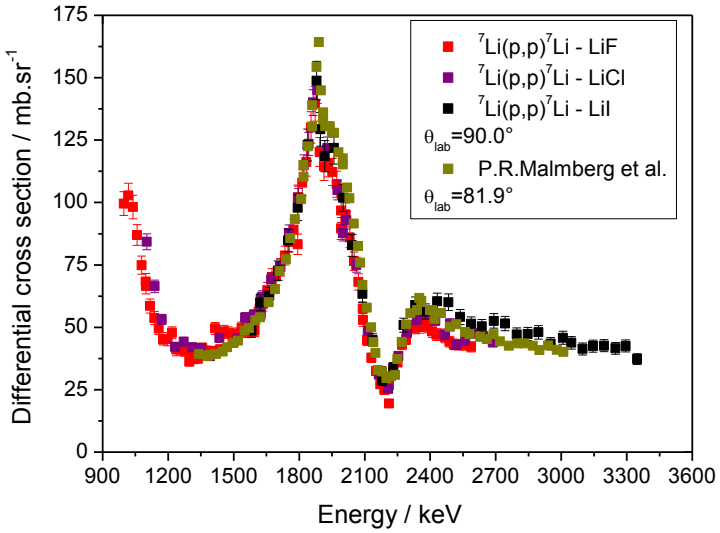

Figure 5.33) ^{7}Li(p,p)^{7}Li differential cross section for present work and comparison with the work from P.R. Malmberg [20] for θ_{lab}=90.0°.

Angular distributions were also measured for 11 different energies for the two targets and results are presented from figures 5.34 to figure 5.44. The dashed line in each figure represents pure Rutherford scattering for the given energy.

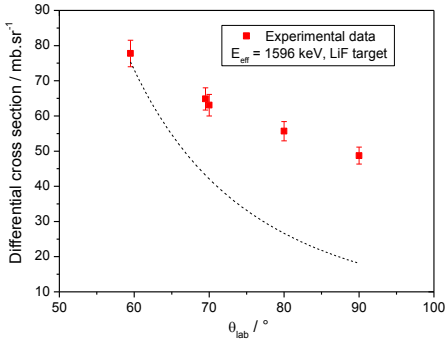

Figure 5.34) $^{7}Li(p,p)^{7}Li$ angular distributions for E_{eff}=1596 keV.

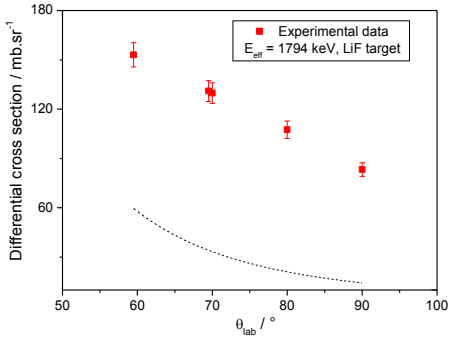

Figure 5.35) $^{7}Li(p,p)^{7}Li$ angular distributions for E_{eff}=1794 keV.

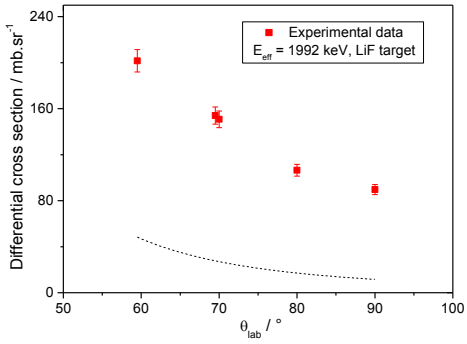

Figure 5.36) $^{7}Li(p,p)^{7}Li$ angular distributions for E_{eff}=1992 keV.

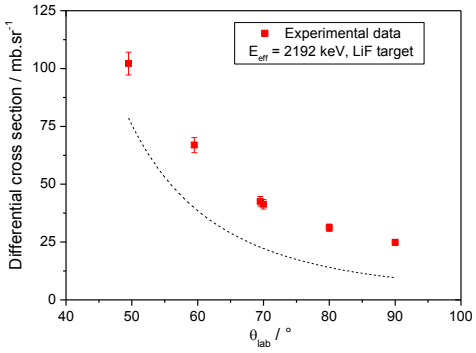

Figure 5.37) $^{7}Li(p,p)^{7}Li$ angular distributions for E_{eff}=2192 keV.

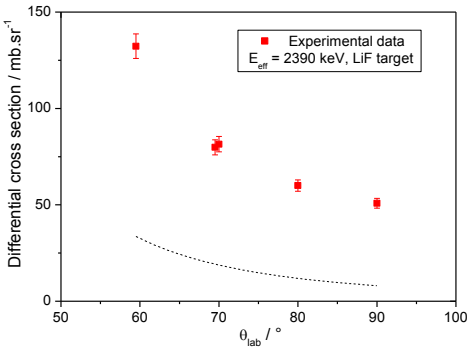

Figure 5.38) $^{7}Li(p,p)^{7}Li$ angular distributions for

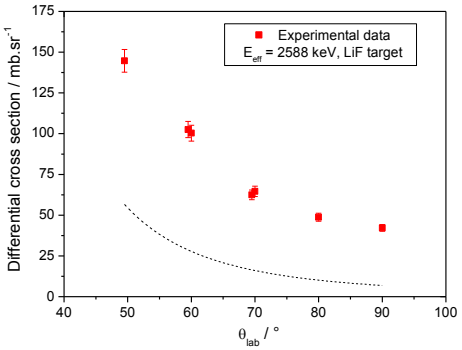

Figure 5.39) $^{7}Li(p,p)^{7}Li$ angular distributions for

E_{eff}=2390 keV.

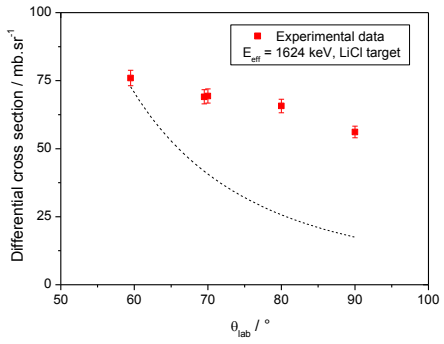

Figure 5.40) ^{7}Li(p,p)^{7}Li angular distributions for E_{eff}=1624 keV.

E_{eff}=2588 keV.

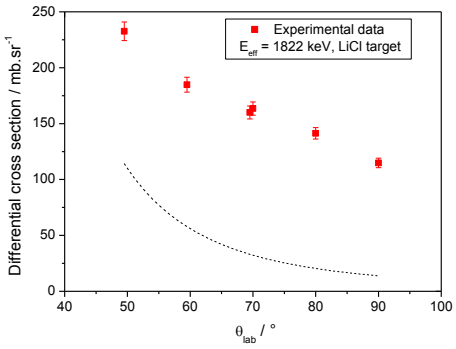

Figure 5.41) ^{7}Li(p,p)^{7}Li angular distributions for E_{eff}=1822 keV.

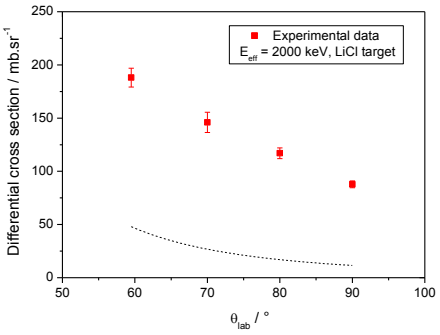

Figure 5.42) ^{7}Li(p,p)^{7}Li angular distributions for E_{eff}=2000 keV.

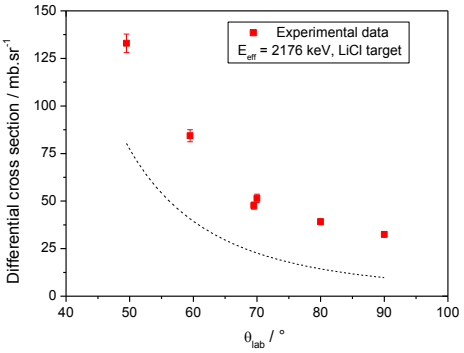

Figure 5.43) ^{7}Li(p,p)^{7}Li angular distributions for E_{eff}=2176 keV.

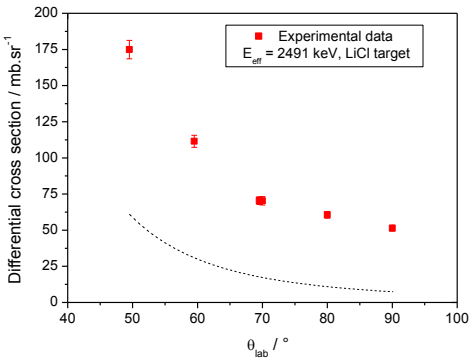

Figure 5.44) ^{7}Li(p,p)^{7}Li angular distributions for E_{eff}=2491 keV.

As we can see from the figures, the angular distributions for ^{7}Li exhibit a nuclear component. In figure 5.45, the ratio to Rutherford cross section for LiF target is presented. As expected, the ratio approaches 1 at small angles, since the impact parameter at small angles is higher, prevailing the Coulomb scattering.

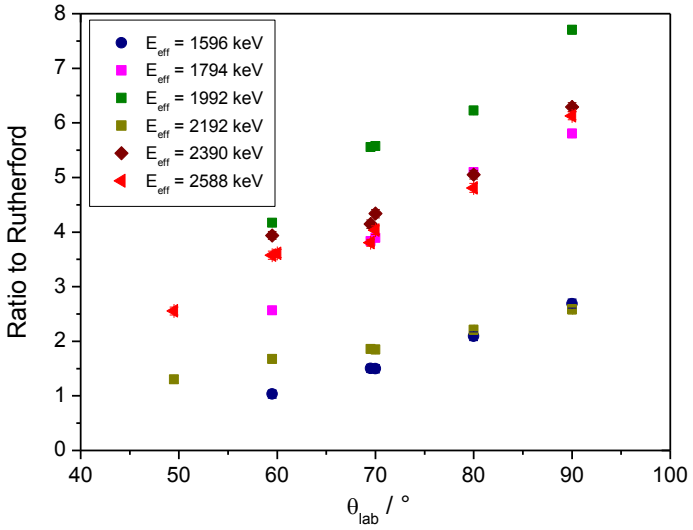

Figure 5.45) Ratio to Rutherford cross section for the six angular distributions for the LiF target.

Since there is no theoretical validation available for this nuclide in IBANDL, a comparison between experimental data and results obtained with optical model parameters given by A. J. Koning [14] was performed. In figure 5.46, the results of this comparison are presented for one energy, E_{eff}=2588 keV.

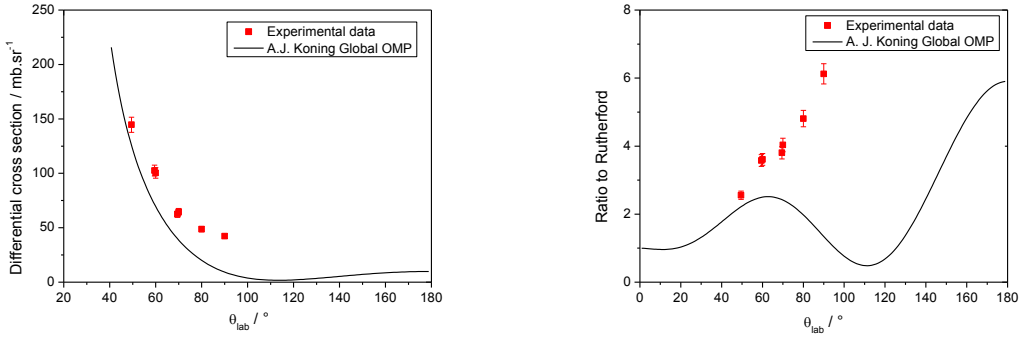

Figure 5.46) a) Experimental and theoretical differential cross section for E_{eff}=2588 keV and b) Experimental and theoretical ratio to Rutherford cross section for E_{eff}=2588 keV.

In this case, the ratio to the Rutherford cross section is presented to show the decrease in the differential cross section for scattering angles near 70°, which is not predicted by experimental data. The use of an imaginary potential in this case is required, due to the presence of inelastic scattering $^{7}Li(p,p_1)^{7}Li$ and nuclear reactions, $^{7}Li,(p,\alpha)^{4}He$. This decrease suggests that the real part of the optical potential needs to be modified by adding a surface term to the Saxon-Woods potential. In this case, optical potentials available are far from describing the experimental data.

Globally, the results of the $^{6}Li(p,p)^{6}Li$ and $^{7}Li(p,p)^{7}Li$ elastic cross sections for the targets studied in the present work showed a very good agreement in the range of energies studied. Concerning the $^{6}Li(p,p)^{6}Li$ elastic cross section, the comparison with another experimental data showed the need of new experimental measurements in this range of energy. Concerning the $^{7}Li(p,p)^{7}Li$ elastic cross section, comparison between the obtained results and previous data showed very good agreement, making the extrapolation for other angles reliable, presenting new data available for theoretical calculations for this element.

5.3.3 $^{19}F(p,p)^{19}F$

The $^{19}F(p,p)^{19}F$ differential cross section was measured for one target, LiF, along with the measurement of the $^{7}Li(p,p)^{7}Li$ and $^{6}Li(p,p)^{6}Li$ differential cross sections. The charge collection was normalized by the Rutherford cross section of ^{129}Xe, as for the elastic scattering of lithium isotopes.

The differential cross sections were measured from 996 keV to 2588 keV for two scattering angles: 69.5° and 90.0°. Also, angular distributions were measured for 6 energies: 1596 keV, 1794 keV, 1992 keV, 2192 keV, 2390 keV and 2588 keV. The differential cross sections and ratio to Rutherford cross sections, for 69.5 and 90.0°, are presented from figure 5.47 to figure 5.50 and angular distributions for the mentioned energies are presented from figure 5.52 to figure 5.57. As for ^{7}Li, the dashed line represents the pure Rutherford cross section. Comparison with theoretical evaluation was done for 69.5 and 90.0° up to 1740 keV.

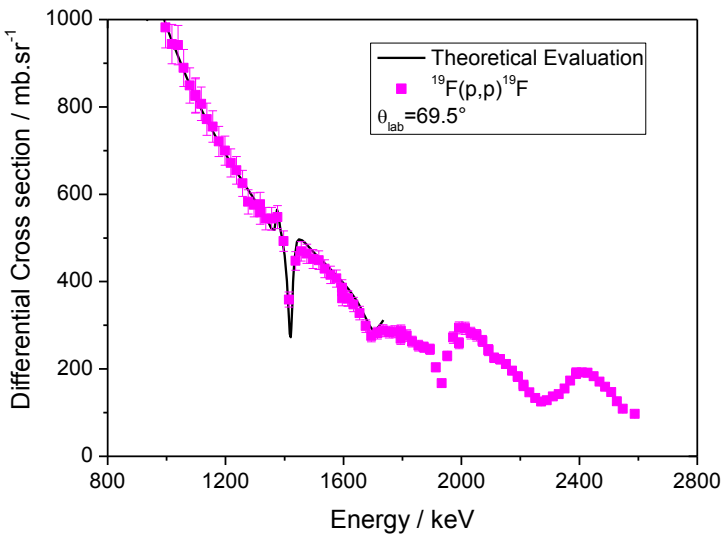

Figure 5.47) ^{19}F(p,p)^{19}F differential cross section for θ_{lab}=69.5°.

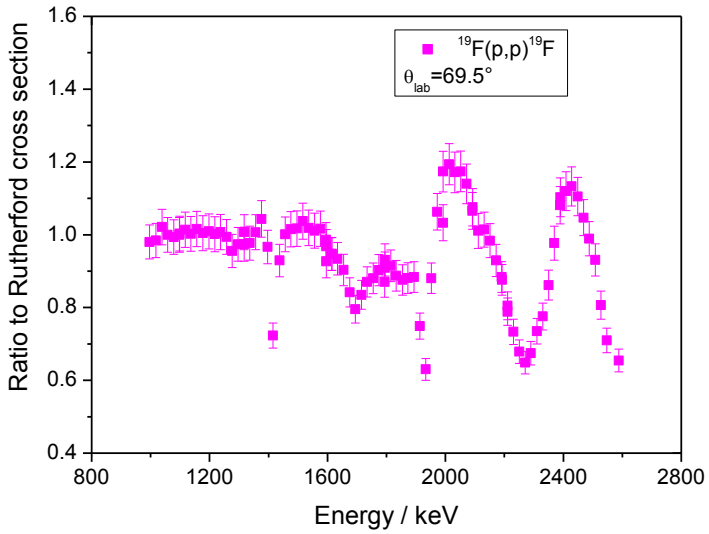

Figure 5.48) Ratio to Rutherford cross section for θ_{lab}=69.5°.

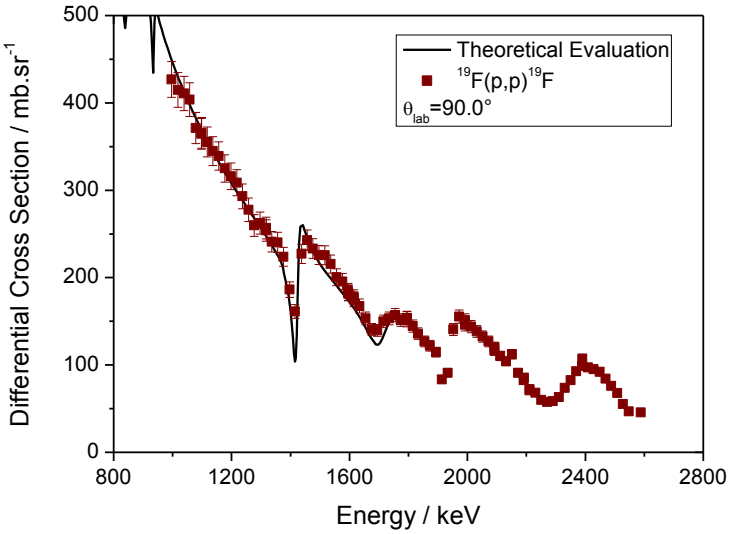

Figure 5.49) ^{19}F(p,p)^{19}F differential cross section for θ_{lab}=90.0°.

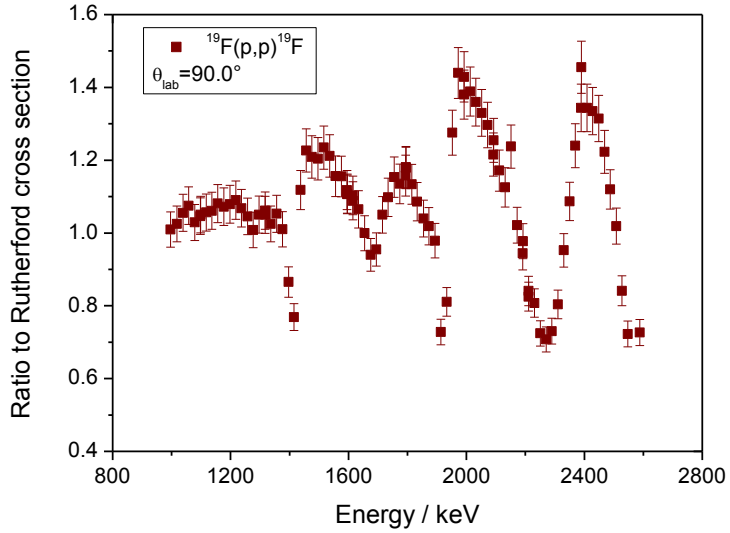

Figure 5.50) Ratio to Rutherford cross section for θ_{lab}=90.0°.

The figures above show a good agreement between experimental data and theoretical evaluation available for the two angles. Since the cross section is purely Rutherford for lower energies, as per the information regarding the ratio to Rutherford cross section, a good benchmark to the results is done using this information. The differential cross section for the two angles exhibits the same behavior with energy as well as the ratio to Rutherford cross section. A comparison between our results (θ_{lab}=69.5°) and the ones obtained by S. Ouichaoui *et al*. [21] (θ_{lab}=69.38°) is presented in figure 5.51.

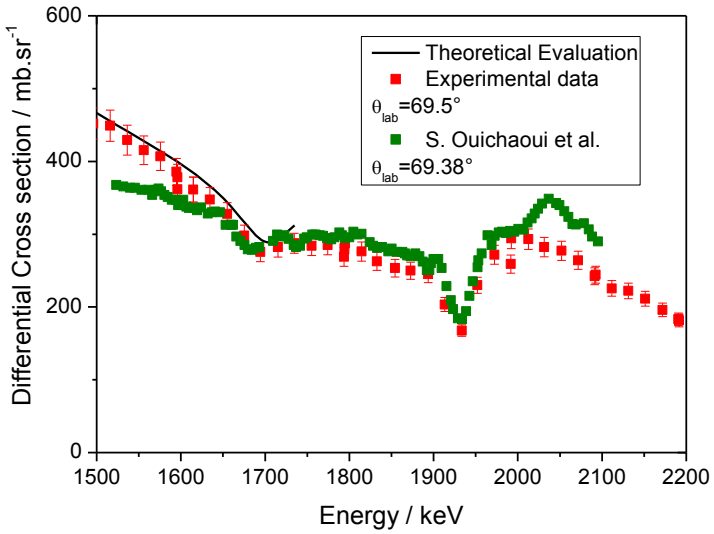

Figure 5.51) a) Comparison between $^{19}F(p,p)^{19}F$ differential cross section for θ_{lab}=69.5° (present work) and θ_{lab}=69.38° (S. Ouichaoui *et al*. [21]).

The results presented in figure 5.51 show a significant discrepancy in the energy region from 1500 keV to 1650 keV and above 2000 keV. However, our results match the theoretical validation up to 1740 keV.

The angular distributions for six different energies are presented from figures 5.52 to 5.57.

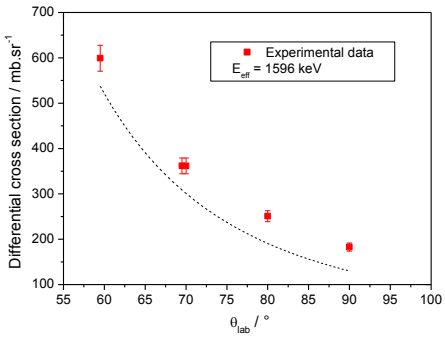

Figure 5.52) $^{19}F(p,p)^{19}F$ angular distributions for E_{eff}=1596 keV.

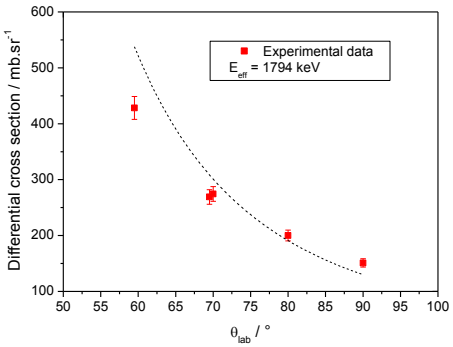

Figure 5.53) $^{19}F(p,p)^{19}F$ angular distributions for E_{eff}=1794 keV.

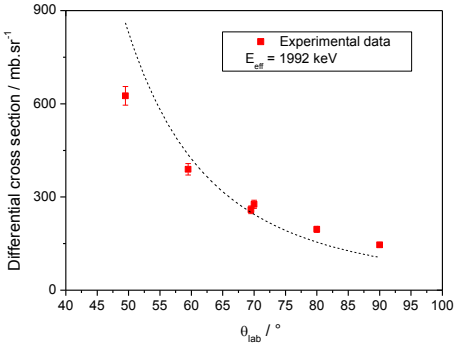

Figure 5.54) $^{19}F(p,p)^{19}F$ angular distributions for E_{eff}=1992 keV.

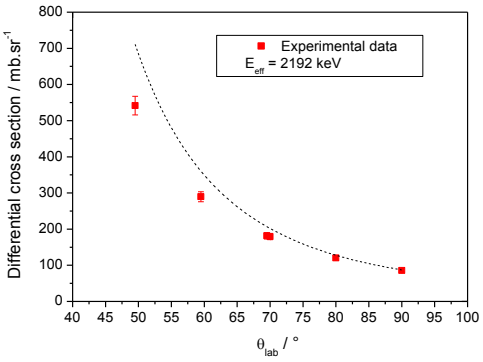

Figure 5.55) $^{19}F(p,p)^{19}F$ angular distributions for E_{eff}=2192 keV.

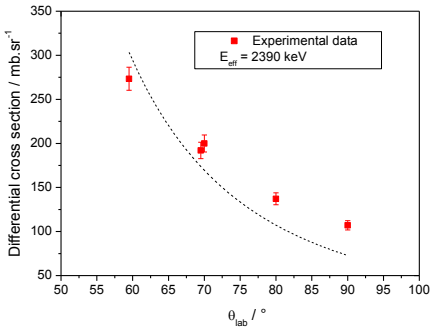

Figure 5.56) $^{19}F(p,p)^{19}F$ angular distributions for E_{eff}=2390 keV.

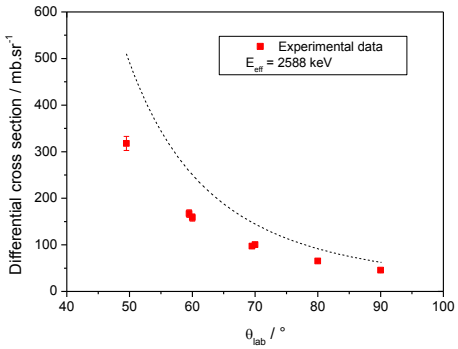

Figure 5.57) $^{19}F(p,p)^{19}F$ angular distributions for E_{eff}=2588 keV.

From the analysis of the $^{19}F(p,p)^{19}F$ angular distributions presented above, we can´t identify a correlation between elastic cross section and Rutherford cross section. In order to test the optical parameters for ^{19}F, a comparison between experimental data and results obtained with optical model parameters given by A. J. Koning [14] was performed. The results are presented in figure 5.58 for two energies, E_{eff}=1596 keV and E_{eff}=1794 keV.

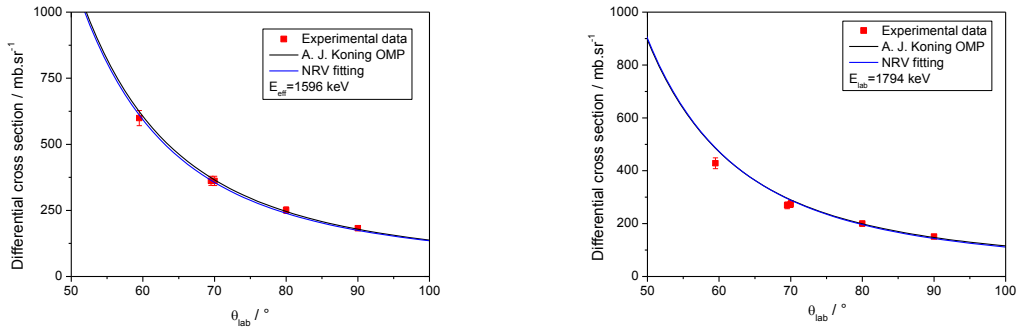

Figure 5.58) a) Experimental and theoretical differential cross section for E_{eff}=1596 keV and b) Experimental and theoretical differential cross section for E_{eff}=1794 keV.

For ^{19}F, the global optical parameters given by A. Koning fit the experimental data. Such as for ^{7}Li, an imaginary potential is applied due to the presence of nuclear reactions and the absolute values of scattering matrix elements are different from unit, $|S_l^+| \neq 1$ and $|S_l^-| \neq 1$, as it is shown in figure 5.59.

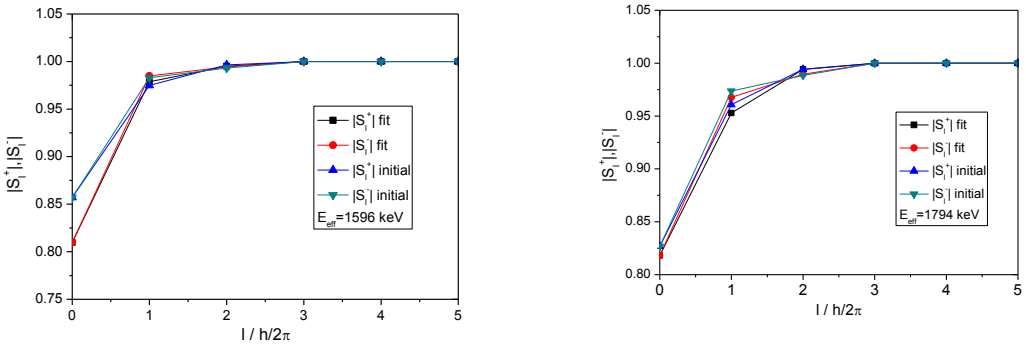

Figure 5.59) a) Scattering matrix elements for E_{eff}=1596 keV and b) Scattering matrix elements for E_{eff}=1794 keV.

As for carbon, incoming protons with $l \leq 3$ must be take into account to fit the data, the approach of $|S_l|$ to 1 corresponds to $\sigma_{re} \to 0$, so few particles are absorbed and only elastic scattering takes place.

5.3.4 $^{31}P(p,p)^{31}P$

The measurements for the $^{31}P(p,p)^{31}P$ were carried out for the energy range from 2.6 MeV to 4 MeV. The beam current at the target was about 100 nA, along with Gamma-ray detection for the $^{31}P(p,p'\gamma)^{31}P$, whose results were part of another PhD thesis.

The elastic scattered particles were measured at backscattering geometry by a PIPS detector with 50 mm^2 active area placed 155.0° to the beam axis, with a depletion layer of 100 μm and nominal resolution of 15 keV. The measured solid angle value was $3.65 \times 10^{-3}\ sr$. Again, to avoid the large uncertainties associated to the measurement of the absolute number of incident protons (beam charge collection) and of the target thickness we have measured the Rutherford backscattering yield of a heavy component of the target (Ag) to obtain the product of the two parameters. The collected charge, for each energy, was 20 μC. The Ag yield, as function of energy, is presented in figure 5.60. It is possible to notice the dependence with $1/E^2$ is present, showing a good reproducibility of data.

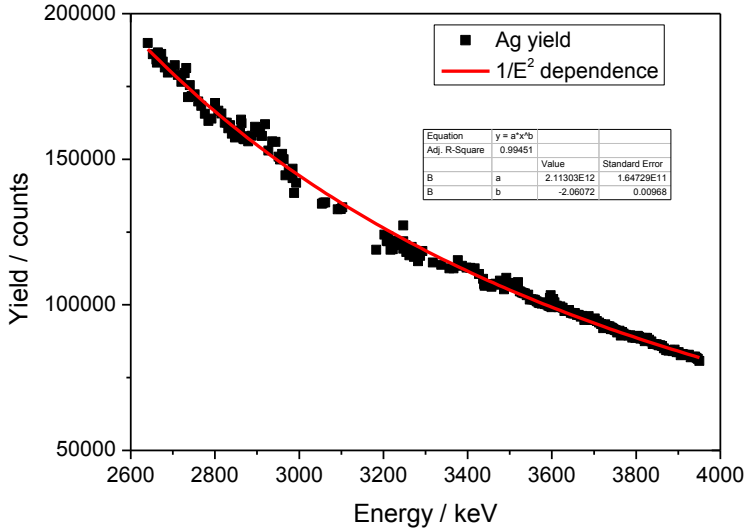

Figure 5.60) $1/E^2$ dependence for protons scattered from Ag, as function of energy.

A spectrum of the scattered protons is given in figure 5.61, for an incident energy of 3735 keV showing that the Ag peak is well defined and separated from the other peaks. This spectrum also shows a presence of C in the spectrum, which is due to carbon build up on the target during the experiment. However, the ratio between P and Ag did not change during the experiment.

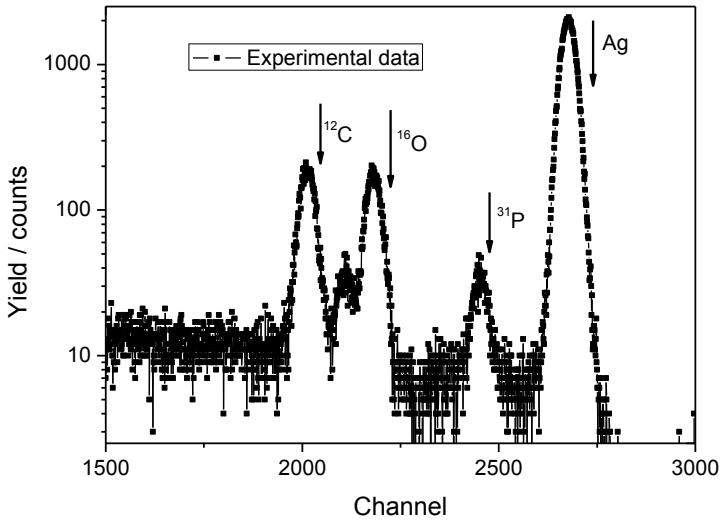

Figure 5.61) The 3735 keV H^+ backscattering spectrum at θ_{lab}=155.0°.

The differential cross section for θ_{lab}=155.0° is presented in figure 5.62. Figure 5.63 shows a comparison of the results obtained with the ones from previous measurements [22,23]

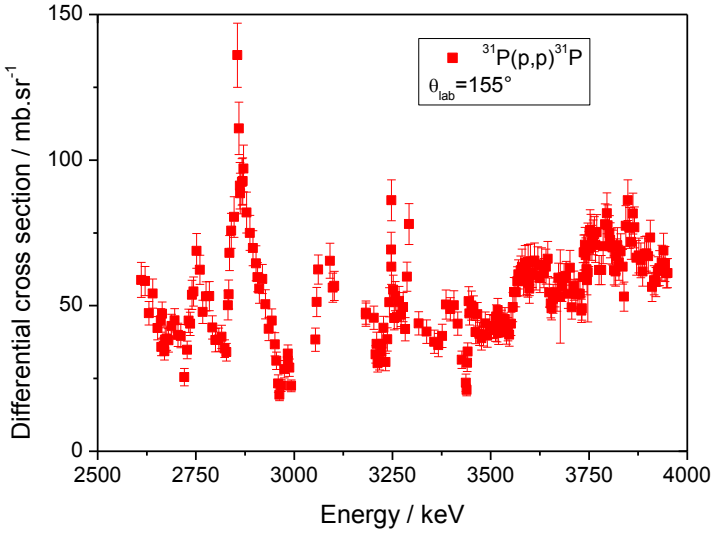

Figure 5.62) ^{31}P(p,p)^{31}P differential cross section for θ_{lab}=155.0°.

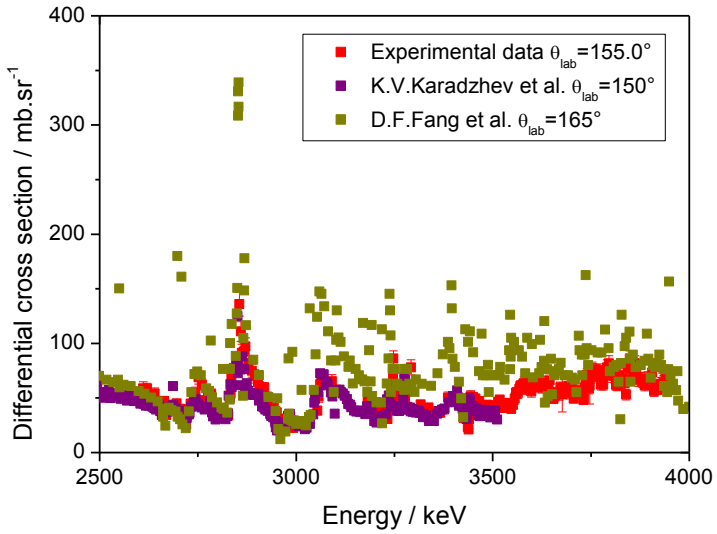

Figure 5.63) $^{31}P(p,p)^{31}P$ differential cross section of present work and comparison with previous works in the same energy range [22,23].

The comparison with previous works show that the experimental data follows the same behavior as in the work from K. V. Karadzhev *et al*. [22], despite the different scattering angle, which does not affect significantly the absolute value of the cross section. However, huge discrepancies can be seen when comparing the present data with the work from D. F. Fang *et al*. [23], which was used for the available theoretical evaluation. This evaluation also showed that many points were out of range in this experimental data and they were not considered. Since in the present work we have a good agreement in our data with little sources of uncertainty, it may be considered as a valid cross section for material analysis in this range of energy.

5.4 Elastic scattering of oxygen

In this section, preliminary results for $^{16}O(^{16}O,^{16}O)^{16}O$ elastic cross section and $^{12}C(^{16}O,^{16}O)^{12}C$ elastic and recoil cross section were determined. Concerning the $^{16}O(^{16}O,^{16}O)^{16}O$ elastic cross section, the target used was the ^{16}O target implanted in C, while for $^{12}C(^{16}O,^{16}O)^{12}C$ elastic and recoil cross section was determined using the target of ^{129}Xe implanted in ^{12}C.

For elastic cross section measurements with oxygen, the 3 MV Tandem accelerator was used. Beam characterization was made using the AMS (Accelerator Mass Spectrometry)

line of the 3 MV Tandem accelerator. Beams of 20 nA, 5 nA and 0.5 nA were obtained for $^{16}O^{3+}$, $^{16}O^{4+}$ and $^{16}O^{5+}$ at the reaction chamber, respectively. The detection setup was the same as the one used for protons. The elastic scattering of oxygen was measured in two steps: a first run was used to determine the $^{16}O(^{16}O,^{16}O)^{16}O$ elastic cross section and a second run to determine $^{12}C(^{16}O,^{16}O)^{12}C$ elastic and recoil cross section. Due to the limitations of the High Energy 90° magnet, the results were obtained for a limited number of energies. However, this was the first time in the LATR/CTN-IST that Oxygen beams were used for nuclear reactions purposes.

The beam characterization, as said before, was carried out using the high sensitive magnet placed in the AMS line of the 3 MV Tandem accelerator. For this purpose, three terminal voltages were used: 1600 kV, 1800 kV and 2000 kV. Figures 5.64, 5.65 and 5.66 show the multiple charge states of the ^{16}O beam.

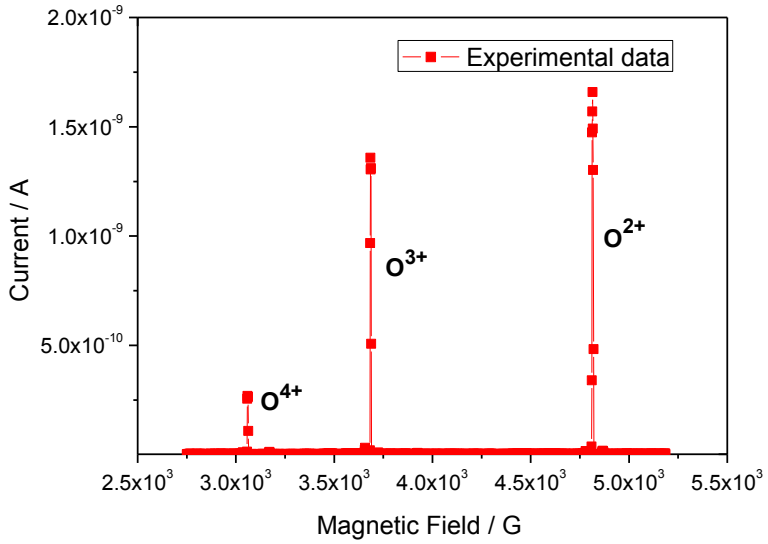

Figure 5.64) Current intensity of multiple charge states for oxygen for 1600 kV.

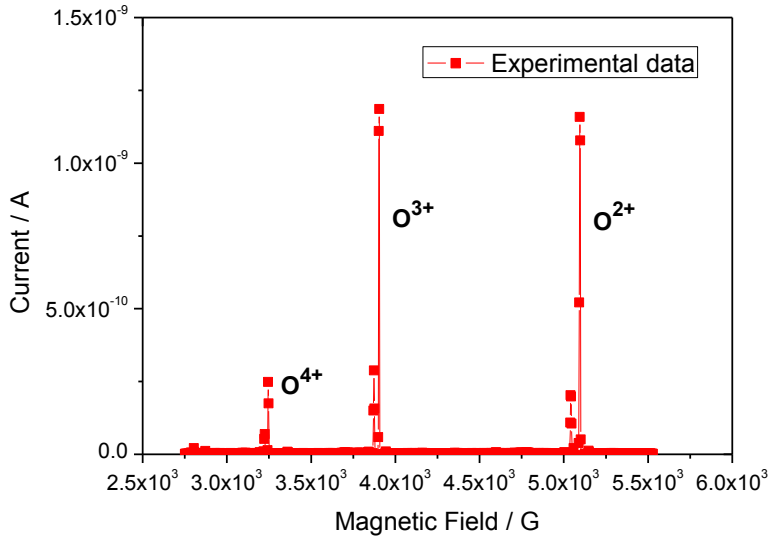

Figure 5.65) Current intensity of multiple charge states for oxygen for 1800 kV.

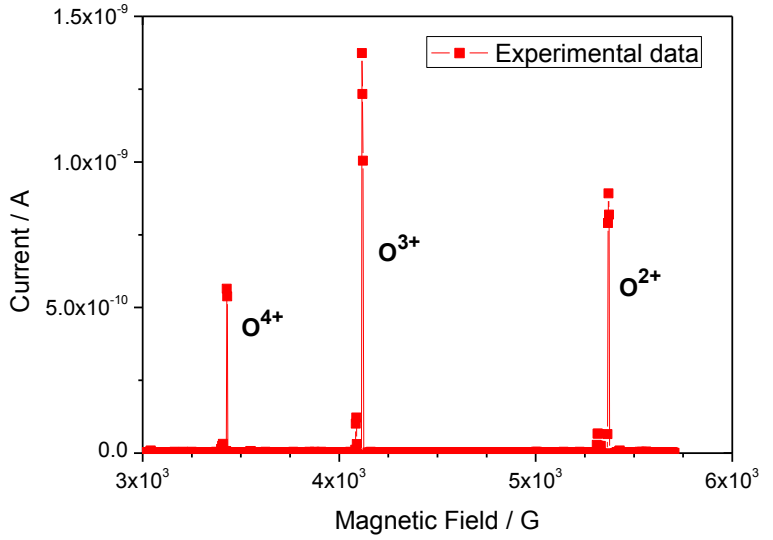

Figure 5.66) Current intensity of multiple charge states for oxygen for 2000 kV.

It is possible to verify the presence of a lower intensity current peak near the ^{16}O peak for each charge state, due to a Faraday Cup effect. There are also some contaminations in the beam, but these are far away from the values of interest. The relative intensities show that the oxygen beam current is higher for the 2+ and 3+ charge states. However, with increasing the energy, the relative intensity of higher charge states increases, as we can see from the figures. Also, there is no ^{12}C contamination in the spectra, which should be avoided due to the superposition of $^{12}C^{3+}$ with $^{16}O^{4+}$ (same m/q ratio). Hence, we have chosen the $^{16}O^{3+}$, $^{16}O^{4+}$ and $^{16}O^{5+}$ beams, which are the most suitable for the measurements.

5.4.1 $^{16}O(^{16}O,^{16}O)^{16}O$ Elastic cross section

For testing the suitability of this experiment, first spectra corresponding to the elastic reaction cross section were taken. The terminal voltage was set at 2000 kV, corresponding to a energy of 8 MeV for $^{16}O^{3+}$. The elastic cross section was measured for 45°. This scattering angle was chosen due to fact that theoretically the $^{16}O+^{16}O$ elastic cross section exhibits a relative maximum at this scattering angle. The collected charge was 5 µC. The elastic cross section for a given effective energy and angle is given by:

$$\sigma_{el}^{O}(E_{eff},\theta_{lab}) = \frac{Y_O(E_{eff},\theta_{lab}).\sigma_{Ruth}^{Co}(E_{eff},\theta_{lab}).N_{Co}}{N_O.Y_{Co}(E_{eff},\theta_{lab})} \qquad 5.22$$

where N_O and N_{Co} is the areal density of ^{16}O and ^{59}Co in the target, respectively $\sigma_{Ruth}^{Co}(E_{eff},\theta_{lab})$ is the Rutherford cross section for a given effective energy and angle for ^{59}Co, $Y_O(E_{eff},\theta_{lab})$ is the yield of ^{16}O and $Y_{Co}(E_{eff},\theta_{lab})$ is the yield of ^{59}Co. For the $^{16}O+^{16}O$ elastic cross section, the yield of ^{16}O must be divided per two, since in the exit channel we have two identical particles. Due to carbon content in the target, a correction was made which subtracts the contribution of the recoil carbon particles, by normalizing to the scattered ^{16}O yield the scattering of ^{16}O from carbon. In figure 5.67, the spectrum for the considered energy and scattering angle is presented.

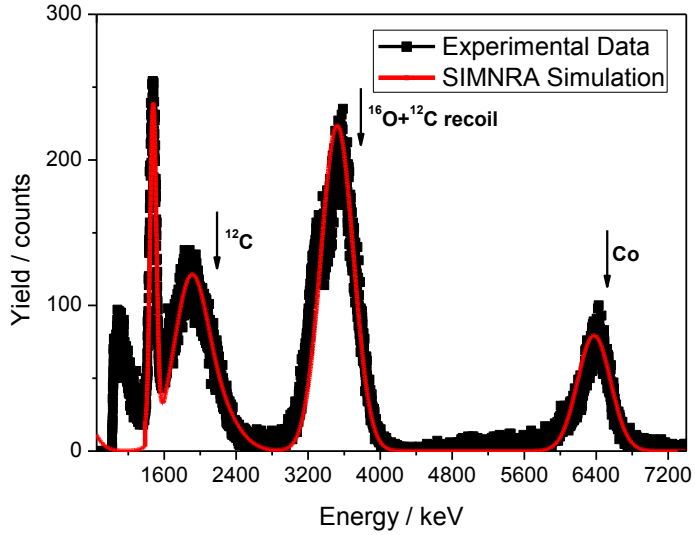

Figure 5.67) Elastic reaction spectrum for 8 MeV of $^{16}O^{3+}$ for θ_{lab}=45°.

A clean spectrum is obtained, where peaks corresponding to the interactions of the oxygen beam with carbon, oxygen and cobalt may be seen. A peak corresponding to the elastic recoil of hydrogen by oxygen is also present in the spectrum. Hydrogen content does not affect the measurements and can be important to energy and angular calibration, due to its high sensitivity to energy and angle. Also its content was seen to decrease with time due to sputtering induced by the beam.

The obtained cross section was $(385 \pm 32) \times 10^{1} mb.sr^{-1}$, which represents a 2.8% deviation from the Rutherford cross section. Note, however, that the uncertainty of the elastic cross section is 8.3%. This is higher than desirable as our ultimate goal is to achieve 1% uncertainty, in order to be able to extract information for fusion reactions also taking place. A simulation with SIMNRA was made, using the same composition obtained by RBS. A self-calibration of the spectra was done, since the heavy ions as oxygen do not interact with the silicon of the detector in the same way as a light particle. The general mechanism of interaction of light particles with silicon detector is valid for heavy ions, however, because of the large mass of the heavy ions, their interaction with silicon detectors are strongly affected by some parameters (such as plasma effects or "pulse-height defect") that are of little or no importance when considering the interaction of lighter particles [24,25]. Considering this, the energy calibration of the spectra used for protons was not valid for oxygen ions and, for simulation purposes, two energy calibrations were done: one for protons and other for heavy ions.

Since these elastic reactions, especially at forward angles, have a high cross section, a low current is enough to measure it, even at higher energies. Thus, the target is not submitted to high currents, implying it will withstand beam bombardment without noticeable deterioration over the time. To confirm the stability of the target, a RBS spectrum was taken after one month tests at different energies and angles and about 1 mC of collected charge. No difference in the elemental composition was found, showing the suitability of the produced targets for this kind of measurement.

5.4.2 $^{12}C(^{16}O,^{16}O)^{12}C$ Elastic cross section

The $^{12}C(^{16}O,^{16}O)^{12}C$ elastic cross section was studied using the ^{129}Xe implanted in ^{12}C target for three different energies, 2783 keV, 5087 keV and 8087 keV and two different angles: 39.5° and 44.5°, since this reaction only happens at angles below 48°. An elastic spectrum for E_{eff}=8087 keV is presented in figure 5.68. As we can see from the spectrum, a very good separation between elements in the spectrum is obtained and the absence of background makes the counts integration an easy task.

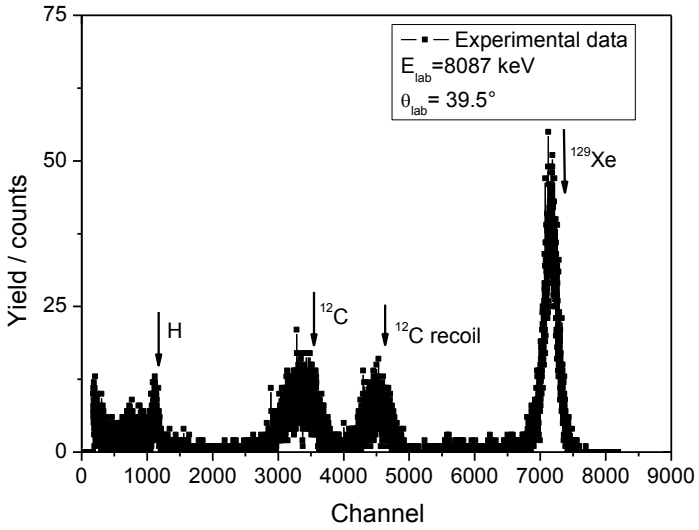

Figure 5.68) Elastic spectrum for 8086 keV of $^{16}O^{5+}$ for θ_{lab}=39.5°.

Figures 5.69 and 5.70 show, for two of the three energies studied, that the yield corresponding to scattering from ^{129}Xe follows the angular dependence of the Rutherford scattering, as expected.

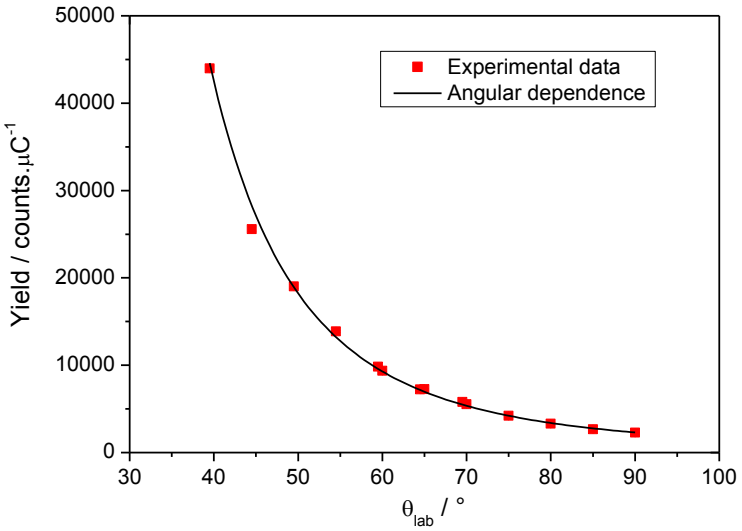

Figure 5.69) ^{129}Xe angular dependence on Rutherford formula for E_{lab}=2783 keV.

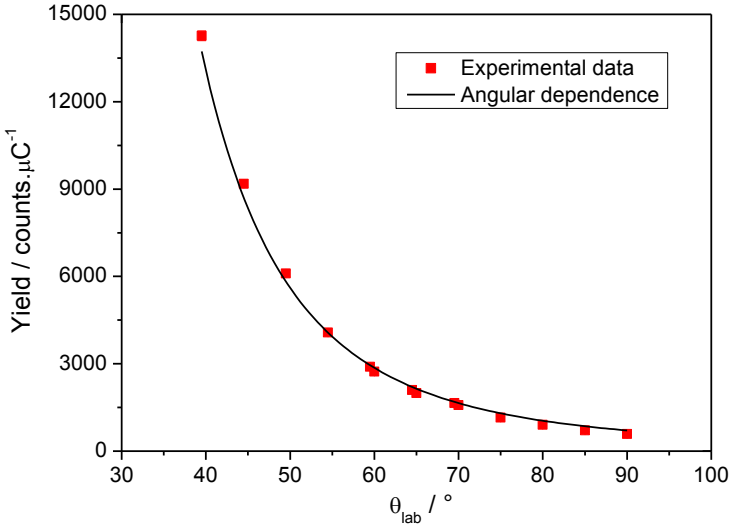

Figure 5.70) ^{129}Xe angular dependence on Rutherford formula for E_{lab}=5087 keV.

The ^{12}C(^{16}O,^{16}O)^{12}C elastic cross section is presented in figure 5.71, Rutherford cross section for same energies and angles is also presented. The results show that there is no deviation from Rutherford scattering at these energies. In this case, the size of the symbols is of the order of uncertainties.

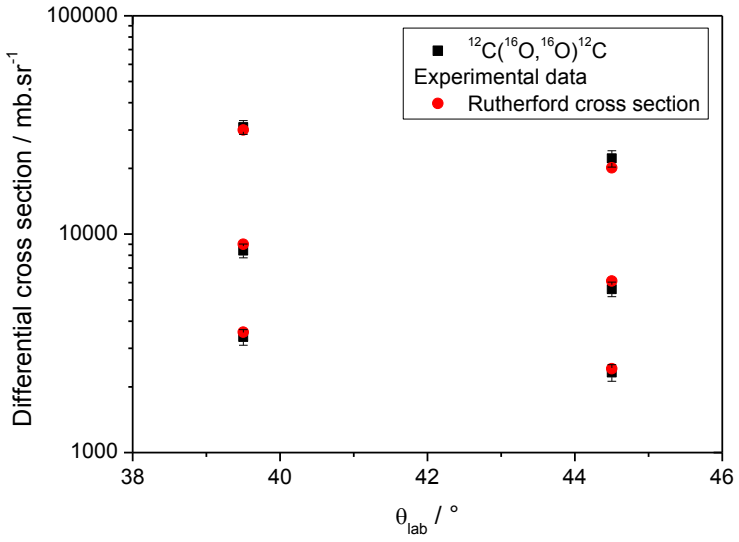

Figure 5.71) $^{12}C(^{16}O,^{16}O)^{12}C$ elastic cross section for E_{lab}=2783 keV, E_{lab}=5087 keV and E_{lab}=8087 keV.

5.4.3 $^{12}C(^{16}O,^{16}O)^{12}C$ Recoil cross section

The $^{12}C(^{16}O,^{16}O)^{12}C$ recoil cross section is presented in figure 5.72. Theoretical (calculated) values for recoil cross section are also presented [26]. Some discrepancies were found at low scattering angles for E_{eff}=5087 keV.

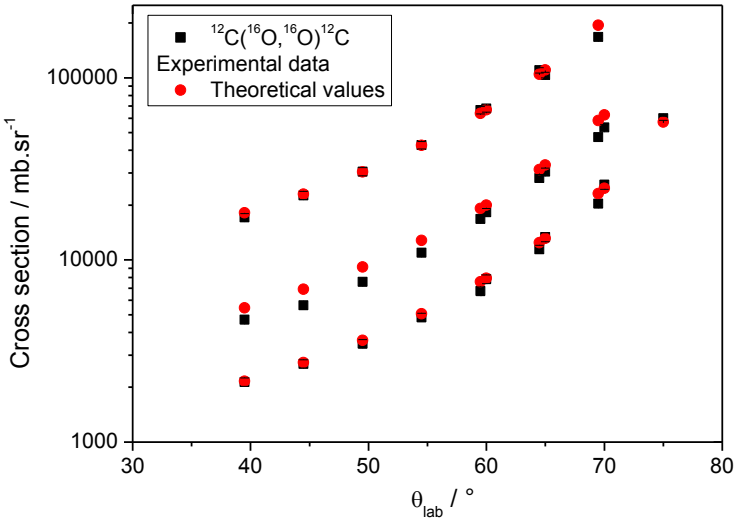

Figure 5.72) $^{12}C(^{16}O,^{16}O)^{12}C$ recoil cross section for E_{lab}=2783 keV, E_{lab}=5087 keV and E_{lab}=8087 keV.

The results obtained for $^{16}O+^{16}O$ elastic reaction, $^{16}O+^{12}C$ elastic reaction and $^{16}O+^{12}C$ recoil reaction represents the first attempt to use ^{16}O for nuclear purposes in LATR laboratory, opening new possibilities. The present results show that the use of ^{16}O beams is a feasible task in our laboratory not only for nuclear reactions purposes but also for elemental quantification of thin targets when needed. Despite the limited number of results obtained, either in energy and angle, these results provides a starting point for measurements using heavy ions. The experimental values obtained were close to expected ones. Also, the beam characterization and heavy ions interaction with detector gave reliable information for future measurements.

To improve the experimental setup available for heavy ions, a new ions source that can provide stable beams with high currents is required, a high resolution 90° H.E. analyzing magnet is needed and a detection setup with particle detection ($\Delta E - E$ detector) is desirable to allow particle identification. Such improvements can allow not only a new measurement of the elastic cross section but also the measurement of fusion cross section involving heavy ions.

5.5 References

[1] C.E. Rolfs, W.S. Rodney, Cauldrons in the Cosmos (The University of Chicago Press, 1988).

[2] K. Spyrou, C. Chromidou, S. Harissopulos, S. Kossionides, T. Paredellis, Z. Phys. A 357 (1997) 283.

[3] J. Cruz, PhD thesis, Lisboa 2006.

[4] F. Ajzenberg-Selove, Nucl. Phys. A523 (1991) 1.

[5] S. Mazzoni, M. Chiari, L. Giuntini, P. A. Mandò and N. Taccetti, Nucl. Instr. And Meth. B 136-138 (1998) 86-90.

[6] R. Amirikas, D.N. Jamieson and S.P. Dooley, Nucl. Instr. And Meth. B 77 (1993) 110.

[7] R. Salomonovi, Nucl. Instr. and Meth B 82 (1993) 1.

[8] G. Yang *et al*., Nucl. Instr. and Meth B 61 (1991) 175.

[9] A.R.L. Ramos, A. Paul, L. Rijniers, M.F. da Silva and J.C. Soares, Nucl. Instr. and Meth. B 190, 95 (2002).

[10] J.C. Armstrong, M.J. Baggett, W.R. Harris and V.A. Latorre, Physical Review 144 (1966) 823, data retrieved from the IBANDL database, IAEA, 2017, at http://www-nds.iaea.org/ibandl/.

[11] P. Hodgson, The Optical Model of Elastic Scattering, Oxford Univ. Press (Clarendon) London, 1963.

[12] A.F. Gurbich, Nucl. Instr. And Meth. B 136-138 (1998) 60-65.

[13] V.I. Zagrebaev *et al*. OM code of NRV, http://nrv.jinr.ru/nrv/.

[14] A.J. Koning *et al*., Nucl. Phys. A 713 (2003) 231.

[15] D.R. Tilley *et al*., Nucl. Phys. A 708 (2002) 3.

[16] J.A. Mccray, Jour. Physical Review 130 (1963) 2034, data retrieved from the IBANDL database, IAEA, 2017, at http://www-nds.iaea.org/ibandl/.

[17] H.J. Kim *et al*., Nuclear Data Tables A2 (1966) 353, data retrieved from the IBANDL database, IAEA, 2017, at http://www-nds.iaea.org/ibandl/.

[18] W.D. Harrison and A.B. Whitehead, Jour. Physical Review 132 (1963) 2607, data retrieved from the IBANDL database, IAEA, 2017, at http://www-nds.iaea.org/ibandl/.

[19] M. Haller, M. Betz, W. Kretschmer, A. Rauscher, R. Schmitt and W. Schuster, Nucl. Phys. A 496 (1989) 189-204, data retrieved from the IBANDL database, IAEA, 2017, at http://www-nds.iaea.org/ibandl/.

[20] P.R. Malmberg, Phys. Review 101 (1956) 114, data retrieved from the IBANDL database, IAEA, 2017, at http://www-nds.iaea.org/ibandl/.

[21] S. Ouichaoui, H. Beaumevieille, N. Bendjaballah, C. Chami, A. Dauchy, B. Chambon, D. Drain and C. Pastor, Il Nuovo Cimento 86 (1985) 170, data retrieved from the IBANDL database, IAEA, 2017, at http://www-nds.iaea.org/ibandl/.

[22] K.V. Karadzhev *et al*., Yadernaya Fizika 7 (1968) 242, data retrieved from the IBANDL database, IAEA, 2017, at http://www-nds.iaea.org/ibandl/.

[23] D.F. Fang, E.G. Bilpuch, C.R. Westerfeldt and G.E. Mitchell, Physical Review C 37 (1988) 28, data retrieved from the IBANDL database, IAEA, 2017, at http://www-nds.iaea.org/ibandl/.

[24] ORTEC Application Note 40, Heavy Ion Spectroscopy with Silicon Surface-Barrier Detectors.

[25] W. Pilz, J.V. Borany, R. Grötzschel, W. Jiang, M. Posselt and B. Schmidt, Nucl. Inst. Meth. Phys. Res. A 419 (1998) 137-145.

[26] J.A. Leavitt, L.C. McIntyre Jr., M.R. Weller, in: J.R. Tesmer, M. Nastasi (Eds.), Handbook of Modern Ion Beam Analysis, MRS, Pittsburgh, PA, 1995.

6

Chapter 6 - Conclusions

The $^{12}C(p,p)^{12}C$, $^{6}Li(p,p)^{6}Li$, $^{7}Li(p,p)^{7}Li$, $^{19}F(p,p)^{19}F$, $^{16}O(^{16}O,^{16}O)^{16}O$ and $^{12}C(^{16}O,^{16}O)^{12}C$ differential cross sections were measured for different scattering angles. The purpose was to obtain accurate cross sections to use as an input for optical model parameters calculations, especially at forward angles, where few datasets exists.

The $^{12}C(p,p)^{12}C$ differential cross section was measured for 8 scattering angles in the energy range from 1600 keV to 3900 keV. For θ_{lab}=90.0°, the differential cross section was obtained for two targets. The results from the present work showed a good agreement with the theoretical evaluation available for this nuclide, except for the 1734 keV resonance, were there is a shift in energy not explainable by energy calibration or target thickness corrections. Also, the position of the 1686 keV resonance in our measurements is in agreement with theoretical values available in the literature. For three energies, a comparison with optical model parameters was done, proving that these parameters are critically affected by the existence of data at low scattering angles. For carbon, the available optical parameters can reproduce the experimental data. At these energies, proton partial waves with $l_i \leq 3$ should be taken into consideration for the theoretical description of the entrance channel.

The $^{6}Li(p,p)^{6}Li$ differential cross section was measured for 2 scattering angles in the energy range from 996 keV to 2686 keV, for two targets. The data from the present work for θ_{lab}=90.0° is consistently higher than the previous ones for θ_{lab}=81.3° and θ_{lab}=80.5°. The position of the 1840 keV resonance was found correctly by our experimental data, but the obtained natural width was higher than the tabulated one. As the $^{6}Li(p,p)^{6}Li$ differential cross section was determined from the same spectra as the $^{7}Li(p,p)^{7}Li$ and $^{19}F(p,p)^{19}F$ differential cross sections (see below), in spite of the small ^{6}Li yield no uncertainties or experimental systematic deviation could be found to explain the discrepancies with previous data.

The $^{7}Li(p,p)^{7}Li$ differential cross section was measured for 2 different scattering angles in the energy range from 996 keV to 2686 keV, for two different targets. For θ_{lab}=90.0°, the differential cross section was obtained for 3 different targets. For this nuclide, our experimental data has replicated the shape of the differential cross section obtained by other authors. Data´s fitting has shown that the available optical model parameters do not replicate the experimental data, especially in the region near 90°, were the decrease in the theoretical cross section is not replicated by experimental data. Since for this nuclide an insertion of an absorptive potential is required, due to the presence of nuclear reactions, clearly improved optical model parameters are desirable to explain the experimental data.

The $^{19}F(p,p)^{19}F$ differential cross section was measured for 2 different scattering angles, θ_{lab}=69.5° and θ_{lab}=90.0°, in the energy range from 996 keV to 2588 keV, for one target. Angular distributions were measured for 6 energies. Experimental data was in agreement with the theoretical evaluation for this nuclide up to 1740 keV, but deviate from other author results for a similar scattering angle (θ_{lab}=69.38°). In this case, the optical model parameters available in the literature are in agreement with our experimental data. As for ^{12}C, a few number of orbital angular momentum l_i is required for the description of entrance channel.

The $^{16}O(^{16}O,^{16}O)^{16}O$ and $^{12}C(^{16}O,^{16}O)^{12}C$ differential cross section were measured for one energy for $^{16}O+^{16}O$ elastic scattering and for three energies for $^{16}O+^{12}C$ elastic scattering. The results obtained show that the scattering is purely Mott/Rutherford for these energies. In this case, in order to have differential cross sections at higher energies an improved experimental setup is required. Also, $^{12}C(^{16}O,^{16}O)^{12}C$ recoil cross section was measured for three energies.

Overall, the methodology applied in the present work for cross section measurement represented a starting point in the measurement of differential cross sections at forward angles with protons and oxygen ions. As future work, elastic scattering of protons can be extended to other light nuclides, such as ^{9}Be, ^{10}B and ^{11}B, for which there is no theoretical evaluation. From the theoretical point of view, further information on interactions concerning these nuclides will be obtained. From the analytical point of view, such "recommended" cross sections will give reliable information for material analysis. Furthermore, since it will cover a wide range of energies and scattering angles, the results will be of great interest and applicability for IBA community. Additionally, the results obtained for oxygen can be used as a starting point to measure both elastic and fusion cross sections in an energy range of interest for Nuclear Astrophysics.

Appendix A

A.1 Relationship of Kinematic Quantities in the Laboratory Coordinate system

If T_X is a target that is at rest in the laboratory we have:

$$\Leftrightarrow \begin{cases} Q = T_Y + T_b - T_a \\ p_a - p_b \cos\theta = p_Y \cos\xi \\ 0 = p_b \sin\theta - p_Y \sin\xi \end{cases} \Leftrightarrow$$

Putting the last two equations squared we obtain:

$$\Leftrightarrow \begin{cases} Q = T_Y + T_b - T_a \\ (p_a - p_b \cos\theta)^2 = (p_Y \cos\xi)^2 \\ (p_b \sin\theta)^2 = (p_Y \sin\xi)^2 \end{cases} \Leftrightarrow$$

Applying some algebra:

$$\Leftrightarrow \begin{cases} Q = T_Y + T_b - T_a \\ p_a^2 - 2p_a p_b \cos\theta + p_b^2 \cos^2\theta = p_Y^2 \cos^2\xi \\ p_b^2 \sin^2\theta = p_Y^2 \sin^2\xi \end{cases} \Leftrightarrow$$

As we know that $\sin^2\xi = 1 - \cos^2\xi$ we have that:

$$\Leftrightarrow \begin{cases} Q = T_Y + T_b - T_a \\ p_a^2 - 2p_a p_b \cos\theta + p_b^2 \cos^2\theta = p_Y^2 \cos^2\xi \\ p_b^2 \sin^2\theta = p_Y^2 (1 - \cos^2\xi) \end{cases} \Leftrightarrow$$

Again, we some algebra:

$$\Leftrightarrow \begin{cases} Q = T_Y + T_b - T_a \\ p_a^2 - 2p_a p_b \cos\theta + p_b^2 \cos^2\theta = p_Y^2 \cos^2\xi \\ p_b^2 \sin^2\theta = p_Y^2 - p_Y^2 \cos^2\xi \end{cases} \Leftrightarrow$$

$$\Leftrightarrow \begin{cases} Q = T_Y + T_b - T_a \\ p_a^2 - 2p_a p_b \cos\theta + p_b^2 \cos^2\theta = p_Y^2 \cos^2\xi \\ \dfrac{-p_b^2 \sin^2\theta + p_Y^2}{p_Y^2} = \cos^2\xi \end{cases} \Leftrightarrow$$

Substituting in the second equation the term $\cos^2\xi$:

$$\Leftrightarrow \begin{cases} Q = T_Y + T_b - T_a \\ p_a^2 - 2p_a p_b \cos\theta + p_b^2 \cos^2\theta = p_Y^2 \left(\dfrac{-p_b^2 \sin^2\theta + p_Y^2}{p_Y^2} \right) \\ \dfrac{-p_b^2 \sin^2\theta + p_Y^2}{p_Y^2} = \cos^2\xi \end{cases} \Leftrightarrow$$

Simplifying:

$$\Leftrightarrow \begin{cases} Q = T_Y + T_b - T_a \\ p_a^2 - 2p_a p_b \cos\theta + p_b^2 \cos^2\theta = -p_b^2 \sin^2\theta + p_Y^2 \\ \dfrac{-p_b^2 \sin^2\theta + p_Y^2}{p_Y^2} = \cos^2\xi \end{cases} \Leftrightarrow$$

$$\Leftrightarrow \begin{cases} Q = T_Y + T_b - T_a \\ p_a^2 - 2p_a p_b \cos\theta + p_b^2 \cos^2\theta + p_b^2 \sin^2\theta = p_Y^2 \\ \dfrac{-p_b^2 \sin^2\theta + p_Y^2}{p_Y^2} = \cos^2\xi \end{cases} \Leftrightarrow$$

$$\Leftrightarrow \begin{cases} Q = T_Y + T_b - T_a \\ p_a^2 - 2p_a p_b \cos\theta + p_b^2(\cos^2\theta + \sin^2\theta) = p_Y^2 \\ \dfrac{-p_b^2 \sin^2\theta + p_Y^2}{p_Y^2} = \cos^2\xi \end{cases} \Leftrightarrow$$

As $\cos^2\theta + \sin^2\theta = 1$, $p_Y^2 = 2m_Y E_Y$, $p_a^2 = 2m_a E_a$ e $p_b^2 = 2m_b E_b$:

$$\Leftrightarrow \begin{cases} Q = T_Y + T_b - T_a \\ 2m_a E_a - 2\sqrt{2m_a E_a 2m_b E_b}\cos\theta + 2m_b E_b = 2m_Y E_Y \\ \dfrac{-p_b^2 \sin^2\theta + p_Y^2}{p_Y^2} = \cos^2\xi \end{cases} \Leftrightarrow$$

Solving in order to E_Y:

$$\Leftrightarrow \begin{cases} Q = T_Y + T_b - T_a \\ \dfrac{m_a E_a - 2\sqrt{m_a E_a m_b E_b}\cos\theta + m_b E_b}{m_Y} = E_Y \\ \dfrac{-p_b^2 \sin^2\theta + p_Y^2}{p_Y^2} = \cos^2\xi \end{cases} \Leftrightarrow$$

Substituting in the first equation:

$$\Leftrightarrow \begin{cases} Q = \dfrac{m_a E_a - 2\sqrt{m_a E_a m_b E_b}\cos\theta + m_b E_b}{m_Y} + E_b - E_a \\ \dfrac{m_a E_a - 2\sqrt{m_a E_a m_b E_b}\cos\theta + m_b E_b}{m_Y} = E_Y \\ \dfrac{-p_b^2 \sin^2\theta + p_Y^2}{p_Y^2} = \cos^2\xi \end{cases} \Leftrightarrow$$

Simplifying:

$$Q = \frac{m_a E_a}{m_Y} - \frac{2\sqrt{m_a E_a m_b E_b}}{m_Y}\cos\theta + m_b E_b + E_b - E_a \Leftrightarrow$$

$$\Leftrightarrow Q = -E_a\left(1 - \frac{m_a}{m_Y}\right) + E_b\left(1 + \frac{m_b}{m_Y}\right) - \frac{2\sqrt{m_a E_a m_b E_b}}{m_Y}\cos\theta$$

Rewriting the previous expression:

$$0 = -\left(Q + E_a\left(1 - \frac{m_a}{m_Y}\right)\right) + E_b\left(1 + \frac{m_b}{m_Y}\right) - \frac{2\sqrt{E_b}\sqrt{m_a E_a m_b}}{m_Y}\cos\theta$$

Making the variable change $y = \sqrt{E_b}$ and applying the solver formula:

$$\sqrt{E_b} = \frac{\frac{2\sqrt{m_a E_a m_b}}{m_Y}\cos\theta \pm \sqrt{\left(\frac{2\sqrt{m_a E_a m_b}}{m_Y}\cos\theta\right)^2 + 4\left(1 + \frac{m_b}{m_Y}\right)\left(Q + E_a\left(1 - \frac{m_a}{m_Y}\right)\right)}}{2 \times \left(1 + \frac{m_b}{m_Y}\right)} \Leftrightarrow$$

$$\Leftrightarrow \sqrt{E_b} = \frac{\sqrt{m_a E_a m_b}\cos\theta \pm \sqrt{m_a E_a m_b \cos^2\theta + (m_Y + m_b)\left(m_Y Q + E_a(m_Y - m_a)\right)}}{m_Y + m_b} \quad \text{A.1}$$

A.2 Change in linear momentum

$$\overrightarrow{\Delta p} = \overrightarrow{p_f} - \overrightarrow{p_f}$$

$$\Delta p^2 = {p_i}^2 + {p_f}^2 - 2p_i p_f \cos\theta \ (p_i = p_f)$$

$$\Delta p^2 = 2{p_i}^2 - 2{p_i}^2\cos\theta$$

$$= 2{p_i}^2(1 - \cos\theta)$$

$$\Delta p = \pm\left(4{p_i}^2\frac{1 - \cos\theta}{2}\right)^{\frac{1}{2}} \quad \text{A.2}$$

A.3 Solutions of the Schrodinger equation in three dimensions

The three-dimensional time-independent Schrodinger equation in Cartesian coordinates is given by:

$$\frac{\hbar}{2m}\left(\frac{\partial^2\psi}{\partial x^2} + \frac{\partial^2\psi}{\partial y^2} + \frac{\partial^2\psi}{\partial z^2}\right) + V(x,y,z)\psi = E\psi \quad \text{A.3}$$

being ψ the total wave function, V the potential, E the total energy and m the particle mass. Usually, the potential depends on the magnitude of the radius vector, but not on its direction, $V(\vec{r}) = V(r)$. Considering this kind of potentials and taking advantage of the symmetry, we

can replace the Cartesian coordinates x, y and z by the spherical coordinates r, θ and ϕ. The wave function for a central potential is then separable in three different equations:

$$\psi(r,\theta,\phi) = R(r)\Theta(\theta)\Phi(\phi) \qquad \text{A.4}$$

The Schrodinger equation is then separable as well and we obtain three different equations, one for each of the variables. The differential equation for Φ is:

$$\frac{d^2\Phi}{d\phi^2} + m_l^2\Phi = 0 \qquad \text{A.5}$$

where m_l^2 is the separation constant. The solution is

$$\Phi_{m_l}(\phi) = \frac{1}{\sqrt{2\pi}} e^{im_l\phi} \qquad \text{A.6}$$

with $m_l = 0, \pm1, \pm2$, ..., and so on. The quantity m_l is called *quantum magnetic number*. The equation for Θ is given by:

$$\frac{1}{\sin\theta}\frac{d}{d\theta}\left(\sin\theta\frac{d\Theta}{d\theta}\right) + \left[l(l+1) - \frac{m_l^2}{\sin^2\theta}\right]\Theta = 0 \qquad \text{A.7}$$

with $l = 0,1,2,\ldots$ and $m_l = 0, \pm1, \ldots, \pm l$. The quantity l is called the *orbital angular momentum quantum number*. The solutions can be expressed in terms of the *associated Legendre Polynomials*, $P_l^{m_l}$:

$$\Theta_{lm_l}(\theta) = \sqrt{\frac{(2l+1)}{2}\frac{(l-m_l)!}{(l+m_l)!}} P_l^{m_l}(\theta) \qquad \text{A.8}$$

The product of the two angle-dependent functions gives the *spherical harmonics*.

$$Y_{lm_l}(\theta,\phi) = \Theta_{lm_l}(\theta)\Phi_{m_l}(\phi) \qquad \text{A.9}$$

which describe the angular part of a wave function for any central potential.

The parity π of a function describe the behaviour under the coordinates transformation $\vec{r} \to -\vec{r}$ (space reflection), or in polar coordinates $r \to r$, $\theta \to \pi - \theta$, $\phi \to \pi + \phi$. Since two such transformations must yield again the original function ($\pi^2 = 1$), the parity can possess only the values $\pi = +1$ (positive or "even" parity) and $\pi = -1$ (negative or "odd" parity). The spherical harmonics have the important property

$$Y_{lm_l}(\pi-\theta,\pi+\phi)=(-1)^l Y_{lm_l}(\theta,\phi) \qquad \text{A.10}$$

And hence the parity is even or odd for l even or odd, respectively. Usually, Y_{lm_l} functions are complex valued. For the special case when $m_l=0$ the spherical harmonics are real valued and we obtain:

$$Y_{l0}(\theta,\phi)=\sqrt{\frac{(2l+1)}{4\pi}}P_l(\cos\theta) \qquad \text{A.11}$$

where the functions $P_l(\cos\theta)$ are called *Legendre Polynomials*. For the lowest values of l they are given by:

$$P_0(x)=1$$

$$P_1(x)=x$$

$$P_2(x)=\frac{1}{2}(3x^2-1)$$

$$P_3(x)=\frac{1}{2}(5x^3-3x)$$

$$P_4(x)=\frac{1}{8}(35x^4-30x^2+3) \qquad \text{A.12}$$

The equation for the radial function R is given by:

$$-\frac{\hbar}{2m}\left(\frac{d^2R}{dr^2}+\frac{2}{r}\frac{dR}{dr}\right)+\left[V(r)+\frac{l(l+1)\hbar^2}{2mr^2}\right]R=ER \qquad \text{A.13}$$

Only the radial function depends in the central potential. The term $l(l+1)$ is called the *centripetal potential*, which keeps the particle away from the origin when $l>0$. It is possible to rewrite the radial equation by substituting $u(r)=rR(r)$, and we obtain:

$$\frac{d^2u}{dr^2}+\frac{2m}{\hbar}\left[E-V(r)-\frac{l(l+1)\hbar^2}{2mr^2}\right]u=0 \qquad \text{A.14}$$

It is possible to write $E=\frac{p^2}{2m}=\frac{\hbar^2k^2}{2m}$, where k is the wave number of the free particle. Applied to nuclear scattering, this equation is only valid for distances larger than the nuclear radius

($r > R$), since the motion inside the nucleus cannot be described by a wave function which depends on only one coordinate.

A.4 Quantum Mechanical Selection Rules

If we consider a system composed by two parts with angular momentum vector $\overrightarrow{J_1}$ and $\overrightarrow{J_2}$. The components have eigenfunctions $\phi_{j_1 m_1}$ and $\phi_{j_2 m_2}$ that are labeled according to the total angular momentum quantum numbers j_1 and j_2. The z-components of their total angular momenta are labeled by the quantum magnetic numbers m_1 and m_2, where

$$m_i = -j_i, -j_i + 1, \dots, j_i - 1, j_i \qquad \text{A.15}$$

The system of angular momentum $\vec{J}$ has an eigenfunction Φ_{JM} labeled according to the total angular momentum quantum number J and the magnetic quantum number M. The eigenfunction can be expanded according to

$$\Phi_{JM}(j_1, j_2) = \sum_{m_1, m_2} (j_1 m_1 j_2 m_2 | JM) \phi_{j_1 m_1} \phi_{j_2 m_2} \qquad \text{A.16}$$

The amplitudes $(j_1 m_1 j_2 m_2 | JM)$ are called *Clebsch-Gordan coefficients*. Their squares represents the probability to find the coupled state $\Phi_{JM}(j_1, j_2)$ in the product state $\phi_{j_1 m_1} \phi_{j_2 m_2}$. This coefficients have important symmetry properties. The coupling of angular momentum vectors, $\vec{J} = \overrightarrow{J_1} + \overrightarrow{J_2}$, must obey to the following rules:

$$|j_1 - j_2| \leq J \leq j_1 + j_2 \qquad \text{A.17}$$

$$M = m_1 + m_2 = -J, -J + 1, \dots, J - 1, J \qquad \text{A.18}$$

In a nuclear reaction, the total angular momentum $\vec{J}$ and the total parity Π are conserved. While $\vec{J}$ is given by the above quantum mechanical rules of angular momentum coupling, the total parity of the system is given by the product of the parities of individual parts. If a channel contains two nuclei 1 and 2 with spins j_1 and j_2 and parities π_1 and π_2, then $\vec{J}$ and Π are given by:

$$\vec{J} = \vec{l} + \overrightarrow{J_1} + \overrightarrow{J_2} = \vec{l} + \vec{s} \qquad \text{A.19}$$

$$\Pi = \pi_1 \pi_2 (-1)^l \qquad \text{A.20}$$

where $l = 0,1,2,3,...$ and is the relative orbital angular momentum of the pair of nuclei and the vector $\vec{s}$ is the *channel spin*.

Appendix B

B.1 $^{12}C(p,p)^{12}C$ differential cross sections

Target: ^{129}Xe implanted in ^{12}C								
$\boldsymbol{\theta_{lab} = 45.0°}$								
$\boldsymbol{E_{eff}}$ $(\boldsymbol{keV})$	$d\sigma/d\theta$ $(mb.sr^{-1})$	$\delta\,(d\sigma/d\theta)$ $(mb.sr^{-1})$	E_{eff} (keV)	$d\sigma/d\theta$ $(mb.sr^{-1})$	$\delta\,(d\sigma/d\theta)$ $(mb.sr^{-1})$	E_{eff} (keV)	$d\sigma/d\theta$ $(mb.sr^{-1})$	$\delta\,(d\sigma/d\theta)$ $(mb.sr^{-1})$
1606	564	28	1739	1999	98	2032	618	31
1606	564	28	1742	1964	97	2061	587	29
1606	572	31	1745	1908	94	2090	571	29
1625	540	27	1747	1879	93	2121	551	28
1634	600	32	1750	1792	88	2151	527	26
1645	589	29	1762	1496	74	2180	512	26
1656	726	39	1783	1200	59	2210	492	25
1665	816	40	1803	1042	52	2238	486	24
1674	1147	61	1823	941	47	2278	471	24
1685	1484	73	1846	862	43	2318	445	22
1693	1785	94	1862	815	40	2357	429	22
1705	1914	94	1884	785	39	2398	420	21
1715	1985	104	1903	752	37	2447	371	20
1723	2008	99	1925	711	35	2496	370	20
1728	2116	111	1946	691	34	2546	356	19
1735	2068	102	1962	679	34	2594	342	19
1735	2090	103	1982	657	33	2645	329	18
1735	2075	102	2001	642	32			
1737	2052	101	2032	613	31			

Table B.1) $^{12}C(p,p)^{12}C$ differential cross section for θ_{lab}=45.0°.

Target: ^{129}Xe implanted in ^{12}C								
$\boldsymbol{\theta_{lab} = 55.0°}$								
$\boldsymbol{E_{eff}}$ $(\boldsymbol{keV})$	$d\sigma/d\theta$ $(mb.sr^{-1})$	$\delta\,(d\sigma/d\theta)$ $(mb.sr^{-1})$	E_{eff} (keV)	$d\sigma/d\theta$ $(mb.sr^{-1})$	$\delta\,(d\sigma/d\theta)$ $(mb.sr^{-1})$	E_{eff} (keV)	$d\sigma/d\theta$ $(mb.sr^{-1})$	$\delta\,(d\sigma/d\theta)$ $(mb.sr^{-1})$
1606	380	20	1823	482	24	2398	254	13
1625	384	19	1846	449	23	2447	244	13
1634	435	23	1862	433	22	2496	223	12
1645	443	22	1884	426	21	2546	212	12
1656	556	30	1903	401	20	2594	208	11
1665	645	32	1925	393	20	2645	207	11
1674	869	46	1946	377	19	2694	196	11
1685	1068	53	1962	365	19	2743	190	10
1693	1196	63	1962	368	19	2791	184	10
1705	1152	57	1982	367	19	2843	177	10
1715	1114	59	2000	347	19	2892	172	10
1723	1020	50	2001	363	18	2941	165	9
1728	1029	55	2032	345	17	2991	159	9
1734	946	47	2061	337	17	2991	150	8
1735	932	46	2090	330	17	3039	155	9
1737	926	46	2121	323	16	3089	153	9
1739	923	46	2151	303	15	3139	147	8
1742	874	43	2180	293	15	3189	145	8
1745	845	42	2210	284	15	3238	144	8
1747	815	41	2238	280	14	3287	142	8
1750	798	40	2278	271	14	3336	139	8
1762	683	34	2318	264	13	3385	135	8
1783	580	29	2357	253	13			
1803	523	26	2397	238	13			

Table B.2) ^{12}C(p,p)^{12}C differential cross section for θ_{lab}=55.0°.

Target: ^{129}Xe implanted in ^{12}C								
$\boldsymbol{\theta_{lab} = 62.7°}$								
$\boldsymbol{E_{eff}}$ $(\boldsymbol{keV})$	$d\sigma/d\theta$ $(mb.sr^{-1})$	$\delta\,(d\sigma/d\theta)$ $(mb.sr^{-1})$	E_{eff} (keV)	$d\sigma/d\theta$ $(mb.sr^{-1})$	$\delta\,(d\sigma/d\theta)$ $(mb.sr^{-1})$	E_{eff} (keV)	$d\sigma/d\theta$ $(mb.sr^{-1})$	$\delta\,(d\sigma/d\theta)$ $(mb.sr^{-1})$
1606	283	14	1745	468	23	2090	235	12
1606	282	15	1747	448	22	2121	229	12
1625	292	15	1750	447	23	2151	227	12
1634	331	18	1762	409	21	2180	215	11
1645	335	17	1783	372	19	2210	210	11
1656	419	22	1803	348	18	2238	193	10
1665	484	24	1823	330	17	2238	196	10
1674	621	33	1846	310	16	2278	189	10
1685	731	36	1862	299	15	2278	206	11
1693	788	42	1884	295	15	2318	193	10
1705	715	36	1903	287	15	2357	190	10
1715	659	35	1925	276	14	2398	188	10
1723	560	28	1946	269	14	2447	168	11
1728	556	30	1962	268	14	2496	172	10
1735	497	25	1982	261	13	2544	163	9
1737	486	24	2001	251	13	2544	165	9
1739	481	24	2032	245	13	2594	159	9
1742	479	24	2061	240	12	2647	152	9

Table B.3) ^{12}C(p,p)^{12}C differential cross section for θ_{lab}=62.7°.

~

Target: ^{129}Xe implanted in ^{12}C								
$\boldsymbol{\theta_{lab} = 67.3°}$								
$\boldsymbol{E_{eff}}$ $(\boldsymbol{keV})$	$d\sigma/d\theta$ $(mb.sr^{-1})$	$\delta\,(d\sigma/d\theta)$ $(mb.sr^{-1})$	E_{eff} (keV)	$d\sigma/d\theta$ $(mb.sr^{-1})$	$\delta\,(d\sigma/d\theta)$ $(mb.sr^{-1})$	E_{eff} (keV)	$d\sigma/d\theta$ $(mb.sr^{-1})$	$\delta\,(d\sigma/d\theta)$ $(mb.sr^{-1})$
1606	267	14	1745	328	17	2397	174	10
1606	268	15	1747	328	17	2398	186	10
1625	277	15	1750	332	17	2447	158	11
1634	302	16	1762	336	17	2496	166	9
1645	315	16	1783	332	17	2496	166	9
1656	384	21	1803	320	16	2546	159	9
1665	427	21	1823	306	16	2594	155	9
1674	529	28	1846	290	15	2645	154	9
1685	592	30	1862	285	15	2694	142	8
1685	600	30	1862	287	15	2743	137	8
1693	631	34	1884	278	14	2791	134	8
1705	516	26	1903	271	14	2843	135	8
1711	474	24	1925	264	14	2892	130	7
1714	435	22	1946	252	13	2941	127	7
1715	446	24	1946	252	13	2991	121	7
1717	410	21	1946	252	13	2991	114	8
1719	394	20	1962	253	13	2991	114	7
1720	380	19	1982	252	13	3039	120	7
1723	365	19	2000	230	13	3089	116	7
1723	362	19	2001	244	13	3139	113	7
1724	351	18	2032	234	12	3189	109	6
1725	347	18	2061	230	12	3238	114	7
1727	332	17	2090	230	12	3287	110	6
1728	347	19	2121	220	11	3336	109	6
1730	324	16	2151	212	11	3385	105	6
1732	313	16	2180	207	11	3437	96	6
1734	314	16	2210	204	11	3484	95	6
1735	316	16	2238	197	10	3535	95	6
1737	314	16	2278	198	10	3584	94	6
1739	313	16	2318	190	10			
1742	318	16	2357	188	10			

Table B.4) ^{12}C(p,p)^{12}C differential cross section for θ_{lab}=67.3°.

Target: ^{129}Xe implanted in ^{12}C								
$\boldsymbol{\theta_{lab} = 67.7°}$								
$\boldsymbol{E_{eff}}$ $(\boldsymbol{keV})$	$d\sigma/d\theta$ $(mb.sr^{-1})$	$\delta\,(d\sigma/d\theta)$ $(mb.sr^{-1})$	E_{eff} (keV)	$d\sigma/d\theta$ $(mb.sr^{-1})$	$\delta\,(d\sigma/d\theta)$ $(mb.sr^{-1})$	E_{eff} (keV)	$d\sigma/d\theta$ $(mb.sr^{-1})$	$\delta\,(d\sigma/d\theta)$ $(mb.sr^{-1})$
1606	244	13	1739	315	16	2032	221	11
1606	252	13	1742	310	16	2061	219	11
1606	252	14	1745	308	16	2090	211	11
1625	257	13	1747	316	16	2121	207	11
1634	290	16	1750	321	16	2151	199	10
1645	293	15	1762	318	16	2180	192	10
1656	358	19	1783	307	16	2210	191	10
1665	402	20	1803	297	15	2238	192	10
1674	510	27	1823	283	14	2278	183	10
1685	586	29	1846	276	14	2318	172	9
1693	616	33	1862	268	14	2357	172	9
1705	510	26	1884	263	13	2398	168	9
1715	441	24	1903	253	13	2447	155	9
1723	368	18	1925	242	12	2496	155	9
1728	348	19	1946	240	12	2546	150	8
1735	314	16	1962	240	12	2594	146	8
1735	311	16	1982	230	12	2645	142	8
1735	314	16	2001	229	12			
1737	313	16	2032	220	11			

Table B.5) ^{12}C(p,p)^{12}C differential cross section for θ_{lab}=67.7°.

Target: ^{129}Xe implanted in ^{12}C								
$\boldsymbol{\theta_{lab} = 72.7°}$								
$\boldsymbol{E_{eff}}$ $(\boldsymbol{keV})$	$d\sigma/d\theta$ $(mb.sr^{-1})$	$\delta\,(d\sigma/d\theta)$ $(mb.sr^{-1})$	E_{eff} (keV)	$d\sigma/d\theta$ $(mb.sr^{-1})$	$\delta\,(d\sigma/d\theta)$ $(mb.sr^{-1})$	E_{eff} (keV)	$d\sigma/d\theta$ $(mb.sr^{-1})$	$\delta\,(d\sigma/d\theta)$ $(mb.sr^{-1})$
1606	222	12	1745	234	12	2061	202	10
1625	227	12	1747	242	12	2090	197	10
1634	252	13	1750	252	13	2121	192	10
1645	253	13	1750	251	13	2151	185	10
1656	323	16	1762	273	14	2180	181	9
1665	333	17	1783	280	14	2210	179	9
1674	430	22	1803	264	13	2238	175	9
1685	440	22	1823	259	13	2278	174	9
1693	487	24	1846	249	13	2318	165	9
1705	355	18	1862	244	12	2357	159	8
1715	311	16	1884	244	12	2398	165	9
1723	220	11	1903	237	12	2447	149	8
1728	229	12	1925	228	12	2496	148	8
1734	203	10	1946	221	11	2546	140	8
1735	205	11	1962	221	11	2594	133	8
1737	213	11	1982	214	11	2645	135	8
1739	218	11	2001	213	11	2645	135	8
1742	225	12	2032	200	10			

Table B.6) ^{12}C(p,p)^{12}C differential cross section for θ_{lab}=72.7°.

Target: ^{129}Xe implanted in ^{12}C								
$\boldsymbol{\theta_{lab} = 77.7°}$								
$\boldsymbol{E_{eff}}$ $(\boldsymbol{keV})$	$d\sigma/d\theta$ $(mb.sr^{-1})$	$\delta\,(d\sigma/d\theta)$ $(mb.sr^{-1})$	E_{eff} (keV)	$d\sigma/d\theta$ $(mb.sr^{-1})$	$\delta\,(d\sigma/d\theta)$ $(mb.sr^{-1})$	E_{eff} (keV)	$d\sigma/d\theta$ $(mb.sr^{-1})$	$\delta\,(d\sigma/d\theta)$ $(mb.sr^{-1})$
1606	199	11	1823	249	13	2397	147	8
1625	196	10	1846	237	12	2398	156	8
1634	217	12	1862	232	12	2447	143	8
1645	215	11	1884	228	12	2496	143	8
1656	249	14	1903	220	11	2546	136	8
1665	274	14	1925	213	11	2594	132	8
1674	317	17	1946	211	11	2645	133	8
1685	334	17	1962	205	11	2694	121	7
1693	329	18	1962	203	10	2743	125	7
1705	236	12	1982	203	10	2791	119	7
1715	179	10	2000	197	11	2843	115	7
1723	137	7	2001	202	10	2892	113	6
1728	130	7	2032	198	10	2941	111	6
1735	150	8	2061	193	10	2991	106	6
1737	159	8	2090	187	10	2991	100	6
1739	167	9	2121	183	10	3039	105	6
1742	181	9	2151	177	9	3089	104	6
1745	200	10	2180	175	9	3139	100	6
1747	216	11	2210	171	9	3189	96	6
1750	225	12	2238	169	9	3238	96	6
1762	257	13	2278	166	9	3287	94	6
1783	261	13	2318	160	8	3336	90	5
1803	263	13	2357	157	8	3385	89	5

Table B.7) ^{12}C(p,p)^{12}C differential cross section for θ_{lab}=77.7°.

Target: ^{129}Xe implanted in ^{12}C								
$\boldsymbol{\theta_{lab} = 90.0°}$								
$\boldsymbol{E_{eff}}$ $(\boldsymbol{keV})$	$d\sigma/d\theta$ $(mb.sr^{-1})$	$\delta\,(d\sigma/d\theta)$ $(mb.sr^{-1})$	E_{eff} (keV)	$d\sigma/d\theta$ $(mb.sr^{-1})$	$\delta\,(d\sigma/d\theta)$ $(mb.sr^{-1})$	E_{eff} (keV)	$d\sigma/d\theta$ $(mb.sr^{-1})$	$\delta\,(d\sigma/d\theta)$ $(mb.sr^{-1})$
1606	156	8	1747	213	11	2447	133	8
1606	153	9	1750	225	12	2496	134	8
1625	149	8	1762	253	13	2496	129	7
1634	152	9	1783	258	13	2546	127	7
1645	148	8	1803	243	12	2594	127	7
1656	158	9	1823	233	12	2645	124	7
1665	158	8	1846	221	11	2694	115	7
1674	165	9	1862	212	11	2743	114	7
1685	157	8	1862	222	11	2791	113	7
1685	155	8	1884	204	10	2843	111	6
1693	132	7	1903	205	11	2892	108	6
1705	80	4	1925	193	10	2941	106	6
1711	60	4	1946	194	10	2991	101	6
1714	53	3	1946	187	10	2991	96	6
1715	51	3	1946	189	10	2991	98	6
1717	49	3	1962	187	10	3039	100	6
1719	46	3	1982	189	10	3089	100	6
1720	47	3	2000	173	10	3139	98	6
1723	52	3	2001	184	10	3189	97	6
1723	53	3	2032	175	9	3238	96	6
1724	56	3	2061	171	9	3287	94	6
1725	59	3	2090	174	9	3336	90	5
1727	66	4	2121	170	9	3385	88	5
1728	68	4	2151	161	8	3437	85	5
1730	84	5	2180	159	8	3484	83	5
1732	98	5	2210	157	8	3535	84	5
1734	107	6	2238	161	8	3584	78	5
1735	115	6	2278	156	8	3633	78	5
1737	136	7	2318	148	8	3682	76	5
1739	152	8	2357	150	8	3733	75	5
1742	173	9	2397	138	8	3781	72	4
1745	197	10	2398	146	8			

Table B.8) ^{12}C(p,p)^{12}C differential cross section for θ_{lab}=90.0°.

Target: Li_2WO_4 evaporated on ^{12}C								
$\boldsymbol{\theta_{lab} = 90.0°}$								
$\boldsymbol{E_{eff}}$ $(\boldsymbol{keV})$	$d\sigma/d\theta$ $(mb.sr^{-1})$	$\delta\,(d\sigma/d\theta)$ $(mb.sr^{-1})$	E_{eff} (keV)	$d\sigma/d\theta$ $(mb.sr^{-1})$	$\delta\,(d\sigma/d\theta)$ $(mb.sr^{-1})$	E_{eff} (keV)	$d\sigma/d\theta$ $(mb.sr^{-1})$	$\delta\,(d\sigma/d\theta)$ $(mb.sr^{-1})$
1607	156	13	1703	89	8	1744	189	16
1625	148	12	1714	53	5	1753	249	20
1646	150	12	1720	48	5	1765	256	21
1667	151	12	1727	64	6	1775	261	21
1687	147	12	1732	94	8	1787	253	20
1696	122	10	1736	128	11	1806	238	19

Table B.9) $^{12}C(p,p)^{12}C$ differential cross section for θ_{lab}=90.0°.

B.2 ^{6}Li(p,p)^{6}Li differential cross sections

Target: LiF evaporated on ^{12}C implanted with ^{129}Xe								
$\boldsymbol{\theta_{lab} = 69.5°}$								
$\boldsymbol{E_{eff}}$ $(\boldsymbol{keV})$	$d\sigma/d\theta$ $(mb.sr^{-1})$	$\delta\,(d\sigma/d\theta)$ $(mb.sr^{-1})$	E_{eff} (keV)	$d\sigma/d\theta$ $(mb.sr^{-1})$	$\delta\,(d\sigma/d\theta)$ $(mb.sr^{-1})$	E_{eff} (keV)	$d\sigma/d\theta$ $(mb.sr^{-1})$	$\delta\,(d\sigma/d\theta)$ $(mb.sr^{-1})$
996	460	32	1576	179	9	2072	207	11
1018	475	32	1595	182	9	2091	191	10
1039	395	28	1596	178	10	2093	188	10
1057	376	27	1596	185	10	2112	189	10
1079	343	25	1615	199	10	2131	173	9
1098	300	24	1615	199	10	2151	166	9
1098	305	23	1634	203	10	2172	163	8
1118	300	15	1655	211	11	2191	159	8
1137	263	13	1675	228	12	2192	160	9
1157	231	12	1694	240	12	2211	161	8
1177	218	11	1715	239	12	2211	156	8
1197	209	11	1735	235	12	2231	146	8
1218	179	9	1755	248	13	2251	148	8
1237	178	9	1774	235	12	2271	145	8
1258	175	10	1794	223	12	2290	144	8
1277	174	17	1794	249	12	2311	143	8
1297	153	8	1795	260	13	2330	140	7
1318	156	16	1814	257	13	2350	145	8
1318	150	8	1833	253	13	2370	147	8
1336	151	8	1854	250	13	2389	145	8
1357	147	8	1873	265	13	2390	151	8
1376	154	9	1894	249	13	2409	132	7
1396	133	7	1913	242	12	2428	126	7
1415	139	7	1934	227	11	2449	131	7
1437	140	7	1952	225	11	2469	131	7
1456	136	7	1972	222	11	2488	129	7
1475	150	8	1992	199	11	2508	133	7
1496	154	8	1992	224	11	2528	127	7
1516	171	9	2012	209	11	2547	123	7
1536	168	9	2031	211	11	2588	124	7
1556	177	9	2052	192	10			

Table B.10) ^{6}Li(p,p)^{6}Li differential cross section for θ_{lab}=69.5°.

Target: LiCl evaporated on ^{12}C								
$\boldsymbol{\theta_{lab} = 69.5°}$								
$\boldsymbol{E_{eff}}$ $(\boldsymbol{keV})$	$d\sigma/d\theta$ $(mb.sr^{-1})$	$\delta\,(d\sigma/d\theta)$ $(mb.sr^{-1})$	E_{eff} (keV)	$d\sigma/d\theta$ $(mb.sr^{-1})$	$\delta\,(d\sigma/d\theta)$ $(mb.sr^{-1})$	E_{eff} (keV)	$d\sigma/d\theta$ $(mb.sr^{-1})$	$\delta\,(d\sigma/d\theta)$ $(mb.sr^{-1})$
1271	187	11	1754	217	12	2339	144	9
1310	147	10	1797	231	13	2383	148	10
1350	136	9	1843	223	13	2424	156	10
1392	133	9	1883	239	14	2467	114	8
1435	142	9	1929	209	12	2491	138	9
1476	145	9	1975	192	11	2518	115	8
1517	152	9	2017	196	12	2561	110	8
1592	176	10	2063	197	12	2595	114	8
1592	176	11	2114	172	11	2644	117	8
1630	191	11	2165	160	10	2686	114	8
1672	209	12	2208	170	11			
1713	217	13	2255	159	10			

Table B.11) ^{6}Li(p,p)^{6}Li differential cross section for θ_{lab}=69.5°.

Target: LiCl evaporated on ^{12}C								
$\boldsymbol{\theta_{lab} = 90.0°}$								
$\boldsymbol{E_{eff}}$ $(\boldsymbol{keV})$	$d\sigma/d\theta$ $(mb.sr^{-1})$	$\delta\,(d\sigma/d\theta)$ $(mb.sr^{-1})$	E_{eff} (keV)	$d\sigma/d\theta$ $(mb.sr^{-1})$	$\delta\,(d\sigma/d\theta)$ $(mb.sr^{-1})$	E_{eff} (keV)	$d\sigma/d\theta$ $(mb.sr^{-1})$	$\delta\,(d\sigma/d\theta)$ $(mb.sr^{-1})$
1102	173	8	1630	133	7	2255	90	5
1138	146	7	1672	139	7	2295	83	5
1171	128	7	1713	153	8	2339	80	5
1232	117	6	1754	167	8	2383	80	5
1271	107	6	1797	163	8	2424	77	5
1310	83	5	1843	170	8	2467	69	5
1350	69	5	1883	167	8	2491	65	5
1392	91	5	1929	156	8	2518	65	4
1435	105	6	1975	141	7	2561	63	4
1476	100	6	2017	140	7	2595	63	4
1517	111	6	2063	126	7	2644	58	4
1553	128	7	2114	117	6	2686	57	4
1592	125	6	2165	102	6			
1592	137	7	2208	94	6			

Table B.12) ^{6}Li(p,p)^{6}Li differential cross section for θ_{lab}=90.0°.

Target: LiF evaporated on ^{12}C implanted with ^{129}Xe								
$\boldsymbol{\theta_{lab} = 90.0°}$								
$\boldsymbol{E_{eff}}$ $(\boldsymbol{keV})$	$d\sigma/d\theta$ $(mb.sr^{-1})$	$\delta\,(d\sigma/d\theta)$ $(mb.sr^{-1})$	E_{eff} (keV)	$d\sigma/d\theta$ $(mb.sr^{-1})$	$\delta\,(d\sigma/d\theta)$ $(mb.sr^{-1})$	E_{eff} (keV)	$d\sigma/d\theta$ $(mb.sr^{-1})$	$\delta\,(d\sigma/d\theta)$ $(mb.sr^{-1})$
1218	110	7	1675	146	8	2131	96	5
1237	114	7	1694	164	9	2151	91	5
1258	101	7	1715	153	8	2172	83	4
1277	100	6	1735	146	8	2191	84	5
1297	108	6	1755	155	8	2192	85	5
1318	109	6	1774	147	8	2211	84	5
1318	86	5	1794	129	8	2211	84	5
1336	100	6	1794	162	9	2231	91	5
1357	117	6	1795	159	9	2251	78	4
1376	103	6	1814	151	8	2271	83	4
1396	93	5	1833	157	9	2290	84	5
1415	107	6	1854	163	9	2311	77	4
1437	103	6	1873	155	10	2330	84	5
1456	107	6	1894	151	8	2350	82	4
1475	108	6	1913	146	9	2370	70	4
1496	111	6	1934	143	8	2389	75	4
1516	120	6	1952	133	7	2390	85	5
1536	117	6	1972	133	7	2409	68	4
1556	125	6	1992	138	8	2428	72	4
1576	121	7	1992	125	9	2449	74	4
1595	116	6	2012	122	7	2469	77	4
1596	104	6	2031	122	6	2488	75	4
1596	132	7	2052	120	6	2508	72	4
1615	142	8	2072	111	6	2528	71	4
1615	138	7	2091	103	6	2547	67	4
1634	137	7	2093	101	5	2588	65	4
1655	137	7	2112	104	6			

Table B.13) $^{6}Li(p,p)^{6}Li$ differential cross section for θ_{lab}=90.0°.

B.3 ^{7}Li(p,p)^{7}Li differential cross sections

Target: LiF evaporated on ^{12}C implanted with ^{129}Xe								
$\boldsymbol{\theta_{lab} = 69.5°}$								
$\boldsymbol{E_{eff}}$ $(\boldsymbol{keV})$	$d\sigma/d\theta$ $(mb.sr^{-1})$	$\delta\,(d\sigma/d\theta)$ $(mb.sr^{-1})$	E_{eff} (keV)	$d\sigma/d\theta$ $(mb.sr^{-1})$	$\delta\,(d\sigma/d\theta)$ $(mb.sr^{-1})$	E_{eff} (keV)	$d\sigma/d\theta$ $(mb.sr^{-1})$	$\delta\,(d\sigma/d\theta)$ $(mb.sr^{-1})$
996	177	9	1576	63	3	2072	113	6
1018	148	8	1595	64	4	2091	91	5
1039	182	9	1596	65	4	2093	88	5
1057	157	8	1596	67	4	2112	77	4
1079	145	8	1615	70	4	2131	66	4
1098	131	7	1615	69	4	2151	54	3
1098	137	7	1634	73	4	2172	48	3
1118	124	7	1655	78	4	2191	45	3
1137	106	6	1675	84	5	2192	43	3
1157	100	5	1694	91	5	2211	49	3
1177	90	5	1715	96	5	2211	46	3
1197	85	5	1735	107	6	2231	55	3
1218	77	4	1755	116	6	2251	60	3
1237	70	4	1774	124	6	2271	71	4
1258	68	4	1794	131	7	2290	80	4
1277	65	4	1794	137	7	2311	80	4
1297	60	3	1795	144	7	2330	80	4
1318	60	4	1814	163	8	2350	84	4
1318	58	3	1833	180	9	2370	82	4
1336	55	3	1854	204	10	2389	80	4
1357	55	3	1873	233	12	2390	80	4
1376	56	3	1894	209	10	2409	74	4
1396	54	3	1913	192	10	2428	72	4
1415	54	3	1934	192	10	2449	69	4
1437	53	3	1952	188	9	2469	71	4
1456	54	3	1972	177	9	2488	67	4
1475	54	3	1992	154	8	2508	69	4
1496	55	3	1992	178	9	2528	66	4
1516	58	3	2012	161	8	2547	66	4
1536	61	3	2031	140	7	2588	62	3
1556	62	3	2052	122	6			

Table B.14) ^{7}Li(p,p)^{7}Li differential cross section for θ_{lab}=69.5°.

Target: LiCl evaporated on ^{12}C								
$\boldsymbol{\theta_{lab} = 69.5°}$								
$\boldsymbol{E_{eff}}$ $(\boldsymbol{keV})$	$d\sigma/d\theta$ $(mb.sr^{-1})$	$\delta\,(d\sigma/d\theta)$ $(mb.sr^{-1})$	E_{eff} (keV)	$d\sigma/d\theta$ $(mb.sr^{-1})$	$\delta\,(d\sigma/d\theta)$ $(mb.sr^{-1})$	E_{eff} (keV)	$d\sigma/d\theta$ $(mb.sr^{-1})$	$\delta\,(d\sigma/d\theta)$ $(mb.sr^{-1})$
1102	123	5	1624	74	3	2176	48	2
1138	106	4	1631	73	3	2208	44	2
1171	85	4	1672	89	4	2255	61	3
1232	65	3	1713	96	4	2295	78	3
1271	64	3	1754	114	5	2339	83	4
1311	57	3	1797	140	6	2383	82	4
1350	58	3	1822	160	6	2424	83	4
1392	57	3	1843	177	7	2467	65	3
1435	60	3	1864	216	8	2491	70	3
1476	59	3	1883	240	9	2518	69	3
1517	60	3	1929	205	8	2561	64	3
1553	60	3	1975	180	7	2595	63	3
1592	66	3	2017	154	6	2644	61	3
1592	63	3	2063	127	5	2686	67	3
1624	66	3	2114	84	4			
1624	69	3	2165	49	2			

Table B.15) ^{7}Li(p,p)^{7}Li differential cross section for θ_{lab}=69.5°.

Target: LiCl evaporated on ^{12}C								
$\boldsymbol{\theta_{lab} = 90.0°}$								
$\boldsymbol{E_{eff}}$ $(\boldsymbol{keV})$	$d\sigma/d\theta$ $(mb.sr^{-1})$	$\delta\,(d\sigma/d\theta)$ $(mb.sr^{-1})$	E_{eff} (keV)	$d\sigma/d\theta$ $(mb.sr^{-1})$	$\delta\,(d\sigma/d\theta)$ $(mb.sr^{-1})$	E_{eff} (keV)	$d\sigma/d\theta$ $(mb.sr^{-1})$	$\delta\,(d\sigma/d\theta)$ $(mb.sr^{-1})$
1102	84	4	1631	62	3	2176	32	2
1138	66	3	1672	69	3	2208	25	2
1171	53	3	1713	74	3	2255	38	2
1232	42	2	1754	88	4	2295	48	2
1271	44	2	1797	102	4	2339	53	3
1311	42	2	1822	115	5	2383	56	3
1350	42	2	1843	123	5	2424	53	3
1392	38	2	1864	140	6	2467	47	2
1435	46	2	1883	145	6	2491	51	3
1517	46	2	1929	122	5	2518	43	2
1553	54	3	1975	105	4	2561	45	2
1592	53	3	2000	88	4	2595	48	2
1592	55	3	2017	93	4	2644	46	2
1624	55	3	2063	75	3	2686	44	2
1624	56	3	2114	49	2			
1624	61	3	2165	31	2			

Table B.16) ^{7}Li(p,p)^{7}Li differential cross section for θ_{lab}=90.0°.

Target: LiF evaporated on ^{12}C implanted with ^{129}Xe								
$\boldsymbol{\theta_{lab} = 90.0°}$								
$\boldsymbol{E_{eff}}$ $(\boldsymbol{keV})$	$d\sigma/d\theta$ $(mb.sr^{-1})$	$\delta\,(d\sigma/d\theta)$ $(mb.sr^{-1})$	E_{eff} (keV)	$d\sigma/d\theta$ $(mb.sr^{-1})$	$\delta\,(d\sigma/d\theta)$ $(mb.sr^{-1})$	E_{eff} (keV)	$d\sigma/d\theta$ $(mb.sr^{-1})$	$\delta\,(d\sigma/d\theta)$ $(mb.sr^{-1})$
996	100	5	1576	50	3	2072	68	4
1018	103	5	1595	49	3	2091	57	3
1039	98	5	1596	49	3	2093	53	3
1057	87	5	1596	53	3	2112	45	3
1079	75	4	1615	55	3	2131	38	2
1098	68	4	1615	56	3	2151	32	2
1098	67	4	1634	59	3	2172	27	2
1118	59	3	1655	65	4	2191	25	2
1137	54	3	1675	70	4	2192	25	2
1157	49	3	1694	70	4	2211	19	1
1177	45	3	1715	74	4	2211	27	2
1197	45	3	1735	79	4	2231	33	2
1218	48	3	1755	84	5	2251	36	2
1237	41	3	1774	89	5	2271	43	3
1258	41	3	1794	83	5	2290	45	3
1277	40	2	1794	102	5	2311	50	3
1297	36	2	1795	102	5	2330	50	3
1318	37	2	1814	108	6	2350	50	3
1318	40	2	1833	116	6	2370	52	3
1336	37	2	1854	130	7	2389	50	3
1357	42	3	1873	140	7	2390	51	3
1376	40	2	1894	120	6	2409	48	3
1396	40	2	1913	114	6	2428	47	3
1415	50	3	1934	116	6	2449	47	3
1437	41	2	1952	112	6	2469	46	3
1456	48	3	1972	107	6	2488	44	3
1475	48	3	1992	90	5	2508	43	3
1496	44	3	1992	97	5	2528	43	3
1516	47	3	2012	95	5	2547	43	3
1536	50	3	2031	86	5	2588	42	3
1556	48	3	2052	76	4			

Table B.17) $^{7}Li(p,p)^{7}Li$ differential cross section for θ_{lab}=90.0°.

Target: LiI evaporated on ^{12}C								
$\boldsymbol{\theta_{lab} = 90.0°}$								
$\boldsymbol{E_{eff}}$ $(\boldsymbol{keV})$	$d\sigma/d\theta$ $(mb.sr^{-1})$	$\delta\,(d\sigma/d\theta)$ $(mb.sr^{-1})$	E_{eff} (keV)	$d\sigma/d\theta$ $(mb.sr^{-1})$	$\delta\,(d\sigma/d\theta)$ $(mb.sr^{-1})$	E_{eff} (keV)	$d\sigma/d\theta$ $(mb.sr^{-1})$	$\delta\,(d\sigma/d\theta)$ $(mb.sr^{-1})$
1582	49	3	2090	63	4	2743	52	3
1621	60	4	2137	45	3	2797	47	3
1664	63	4	2179	29	2	2847	47	3
1703	73	4	2232	34	2	2896	48	3
1749	85	5	2278	51	3	2952	43	3
1793	98	6	2332	59	4	3008	46	3
1839	123	7	2378	56	4	3046	44	3
1880	149	8	2432	60	4	3098	41	3
1917	119	7	2483	60	4	3145	42	3
1897	129	7	2538	54	3	3196	43	3
1960	122	7	2587	51	3	3249	42	3
2001	102	6	2636	50	3	3295	43	3
2042	83	5	2691	53	3	3347	37	3

Table B.18) $^{7}Li(p,p)^{7}Li$ differential cross section for θ_{lab}=90.0°.

B.4 $^{19}F(p,p)^{19}F$ differential cross sections

Target: LiF evaporated on ^{12}C implanted with ^{129}Xe								
$\theta_{lab} = 69.5°$								
E_{eff} (keV)	$d\sigma/d\theta$ $(mb.sr^{-1})$	$\delta(d\sigma/d\theta)$ $(mb.sr^{-1})$	E_{eff} (keV)	$d\sigma/d\theta$ $(mb.sr^{-1})$	$\delta(d\sigma/d\theta)$ $(mb.sr^{-1})$	E_{eff} (keV)	$d\sigma/d\theta$ $(mb.sr^{-1})$	$\delta(d\sigma/d\theta)$ $(mb.sr^{-1})$
996	982	47	1576	407	20	2072	264	13
1018	944	45	1595	386	19	2091	242	12
1039	941	45	1596	362	18	2093	244	12
1057	889	43	1596	378	18	2112	225	11
1079	849	41	1615	361	18	2131	222	11
1098	825	40	1615	361	18	2151	211	11
1098	827	40	1634	348	17	2172	196	10
1118	807	39	1655	328	16	2191	183	9
1137	772	37	1675	298	15	2192	181	9
1157	755	37	1694	276	14	2211	164	8
1177	721	35	1715	282	14	2211	160	8
1197	700	34	1735	288	14	2231	147	7
1218	672	33	1755	284	14	2251	133	7
1237	655	32	1774	285	14	2271	125	6
1258	625	30	1794	269	13	2290	128	7
1277	583	28	1794	281	14	2311	137	7
1297	576	28	1795	287	14	2330	142	7
1318	577	28	1814	276	14	2350	155	8
1318	558	27	1833	263	13	2370	173	9
1336	544	27	1854	253	13	2389	188	9
1357	544	27	1873	250	12	2390	192	10
1376	548	27	1894	245	12	2409	192	10
1396	493	24	1913	203	10	2428	191	10
1415	359	18	1934	168	8	2449	183	9
1437	447	22	1952	230	11	2469	171	9
1456	469	23	1972	272	13	2488	159	8
1475	464	23	1992	259	13	2508	147	8
1496	452	22	1992	294	14	2528	126	6
1516	449	22	2012	293	14	2547	109	6
1536	429	21	2031	282	14	2588	97	5
1556	415	20	2052	277	14			

Table B.19) $^{19}F(p,p)^{19}F$ differential cross section for θ_{lab}=69.5°.

Target: LiF evaporated on ^{12}C implanted with ^{129}Xe								
$\boldsymbol{\theta_{lab} = 90.0°}$								
$\boldsymbol{E_{eff}}$ $(\boldsymbol{keV})$	$d\sigma/d\theta$ $(mb.sr^{-1})$	$\delta\,(d\sigma/d\theta)$ $(mb.sr^{-1})$	E_{eff} (keV)	$d\sigma/d\theta$ $(mb.sr^{-1})$	$\delta\,(d\sigma/d\theta)$ $(mb.sr^{-1})$	E_{eff} (keV)	$d\sigma/d\theta$ $(mb.sr^{-1})$	$\delta\,(d\sigma/d\theta)$ $(mb.sr^{-1})$
996	427	21	1576	195	10	2072	127	7
1018	415	20	1595	185	9	2091	117	6
1039	411	20	1596	183	9	2093	120	6
1057	404	20	1596	182	9	2112	110	6
1079	371	18	1615	175	9	2131	104	6
1098	365	18	1615	178	9	2151	112	6
1098	366	18	1634	167	9	2172	91	5
1118	355	18	1655	153	8	2191	83	4
1137	345	17	1675	141	7	2192	85	5
1157	339	17	1694	140	7	2211	72	4
1177	325	16	1715	150	8	2211	71	4
1197	316	16	1735	153	8	2231	68	4
1218	309	15	1755	157	8	2251	60	3
1237	293	15	1774	151	8	2271	58	3
1258	278	14	1794	151	8	2290	58	3
1277	260	13	1794	154	8	2311	63	4
1297	262	13	1795	154	8	2330	74	4
1318	257	13	1814	145	8	2350	83	5
1318	254	13	1833	136	7	2370	93	5
1336	241	12	1854	127	7	2389	99	5
1357	240	12	1873	122	7	2390	107	6
1376	224	11	1894	115	6	2409	97	5
1396	186	9	1913	83	5	2428	95	5
1415	161	8	1934	91	5	2449	92	5
1437	227	11	1952	141	7	2469	84	5
1456	243	12	1972	155	8	2488	76	4
1475	233	12	1992	146	8	2508	68	4
1496	226	11	1992	151	8	2528	55	3
1516	226	11	2012	144	7	2547	47	3
1536	216	11	2031	138	7	2588	46	3
1556	201	10	2052	133	7			

Table B.20) $^{19}F(p,p)^{19}F$ differential cross section for θ_{lab}=90.0°.

B.5 $^{31}P(p,p)^{31}P$ differential cross sections

Target: $Ca_3(PO_4)_2$ evaporated on Ag								
$\theta_{lab} = 155.0°$								
E_{eff} (keV)	$d\sigma/d\theta$ $(mb.sr^{-1})$	$\delta\,(d\sigma/d\theta)$ $(mb.sr^{-1})$	E_{eff} (keV)	$d\sigma/d\theta$ $(mb.sr^{-1})$	$\delta\,(d\sigma/d\theta)$ $(mb.sr^{-1})$	E_{eff} (keV)	$d\sigma/d\theta$ $(mb.sr^{-1})$	$\delta\,(d\sigma/d\theta)$ $(mb.sr^{-1})$
2611	59	6	2836	68	6	3183	48	4
2621	58	5	2840	76	6	3183	47	4
2630	47	4	2847	80	7	3202	46	4
2640	54	5	2855	136	11	3207	33	3
2652	42	4	2860	111	9	3209	37	4
2661	45	4	2862	91	8	3212	30	3
2662	36	3	2863	89	7	3217	31	3
2664	47	4	2867	92	8	3222	34	3
2668	36	3	2869	93	8	3223	37	4
2670	34	3	2871	97	8	3227	42	4
2672	38	4	2879	82	7	3232	31	3
2676	39	4	2887	75	6	3237	38	4
2680	38	4	2895	70	6	3242	51	5
2688	43	4	2903	65	6	3247	69	6
2696	45	4	2907	60	5	3247	63	6
2704	40	4	2911	56	5	3247	86	7
2712	40	4	2919	59	5	3252	56	5
2720	25	3	2927	50	5	3254	46	4
2728	35	3	2935	42	4	3257	53	5
2732	45	4	2943	45	4	3262	46	4
2736	44	4	2951	37	4	3267	52	5
2740	54	5	2955	31	3	3272	47	4
2744	55	5	2959	23	3	3277	50	5
2752	69	6	2963	19	2	3282	42	4
2760	62	5	2967	23	2	3287	60	5
2767	48	4	2975	28	3	3292	78	7
2776	53	5	2984	31	3	3317	44	4
2784	53	5	2984	33	3	3337	41	4
2792	42	4	2988	29	3	3357	38	4
2800	38	4	2992	22	2	3367	36	4
2808	38	4	3054	38	4	3376	40	4
2815	39	4	3057	51	5	3386	50	5
2823	35	3	3061	62	5	3397	49	4
2828	34	3	3091	65	6	3406	50	5
2832	50	5	3098	56	5	3416	44	4
2834	54	5	3102	57	5	3427	31	3
3437	24	3	3596	61	5	3747	61	17
3439	21	2	3597	61	5	3750	69	6
3440	30	3	3599	56	5	3753	76	7

3441	34	3	3599	58	5	3755	75	6
3444	52	5	3601	65	6	3757	72	6
3446	47	4	3603	61	5	3760	73	6
3451	50	5	3606	61	5	3764	75	6
3456	49	4	3611	66	6	3766	71	6
3461	41	4	3615	60	5	3770	75	6
3466	47	4	3620	64	6	3775	62	5
3471	40	4	3625	60	5	3782	62	5
3476	39	4	3630	64	6	3786	70	6
3482	40	4	3635	61	5	3791	78	7
3486	44	4	3640	63	6	3796	82	7
3491	40	4	3645	66	6	3798	78	7
3498	43	4	3649	54	5	3802	75	6
3502	43	4	3653	51	5	3804	72	6
3507	43	4	3655	49	4	3807	70	6
3512	42	4	3659	52	5	3810	70	6
3514	46	4	3664	55	5	3814	62	5
3516	42	4	3669	53	5	3818	62	5
3517	43	4	3672	60	5	3820	67	6
3518	48	4	3677	53	16	3822	71	6
3520	41	4	3682	56	5	3826	65	6
3524	44	4	3687	59	5	3831	69	6
3528	44	4	3692	60	5	3836	63	6
3532	43	4	3697	54	5	3839	53	5
3536	45	4	3701	63	6	3843	77	7
3540	41	4	3706	49	4	3849	86	7
3544	42	4	3712	57	5	3853	77	7
3547	40	4	3717	54	5	3857	72	6
3552	44	4	3722	54	5	3862	82	7
3556	49	5	3727	54	5	3866	77	7
3560	55	5	3730	48	4	3871	66	6
3564	55	5	3732	49	4	3877	67	6
3568	58	5	3734	60	5	3882	66	6
3570	61	5	3737	68	6	3887	62	5
3576	62	5	3739	68	6	3891	68	6
3580	63	6	3740	71	6	3896	68	6
3583	58	5	3742	67	6	3901	67	6
3588	65	6	3743	62	5	3906	73	6
3592	59	5	3745	59	5	3911	56	5
3595	58	5	3596	61	5	3916	59	5
3920	58	5	3935	65	6	3947	61	5
3925	62	5	3940	69	6	3950	61	5
3929	63	6	3943	64	6			

Table B.21) $^{31}P(p,p)^{31}P$ differential cross section for θ_{lab}=155.0°.

Appendix C

C.1 ^{7}Li(p,p)^{7}Li angular distributions

Target: LiF evaporated on ^{12}C implanted with ^{129}Xe								
$\boldsymbol{E_{eff} = 1596\ keV}$			$E_{eff} = 1794\ keV$			$E_{eff} = 1992\ keV$		
$\boldsymbol{\theta_{lab}}(°)$	$d\sigma/d\theta$ $(mb.sr^{-1})$	$\delta\,(d\sigma/d\theta)$ $(mb.sr^{-1})$	$\theta_{lab}(°)$	$d\sigma/d\theta$ $(mb.sr^{-1})$	$\delta\,(d\sigma/d\theta)$ $(mb.sr^{-1})$	$\theta_{lab}(°)$	$d\sigma/d\theta$ $(mb.sr^{-1})$	$\delta\,(d\sigma/d\theta)$ $(mb.sr^{-1})$
59.5	78	4	59.5	153	8	59.5	202	10
69.5	65	4	69.5	131	7	69.5	154	8
70	63	4	70	130	7	70	151	8
80	56	3	80	107	6	80	107	6
90	49	3	90	83	5	90	90	5
$\boldsymbol{E_{eff} = 2192\ keV}$			$E_{eff} = 2390\ keV$			$E_{eff} = 2588\ keV$		
$\boldsymbol{\theta_{lab}}(°)$	$d\sigma/d\theta$ $(mb.sr^{-1})$	$\delta\,(d\sigma/d\theta)$ $(mb.sr^{-1})$	$\theta_{lab}(°)$	$d\sigma/d\theta$ $(mb.sr^{-1})$	$\delta\,(d\sigma/d\theta)$ $(mb.sr^{-1})$	$\theta_{lab}(°)$	$d\sigma/d\theta$ $(mb.sr^{-1})$	$\delta\,(d\sigma/d\theta)$ $(mb.sr^{-1})$
49.5	102	5	59.5	132	7	49.5	145	7
59.5	67	4	69.5	80	4	59.5	103	5
69.5	43	3	70	81	4	60	100	5
70	41	3	80	60	3	69.5	62	3
80	31	2	90	51	3	70	65	4
90	25	2				80	49	3
						90	42	3

Table C.1) ^{7}Li(p,p)^{7}Li angular distributions (LiF target).

Target: LiCl evaporated on ^{12}C								
$E_{eff} = 1624\ keV$			$E_{eff} = 1822\ keV$			$E_{eff} = 2000\ keV$		
$\theta_{lab}(°)$	$d\sigma/d\theta$ $(mb.sr^{-1})$	$\delta\,(d\sigma/d\theta)$ $(mb.sr^{-1})$	$\theta_{lab}(°)$	$d\sigma/d\theta$ $(mb.sr^{-1})$	$\delta\,(d\sigma/d\theta)$ $(mb.sr^{-1})$	$\theta_{lab}(°)$	$d\sigma/d\theta$ $(mb.sr^{-1})$	$\delta\,(d\sigma/d\theta)$ $(mb.sr^{-1})$
59.5	76	3	49.5	233	9	59.5	188	9
69.5	69	3	59.5	185	7	70	146	10
70	69	3	69.5	160	6	80	117	6
80	66	3	70	163	6	90	88	4
90	56	3	80	141	6			
			90	115	5			
$E_{eff} = 2176\ keV$			$E_{eff} = 2491\ keV$					
$\theta_{lab}(°)$	$d\sigma/d\theta$ $(mb.sr^{-1})$	$\delta\,(d\sigma/d\theta)$ $(mb.sr^{-1})$	$\theta_{lab}(°)$	$d\sigma/d\theta$ $(mb.sr^{-1})$	$\delta\,(d\sigma/d\theta)$ $(mb.sr^{-1})$			
49.5	133	5	49.5	175	7			
59.5	84	4	59.5	111	5			
69.5	48	2	69.5	70	3			
70	51	3	70	70	3			
80	39	2	80	61	3			
90	32	2	90	51	3			

Table C.2) ^{7}Li(p,p)^{7}Li angular distributions (LiCl target).

C.2 ^{19}F(p,p)^{19}F angular distributions

Target: LiF evaporated on ^{12}C implanted with ^{129}Xe								
$E_{eff} = 1596\ keV$			$E_{eff} = 1794\ keV$			$E_{eff} = 1992\ keV$		
$\theta_{lab}(°)$	$d\sigma/d\theta$ $(mb.sr^{-1})$	$\delta\,(d\sigma/d\theta)$ $(mb.sr^{-1})$	$\theta_{lab}(°)$	$d\sigma/d\theta$ $(mb.sr^{-1})$	$\delta\,(d\sigma/d\theta)$ $(mb.sr^{-1})$	$\theta_{lab}(°)$	$d\sigma/d\theta$ $(mb.sr^{-1})$	$\delta\,(d\sigma/d\theta)$ $(mb.sr^{-1})$
59.5	599	29	59.5	428	21	49.5	626	30
69.5	362	18	69.5	269	13	59.5	389	19
70	362	18	70	274	14	69.5	259	13
80	251	13	80	200	10	70	276	14
90	183	9	90	151	8	80	196	10
$E_{eff} = 2192\ keV$			$E_{eff} = 2390\ keV$			$E_{eff} = 2588\ keV$		
$\theta_{lab}(°)$	$d\sigma/d\theta$ $(mb.sr^{-1})$	$\delta\,(d\sigma/d\theta)$ $(mb.sr^{-1})$	$\theta_{lab}(°)$	$d\sigma/d\theta$ $(mb.sr^{-1})$	$\delta\,(d\sigma/d\theta)$ $(mb.sr^{-1})$	$\theta_{lab}(°)$	$d\sigma/d\theta$ $(mb.sr^{-1})$	$\delta\,(d\sigma/d\theta)$ $(mb.sr^{-1})$
49.5	541	26	59.5	273	14	49.5	318	16
59.5	290	14	69.5	192	10	59.5	167	9
69.5	181	9	70	200	10	60	159	8
70	179	9	80	137	7	69.5	97	5
80	120	6	90	107	6	70	101	5
90	85	5				80	65	4
						90	46	3

Table C.3) ^{19}F(p,p)^{19}F angular distributions (LiF target).